Dense, room-temperature polarized nuclear targets using SABRE chemical hyperpolarization

Benjamin G. Collins

PhD

University of York

Physics, Engineering and Technology

April 2025

Abstract

Polarized nuclear targets are a crucial tool in particle physics experiments for accessing spin-dependent observables. Current experiments use dynamic nuclear polarization (DNP) to generate high levels of spin order, achieving polarization levels in excess of 90% for the ^{1}H nucleus [1,2]. While DNP targets have been very successful, they suffer from depolarization effects with high intensity beams and thus are unable to be used at the intensity frontier with the upcoming generation of accelerator facilities.

This thesis assesses the capability of a recently developed nuclear polarization technique, Signal Amplification By Reversible Exchange (SABRE), to address the issues facing DNP targets. SABRE catalytically converts the high spin order of *para*hydrogen into nuclear spin polarization. It operates in the solution state at room temperature within weak applied fields, generating the polarization on timescales of seconds.

Chapter 2 assesses the factors that affect polarization transfer efficiency through SABRE, also presenting the synthesis of a novel selectively-deuterated substrate for SABRE, 3,5-pyridine-d_2. In Chapter 3, the factors affecting spin order relaxation in SABRE substrates are investigated, finding that the minimal rate of spin order relaxation for 3,5-dichloropyridine is achieved at close to room temperature and in fields not exceeding 1 tesla. Chapter 4 presents the first in-beam measurements of the resilience of SABRE-polarized material to an incident particle beam, performed at the Mainz Microtron facility. Here it is found that there is no evidence for a depolarizing effect in the samples subject to the A2 photon beam, and that a sample subject to a high radiation dose from proximity to the electron beam dump in the A2 Hall exhibited significant repolarizability. In Chapter 5, the development and performance of a prototype SABRE-polarized target is presented, with polarization levels in excess of 20% being achieved with the substrate 3,5-pyridine-d_2.

Author's declaration

I declare that this thesis is a presentation of original work and I am the sole author. This work has not previously been presented for a degree or other qualification at this University or elsewhere. All sources are acknowledged as references. I acknowledge that I received assistance from my supervisor and software assistance to proofread this thesis in line with the Policy on Transparency in Authorship in PGR Programmes.

The synthesis of the iridium precatalysts used throughout this work was performed by Dr Victoria Annis, Dr Peter J. Rayner or Dr Kieren J. Evans. The synthesis of the compound 3,5-pyridine-d_2 presented in Chapter 2 was performed by Elliott Crocker. The inverse Henry's constants for various solvents presented in Chapter 2 were found by Dr Callum A. Gater and Orry J. Mayne, alongside some of the catalyst solubility measurements. Photon flux measurements at MAMI, used in Chapter 4, were conducted by Mamad Eslami. Geant4 simulation results of particle energy depositions, also used in Chapter 4, were performed by Dr Mikhail Bashkanov.

Portions of the work presented in this thesis have been presented in the publications listed below.

- C. A. Gater, O. J. Mayne, B. G. Collins, K. J. Evans, E. M. Storr, A. C. Whitwood, D. P. Watts, B. J. Tickner, and S. B. Duckett, The Journal of Physical Chemistry Letters 16, 510 (2024).
- B. J. Tickner, M. Dennington, B. G. Collins, C. A. Gater, T. F. Tanner, A. C. Whitwood, P. J. Rayner, D. P. Watts, and S. B. Duckett, ACS catalysis 14, 994 (2024).

Acknowledgements

I would firstly like to thank my supervisors Dan Watts and Nick Zachariou for their support and advice throughout this PhD. Dan, you have always been supportive of my work and have helped motivate me to achieve. Thank you for allowing me the freedom to influence the direction of the project, I am a better scientist for it. Nick, I am very grateful for the help you have given me with Geant4 and ROOT over the years.

A massive thank you must go out to Simon Duckett, who has been more than generous with his time since I arrived at CHyM, and has continuously provided valuable insights, making the project what it is. Big thanks must also go to Mikhail Bashkanov for his contributions to the experiment at MAMI and our productive discussions.

I would like to acknowledge the support of the Budker group at JGU Mainz who were especially welcoming and without whom the experiment at MAMI would not have been possible. In particular, thank you to Raphael for dropping everything to assist me and for putting up with my many requests.

To Callum, thanks for almost singlehandedly teaching me NMR spectroscopy and for answering my incessant questions over the years. I don't know where I would have been without you. I had the privilege of attending your wedding recently and I wish you many happy years with your lovely wife. To Vicky L, thank you for acting as my office therapist and for always being a calming influence. To Ben T, thank you for your friendship and for indulging my love of gossip. To Vicky A, thank you for all the help you have provided me with and sorry for all the times I forgot to do lab duty! To the members of CHyM, past and present, thank you all for making me feel welcome and for making CHyM an enjoyable place to work.

To Ali, thank you for keeping me sane for the last three and a half years. Our pub trips and trips to the climbing wall have provided some much-needed relief from work, and your friendship has been invaluable to me. When we first met, we decided we would drink at every pub in York during the PhD. While we didn't quite achieve this, we sure gave it a good go!

To my amazing girlfriend Helena, thank you for all you've done for me. From your endless support, to providing me somewhere to stay when I was (temporarily) homeless, to our adventures across Yorkshire which have been some of the best days of my life. I would not be the man I am today without your guiding influence.

To Rhys, Joe, Nathan, and Kieran, thanks for your continued friendship over the years, and for listening to (or at least pretending to) my explanations of spin physics.

To my family, thank you for always believing in me, it has never gone unappreciated. You have always provided a welcome escape from the stresses of work and have helped me keep things in perspective.

List of Contents

List of Figures

List of Tables

Chapter 1 - Introduction

This chapter will provide the theoretical background and an overview of the literature that will aid in understanding the aims and contents of this thesis. The primary aim of this thesis is to evaluate the capability of a recently developed nuclear polarization method, Signal Amplification By Reversible Exchange (SABRE), to address the shortfalls of current polarized nuclear targets in nuclear and particle physics. It will start with an overview of the current status of polarized targets, the impact they have had on the field to date, and the challenges they face at the intensity frontier of particle beam experiments. It will be followed by a section explaining the fundamentals of magnetic resonance imaging, which has been a crucial tool for the study of polarized media in this thesis. Following this will be a review of *para*hydrogen-based polarization methods, with a focus on the SABRE nuclear polarization method. Lastly, there will be a summary of the aims of this thesis.

1.1 Polarized nuclear targets

A polarized nuclear target is a material in which there is a high alignment of the nuclear spins in a specified direction, resulting in a net polarization, that is used for scattering experiments in particle physics. Polarized targets are a highly desirable fixture at particle beam facilities internationally. The scattering (or absorption) of particles by nuclear targets in which the intrinsic spin of the nucleus can be oriented in space gives access to observables that are far more powerful than measuring cross-sections alone. Since the development of polarized nuclear targets in the 1960s, major programmes utilizing them have been instigated at the world's leading facilities. These have revealed the nature of the structure of nucleons and tested the fundamentals of quantum chromodynamics.

At the nucleonic level, measurements of the proton and deuteron spin structure functions g_1 and g_2 have provided information on how the spin of a nucleon derives from its constituent quarks and gluons. The measurements have been made at SLAC [3,4], CERN [5] and DESY [6] using polarized lepton beams and polarized proton/deuteron targets. Additionally, polarized photon beams have been used with polarized targets at Mainz [7] and Bonn [8] in order to experimentally verify the Gerasimov-Drell-Hearn (GDH) sum rule, which relies on the base assumptions of quantum field theory.

1.1.1 Introduction to polarized nuclear targets

The degree of polarization of the target material in a polarized nuclear target is quantified by the parameter P, where:

$$P = \frac{N_\uparrow - N_\downarrow}{N_\uparrow + N_\downarrow}. \qquad (Eq. 1.1)$$

Here, $N_\uparrow$ and $N_\downarrow$ are the populations of the spin states that are aligned parallel (spin up) and antiparallel (spin down) to the measurement axis. A value of $P = 1$ denotes a complete alignment of the spins in one direction, whilst $P = 0$ signifies no net alignment. The thermal equilibrium polarization for electrons, protons, and nuclei with a spin quantum number of ½ is given by:

$$P_{TE} = \frac{N_\uparrow - N_\downarrow}{N_\uparrow + N_\downarrow} = \tanh\left(\frac{\gamma \hbar B_0}{2k_B T}\right) \qquad (Eq. 1.2)$$

where $\hbar$ is the reduced Planck constant, k_B is the Boltzmann constant, T is the temperature, γ is the gyromagnetic ratio and B_0 is the magnitude of the applied field.

As can be seen from Eq. 1.2, the thermal equilibrium polarization of protons increases with increasing magnetic field strength and decreasing temperature, however even at conditions such as 2.5 T and 1 K, the expected polarization of the proton is only 0.25%. For harnessing polarized targets for spin-dependent scattering effects it is necessary to have a polarization as close to unity as possible, and thus it is clear that polarized nuclear targets need to make use of non-equilibrium polarization levels.

The first step towards polarized nuclear targets was taken in 1953 with Overhauser's proposal that the high equilibrium polarization of the electron could be harnessed for nuclear polarization [9]. He proposed that this could be achieved by creating a large population difference in the spins of conduction band electrons in metals, where the transfer of electronic spin to nuclear spin could be induced through microwave irradiation. This proposal suggested a method for achieving high nuclear polarizations which would have otherwise been unachievable, and utilized the fact that the gyromagnetic ratio of the electron is orders of magnitude higher than that of the proton, shown in Table 1.1. Under the aforementioned conditions of 2.5 T and 1 K, the thermal equilibrium polarization of the electron is 92%.

Table 1.1 - Gyromagnetic ratios of the electron and proton.

Particle	Gyromagnetic ratio, γ (rad s^{-1} T^{-1})
Electron	1.761×10^{11}
Proton	2.675×10^{8}

Overhauser's proposal was experimentally verified by Carver et al. in the same year [10], and the proposal was extended to non-metals by Abragam in 1955 [11]. The first experiment using a polarized nuclear target was performed by Abragam et al. at Saclay in 1962 [12] and was quickly followed by the first high energy experiment performed by Chamberlain et al. at Berkeley [13]. This experiment involved pion-proton scattering on polarized protons in a crystalline LMN ($La_2Mg_3(NO_3)_{12}\bullet 24H_2O$) target produced using a method developed by Leifson and Jeffries termed dynamic nuclear polarization (DNP) [14].

After first being termed the 'Overhauser effect' and later the 'Solid effect', dynamic nuclear polarization became the agreed term for the nuclear polarization technique that made use of transferring polarization from electron spins to nuclear spins using microwave irradiation at their resonance frequency in a strong magnetic field. The ongoing development of the DNP process has made it possible to polarize ^{1}H and ^{2}H spins up to levels exceeding 90% and 50% respectively [1], however the average polarization of a polarized target during operation is often less than this due to beam-induced depolarization effects [15], which will be discussed further in Chapter 4. The DNP technique has also been applied to other nuclei, with notable results including 75% ^{13}C polarization in pyruvic acid [16], 80% ^{19}F polarization in hexafluoroisopropanol [17] and the observation of DNP-enhanced ^{17}O signals in water [18].

1.1.2 DNP polarization mechanism

A simplistic explanation of the mechanism behind DNP is as follows. The target material is prepared by first doping a suitable solution of it with paramagnetic radicals before solidifying it by cooling to temperatures of around 1 K at fields of a few teslas (for NH_3 targets the radicals are provided by irradiation of the NH_3 using an electron beam). Here the radicals provide the necessary unpaired electron spins for DNP.

The dipole-dipole interaction between the electron and nucleon spins brings the spin populations into contact. Through microwave irradiation at close to the electron spin resonance frequency, polarization can be transferred from the electron spins to the nuclear spins by utilizing the hyperfine interaction [19]. Changes in the microwave frequency allow for the selection of polarization parallel or antiparallel to the applied field [19].

DNP makes use of the fact that the longitudinal relaxation rate of electrons (the rate at which the spins return to thermal equilibrium polarization) is much faster than that of protons, meaning that many electron-to-proton spin transitions can occur before a proton spin relaxes towards equilibrium.

1.1.3 Experimental considerations of polarized nuclear targets

Important criteria for target materials in polarized targets are as follows:

a) Degree of polarization, P.
b) Dilution factor, f.
c) Areal density, N (nucleons cm^{-2}).
d) Polarization build-up time (s).
e) Resistance to radiation damage.
f) Presence of other polarizable nuclei.

Here the dilution factor can be thought of as the 'useful' fraction of nucleons in the target material, and can be calculated as:

$$f = \frac{Number\ of\ polarizable\ nucleons}{Total\ number\ of\ nucleons}. \qquad (Eq.1.3)$$

The areal density of the material, N (nucleons cm^{-2}), can be combined with the beam intensity, I (particles s^{-1}), to form the beam luminosity, $L = NI$, where L has units of Hz cm^{-2}.

The degree of polarization, dilution factor, and beam luminosity can then be combined to produce a quantity called the Figure of Merit (FoM):

$$FoM = Lf^2P^2. \qquad (Eq.1.4)$$

This quantity is crucial to determining the effectiveness of a polarized target, as the productivity of a scattering experiment is proportional to the FoM. For example, halving the polarization will increase the running time needed for an experiment to achieve a specified accuracy by a factor of four.

1.1.4 Continuously polarized, frozen-spin and brute force targets

Polarized nuclear targets have been used at numerous accelerator facilities worldwide, however they have been a particular focus of Hall B at Jefferson Lab, where currently all three forms of solid polarized target (continuously polarized, frozen-spin and brute force) are utilized [20]. In fact,

Jefferson Lab has currently allocated one third of the beam time at Hall B's upgraded CLAS12 detector to polarized targets [21]. For this reason, polarized targets at Jefferson Lab will feature heavily in this section.

Continuously polarized

Continuously polarized targets were the first type of DNP polarized target and are typically used for high luminosity experiments that are prone to beam-induced depolarization effects, thus needing continual replenishment of the polarization. Typical operating conditions are around 5 T and 1 K, provided by superconducting magnets and a ^{3}He or ^{4}He evaporation refrigerator [19].

Initial experiments used an LMN target [13], however a transition was made to target materials with a higher dilution factor such as butanol [22], propanediol [23], and ammonia [24]. Butanol and propanediol targets are typically chemically doped with the radicals necessary for DNP [25], whereas for ammonia targets the radicals are produced by irradiation of the target material [24]. NH_3 targets typically have higher radiation resistance than alcohol or diol targets [19], however they also contain the unwanted polarized background nuclei ^{14}N and ^{15}N.

Hall B at Jefferson Lab has recently constructed a new longitudinally-polarized continuously polarized target for use with the CLAS12 upgrade [21]. Here the operating conditions are 5 T, provided by the CLAS12 solenoid, and 1 K, provided using a ^{4}He evaporation refrigerator, with the target samples consisting of mm-sized beads of frozen NH_3/ND_3. This target is anticipated to be able to operate with luminosities an order of magnitude higher than the previous generation [21].

A key drawback of continuously polarized targets is their reliance on ^{3}He or ^{4}He evaporation refrigerators, which necessitate constant operation due to the relatively short nucleon relaxation time constant (T_1) at these temperatures. In contrast, dilution refrigerators can achieve lower temperatures, extending the T_1 and reducing the need for continuous polarization. Continuous polarization brings constraints on the acceptance angles of the spectrometer due to the large size of the superconducting magnets needed. These constraints are particularly restrictive for low luminosity experiments that desire a large angular acceptance from the spectrometer in order to maximise counting rates. Continuously polarized targets do however benefit from a higher rate of cooling power due to the use of an evaporation refrigerator, increasing the usable beam currents.

Frozen-spin

This poor angular acceptance of continuously polarized targets was addressed by the advent of 'frozen-spin' targets [26], made possible due to the development of ^{3}He/^{4}He dilution refrigerators capable of temperatures as low as 50 mK. Frozen-spin targets utilize the strong temperature and

field dependence of the nucleon relaxation rate, with the T_1 extending from minutes at 1 K to days below 100 mK [19]. Thus, the principle of frozen-spin target operation is to polarize the material under regular DNP conditions (e.g. 5 T, 1 K), then maintain the polarization by dropping the temperature to around 50 mK. This allows for a lower strength holding field to be used whilst maintaining a long T_1. These holding fields can be provided by much smaller magnets which can allow for angular acceptance of the spectrometer of almost 4π.

Frozen-spin targets have been implemented at numerous facilities including at MAMI [27], Bonn [28] and Jefferson Lab [2]. One such example is the frozen-spin target at Hall B at Jefferson lab, FROST [2], designed to be complementary to the continuously polarized target at Hall B [1]. The existing continuously polarized target had been used with strong electron beam currents of up to 10 nA, however the 5 T superconducting magnet that was used for polarizing limited the spectrometer's acceptance of forward-scattered particles to ± 55°. This made it ill-suited to the photoproduction studies that were due to take place for the NSTAR programme for which maximising angular acceptance was crucial [2]. The smaller 0.56 T and 0.5 T superconducting holding magnets used in FROST, shown in Figure 1.1, allowed angular acceptance to be increased to ±135°, with the added benefit that the frozen-spin target can provide either longitudinal or transverse polarization, a feature not available for the continuously polarized target.

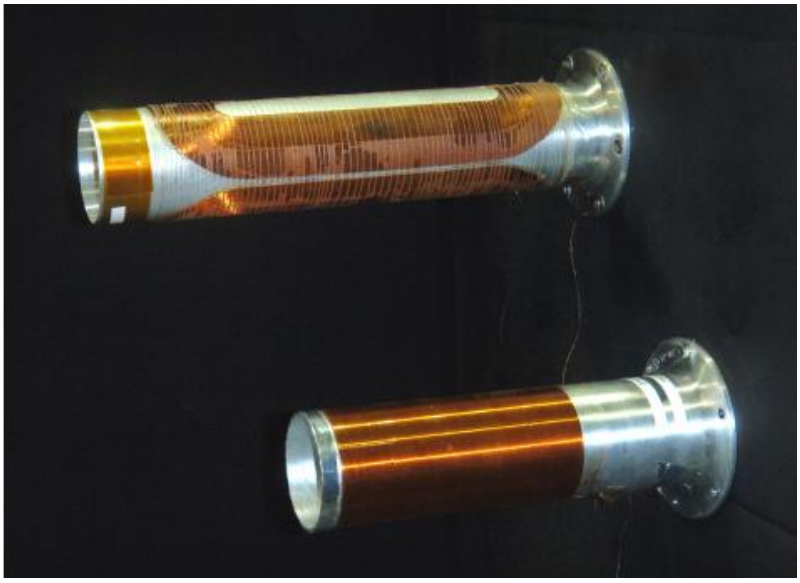

Figure 1.1 - Superconducting coils used to maintain the polarization of the FROST target in frozen-spin mode for runs g9b (top) and g9a (bottom). The holding coil for run g9a measures just 110 mm long and 50 mm in diameter. From [2].

The target material used in FROST was butanol doped with the nitroxyl radical TEMPO ((2,2,6,6-Tetramethylpiperidin-1-yl)oxyl). The butanol was formed into frozen beads before the addition of the radical, followed by the addition of water prior to freezing to ensure the formation of a non-crystalline solid. The target was able to be polarized up to around 90% outside the spectrometer over the course of 5-6 hours, using conditions of 5 T and 200-300 mK [2].

Once the polarized target was returned to the spectrometer, operation was performed in the holding magnets while the target was maintained at temperatures of 30 mK. Figure 1.2 shows a schematic of how FROST may be operated in a typical experiment. FROST was used in a so-called "complete" photoproduction experiment whereby all combinations of a circularly/linearly polarized photon beam and a longitudinally/transversely polarized target were used, and facilitated the investigation of excited baryonic states as part of Jefferson Lab's NSTAR programme.

A notable feature of frozen-spin targets is the extremely long lifetimes of the polarization that are achievable. Figure 1.3 shows how the relaxation rate of the proton polarization depends on temperature in the absence of the beam, demonstrating results for the frozen-spin targets at Bonn and Jefferson Lab. It can be seen that for FROST, at temperatures of 30 mK the T_1 extends to 4000 hours (167 days), taking over two weeks for the polarization to drop by 10%. With beam-on running a polarization loss of around 1% per day was experienced and data collecting runs lasted for 5-10 days before the target was repolarized [2].

Despite these successes, it must be noted that frozen-spin targets are limited to low beam intensity experiments as the cooling power of ^{3}He/^{4}He dilution refrigerators is restricted by the phenomenon of Kapitza resistance [29], whereby thermal phonons are unable to cross the interface between the helium and the target. This low cooling power restricts the rate of energy deposition that can occur whilst keeping the target material within the necessary temperature range for frozen-spin operation.

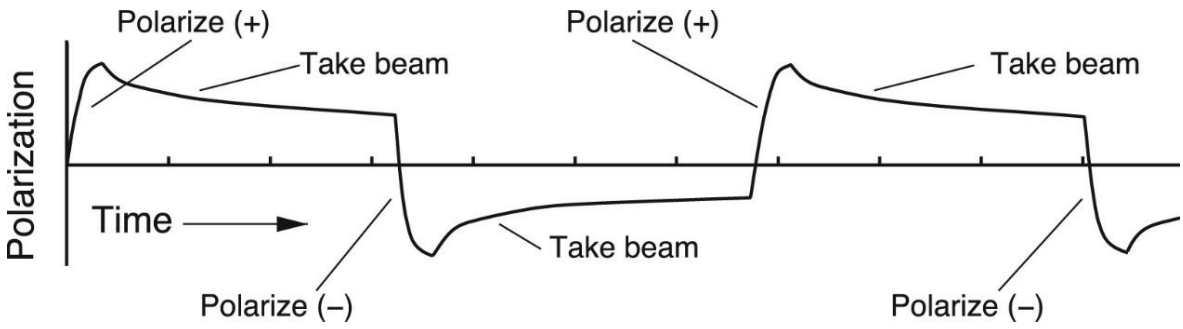

Figure 1.2 - Schematic of the operation of the FROST target at Jefferson Lab. From [2].

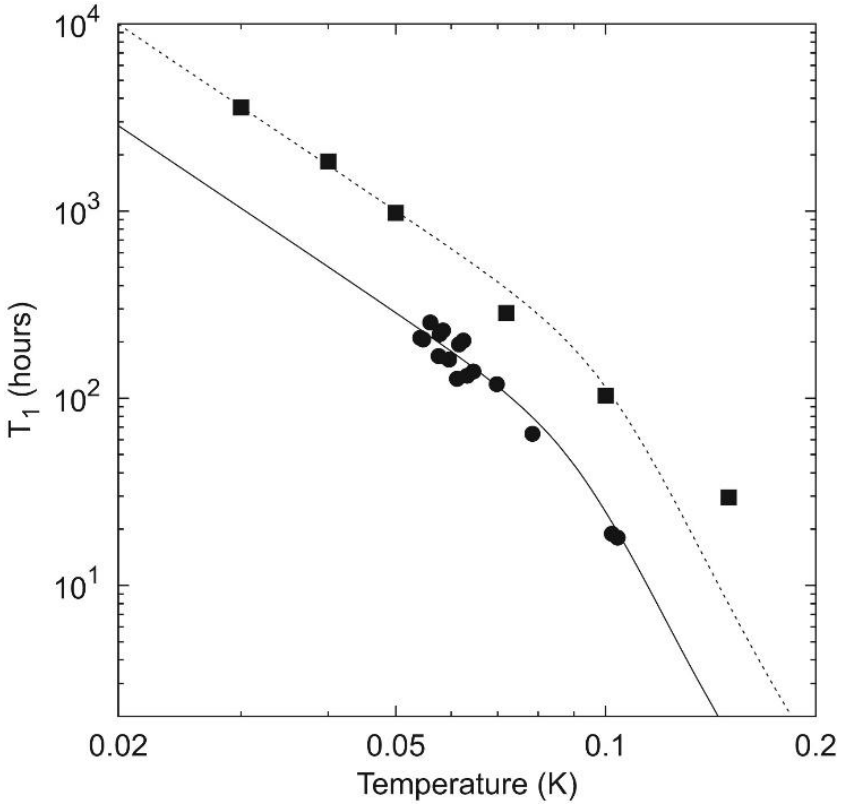

Figure 1.3 - Proton polarization relaxation constant as a function of temperature, measured for the Bonn frozen-spin target at 0.42 T (circles) and the Jefferson Lab frozen-spin target at 0.56 T (squares). From [2].

Brute force

An interesting development coming from the advent of frozen-spin polarized targets is the use of 'brute force' polarized targets, making use of thermal equilibrium polarization without the need for radicals or microwave irradiation. Brute force polarized targets of HD (hydrogen deuteride) were first proposed by Honig in 1967 [30] for their high dilution factor, where both ^{1}H and ^{2}H can be polarized, giving dilution factors of 0.67 and 0.33 respectively. The only material bettering this dilution factor for protons would be molecular hydrogen, however this converts to its magnetically inert *para* state at low temperatures making it unable to be polarized. The drawbacks of brute force polarization are that without the utilization of the short relaxation constant of the electrons as in DNP, polarization build-up is exceptionally slow.

An example of the utilization of a brute force polarized target is HDice, used at Hall B at Jefferson Lab [31]. Here, in order to achieve the necessary high thermal equilibrium polarization of the nucleons the polarizing conditions used were 15 T and 10 mK, significantly more extreme conditions than are necessary for DNP.

In order to address the long polarization build-up times, the HD target was doped with small quantities of *ortho*-H_2 (*o*-H_2) and *para*-D_2 (*p*-D_2) which polarize on much shorter time scales and readily transfer spin to HD. As *o*-H_2 and *p*-D_2 are meta-stable states, they eventually decay back to their magnetically inert states. This process happens whilst the polarization of the HD target builds up, allowing the target to exhibit a long T_1 post-polarizing [19]. Even after doping, the polarization build-up on an HD target takes months [20].

Brute force targets are also operated in frozen-spin mode, meaning that lower strength 'holding' fields can be used during operation. HDice was successfully used at Jefferson Lab for tagged photon experiments [20], however experiments with electron beams showed rapid depolarization effects due to the production of radicals in the target material [31].

1.1.5 The 'Proton spin crisis'

One of the most notable uses of polarized targets in nuclear and particle physics is in the investigation into how the spin of nucleons is distributed amongst their constituent partons, the valence quarks, sea quarks and gluons. The distribution of spin in the proton is parametrised by the proton structure function, g_1, and has been a key subject of interest in the particle physics community for decades [32].

In 1988 an experiment studying the structure factor g_1 was performed by the European Muon Collaboration (EMC) at CERN using a beam of polarized muons and a polarized target [5]. Here they obtained a result that sent shockwaves through the field - the proportion of the spin of the proton that came from the valence quarks was consistent with zero to within error. This result sparked the problem known as the "proton spin crisis" which has still not been definitively resolved to this day.

In the experiment by the EMC, g_1 was calculated using the virtual-photon spin-dependent asymmetry A_1, where A_1 was a measured scattering asymmetry

$$A_1 \propto A = \frac{d\sigma^{\uparrow\downarrow} - d\sigma^{\uparrow\uparrow}}{d\sigma^{\uparrow\downarrow} + d\sigma^{\uparrow\uparrow}} \qquad (Eq.\ 1.5)$$

and $d\sigma^{\uparrow\uparrow\,(\uparrow\downarrow)}$ is the cross section when the lepton and nucleon spins are parallel (antiparallel).

1.1.6 Trouble at the intensity frontier

With a new generation of accelerator facilities, there is a need for polarized targets that can operate at the intensity frontier, such as with the 12 GeV upgrade at Jefferson Lab and the upcoming Electron-Ion Collider at Brookhaven National Laboratory. The luminosity and beam energy achievable by this new generation of particle accelerator capable of e-p scattering (key for new physics searches) is shown relative to current generation facilities in Figure 1.4.

Depolarization effects are frequently observed in current polarized target experiments and will only get worse with increasing beam energies and luminosities. These effects have been observed for all forms of solid polarized target, including the brute force target HDice [31], the frozen-spin NH_3 target at COMPASS [15], and the continuously polarized NH_3 targets used SLAC and at CLAS12 [33,34].

The main mechanisms for depolarization are beam-heating effects, taking the target away from its optimal operating temperature, and the production of paramagnetic radicals, which cause relaxation through dipole interactions. For the upgraded continuously polarized target at Jefferson Lab Hall B, part of the newest generation of DNP targets, the target material has to be replaced every 2-3 days of running at 8 nA due to radiation damage [35]. For the upcoming Electron-Ion Collider at Brookhaven, the projected beam current for e-p scattering at 12 GeV is 2.5 A, over two orders of magnitude higher than at Hall B. DNP targets are unable to be used under these conditions, and thus there is a desire for polarized target technologies that can.

An example of such a technology that could address the issues with DNP and brute force targets is the nuclear polarization method Signal Amplification By Reversible Exchange (SABRE) which will be discussed in Section 1.4. SABRE is a technique that catalytically transfers spin order from a spin isomer of molecular hydrogen (called *para*hydrogen) to the target material, operating at room temperature and building up polarization on timescales of seconds to minutes, rather than hours. Room temperature operation should mean that SABRE is less sensitive to beam heating effects, and fast polarization build-up should make SABRE more resilient to radical-induced depolarization effects.

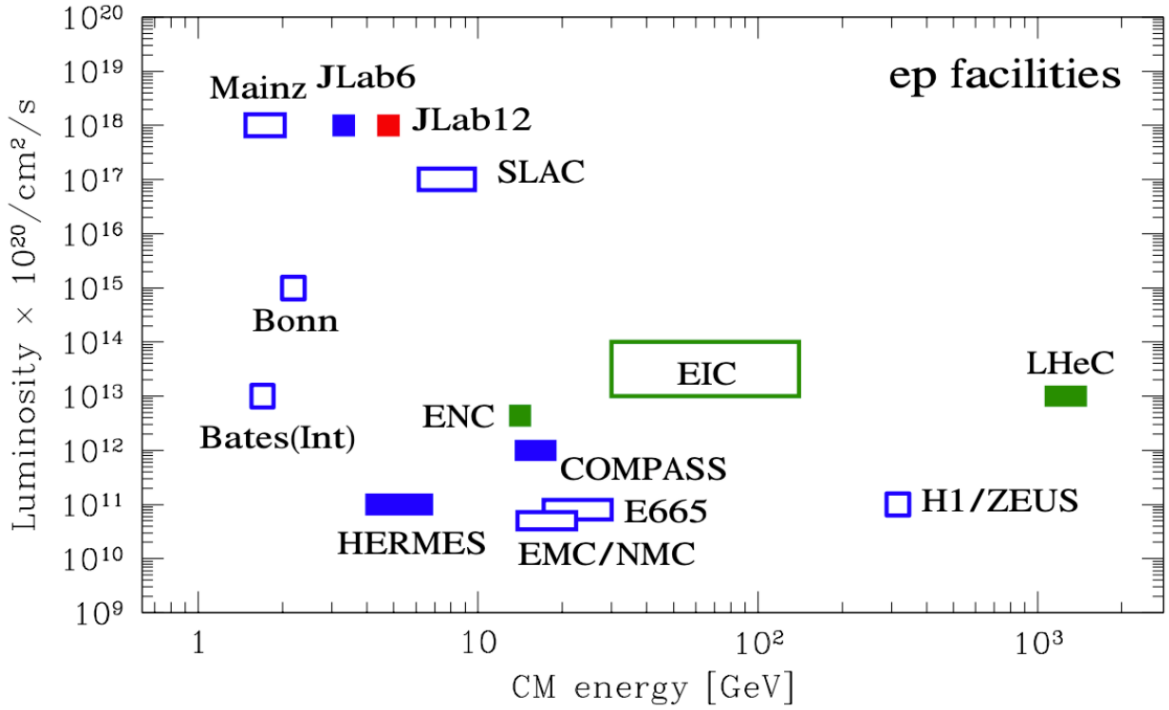

Figure 1.4 - Luminosity and centre of mass energy achievable by current accelerators (blue), planned accelerators (green), and the 12 GeV upgrade at Jefferson Lab (red). From [36].

1.2 Magnetic Resonance

1.2.1 NMR basics

Spins, energy levels and sensitivity.

Nuclear magnetic resonance (NMR) is a powerful analytical technique which gives information about the local magnetic environments of nuclei within a sample and can be applied to any magnetic nuclei. A magnetic nucleus is any nucleus that doesn't have both an even number of protons and neutrons, and thus has a nonzero spin quantum number, $S \neq 0$. A nonzero spin, $\vec{S}$, results in a magnetic dipole moment, $\vec{\mu}$, via the relation:

$$\vec{\mu} = \gamma \vec{S} \qquad Eq.1.6$$

where γ is the gyromagnetic ratio of the nucleus.

When a magnetic nucleus is placed in an applied field the magnetic quantum number, m, is the spin component along the axis of the applied field, taking values from $-S$ to $+S$ in integer steps, resulting in $2S + 1$ angular momentum states. Thus:

$$S_Z = m\hbar \qquad Eq.1.7$$

$$\mu_Z = \gamma S_Z = \gamma m\hbar \qquad Eq.1.8$$

where S_Z and μ_Z are the components of the spin and magnetic dipole moment in the direction of the applied field.

In NMR spectroscopy, a sample is placed inside an NMR spectrometer which contains a strong, uniform magnetic field, causing the precession of the nuclear spins in the sample. These spins precess at the Larmor frequency

$$\omega = -\gamma B_0 \qquad Eq.1.9$$

where ω is the angular precession frequency and B_0 is the magnitude of the applied field. The spins will align either parallel or antiparallel with the applied field, with corresponding energies of:

$$E = -\vec{\mu} \cdot \overrightarrow{B_0} = -\mu_z B_0 = -\gamma m\hbar B_0 \qquad Eq.1.10$$

which for a spin-1/2 nucleus (such as ^{1}H, ^{13}C, ^{15}N, ^{19}F) results in:

$$E = \pm\frac{1}{2}\gamma\hbar B_0 \qquad Eq.1.11$$

$$\Delta E = \gamma\hbar B_0. \qquad Eq.1.12$$

The transition from the lower energy to the higher energy state can be driven by the absorption of a photon exactly matching the gap between energy levels, such that

$$h\nu = \gamma\hbar B_0 \qquad Eq.\,1.13$$

$$\nu = {}^{\gamma B_0}/_{2\pi} \qquad Eq.\,1.14$$

where $h(\hbar)$ is the (reduced) Planck constant, γ is the gyromagnetic ratio of the nucleus, B_0 is the magnitude of the applied field and ν is the frequency of the photon. For NMR spectrometers, ν will lie in the radiofrequency (RF) range. A common field strength for an NMR spectrometer is 9.4 T, and thus following from Eq. 1.14, the frequency of a photon needed to excite the spin of a ^{1}H nucleus is 400 MHz, the same as the Larmor frequency for that nucleus. For this reason, the field strength of an NMR spectrometer is often quoted in MHz for convenience.

NMR is a technique that relies on the net magnetic moment of a sample. It is favourable energetically for the spins to align with the applied field, however this alignment is opposed by the random thermal motion of the molecules, driving the system to a state where the magnetic moments have random orientations [37]. The energy of this thermal motion at room temperature is much greater than the energy levels corresponding to different spin states, and thus the thermal motion easily disrupts the alignment of the magnetic moments [37]. As it is slightly favourable energetically for a magnetic moment to align with the field, this results in an effect across the sample called bulk magnetization, a slight net alignment of the magnetic moments in the direction of the field.

This bulk magnetization is otherwise described as the thermal equilibrium polarization of the sample, P_{TE}, and can be quantified as:

$$P_{TE} = \frac{N_\uparrow - N_\downarrow}{N_\uparrow + N_\downarrow} = \tanh\left(\frac{\hbar\omega}{2k_B T}\right) = \tanh\left(\frac{\gamma\hbar B_0}{2k_B T}\right) \qquad Eq.\,1.15$$

where $N_\uparrow$ and $N_\downarrow$ are the populations of the spin up and spin down states, ω is the Larmor frequency, k_B is the Boltzmann constant, and T is the temperature.

This is a simplification as most spins cannot be neatly classified as wholly spin up or wholly spin down. Eq. 1.15 shows that at room temperature (298 K) and at an approximate value of the Earth's magnetic field strength (50 μT), the thermal equilibrium polarization of a ^{1}H nucleus will be 1.7 x 10^{-10}. For an NMR spectrometer, sensitive to the bulk magnetization, this is equivalent to only seeing roughly 1 in 6 billion nuclei. As can also be seen in Eq. 1.15, the thermal equilibrium polarization can be increased by using a strong applied magnetic field, as is done in NMR spectrometers. Keeping at 298 K and increasing the field strength to 9.4 T results in a polarization

of 3.2 x 10^{-5}, an improvement by over 5 orders of magnitude. This still only corresponds to seeing 1 in over 30,000 nuclei, a number which only gets worse for nuclei with a smaller gyromagnetic ratio such as ^{13}C and ^{15}N.

The fact that an NMR spectrometer is only sensitive to circa 1 in 10^5 nuclei is why NMR is considered a low sensitivity analytical technique. In comparison with other EM spectroscopies such as UV-vis and IR, the sample concentrations needed are orders of magnitude higher [38]. As the sensitivity of MR imaging is directly proportional to the polarization of the sample, there is huge potential for sensitivity improvements by analysing samples that have high, non-equilibrium spin polarization, termed hyperpolarization. Hyperpolarization techniques have been available since almost the invention of NMR, however they have gained in popularity more recently since medical imaging applications were realized, starting with lung imaging using optically pumped ^{129}Xe [39]. Hyperpolarization techniques will be discussed further in the subsequent section.

FIDs and FFTs

As previously explained, magnetic nuclei have a magnetic moment and precess in an applied field. It is helpful to think about an NMR experiment in terms of the net magnetic moment in the sample, rather than thinking about individual spins, as it is the net magnetization vector that can be detected in an experiment. This net magnetization vector is stationary and aligned with the applied field when the sample is at equilibrium, however if it is tipped away from the axis of the applied field it will undergo precession, tracing out a cone shape. This is shown in Figure 1.5. The angle the magnetization is tipped by, denoted as θ, is known as the tip angle.

This precession of the magnetization vector is what is detected in an NMR experiment. It is used to induce a current in a detector coil which is amplified and recorded as the 'free induction decay' signal (FID). In a typical NMR experiment, a tip angle of 90° is used, which rotates the magnetization into the XY-plane. As seen in Figure 1.6a, an FID takes the form of a damped sine wave. Due to the geometry of the detector coil, the detected signal arises from the component of the magnetic precession in the XY-plane, thus the FID signal decays as the magnetization vector returns to its equilibrium position, as can be seen in Figure 1.6b.

FIDs are recorded as a time-domain signal, whereas the useful information in an NMR experiment is in the frequency domain. To extract the component frequencies of an FID, a Fast Fourier Transform (FFT) is performed, producing an NMR spectrum, an example of which is shown in Figure 1.6c.

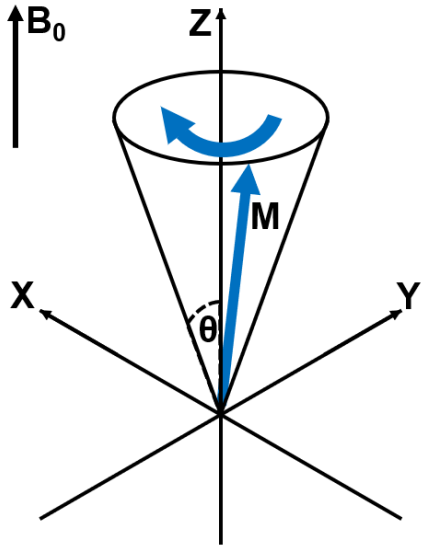

Figure 1.5 - Illustration of the precession of the magnetization vector once tipped by an angle θ. Recreated from [37].

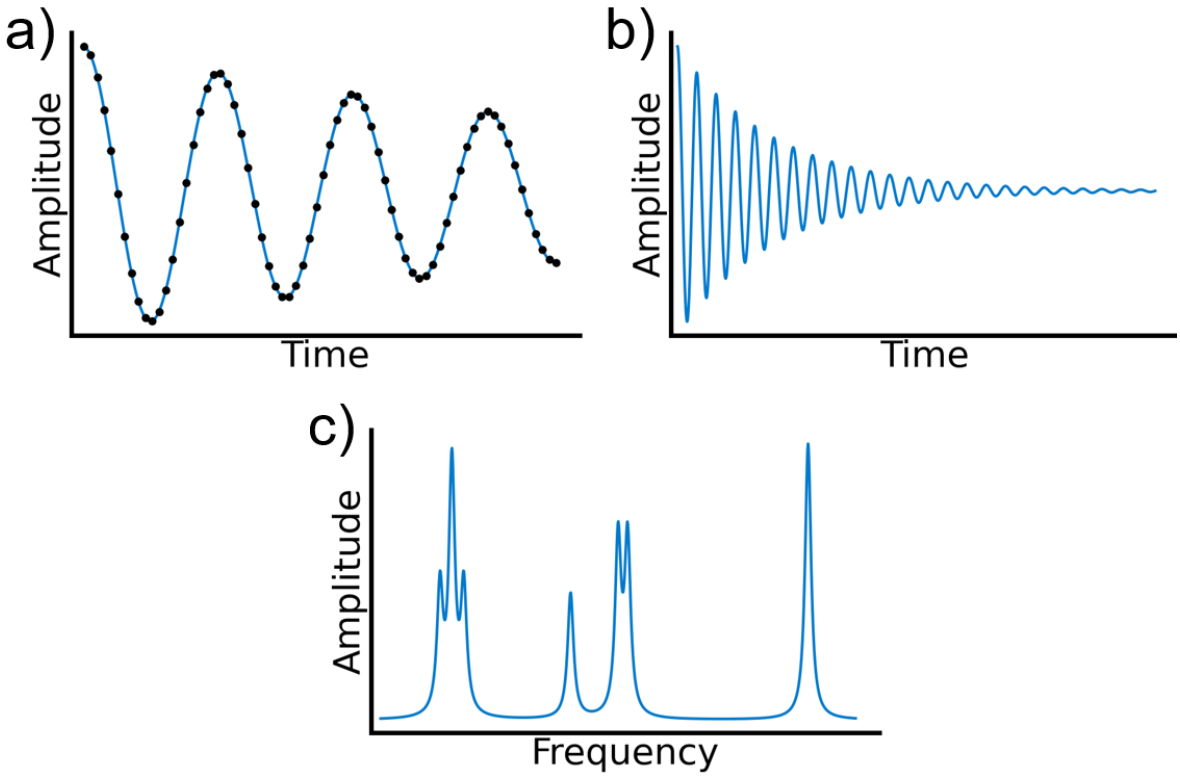

Figure 1.6 - a) Close up of the FID signal, comprised of many sample points of the induced voltage in the detector coil. b) Full FID signal. c) Resultant spectrum after a Fourier Transform is performed on the FID.

Spectrums, spin coupling and multiplets

NMR spectra contain multiple peaks, rather than a single peak at the Larmor frequency of the nucleus of interest, due to the local magnetic environments in the sample. These local magnetic environments contain the information necessary to distinguish chemicals from each other and are part of why NMR is such a powerful analytical tool. These local magnetic environments in a sample result in a slight changing of the Larmor frequency for each nucleus, and are caused by the distribution of electrons in chemical bonds [40]. It is thus possible to gain information about molecular structures in the sample by analysing the distributions of frequencies in the NMR spectrum.

The frequency position of a signal in an NMR spectrum is called the chemical shift. If the observed Larmor frequency is $\nu_0 + \Delta\nu$, then ν_0 is the reference frequency for that nucleus and $\Delta\nu$ is the chemical shift in Hz [40]. For ^{1}H NMR the chosen reference frequency is the signal from tetramethylsilane (**TMS**) [40] which has the useful property of containing 12 magnetically equivalent protons which produce a strong singlet peak. Chemical shifts of signals are typically quoted in parts per million (ppm) rather than Hz, where the ppm shift is the fractional shift from the reference frequency and is usefully independent of the field strength of the spectrometer.

Alongside the information that can be gained from the chemical shift of a signal, information can also be gained from its multiplicity. Spin-spin couplings coming from through-bond interactions between nuclei in a sample result in the line splitting of resonances [40]. These couplings are called J-couplings and their strength is measured in Hz rather than ppm due to being independent of the external field. J-couplings produce splitting patterns where the multiplicity of the line splitting equals $n + 1$ (for ^{1}H), where n is the number of nuclei in the neighbouring group. The relative intensities within the multiplet follow Pascal's triangle. Splitting patterns can be useful for characterisation of a sample, for example if a ^{1}H peak is a doublet/triplet/quartet, then there must be 1/2/3 protons in the neighbouring group.

1.2.2 NMR relaxation

Longitudinal and Transverse relaxation

Longitudinal relaxation (T_1) is the process associated with the Z-component of the magnetization returning to equilibrium from a non-equilibrium state. This quantity governs the rate at which repeated scans can be taken in an NMR experiment, and one typically needs to wait a period of 5 T_1s before the sample is considered sufficiently relaxed (see Figure 1.7b). It also governs the relaxation of hyperpolarized signals, which decay as:

$$S.E = (\varepsilon - c)e^{-t/T_1} + c$$

$$\approx \varepsilon \cdot e^{-t/T_1}$$

$$for\ \varepsilon \gg |c|, \qquad t \sim T_1. \qquad Eq.1.16$$

where $S.E$ is the signal enhancement factor, ε is the maximal signal enhancement, c is the thermal equilibrium signal (+/- 1 for positively/negatively enhanced signals) and t is time. This decay of the signal enhancement is shown in Figure 1.7a.

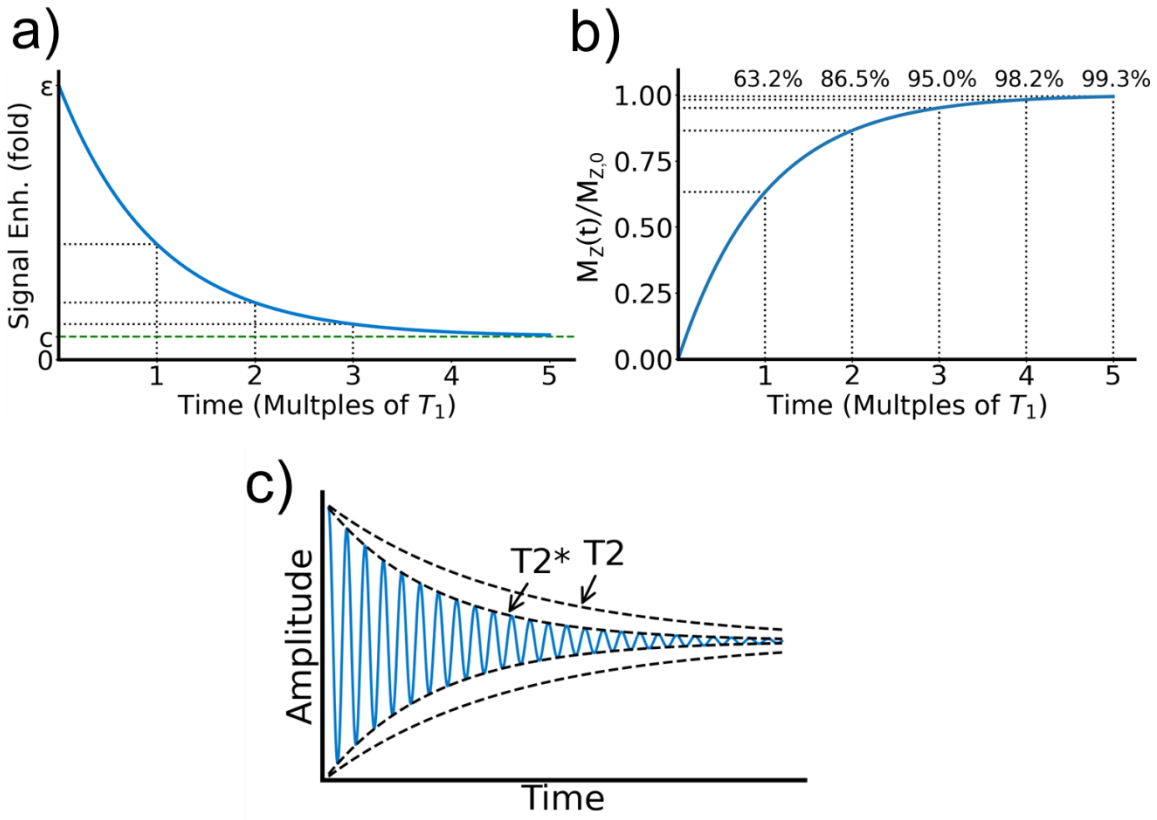

Figure 1.7 - a) Hyperpolarized T_1 decay. b) Thermal T_1 recovery, here $M_Z(t)/M_{Z,0}$ is the longitudinal magnetization as a fraction of the longitudinal magnetization at thermal equilibrium. c) T_2/T_2^* relaxation.

Transverse relaxation (T_2) is the process by which the XY-component of the magnetization returns to its equilibrium value of zero. This process occurs from the dephasing of its component spins due to differing precession frequencies within the sample, which occurs for two reasons. The first is the difference in Larmor frequency for different nuclei in the sample due to their local magnetic environments - this causes pure T_2 relaxation. The second contribution is from inhomogeneities in the applied field, with the time constant for samples relaxing due to both effects being termed T_2^*.

T_2/T_2^* relaxation (shown in Figure 1.7c) determines the length of acquisition times that can be used in an NMR experiment. If T_2^* is short, leading to short acquisition times, then this results in broader peaks in the acquired spectrum, reducing the quality of the information that can be gathered. Fast T_2^* relaxation can be accommodated for with the use of special pulse sequences, such as the Carr-Purcell-Meiboom-Gill (CPMG) sequence [41] which can 'refocus' the magnetization vector.

Relaxation mechanisms

The dominant forms of relaxation for spin-1/2 nuclei are the dipolar mechanism and chemical shift anisotropy. The dipolar mechanism is relaxation caused to a nucleus by the rotating magnetic moment of nearby nuclei. The strength of the effect is dependent on the distance between the two spins, the gyromagnetic ratio of the spin contributing to relaxation ('relaxing' spin) and the gyromagnetic ratio of the spin experiencing relaxation ('relaxed' spin) [37]. The interaction reduces with distance, r, as $\frac{1}{r^3}$, and thus it is strongly dependent on the local concentration of 'relaxing' nuclei. The effect increases with the gyromagnetic ratio of the 'relaxing' nuclei as the magnetic moment of the nucleus is proportional to γ, as well as increasing with the gyromagnetic ratio of the 'relaxed' nucleus as the rate at which the local field rotates the magnetic moment is also proportional to γ.

Another source of relaxation similar to the dipolar mechanism is relaxation by paramagnetic species. Unpaired electrons in a molecule also generate local fields in an analogous way, however due to the much larger gyromagnetic ratio of the electron compared to the proton this effect can be particularly strong. A common source of paramagnetism in NMR experiments is O_2, which is necessary to remove if low relaxation rates are required.

Chemical shift is the phenomenon whereby in the presence of a strong applied field the electrons in the molecule give rise to a small induced local field at the nucleus, therefore the nucleus experiences the sum of the applied field and the induced field. This local field is not necessarily aligned with the applied field and can thus act as a source of relaxation called chemical shift

anisotropy. This effect is less pronounced for ^{1}H, which typically sees a chemical shift of a few ppm, and is more pronounced in nuclei such as ^{13}C for which the chemical shift can exceed 100 ppm.

Rather than these local fields themselves, it is their time dependence that drives relaxation. Rotational motion of the molecules in the sample causes these local fields to vary (shown in Figure 1.8), with the rate of rotation being described by the correlation time, τ_c, the average time taken for a molecule to rotate by one radian. The correlation function, $G(\tau_c)$, describes the time dependence of the rotational motion throughout the sample. Its Fourier pair, the spectral density function, $J(\omega)$, gives the frequency distribution of the motion. The rate of longitudinal relaxation (T_1) is dependent on the magnitude of the spectral density function at the Larmor frequency of the nucleus, $J(\omega_0)$.

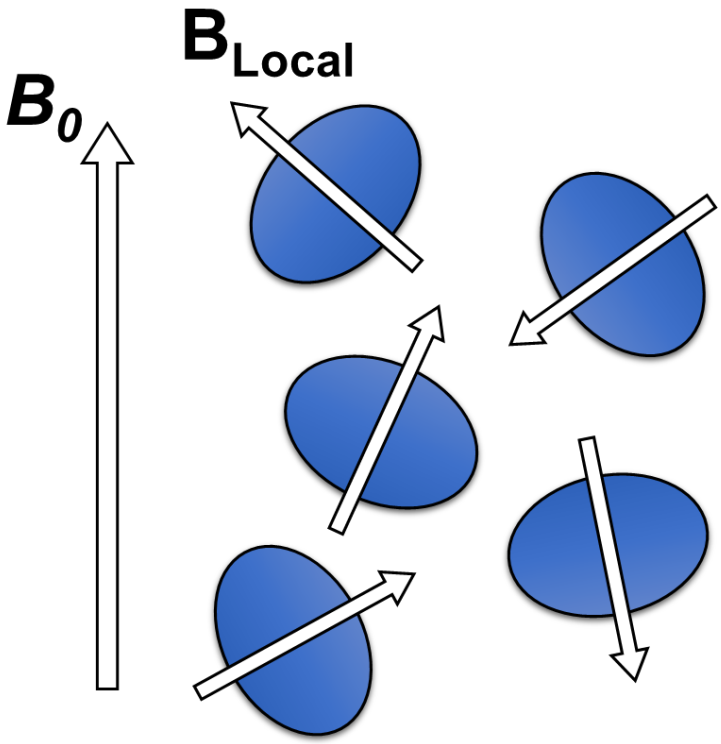

Figure 1.8 - Variance in the local magnetic field occurs due to molecular tumbling. Reproduced from [37].

1.3 Hyperpolarization in NMR

Hyperpolarization has been used in NMR since the 1950s [42,43], with DNP-NMR being utilized to address NMR's inherent sensitivity issue. Hyperpolarization in NMR remained relatively inaccessible for decades until in 1986 Bowers and Weitekamp theorised a hyperpolarization method utilizing the high spin order of *para*hydrogen [44].

1.3.1 *Para*hydrogen

Molecular hydrogen, H_2, is formed from two coupled ^1H nuclei and can exist as either of two nuclear spin isomers, the triplet state, *ortho*hydrogen (*o*-H_2) or the singlet state, *para*hydrogen (*p*-H_2). *Ortho*hydrogen has spin $I = 1$ and is triply degenerate whereas *para*hydrogen has spin $I = 0$ and has no degeneracy, shown in Figure 1.9. The *para* configuration of H_2 is energetically favourable, however at room temperature the difference between the spin energy levels is negligible compared to the thermal energy of the molecule, and thus each of the four spin states are almost equally populated, resulting in a 75:25 *ortho/para* ratio, as shown in Figure 1.10. It is possible to enrich the *p*-H_2 fraction by sufficiently cooling the H_2 in the presence of a ferromagnetic catalyst such as iron(III) oxide or activated charcoal. Using a liquid nitrogen cooled *para*hydrogen generator operating at 77 K would allow for a *p*-H_2 fraction of 52%, whereas by taking H_2 down to its boiling point of 20.3 K it is possible to achieve a *p*-H_2 fraction of up to 99.9% [45].

1.3.2 *Para*hydrogen-induced polarization (PHIP)

A year after Bowers and Weitekamp theorized of a hyperpolarization method using *para*hydrogen, they successfully executed the first *para*hydrogen-induced polarization (PHIP) experiment with the hydrogenation of acrylonitrile to propionitrile (Figure 1.11) [46] in an experiment they termed *Para*hydrogen and Synthesis Allow Dramatically Enhanced Nuclear Alignment (PASADENA). PHIP involves the incorporation of a *para*hydrogen molecule into a target molecule at the location of an unsaturated bond, mediated by a hydrogenation catalyst. These molecules then retain the magnetisation of the incorporated *p*-H_2 molecule, vastly altering the populations of the spin states compared to the product molecule without *p*-H_2 incorporation [47] and allowing for greatly enhanced NMR detectability. It is important that the symmetry of the *p*-H_2 molecule is broken upon incorporation, as *p*-H_2 by itself is NMR silent [48].

This technique came with numerous advantages in comparison to DNP-NMR. It was able to be performed at room temperature without the need for sophisticated hardware, and the polarization could be generated in seconds [46]. It did however come with a number of drawbacks, such as that the PHIP target molecule must have available an unsaturated precursor that can undergo a

hydrogenation reaction with *p*-H_2, alongside the fact that the polarization process is irreversible, meaning that each sample may only be polarized once.

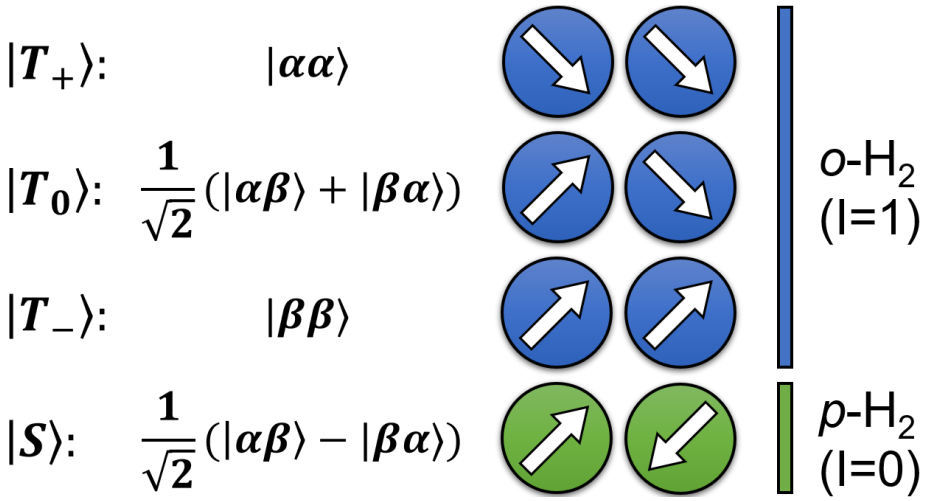

Figure 1.9 - Spin states of molecular hydrogen. Here the diagram gives a pictorial representation of the total spin, $\hat{S}$, and spin projection, m_s. For $|T_+\rangle$, $|T_0\rangle$ and $|T_-\rangle$, $\hat{S} = 1$ and $m_s = +1, 0, -1$ respectively. For $|S\rangle$, $\hat{S} = 0$ and $m_s = 0$.

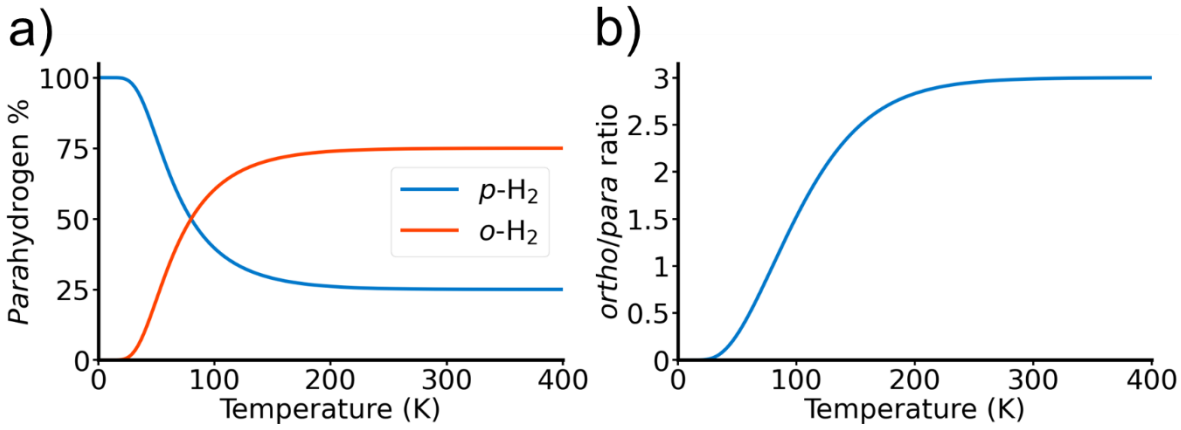

Figure 1.10 - a) ortho/parahydrogen conversion percentage. b) ortho/parahydrogen conversion ratio.

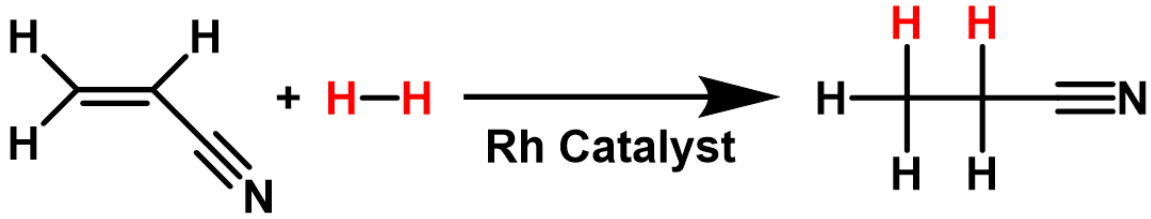

Figure 1.11 - Diagram of Bowers and Weitekamp's first PASADENA PHIP experiment in 1997, incorporating parahydrogen into propionitrile.

1.4Signal Amplification By Reversible Exchange (SABRE)

The aforementioned limitations with PHIP are the issue that SABRE set out to solve. Signal Amplification By Reversible Exchange (SABRE) is a variant of PHIP that takes an alternative approach to harnessing the high spin order of *para*hydrogen. SABRE is a technique first demonstrated in 2009 by Adams et al. [49] that catalytically transfers the high spin order present in *p*-H_2 to a target molecule without the need for *p*-H_2 incorporation.

The precatalyst used in SABRE is typically of the form [Ir(NHC)(COD)Cl], which undergoes hydrogenation and substitution reactions in the presence of H_2 and the target substrate to form the active catalyst, such as $[Ir(H)_2(NHC)(Sub)_3]Cl$. Here NHC = *N*-heterocyclic carbene, COD = cis,cis-1,5-cyclooctadiene and Sub = the target substrate. A simple SABRE solution would involve four components, the catalyst, the substrate, a solvent and a supply of *p*-H_2.

The SABRE polarization process involves the following steps:

1. Active SABRE catalyst is formed through hydrogenation and substitution reactions of the SABRE precatalyst (see Figure 1.12a).
2. A *p*-H_2 molecule replaces the hydrides of the active catalyst and acts as the source of spin order for the polarization step.
3. J-couplings (spin-spin couplings mediated through chemical bonds) between the *p*-H_2-derived hydrides and the target nucleus facilitate the transfer of spin from the *p*-H_2 molecule to the substrate, leaving it polarized.
4. The polarized substrate dissociates from the catalyst and returns to solution. The substrate is chemically unchanged and is free to be polarized again.
5. The vacant site on the catalyst is occupied by another substrate molecule and the process repeats from step 2, accumulating polarized substrate molecules in solution.

1.4.1 SABRE magnetization transfer

SABRE magnetization transfer occurs when *p*-H_2 is incorporated into the active SABRE catalyst through oxidative addition. The *p*-H_2 protons couple to the *trans*-bound substrates through a J-coupling network, facilitating spin mixing. This process typically takes place at a level anti-crossing (LAC) where polarization transfer is most efficient [50,51]. LACs arise at a magnetic field in which two energy levels, corresponding to quantum states $|a\rangle$ and $|b\rangle$, would otherwise cross but due to spin-spin coupling the degeneracy of the states is removed and the states avoid crossing [50]. An illustration of an LAC for an AA'B spin system is shown in Figure 1.13.

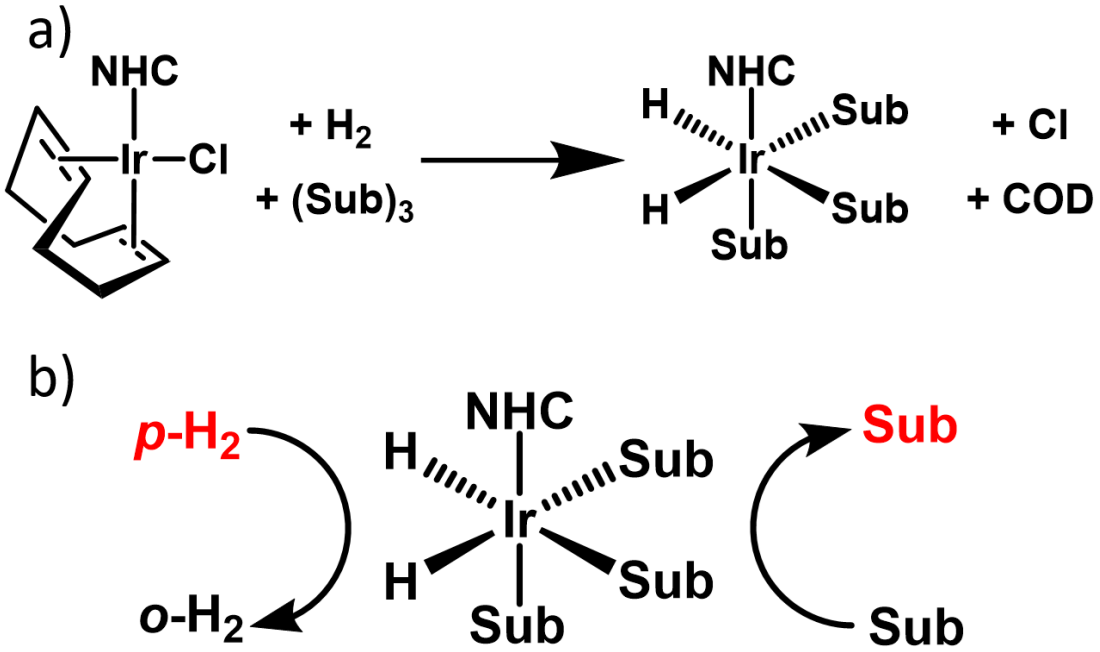

Figure 1.12 - a) Formation of active SABRE catalyst. b) Magnetization transfer from p-H_2 derived hydride ligands to a ligated substrate. The substrates are in reversible exchange with the catalyst.

The AA'B system (shown in Figure 1.14) is a simplistic yet helpful approximation of the spin system involved in SABRE. This is a system where the coupling $J_{AA'}$ (here the coupling between the two *p*-H_2 protons) is much larger than the couplings J_{AB} and $J_{A'B}$ (the similar but inequivalent couplings between the *p*-H_2 protons and the target nucleus). In an AA'B spin system for SABRE the states brought together at the LAC are $|S\alpha\rangle$ and $|T_+\beta\rangle$, where $|S\rangle$ and $|T_+\rangle$ are the singlet and triplet spin states of *p*-H_2-derived protons, and $|\alpha\rangle$ and $|\beta\rangle$ are the two possible spin states of the to-be-polarized nucleus. When the states $|S\alpha\rangle$ and $|T_+\beta\rangle$ are brought together at an LAC, spin mixing between the two states is possible, as can be seen in Eq. 1.17. If the system is created with an overpopulation of the $|S\alpha\rangle$ state, then the dominant transitions will be $|\alpha\rangle \rightarrow |\beta\rangle$ and $|S\rangle \rightarrow |T_+\rangle$, the conversion of an unpolarized spin to a polarized spin and the conversion of *para*hydrogen to *ortho*hydrogen respectively.

$$|S\alpha\rangle \rightleftarrows |T_+\beta\rangle \qquad (Eq.\ 1.17)$$

The evolution between $|S\alpha\rangle$ and $|T_+\beta\rangle$ is reversible and oscillatory in nature, thus for efficient polarization transfer it is necessary that the coupling from the *p*-H_2 derived hydrides to the target nuclei lasts a specific amount of time, namely $t = \frac{1}{2\sqrt{2}(J_{AB}-J_{A'B})}$ [52], where J_{AB}, $J_{A'B}$ are the coupling strengths between the hydrides and substrate in Hz [52]. An illustration of this is shown in Figure 1.15. The transfer efficiency can be altered by altering the length of time the substrate is

bound for, for example by changing the active catalytic species. Due to the difference in coupling strengths between the hydrides and nucleus for different nuclei, the LAC field varies. For ^{1}H polarization the LAC is met at millitesla fields [50-52], whereas for $^{13}C/^{15}N$ polarization the transfer field is on the order of microtesla [53-55].

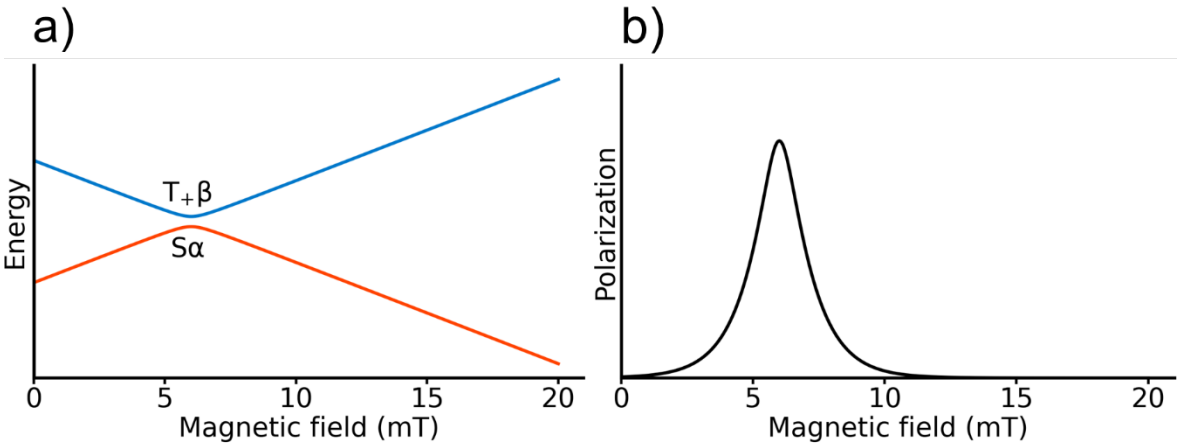

Figure 1.13 - Illustration of the LAC in an AA'B spin system, where B is a ^{1}H nucleus. a) Energy levels of the spin states $|S\alpha\rangle$ and $|T_{+}\beta\rangle$ through which spin mixing can occur. b) Magnetic field dependence of the polarization achievable for a ^{1}H nucleus. Reproduced from [52].

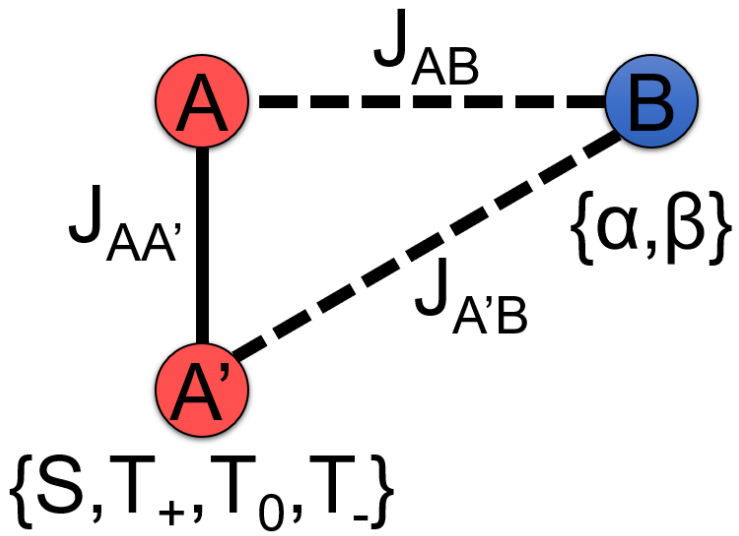

Figure 1.14 - Diagram of an AA'B spin system.

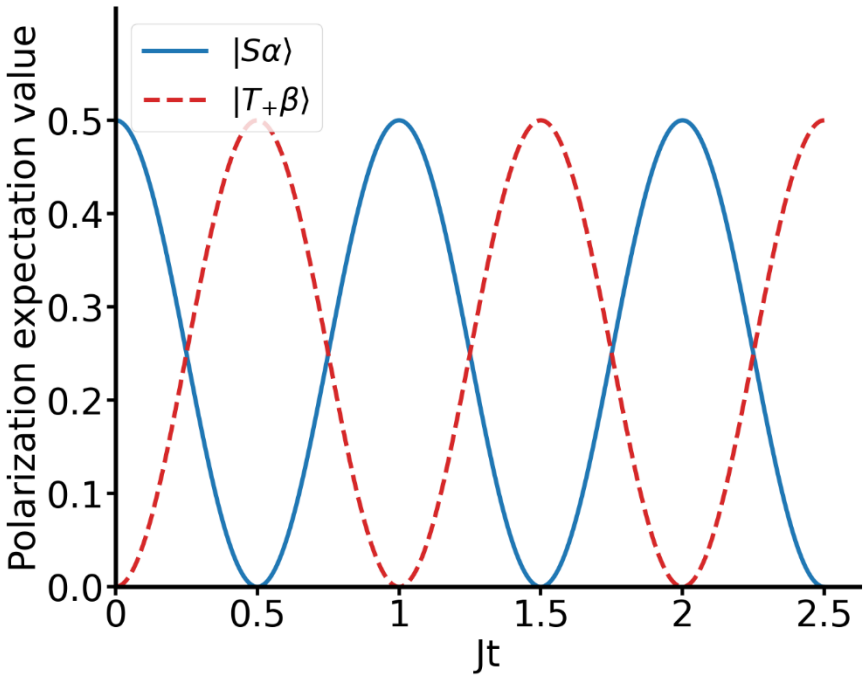

Figure 1.15 - Evolution of the polarization expectation value in an AA'B spin system. Reproduced from [52].

1.4.2 SABRE substrates and nuclei

SABRE is a technique that is amenable to a large variety of typically nitrogen-containing substrates, with the stipulation that the substrate must coordinate to the iridium catalyst. Some of the classes of substrates that have been polarized by SABRE include pyridines [49,56,57], amines [58], nitriles [59] and diazoles [60], shown in Figure 1.16.

A recent development in SABRE-based hyperpolarization has expanded the scope of molecules that can be polarized by SABRE. In 2018 Roy et al. demonstrated that subsequent to the transfer of polarization to a substrate molecule, the *p*-H_2-derived polarization could be further transferred to another molecule, here demonstrated by the polarization of a ^{31}P nuclei inside a tetracoordinate Pt complex [61]. This technique was named SABRE-Relay and was theorized at the time to be a way of polarizing classes of substrates that are not amenable to traditional SABRE. This theory was then realized in 2019 when the SABRE-Relay effect was demonstrated for the relayed polarization of alcohols [62], which are unable to coordinate to the iridium catalyst in order to receive direct polarization transfer.

With the increasing interest in using hyperpolarized molecules for biomedical imaging, in 2015 Truong et al. developed a technique for efficiently polarizing heteronuclei such as ^{13}C and ^{15}N, desirable as imaging agents due their longer relaxation times in comparison to ^{1}H. This technique was dubbed SABRE-SHEATH [54] (SABRE in SHield Enables Alignment Transfer to Heteronuclei) and

operates at μT fields, requiring the sample to be magnetically shielded. A large variety of magnetic nuclei can be polarized by SABRE and SABRE-SHEATH including ^{1}H, ^{13}C, ^{15}N, ^{19}F, ^{29}Si, ^{31}P, and ^{119}Sn [49,54,63-66], however the most common are ^{1}H, ^{13}C and ^{15}N.

The maximum reported ^{1}H polarization to date through SABRE is the 63% polarization of a proton site in methyl-4,6-nicotinate-d_2 achieved by Rayner et al. [67]. This used a variety of optimization techniques such as selective ^{2}H labelling of the catalyst and substrate, use of co-ligands, and higher than typical pressures. These techniques will be discussed further later on. For ^{15}N, the highest documented polarization achieved is 79% in pyrazine [68], which similarly made use of some of the optimization techniques seen in [67].

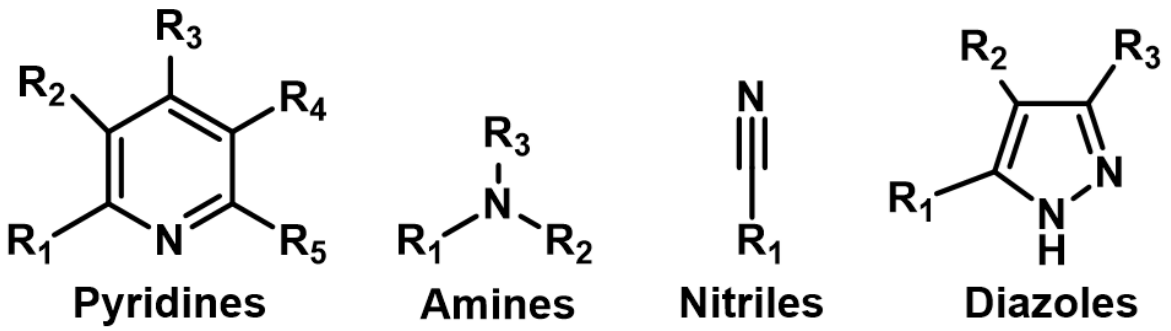

Figure 1.16 - A selection of the classes of molecule which can be polarized by SABRE.

1.4.3 Complementary techniques for SABRE

SABRE polarization optimization techniques

^{2}H labelling

Relaxation is a key factor in creating high levels of usable polarization through SABRE, both during and after the polarization build-up process. It is known that ^{1}H nuclei are particularly susceptible to relaxation due to their high gyromagnetic ratio, and thus additional efforts need to be taken to minimize this effect.

One of the ways to achieve this is by using ^{2}H labelling, replacing some (or all) of the ^{1}H (protium) atoms in a molecule with ^{2}H (deuterium). This uses the fact that the gyromagnetic ratio for deuterium is 6.5 times lower than for protium, and thus it will contribute much less to relaxation of the ^{1}H nucleus.

This effect was demonstrated particularly elegantly by Norcott et al. [69] in a study that investigated selectively-deuterated pyridines, in which for each of these molecules they only left one position, (*ortho*/*meta*/*para*) undeuterated. The molecules investigated can be seen in Figure 1.17.

The control molecule for this study was protonated pyridine, for which the relaxation T_1 values were measured as 28 s, 26 s and 34 s at 9.4 T for the *ortho*, *meta* and *para* sites respectively. For the selectively deuterated molecules where just one position remained protonated, the new T_1 values were 51 s, 113 s and 85 s for the *ortho*, *meta* and *para* sites. These results, shown in Table 1.2, demonstrate an increase in the T_1 of 82%, 332% and 151%, an incredible extension in lifetime.

It should be noted that although the relaxation rate can be significantly extended using ^{2}H labelling, care needs to be taken with the sites that are deuterated. SABRE is a technique that transfers polarization through J-couplings between the metal hydrides and the substrate nucleus, which for ^{1}H polarization happens predominantly through ^{4}J couplings from the hydrides to the *ortho* proton in the target molecule. This ^{4}J coupling is considerably stronger than the ^{5}J and ^{6}J couplings between the hydrides and the *meta* and *para* protons, which are less efficient routes for polarization transfer.

This was seen in the same investigation by Norcott et al. [69], whereby the *ortho/para*-deuterated pyridine and the *ortho/meta*-deuterated pyridines saw a large reduction in polarization value of 82% and 90% respectively relative to proteo-pyridine, shown in Table 1.3. The *meta/para*-deuterated pyridine saw an increase in polarization as might be expected from a reduced rate of dipolar relaxation.

Table 1.2 - Changes in T_1 values at different sites upon selective deuteration of pyridines found by Norcott et al. [69].

Substrate	**Site T_1 (s)**		
	Ortho	*Meta*	*Para*
a) Pyridine	28	26	34
b) 3,4,5-pyridine-d_3	51 (+82%)	---	---
c) 2,4,6-pyridine-d_3	---	113 (+332%)	---
d) 2,3,5,6-pyridine-d_4	---	---	85 (+151%)

Table 1.3 - Changes in polarization values at different sites upon selective deuteration of pyridines found by Norcott et al. [69].

Substrate	Polarization level (%)		
	Ortho	*Meta*	*Para*
a) Pyridine	4.3	3.4	5.4
b) 3,4,5-pyridine-d_3	5.8 (+35%)	---	---
c) 2,4,6-pyridine-d_3	---	0.6 (-82%)	---
d) 2,3,5,6-pyridine-d_4	---	---	0.5 (-90%)

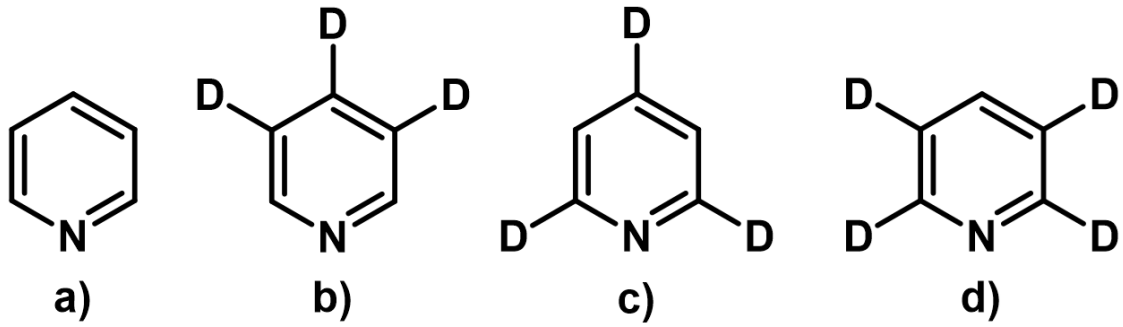

Figure 1.17 - Selectively deuterated pyridines investigated in [69]. a) pyridine. b) 3,4,5-pyridine-d_3. c) 2,4,6-pyridine-d_3. d) 2,3,5,6-pyridine-d_4. Molecules b-d leave protons in just the ortho, meta and para sites respectively.

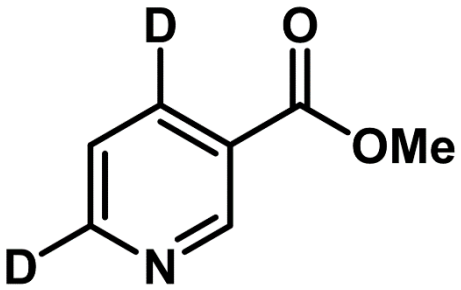

Figure 1.18 - Methyl-4,6-nicotinate-d_2.

The use of selective deuteration was performed by Rayner et al. in order to achieve the maximum reported ^{1}H polarization through SABRE of 63% for methyl-4,6-nicotinate-d_2 [67] (Figure 1.18). In this molecule the *ortho* and *meta* protons are magnetically isolated from each other with only a weak ^{5}J coupling between them, and the other nuclei in the molecule possess low gyromagnetic ratios. This allowed for a T_1 on the *ortho* and *meta* sites of 66 s and 98 s respectively. The performance of a novel selectively deuterated SABRE substrate designed to achieve high polarization levels and long T_1s whilst maximizing the dilution factor will be presented in Chapter 2.

As well as the selective deuteration of the substrate molecule, ^{2}H labelling can also be applied to the polarization transfer catalyst. As previously discussed, polarization happens in SABRE due to the transition between the $|S\alpha\rangle$ and $|T_+\beta\rangle$ spin states, as shown in Figure 1.15. In reality, there in an additional process to this transfer, the decay of the non-equilibrium magnetization back to equilibrium, which turns the sinusoidal nature of the polarization expectation value into a damped sine wave, as shown in Figure 1.19. The rate at which this function is damped is dependent on the effective T_1 of the magnetization within the catalyst complex, and thus polarization efficiency can be optimized by reducing the relaxation in the complex. Reducing catalyst-derived relaxation is also important for elongating the lifetimes of already-polarized molecules, which experience relaxation through interactions with the catalyst even if polarization transfer is not occurring.

Elongating the T_1 of the magnetization within the catalyst complex can be achieved analogously to how it is achieved for substrate molecules, by applying the concept of ^{2}H labelling to the selective deuteration of the polarization transfer catalyst. This experiment was performed by Rayner et al. by selectively deuterating the NHC ligand of the polarization transfer catalyst [70]. They compared the **IMes** NHC to its *d_2, d_{22} and d_{24}* counterparts (shown in Figure 1.20) and found that significant gains could be made in the effective T_1 of both the bound substrate and the free substrate in solution. All deuterated catalysts extended the T_1 for both the free and bound substrate, however the **IMes-*d_{22}*** catalyst was found to exhibit the largest improvement for the free substrate, whilst the **IMes-*d_{24}*** catalyst showed the biggest improvement for the bound substrate. These results are shown in Table 1.4.

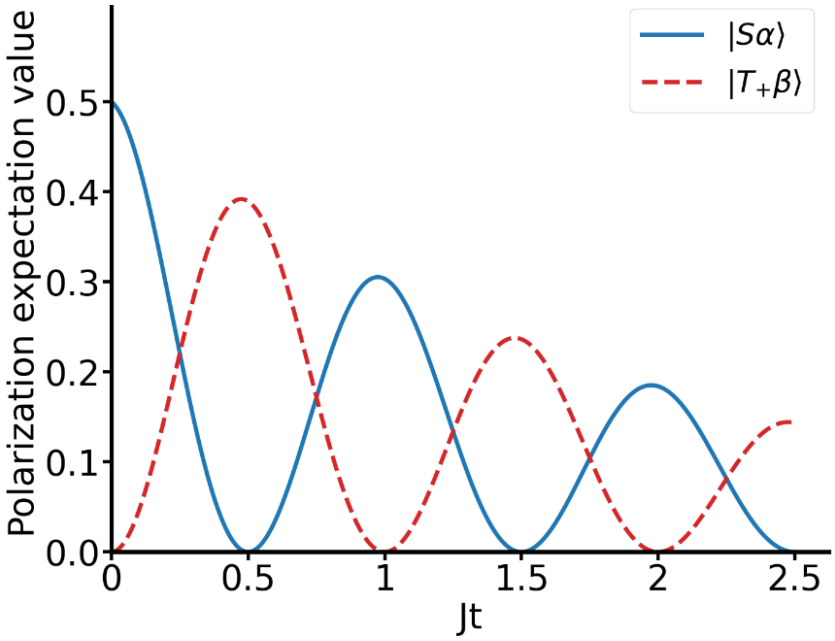

Figure 1.19 - Updated visualization of the polarization transfer in an AA'B system considering the decay of the non-equilibrium magnetization.

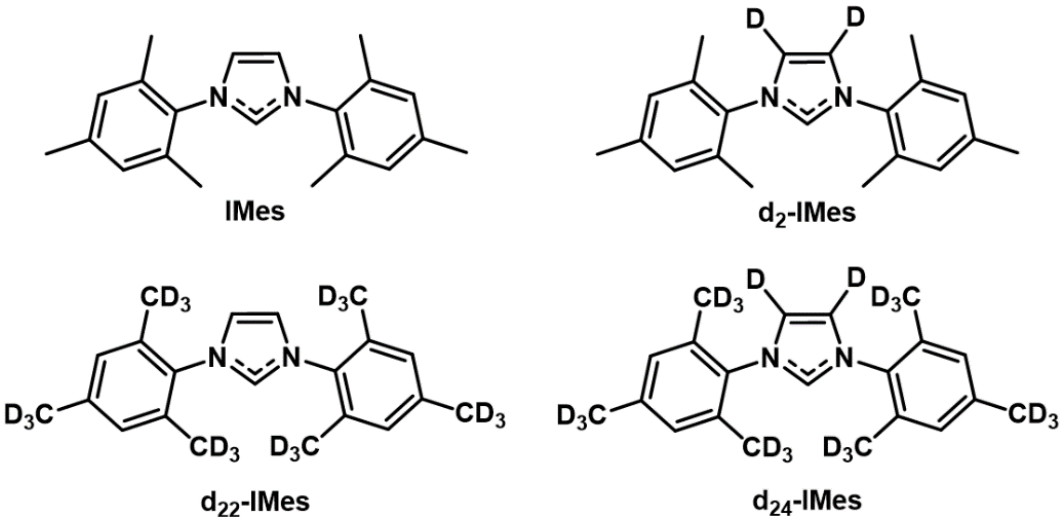

*Figure 1.20 - Selectively deuterated NHCs used in [70]. Here **IMes** = 1,3-Bis(2,4,6-trimethylphenyl)-1,3-dihydro-2H-imidazol-2-ylidene.*

Table 1.4 - Effective T_1 values for the ortho proton in 4-methyl-1,3-nicotinate-d_2 with varying catalyst NHCs, adapted from Rayner et al. [70]. Here the Free and Eq. bound sites refer to whether the substrate molecule is free in solution or is bound in the equatorial plane to the catalytic complex.

Catalyst	**Site T_1 (s)**	
	Free	Eq. bound
IMes	10.6	1.4
***d*$_2$-IMes**	13.1 (+24%)	2.0 (+43%)
***d*$_{22}$-IMes**	13.5 (+27%)	2.0 (+43%)
***d*$_{24}$-IMes**	12.1 (+14.2%)	3.2 (+129%)

Co-ligands and choice of NHC

As previously mentioned, the scope of molecules that can be directly polarized by SABRE is limited to molecules that can coordinate to the iridium catalyst. We have also seen that the efficiency of the polarization transfer is dependent on the substrate dissociation time, thus it makes sense to redefine our definition of substrates which are amenable to direct SABRE polarization as “Molecules which can be efficiently polarized by SABRE can coordinate to the catalyst and have a dissociation rate constant which is compatible with the frequency of the coherent evolution at the LAC.”. Here coherent evolution is the term for the mixing of spin states at the LAC that allows for SABRE polarization transfer. This new definition would then also be dependent on the nuclei to be polarized, as the LAC conditions will be different for different nuclei.

There is a way in which molecules that don't meet this definition of substrates amenable to SABRE can be brought into the set of suitable SABRE substrates, which is through the use of co-ligands and alternative NHCs. The rate of dissociation of a substrate molecule is not immutable and is a function of both electronic and steric effects of the substrate and catalyst complex. One of the ways the substrate dissociation rate can be altered is by adding a stabilizing ligand to the catalytic complex, termed a co-ligand. Iali et al. [71] found that the use of a dimethyl sulfoxide (**DMSO**) co-ligand would form the catalytic complex $[Ir(H)_2(Sub)(\mathbf{DMSO})_2(\mathbf{IMes})]Cl$, where here the substrate was the pyruvate anion. Without a co-ligand, pyruvate was too weakly binding to receive efficient polarization transfer, however the addition of **DMSO** stabilized the complex.

Co-ligands can also be used to help the coordination of sterically hindered substrates. Rayner et al. demonstrated this on *ortho*-substituted pyridines [72]. It had been previously shown for 2-picoline and 2,5-lutidine that no signal enhancements were observed when employing typical SABRE techniques [73], as the ligation of these substrates to the SABRE catalyst is sterically hindered. Rayner et al. found that upon the addition of 6 equivalents of **DMSO-*d*$_6$** with respect to the metal, signal enhancements were now observed in both substrates. **DMSO** fulfils the requirements for a co-ligand to a weakly-binding substrate as it will bind to the metal centre with similar affinity to the substrate, in order to not totally displace it.

An additional technique for optimizing SABRE is the choice of NHC ligand for the catalyst. It has been shown by Rayner et al. [67] that the choice of NHC influences the rate of substrate dissociation and the size of the J_{AB} coupling in the metal complex. The most common NHC used in SABRE catalysts is the **IMes** NHC which can be seen in Figure 1.20. To change the dissociation rate of the substrate, modifications can be made at the *para*-position of the mesityl ring or to the imidazole ring. Here the electronic properties of the catalyst can be changed by the addition of an electron withdrawing/donating group such as chloro or methyl, which will decrease/increase the rate of ligand dissociation respectively [67].

As well as the electronic properties of the catalyst, the steric properties can also be varied. Wong et al. [74] found that for sterically-hindered substrates, improvements in the polarization level could be achieved with the use of catalysts containing asymmetric NHCs. Here it was shown that the replacement of one of the two mesityl ligands in the **IMes** NHC with a benzyl ligand resulted in a 78% increase in polarization for 3,5-lutidine. More generally, reducing the steric bulk of the NHC may be suitable for sterically hindered substrates such as 3,5-lutidine, and increasing the steric bulk of the NHC may be suitable for sterically unhindered substrates such as acetonitrile.

Pressure

It has been both theorized and observed experimentally that the availability of *para*hydrogen is frequently a limiting factor for SABRE. Barskiy et al. [75] have formulated an analytical model for the achievable polarization in a SABRE reaction in which they theorize that the polarization level should be linearly dependent on the rate of *para*hydrogen supply. The solubility of hydrogen in solution is known to be directly proportional to the pressure of hydrogen above the solution [76], and thus pressure can be used as a tool for controlling the dissolved hydrogen concentration.

This theory of Barskiy et al. has been tested experimentally by Duchowny et al. [76]. Here an especially high-pressure setup was constructed and the SABRE-derived polarization of pyrazine was investigated at 3 concentrations over the pressure range 1-200 bar. It was observed that for the most concentrated sample (60 mM, mM = mmol L^{-1}) that polarization levels showed an apparent linear dependence on *p*-H_2 pressure over the range 1-10 bar. This dependence didn't hold past 10 bar, however a further twofold gain in polarization was observed by increasing the *p*-H_2 pressure up to 200 bar. Less concentrated samples (17.5 and 4.8 mM) showed moderate and no dependence on the *p*-H_2 pressure respectively over the range 20-200 bar.

The results of this investigation tell us that samples can be classified into three categories, strongly *p*-H_2 deficient, mildly *p*-H_2 deficient and non-*p*-H_2 deficient, where strongly deficient samples show linear dependence on pressure, mildly deficient samples show non-linear dependence on pressure, and non-deficient samples show almost no pressure dependence. Highly concentrated samples are more likely strongly *p*-H_2 deficient due to their higher demand for *p*-H_2, whereas less concentrated samples are likely to have other rate-limiting factors. An investigation into the pressure dependence for an optimized SABRE system will be presented in Chapter 5.

Manipulation of polarized material

SABRE in neat liquids

SABRE is typically performed in solutions with dilute substrate concentrations due to the cost or solubility of the reagents. For solid-phase substrates it is obvious that SABRE should be performed in solution, but for substrates such as pyridine, which in itself is a good solvent, is there a need for a separate solvent? Methods for producing highly concentrated SABRE samples are of key interest for both medical imaging and possible nuclear physics applications.

Shchepin et al. tested SABRE polarization in 'neat' liquids in an study on the detectability of unlabelled ^{15}N samples [73]. Here they trialled pyridine, pyridine-d_5 and ^{15}N-labelled pyridine as both the substrate and the solvent for SABRE. Their results, shown in Table 1.5, were as expected if one takes into consideration the concentration of each nuclei in the sample. For the ^{1}H polarization of neat pyridine, a signal enhancement of the *ortho* protons of only 4.2-fold was observed, a factor of 500 lower than might be expected under traditional SABRE conditions. This can be easily explained as here the substrate concentration is a factor of 500 higher (12,400 mM vs 25 mM) and the catalyst concentration is a factor of 18 higher (90 mM vs 5 mM) than a typical SABRE experiment, whereas the *p*-H_2 concentration in solution is effectively unchanged.

More interesting is that when pyridine is replaced with pyridine-d_5, reducing the protonated fraction of *ortho* H nuclei in the substrate by a factor of 200, the enhancements only increase by a factor of 15. It makes sense to rationalize this as a situation where *p*-H_2 is no longer limiting, and instead the transfer efficiency is the limiting factor. For every substrate molecule only 1 in 200 H nuclei can be polarized, leading to many wasted *p*-H_2 association/dissociation cycles that do not result in spin exchange. For ^{15}N, similar trends are seen. Enhancements seen in neat ^{15}N-labelled pyridine are clearly limited due to *p*-H_2 availability and transfer efficiency. In Chapter 2, it will be investigated as to whether increased catalyst concentrations can address the issues with SABRE in neat liquids.

Table 1.5 - Data from [73], showing the concentrations in solution and enhancements for ^{15}N and ortho-^{1}H nuclei for various 'neat' liquids. Note that that catalyst concentration used here was fixed at 90 mM.

'Neat' liquid	^{15}N conc. (mM)	^{15}N Enh. (fold)	*O*-^{1}H conc. (mM)	*O*-^{1}H Enh. (fold)
Pyridine	45	2,900	25,000	4.2
Pyridine-d_5	45	850	125	60
^{15}N-pyridine	12,500	33	25,000	0.3

Catalyst poisoning

It has been shown that high relative catalyst concentrations (low substrate excesses) are key to achieving high polarization levels with SABRE [67], however the short effective T_1 time of substrate polarization whilst bound to the catalyst is a key contributor to relaxation, inhibiting the usefulness of SABRE-polarized material. A solution to this problem is the deactivation of the catalyst subsequent to the polarization of the sample, such that the substrate no longer coordinates and instead relaxes similarly to its inherent T_1. This deactivation of the catalyst is of interest for medical imaging applications of SABRE, as the extension of the lifetime of polarized material will allow for higher polarization levels at the point of use, as well as time for post-processing of the sample to reduce catalyst concentrations to biocompatible levels. For similar reasons, catalyst deactivation is also of interest for the application of SABRE to polarized targets.

Successful catalyst deactivation has been shown by Mewis et al. with the use of the bidentate ligands 2,2'-bipyridine (**bpy**) and 1,10-phenanthroline (**phen**) [77]. Here the active SABRE catalyst was $[Ir(H)_2(\textbf{IMes})(Sub)_3]Cl$, where the substrate was nicotinamide. When 1 equivalent of **bpy** was added to the active catalyst it was found that two resultant complexes of $[Ir(H)_2(\textbf{IMes})(\textbf{bpy})(Sub)]Cl$ were formed with **bpy** lying *trans* to both hydrides in the major isomer and *trans* to a hydride and **IMes** in the minor isomer, see Figure 1.21. The major isomer, where **bpy** lies *trans* to both hydrides, is the successfully deactivated SABRE catalyst and was formed in a 25:1 ratio to the minor isomer. Note that the axial substrate ligand in the major isomer is not free to exchange and thus is unable to perform SABRE, whereas the equatorial substrate ligand in the minor isomer may still exchange and perform SABRE.

Before **bpy** addition, the T_1 values of over the four proton positions in the substrate ranged from 16-65% of their free T_1 values, whereas subsequent to the addition these T_1 values recovered to at least 88% of their free values, shown in Table 1.6. It was thus successfully shown that catalyst poisoning can indeed return the T_1 value of the substrate to close to its free value. The experiments with **bpy** were repeated using **phen** to similar results. Similarly, the deactivated catalyst was the major isomer whilst the still-active catalyst was the minor isomer, and extensions of the polarization lifetime were seen.

*Table 1.6 - Results from [77] showing the T_1s for the free substrate (no catalyst), the substrate in solution with the active catalyst, and the substrate in solution after the addition of **bpy** for the four proton positions in nicotinamide. Percentages given are in relation to the free T_1 value.*

Proton position	Free T_1 (s)	T_1 before bpy addition (s)	T_1 after bpy addition (s)
1	43.1	7.0 (16%)	38.0 (88%)
2	11.3	6.1 (54%)	11.5 (102%)
3	13.5	3.7 (27%)	14.0 (104%)
4	6.6	4.3 (65%)	6.8 (103%)

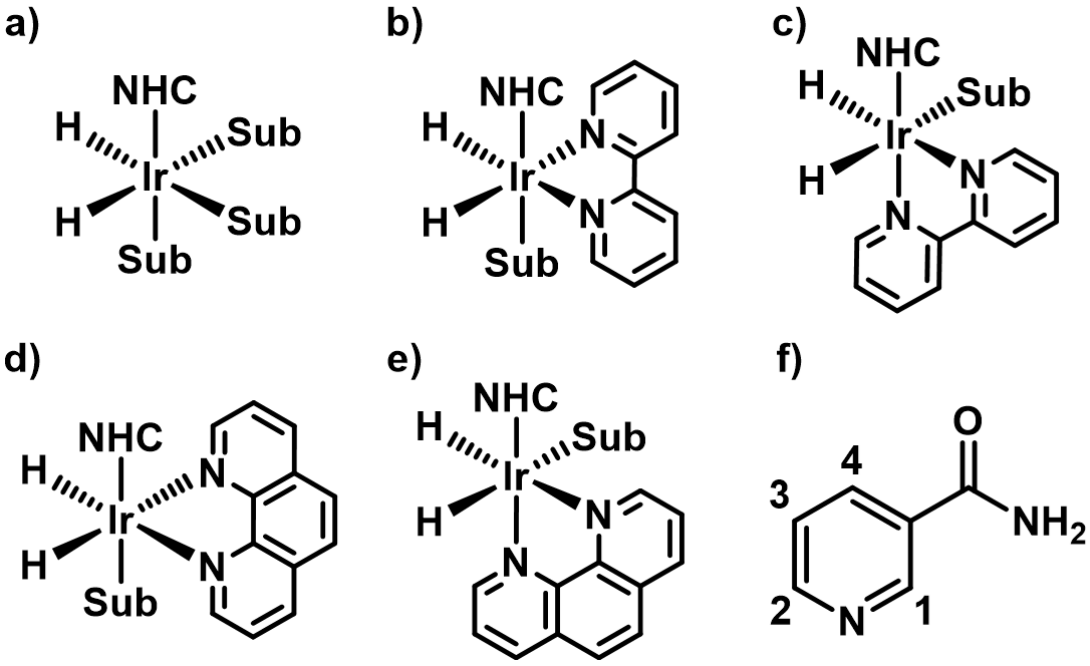

*Figure 1.21 - Schematic of (de)activated catalysts from [77]. a) Active SABRE catalyst $[Ir(NHC)(H)_2(Sub)_3]Cl$. b) Major isomer of $[Ir(NHC)(H)_2$(**bpy**)$(Sub)]Cl$. c) Minor isomer of $[Ir(NHC)(H)_2$(**bpy**)$(Sub)]Cl$. d) Major isomer of $[Ir(NHC)(H)_2$(**phen**)$(Sub)]Cl$. e) Minor isomer of $[Ir(NHC)(H)_2$(**phen**)$(Sub)]Cl$. f) Nicotinamide substrate. Note that for b) and d) the axial substrate does not exchange, whereas for c) and e) the equatorial ligand is free to exchange and can participate in SABRE.*

Fluorinated solvents

It was previously explained how *p*-H_2 availability in solution is often the limiting factor for SABRE, and that this can be helped by increasing the pressure of *p*-H_2 in the sample. An alternative solution is to choose solvents for SABRE that have inherently high gas solubility. A candidate group for these solvents are perfluorocarbons (PFCs), which have already found use in the medical industry as blood substitutes due to their high gas solubility making them good carriers of oxygen [78,79].

Another quality of PFCs that may prove beneficial for use in SABRE is their lack of miscibility with water, which may allow a biphasic separation approach to be used in order to remove the catalyst after polarization. This approach would involve performing SABRE in an organic solvent and adding an aqueous layer to the sample, causing the substrate to transition into the aqueous layer due to its higher solubility, and leaving the catalyst in the organic layer.

This biphasic approach using PFCs was investigated by Ettedgui et al. [80], in which they trialled the use of a fluorinated SABRE catalyst, solvent and co-ligand prior to a biphasic separation in order to produce a polarized biocompatible solution. PFCs are notorious for poorly dissolving metal complexes and thus a mixture of the fluorinated solvent methyl perfluorobutylether and methanol-d_4 was used to improve catalyst solubility. It was found that this combined solvent allowed for a 20% increase in the polarization of the substrate [1-^{13}C] pyruvate in comparison to a pure methanol-d_4 solvent, which was here attributed to the high gas solubility of PFCs. This demonstration of improved ^{13}C polarization using PFCs is encouraging, however it should be noted that, due to the high gyromagnetic ratio of ^{19}F, fluorinated solvents contribute more to dipolar relaxation than a deuterated solvent which may be significant in the case of ^{1}H SABRE. PFCs will be investigated for use for ^{1}H polarization through SABRE in Chapter 2.

Phase transitions

One of the ways in which SABRE may be used for polarized targets in physics experiments is in a frozen pellet target, used at storage ring facilities. This will be discussed further in Chapter 5. Frozen pellet targets typically use µm-sized frozen droplets of material and are considered promising for high luminosity experiments [81], making them a prospective candidate for producing polarized targets that can operate at the intensity frontier, such as at the upcoming Electron Ion Collider (EIC) at Brookhaven National Lab.

Since SABRE is a process that occurs in the solution state, it is apparent that for SABRE material to be used in a frozen pellet target that the polarization would need to be maintained through the liquid-to-solid phase transition. Preserving polarization through a phase transition has also been important for medical imaging applications since the invention of dissolution-DNP (d-DNP) by Ardenkjær-Larsen et al. in 2003 [82]. d-DNP is a technique for producing solution-state hyperpolarized material through the rapid dissolution of solid-state DNP-polarized material. Ardenkjær-Larsen et al. achieved this for ^{13}C urea with the use of an 'injection wand' to rapidly inject hot water over the sample to thaw it within the polarizing magnet.

Whilst solid-to-liquid phase transitions are needed for d-DNP, liquid-to-solid phase transitions have recently been utilized for PHIP and SABRE experiments in order to produce biocompatible solutions

of polarized metabolic agents [83-85]. The main substrates of interest in this field are fumarate and pyruvate, which are important biosensors due to their role in human metabolism. A key roadblock for in vivo studies using PHIP/SABRE is the toxicity associated with traditional PHIP/SABRE solvents and catalysts, and thus there are strong motivations to produce hyperpolarized biosensors in catalyst-free aqueous solution.

In pioneering work by Knecht et al. [83] it was shown that PHIP ^{13}C-polarized fumarate would maintain its polarization through two successive phase changes, firstly through the precipitation of fumarate out of organic solution and secondly through the redissolution of the fumarate into aqueous solution. The precipitation step was performed upon a fritted funnel inside a 100 mT permanent magnet, separating the fumarate from the PHIP catalyst and solvent. This precipitation reaction was induced through the addition of HCl to the solution, and the precipitate was washed with deionized water and acetone before being dissolved into aqueous solution, all whilst inside the magnet. Upon measurement it was found that the residual polarization of the ^{13}C fumarate remained in excess of 20% and that the catalyst concentration in solution was reduced by 99.7%. Notably, experiments where the precipitation happened in the absence of the holding magnet showed no residual polarization post-redissolution.

This catalyst removal technique using precipitation and redissolution was shown to work more generally by Schmidt et al. in a process they call Re-Dissolution SABRE (Re-D SABRE) [84]. In this study, the redissolution of SABRE-polarized pyruvate was investigated in a broadly similar method to [83]. Here, the nonpolar solvent ethyl acetate was used to encourage the precipitation of pyruvate, and the removal of the catalyst was achieved via phase separation rather than filtration. The redissolution step was trialled at four different fields, Earth's field (approximately 50 μT), 10 mT, 0.3 T and 1.4 T, with the Earth's field and 10 mT trials producing none and very low polarization respectively. Only at 0.3 T and 1.4 T was significant residual polarization seen, at 4.0% and 3.6% respectively. This leads to speculation about at which point in the 10-300 mT range is the holding field strong enough to maintain the polarization through the phase change.

1.5 Thesis aims

This work focuses on assessing the capability for SABRE chemical hyperpolarization to be used to overcome the challenges faced by current polarized nuclear target technologies. Current targets typically rely on DNP, however advances in accelerator technologies mean that the new intensity frontier brings levels of radiation and heat deposits which will greatly challenge traditional cryogenic methods of polarization.

Signal Amplification By Reversible Exchange (SABRE) is a novel nuclear polarization technique, developed to enhance the sensitivity of target molecules in magnetic resonance imaging applications. It has attracted widespread interest for biomedical imaging applications as an alternative to DNP for producing hyperpolarized media, however as of yet there has been little attempt to develop the technology towards use for a polarized nuclear target, the needs of which are high proton polarization (preferably of order unity), a high dilution factor, and good radiation resistance. The attractive attributes of SABRE are its ability to operate at room temperature and at low (millitesla) magnetic fields, which is a stark contrast to the high (tesla) fields and cryogenic temperatures (around 1 K) needed for DNP. SABRE is also advantageous as the polarization can be produced in seconds rather than hours and that once generated the orientation of the polarization can be easily manipulated using weak applied fields.

Typical SABRE-polarized solutions for well-optimized systems may produce ^{1}H polarization levels of 1-10% with substrate concentrations of 10-100 mM. For SABRE to be used in a polarized target it is crucial to bring the polarization levels closer to that of DNP which can reach in excess of 90% for ^{1}H. It is also crucial that the dilution factor is maximized, which involves maximizing the substrate concentration and minimizing the quantities of catalyst and solvent used, in addition to choosing substrates themselves that have a high dilution factor.

This work presents results towards addressing these challenges facing SABRE. It presents work on optimizing the polarization transfer efficiency of SABRE in Chapter 2, which is needed in combination with the extension of polarization lifetimes, seen in Chapter 3, to reach the desired high polarization levels. This work will also feature the first ever test of the resilience of SABRE-polarized material to an incident particle beam in Chapter 4. Finally, Chapter 5 will present the results from a prototype SABRE-polarized target, capable of continuous polarization with precise digital timing and flow rate control.

Chapter 2 - Studies in polarization efficiency

2.1 Introduction

This chapter aims to investigate the factors that affect the levels of polarization delivered by the SABRE hyperpolarization method. It will include studies dealing with the screening of a selection of promising substrates, as well as the synthesis of a novel selectively-deuterated substrate that was inspired by these findings. The polarization levels of these substrates will be investigated as a function of a series of parameters, such as the identity of an additional co-ligand, and the relative concentrations of the substrate and the SABRE catalyst. Other studies presented in this chapter include an investigation into the effects of performing SABRE in a 'neat' liquid (with no additional solvent), a study into novel high H_2 gas solubility solvents, and a study on the polarization of the ^{15}N nucleus.

Throughout this thesis it will be necessary to refer to specific proton sites in molecules, as they exhibit different behaviour in regards to both polarization efficiency and spin order lifetime. Almost all of the substrates discussed will be pyridine derivatives and thus can be described similarly. Two naming conventions will be used, seen in Figure 2.1. The first will be *ortho*, *para*, and *meta*, where *ortho* refers to the proton positions next to the nitrogen, *para* refers to the proton opposite the nitrogen, and *meta* refers to the two positions between *ortho* and *para* protons. The second naming convention uses numbering, whereby the positions are numbered anticlockwise from the nitrogen. An example is 3,5-dichloropyridine (**3,5-dcpy**), pyridine substituted with two chloride groups in the 3 and 5 positions, also referred to as the *meta* positions.

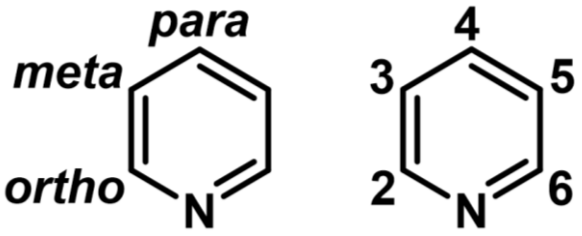

Figure 2.1 - Labelling of proton positions in pyridine and derivatives.

The quantification of substrate polarization levels is also a focus throughout this thesis. These values are reported either as the signal enhancement factor (fold increase, which is field-

dependent) or as the polarization level (percentage, which is field-independent). Unless otherwise stated, signal enhancement factors refer to ^{1}H nuclei at 9.4 T (400 MHz). The thermal equilibrium polarization of a ^{1}H nucleus at 9.4 T is approximately 0.0032%, therefore a signal enhancement of 310-fold corresponds to a polarization level of around 1%. Enhancement factors may be positive or negative, indicating whether the enhanced signal is the same (positive) or opposite (negative) phase as the thermal equilibrium signal. The direction of the polarization is generally inconsequential, as it can be manipulated by changing the applied field to the sample.

In this chapter the longitudinal relaxation time (T_1) will be measured for each proton in the substrate. However, for comparison across SABRE substrates and reaction conditions, the average T_1 is typically reported. Exceptions are made where individual proton sites dominate the relaxation dynamics and merit separate discussion.

Catalysts in this thesis are referenced by the identity of their NHC ligand. For example, the precatalyst [Ir(**IMes**)(COD)Cl] is referred to as the **IMes** precatalyst. For simplicity, the activated catalysts will be called by the same name despite actually taking a number of forms, for example the active catalyst [Ir(**IMes**)$(H)_2(Sub)_3$]Cl that forms in methanol-d_4 and [Ir(**IMes**)$(H)_2(Sub)_2$Cl] that forms in dichloromethane-d_2 will both be referred to as the **IMes** catalyst, unless the specific active catalyst has been characterized. Here the actual identity of the catalyst links to the choice of solvent, and potentially the strength of the substrate as a base.

2.2 Substrate comparison study

SABRE can be applied to a growing range of molecules, however the ideal molecule for use as a polarized nuclear target must have a high dilution factor (fraction of polarizable nucleons), f, a high polarization, P, and a long polarization lifetime, T_1. A high dilution factor and polarization is important as these feature in the Figure-of-Merit as:

$$FoM = Lf^2P^2 \qquad (Eq. 2.1)$$

and thus the running time necessary to achieve a specified measurement accuracy is inversely proportional to the square of each. A long T_1 is necessary as it, alongside the rate of polarization transfer, will influence the maximum polarization that can be reached for a continuously polarized SABRE target.

It was decided to investigate a number of possible substrates, determine their achievable polarization and T_1 values, and use these as a rationale to identify potential candidates for use in a polarized target.

All substrates were tested under identical conditions with 5 mM of [Ir(I**Mes**)(COD)Cl] (**IMes**) precatalyst, 20 mM of the co-ligand dimethyl sulfoxide-d_6 (**DMSO-d_6**) and 200 mM of substrate, in 0.6 mL of the solvent dichloromethane-d_2 (**DCM-d_2**). The conditions were chosen to reflect a trade-off between polarization (decreases with reduced *p*-H_2 excess) and lifetime (increases with substrate excess). The addition of **DMSO** proved necessary to promote the controlled ligation of the more sterically-hindered substrates. The samples were prepared and activated as described in Section 7.2.1 and were polarized using the 'Shake and drop' method described in Section 7.2.2. The T_1 values were found using a thermally polarized T_1 inversion recovery sequence, detailed in Section 7.3.3.

Eight different substrates were investigated, all of which were *N*-heterocycles. The features selected for variation across the tested substrates were the number and position of nitrogen atoms in the aromatic ring, alongside the effects of halogenation and methylation.

The results of these studies are summarized in Table 2.1, with the investigated substrates being split into 3 categories: *N*-heterocycles, halogenated *N*-heterocycles, and methylated *N*-heterocycles, for ease of reference. For comparison, a new quantity will be introduced, the average nucleon polarization (fP), which is the product of the dilution factor, f, and the average ^{1}H polarization, P. As can be seen from Eq. 2.1, the FoM will be proportional to the square of the average nucleon polarization.

2.2.1 Results

Of the *N*-heterocycles, pyridine (**py**) and pyrazine (**pz**) delivered the highest average nucleon polarization of 0.069% and 0.070% respectively, equivalent within their respective error margins. Pyrimidine (**pm**) and pyridazine (**pd**) are stereoisomers of **pz**, however both yielded significantly lower average nucleon polarizations of 0.025% and 0.020% respectively.

Of the halogenated *N*-heterocycles, no signal enhancements were observed for 2,5-dichloropyrazine (**2,5-dcpz**), whereas **3,5-dcpy** and 2,6-dichloropyrazine (**2,6-dcpz**) had average nucleon polarizations of 0.050% and 0.009% respectively. Despite the high dilution factor in 3,5-dimethylpyridine (**3,5-dmpy**), it delivered an average nucleon polarization of just 0.005%.

Across the *N*-heterocycles, the average ^{1}H $T_1$was largely consistent, with **py** having the lowest average T_1 at 39 s and **pm** having the highest at 49 s, with the group average being 42 s. Significantly higher T_1s were seen with the halogenated *N*-heterocycles, where the average T_1s were found to be 83 s, 133 s, and 63 s for **3,5-dcpy**, **2,5-dcpz,** and **2,6-dcpz** respectively. The methylated *N*-heterocycle **3,5-dmpy** showed the lowest average T_1 of all investigated substrates at 12 s.

2.2.2 Discussion

The highest average nucleon polarizations are found in **py** and **pz**, due to their combination of a high dilution factor and a high polarization yield, whilst the longest average T_1 for substrates exhibiting SABRE polarization was found in **3,5-dcpy**.

Halogenation was shown to significantly extend the polarization T_1, whereby **3,5-dcpy** saw a 110% increase and **2,6-dcpz** saw a 50% increase compared to their non-halogenated counterparts. It is theorized that this is due to the decrease in the rate of dipolar relaxation brought about by the replacement of the high gyromagnetic ratio ^{1}H nuclei with the lower gyromagnetic ratio ^{35}Cl/^{37}Cl nuclei. Similar trends would be expected with the substitution of bromide groups, but not with fluoride groups, due to their corresponding low/high gyromagnetic ratios.

Methylation of the *N*-heterocycles increases the fraction of ^{1}H nuclei and thus may have been considered as a promising way to increase the dilution factor of the substrate. However, due to the mechanism behind SABRE, the increase in the number of polarizable nuclei is expected to decrease the polarization value of each. This is because the rate of spin order transfer in SABRE is constrained by factors such as the catalyst and dissolved *p*-H_2 concentrations. As the rate of spin order transfer through SABRE will not correspondingly increase with the number of polarizable nuclei, the average ^{1}H polarization levels will fall for methylated *N*-heterocycles.

The very low polarization observed for **3,5-dmpy** can be attributed to poor ligand dissociation rates due to steric effects, in addition to the shortened polarization lifetimes due to the presence of the methyl groups. The 12 s average T_1 for **3,5-dmpy** was significantly impacted by the short 8 s T_1 of the methyl protons, whereas for the other ^{1}H sites the T_1s were 17 s and 27 s for the *ortho* and *para* positions respectively. The lack of polarization of **2,5-dcpz** can also be attributed to the substrate being sterically hindered, with the bulky chloride group at the 2-position interfering with ligation to the catalyst.

In this study, **Py** and **3,5-dcpy** were found to be the main substrates of interest, due to their high average nucleon polarization and high T_1s respectively, and were thus chosen to be investigated further.

*Table 2.1 - Results from substrate comparison study. All substrates were tested under identical SABRE conditions using 5 mM of **IMes**, 20 mM of **DMSO-d_6** and 200 mM of the substrate in 0.6 mL of **DCM-d_2**. The referenced results from butanol and ammonia are not from this study and have been included for comparison.*

	Substrate	Formula	Dilution factor, f	Polarization, P (%)	Avg. T_1 (s)	Structure
***N*-heterocycles**	Pyridine	C_5H_5N	0.063	1.1 ± 0.1	39.0 ± 0.7	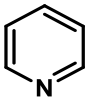
	Pyrazine	$C_4H_4N_2$	0.050	1.4 ± 0.1	41.9 ± 0.7	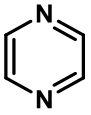
	Pyrimidine	$C_4H_4N_2$	0.050	0.5 ± 0.1	48.8 ± 0.3	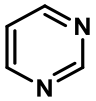
	Pyridazine	$C_4H_4N_2$	0.050	0.4 ± 0.1	39.6 ± 0.3	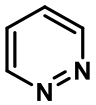
Halogenated	3,5-dichloropyridine	$C_5H_3Cl_2N$	0.020	2.5 ± 0.2	83 ± 3	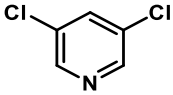
	2,5-dichloropyrazine	$C_4H_2Cl_2N_2$	0.013	No enhancement observed.	133 ± 7	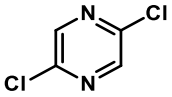
	2,6-dichloropyrazine	$C_4H_2Cl_2N_2$	0.013	0.7 ± 0.1	63 ± 1	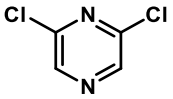
Methylated	3,5-dimethylpyridine	$(CH_3)_2C_5H_3N$	0.084	0.06 ± 0.01	12.2 ± 0.1	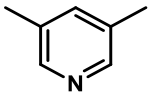
DNP	Butanol (Frozen-spin)	C_4H_9OH	0.135	94 [2]	1.4 x 10^7 [2]	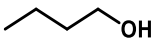
	Ammonia (Continuously polarized)	NH_3	0.176	96 [1]	300-1800 [86]	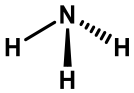

2.3 Polarization of pyridine

In the substrate comparison study, **py** was found to have the second highest dilution factor in addition to the joint highest average nucleon polarization with **pz**. Coincidentally, **py** was also the first substrate to be polarized by SABRE by Adams et al. [49].

It was decided to investigate whether the polarization levels of **py** could be increased by making alterations to the most commonly used SABRE conditions (5 mM of **IMes** catalyst and a 5-fold substrate excess), and by finding the substrate excess which would produce the highest molar polarization. Here the molar polarization is the product of the average ^{1}H polarization and the concentration of ^{1}H nuclei in solution, a metric that illustrates the total polarization transfer that has occurred, informative for polarized target applications.

2.3.1 Polarization optimization

In this study, the effects of the addition of a deuterated co-ligand and the deuteration of the catalyst NHC on the polarization of **py** were investigated for 5 samples, containing the **IMes** and [Ir(**IMes-*d*$_{22}$**)(COD)Cl] (**IMes-*d*$_{22}$**, Figure 2.13) catalysts with and without the co-ligand **DMSO-*d*$_6$**. A sample with **IMes** where the substrate **py** was replaced by a mixture of **py** and **py-*d*$_5$** in a 1:2 ratio was additionally run.

All samples contained 5 mM of precatalyst, 25 mM of substrate and 25 mM of co-ligand (where applicable) in 0.6 mL of methanol-d_4. The samples were prepared and activated as described in Section 7.2.1 and were polarized using the 'Shake and drop' approach as described in Section 7.2.2. The T_1 values were measured using a hyperpolarized T_1 recovery as described in Section 7.3.2.

Results

As shown in Figure 2.2 and Table 2.2, the transfer efficiency to each ^{1}H site in the substrate varies substantially for each sample. For the **IMes** sample, strong polarization transfer was observed to both the *ortho* and *para* sites, with enhancements of -1260-fold and -1230-fold respectively, however the enhancement for the meta site was significantly lower at only -220-fold.

For the sample containing **IMes** and a 1:2 ratio of **py**/**py-*d*$_5$**, a drop in the polarization of the *ortho* site was observed compared to the **IMes** sample. This decrease was offset by gains in the polarization of the *meta* and *para* positions, resulting in a slight overall increase in the average enhancement.

The **IMes-*d*$_{22}$** sample exhibited a distribution of polarization similar to that of the **IMes** sample, characterized by strong polarization of the *ortho* and *para* sites and comparatively weaker

polarization of the *meta* site. Notably, the polarization of each site was higher than for the **IMes** sample, leading to a higher average polarization.

The **IMes + DMSO-*d*$_6$** sample showed strong polarization of the *ortho* sites but comparatively weaker polarization of the *meta* and *para* sites. In contrast, the **IMes-*d*$_{22}$ + DMSO-*d*$_6$** sample displayed poor polarization of the *ortho* site, exhibiting variability in the sign of the signal enhancement, accompanied by moderate polarization of the *meta* and *para* sites.

Among the five samples tested, the highest polarization was achieved in the **IMes-*d*$_{22}$** sample, which yielded an average signal enhancement of -1280-fold, corresponding to a polarization level of 4.1%.

For four out of the five tested samples, the signal decay for the *meta* position was observed to be non-exponential, preventing a reliable fit to determine its T_1 value. This behaviour suggests the creation of a mixture of magnetic states, an effect previously reported by Mewis et al. [87]. Consequently, the average T_1 values reported in Table 2.2 were calculated using only the data from the *ortho* and *para* positions.

A 27% gain in the average T_1 was observed with the **IMes-*d*$_{22}$** catalyst relative to the **IMes** catalyst, corresponding to an increase from 6.2 s to 7.9 s. The addition of **DMSO-*d*$_6$** also had the effect of increasing the T_1. The average T_1 for the **IMes + DMSO-*d*$_6$** sample was 56% longer than for the **IMes** sample, and the average T_1 for the **IMes-*d*$_{22}$ + DMSO-*d*$_6$** sample was 76% longer than for the **IMes-*d*$_{22}$** sample. Using a 1:2 ratio of **py/py-*d*$_5$** as the substrate with the **IMes** catalyst resulted in the largest effect, increasing the average T_1 by 140% from 6.2 s to 14.9 s.

Based on these results, it can be concluded for these sample conditions that the ranking of deuteration effects on the T_1 increase is *Deuterated co-substrate* $>$ *Deuterated co-ligand* $>$ *Deuterated catalyst NHC*. This observation aligns with the expectation that a deuterated co-substrate and deuterated co-ligand would have a larger impact than the deuteration of the catalyst NHC, owing to their closer proximity to the substrate ^{1}H sites within the catalytic complex.

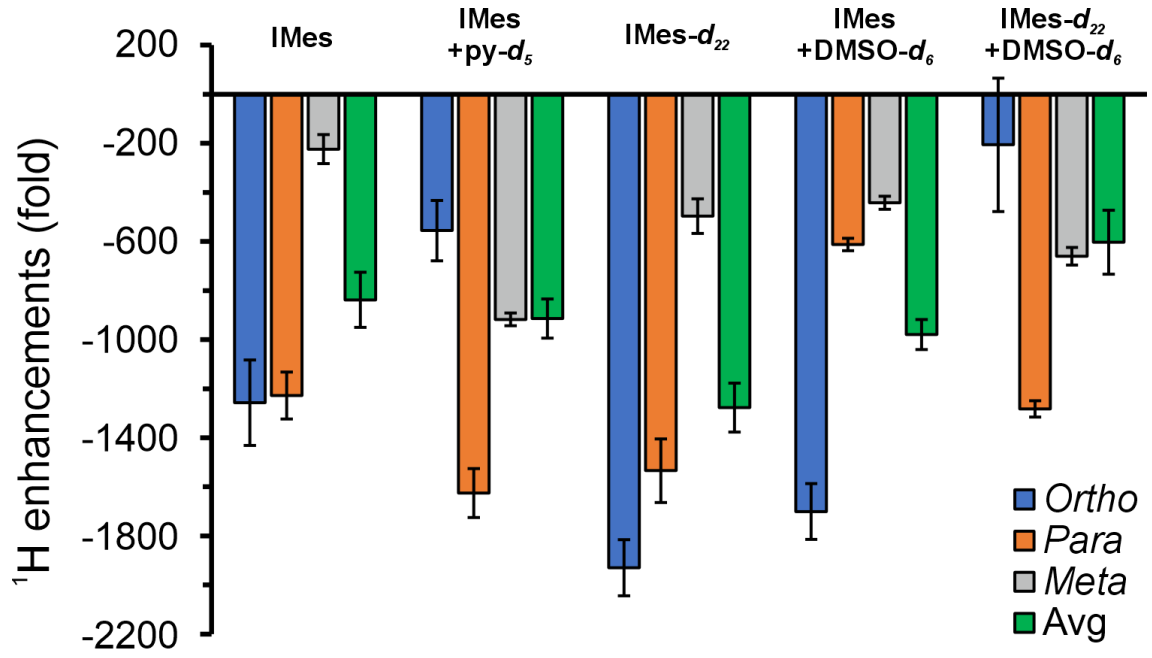

*Figure 2.2 - ^{1}H enhancements for **py** in methanol-d_4 with varying catalyst NHCs and co-ligands.*

*Table 2.2 - Summary of results for the enhancement optimization of **py**.*

System	^{1}H Enhancements (fold) [%]				Avg ^{1}H T_1 (s)[i]
	Ortho	Para	Meta	Avg.	
IMes	-1260 ± 120	-1230 ± 100	-220 ± 30	-840 ± 80 [2.7 ± 0.3]	6.2 ± 0.1
IMes + py-d_5	-560 ± 170	-1630 ± 100	-920 ± 60	-910 ± 110 [2.9 ± 0.4]	14.9 ± 0.5
IMes-d_{22}	-1930 ± 110	-1530 ± 130	-500 ± 70	-1280 ± 100 [4.1 ± 0.3]	7.9 ± 0.2
IMes + DMSO-d_6	-1700 ± 110	-610 ± 30	-440 ± 30	-980 ± 60 [3.2 ± 0.2]	9.7 ± 0.2
IMes-d_{22} + DMSO-d_6	-210 ± 270	-1280 ± 30	-660 ± 40	-600 ± 130 [1.9 ± 0.4]	13.9 ± 0.3

[i] Here the T_1s were calculated using the average of only the *ortho* and *para* position protons.

2.3.2 Effect of substrate excess

It is well established that in SABRE the catalyst acts as a source of dipolar relaxation which can shorten the T_1 of nuclei in the substrate [75]. Furthermore, for the application of SABRE for polarized nuclear targets, any unpolarizable material is undesirable as it decreases the dilution factor, a critical feature in the FoM (Eq. 2.1). Consequently, minimizing the quantity of catalyst present relative to the substrate is desirable. There are, however, conflicting pressures to increase the catalyst concentration in solution relative to the substrate, as this will deliver a higher catalyst turnover, and thus typically a higher rate of polarization transfer.

Recently, the possibility for the removal of the catalyst after the SABRE polarization process has been demonstrated. Notably, Iali et al. showed that the poor water solubility of active SABRE catalysts can be exploited by employing a phase separation technique [88]. With substrates such as **pz,** they found that polarization transfer could take place in an organic layer, after which the substrate could be efficiently transferred into an aqueous layer, separating it from the catalyst which remains in the organic phase.

This technique was named CASH-SABRE (CAtalyst Separated Hyperpolarization through SABRE). CASH-SABRE has been developed further by Barskiy et al. and Robertson et al. [89,90], who have employed silica-mounted catalyst scavengers in order to reach <1 ppb catalyst concentrations in solution. These catalyst removal techniques can be implemented rapidly (on timescales of seconds), offering a promising route to producing highly polarized solutions with low catalyst concentrations.

The availability of these catalyst removal techniques diminishes the need for low catalyst concentrations during SABRE solely for the purposes of optimizing the dilution factor. There is, however, still the need to optimize the substrate to catalyst ratio, balancing the higher rates of polarization transfer at a low substrate excess against the lower rates of dipolar relaxation at a high substrate excess.

Therefore, it was decided to investigate the effects of varying the substrate excess on the signal enhancement and the T_1 for the substrate **py,** whilst keeping a fixed catalyst loading. The signal enhancements allow for the calculation of the substrate polarization levels and the molar polarization P_{Molar}, defined as:

$$P_{Molar}(mM\ \%) = P(\%) \times C(mM). \qquad (Eq.\ 2.2)$$

Here P is the average polarization of polarizable nuclei (^{1}H in this study), and C is the molar concentration of these nuclei in solution. This quantity shares similarities with the term fP in the

Figure of Merit (Eq. 2.1), whereby the dilution factor, f, the fraction of polarizable nuclei, is replaced by the concentration of polarized nuclei in solution, C.

The samples in this study contained 5 mM of **IMes** and 25-600 mM (5-fold to 120-fold excess) of **py** in 0.6 mL of methanol-d_4. The samples were prepared and activated as described in Section 7.2.1 and were polarized using the 'Shake and drop' method as described in Section 7.2.2. The T_1 values were measured using a hyperpolarized T_1 recovery method, as described in Section 7.3.2.

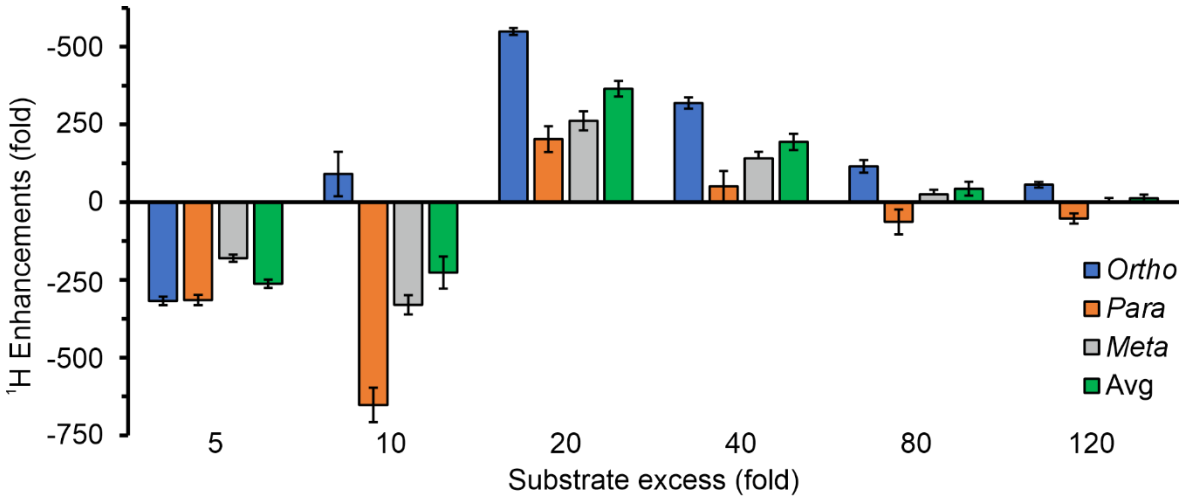

*Figure 2.3 - ^{1}H enhancements for **py** with varying substrate excess.*

*Table 2.3 - ^{1}H enhancements, polarization, and molar polarization for **py** with varying substrate excess.*

Catalyst concentration (mM)	Substrate concentration (mM) [excess]	Avg ^{1}H enhancement (fold)	Avg ^{1}H polarization (%)	Molar polarization (mM %)
5	25 [5]	-260 ± 10	-0.8% ± 0.1	-106 ± 5
5	50 [10]	-230 ± 50	-0.7 ± 0.2	-180 ± 40
5	100 [20]	370 ± 20	1.2 ± 0.1	590 ± 40
5	200 [40]	190 ± 30	0.6 ± 0.1	630 ± 80
5	400 [80]	40 ± 20	0.1 ± 0.1	280 ± 140
5	600 [120]	10 ± 10	0.0 ± 0.1	120 ± 110

Results

As can be seen in Figure 2.3 and Table 2.3, the signs of the signal enhancements for **py** were not constant across the range of substrate excesses investigated. For the 5-fold and 10-fold substrate excesses, the average signal enhancements were predominantly negative, whereas for substrate excesses of 20-fold and above, the signal enhancements were mostly positive. Notably, for some samples positively and negatively enhanced substrate peaks were observed simultaneously within the same spectrum.

The highest average signal enhancements for **py** were found at a 20-fold substrate excess, reaching 370-fold and corresponding to a polarization level of 1.2%. The molar polarization of **py** peaked at a value of 630 mM % for the 40-fold excess sample, equivalent to the 20-fold excess sample within error. There is a sharp drop-off in the measured signal enhancements after a 40-fold excess, dropping by 79% from 190-fold to 40-fold from a 40-fold substrate excess to an 80-fold substrate excess. The lowest average signal enhancements of only 10-fold are observed for the 120-fold excess sample.

For samples containing a 10-fold or higher **py** excess, it was observed that the signal decay behaviour could not be accurately described by a single exponential function. Consequently, a reliable fitting for the T_1 was unable to be found. It is proposed that was due to the contribution of short-lived states derived from longitudinal two-spin order terms, which are typically absent in NMR experiments. The detection of such coherences has previously been observed in SABRE-polarized nicotinamide by Mewis et al. [87]. Normally, when a 90^o RF pulse is applied these states will not contribute to the detected signal, however here the use of low-tip angle excitation makes them visible.

2.3.3 Discussion

Polarization optimization study

In the polarization optimization study, some observed trends aligned with expectations, while others did not.

As anticipated, the **IMes-*d_{22}*** sample showed increased polarization levels relative to the **IMes** sample, attributed to the deuteration of the catalyst NHC reducing the rate of relaxation of the spin order during polarization transfer. This effect is discussed further in Section 1.4.3.

A larger increase in the signal enhancements of **py** was expected with the use of the deuterated co-substrate **py-*d_5***. A prior study by Rayner et al. found that using methyl-4,6-d_2-nicotinate and its fully-deuterated analogue methyl-2,4,5,6-d_4-nicotinate in a 1:3 ratio increased the polarization levels by 20% from 41.7% to 50% relative to methyl-4,6-d_2-nicotinate on its own [70]. In contrast, this study found a more modest 7% increase in polarization, from 2.7% to 2.9%.

Substrate excess study

In the substrate excess study, it was initially expected that signal enhancements would decrease with increasing substrate excess, with the 5-fold excess sample providing the highest enhancements due to the higher *p*-H_2 and catalyst concentrations relative to the substrate. However, this trend was not observed. One explanation is that the lower excess samples experienced greater polarization losses prior to measurement due to faster relaxation, thus masking the true polarization levels achieved.

An unexpected result was the significant decrease in the molar polarization beyond a 40-fold substrate excess. This suggests that the total polarization transfer declines for higher substrate concentrations. As demonstrated by Cowley et al. [57] and Appleby et al. [91], substrate exchange in SABRE typically follows a dissociative mechanism, meaning that the exchange rate, known to be a key factor in polarization transfer efficiency, is independent of the substrate concentration. Therefore, a change in the substrate exchange rate cannot explain the decreased polarization transfer that occurred.

Instead, a proposed explanation involves the effect of increasing substrate concentrations in solution on the *p*-H_2 exchange rates. It has been shown by Appleby et al. [91] that the rate of H_2 exchange is reduced with increasing substrate concentration, which can be explained by hydrogen substitution being an associative process with an intermediate step needed. It is proposed that H_2 exchange is inhibited by the intermediate complex $[Ir(NHC)(H)_2(S)_2]Cl$ reacting with a substrate molecule rather than H_2, resulting in 'spent' *o*-H_2 being replaced by 'fresh' *p*-H_2 at a lower rate. The

rate of H_2 exchange is known to frequently be the limiting factor for polarization transfer [76], and thus this effect will reduce the polarization transfer efficiency. The substrate and *p*-H_2 ligand exchange pathways are shown in Figure 2.4.

A further explanation for the reduced molar polarization observed beyond a 40-fold substrate excess lies in the directionality of the signal enhancements. As shown in Figure 2.3, the 80-fold and 120-fold excess samples exhibit signal enhancements of opposite signs at different proton positions. These opposing enhancements partially cancel when averaged, leading to an apparent drop in the polarization. By instead considering the magnitude of the signal enhancements, the recalculated molar polarization for the 120-fold excess sample (shown in Table 2.4) is found to be only a factor of two lower than that of the 40-fold excess sample. This is more readily explained by the changing rates of *p*-H_2 exchange at higher substrate concentrations.

The observation of both positively and negatively enhanced substrate peaks is an effect that is not unexpected for a system of many coupled spins, such as [Ir(**IMes**)(**py**)$_3$(H)$_2$]Cl, where the approximations made for an AA'B spin system break down. Adams et al. [92] have previously predicted enhanced peaks of different signs for a SABRE-polarized substrate within more complex spin systems.

A possible explanation is that increasing the concentration of **py** lowers the dielectric constant of the solvent mixture as **py** is less polar than methanol. As the polarity of the solvent mixture decreases, it is expected that the proportion of the charged catalyst [Ir(H)$_2$(**IMes**)(**py**)$_3$]Cl (favoured in polar solvents) will decrease and the proportion of the neutral catalyst [Ir(Cl)(H)$_2$(**IMes**)(**py**)$_2$] (favoured in less polar solvents) will increase. A change in the catalytic complex would change the pathway by which the polarisation evolves, potentially resulting in different relative peak phases at the point of substrate dissociation.

2.3.4 Conclusion

The optimization techniques that have been investigated here for the polarization of **py** are the use of a deuterated NHC for the SABRE catalyst, the addition of a deuterated co-ligand, and the use of a deuterated co- substrate. The highest polarization levels were found using the **IMes-*d*$_{22}$** catalyst without the use of a co-ligand or deuterated co-substrate. This system benefitted from the reduced rate of relaxation of the spin order during polarization transfer, which is to be expected from the substitution of a low gyromagnetic ratio nuclei into the polarization transfer catalyst.

It was also found that the optimum substrate excess to maximize the total polarization transfer (also called the molar polarization) was either a 20-fold or 40-fold excess, which performed

similarly. Prior to the experiment it was expected that the molar polarization would reach a maximum and stay there with increasing substrate excess, however it has since been rationalized that an increasing substrate concentration in solution would decrease the H_2 dissociation rate and thus the rate of 'fresh' *p*-H_2 being brought into the catalytic complex. This would in turn reduce the capacity of the SABRE catalyst for spin order transfer.

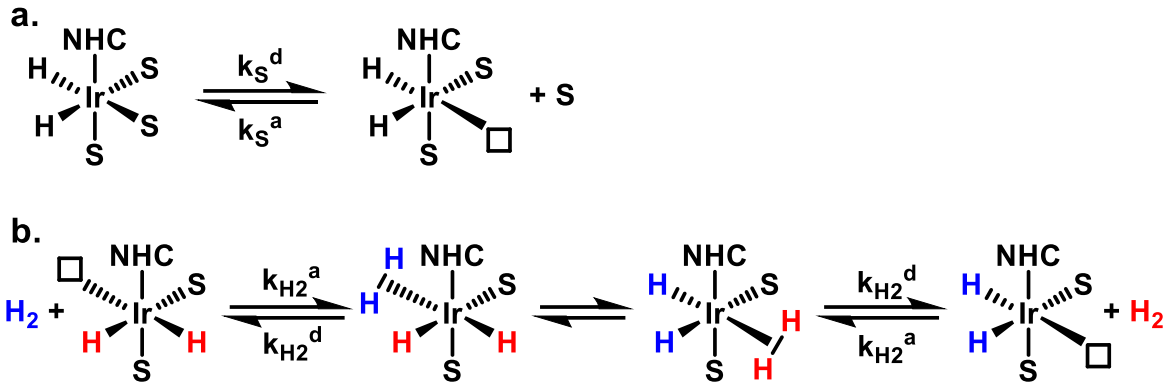

Figure 2.4 - Schematic of ligand exchange pathways in SABRE for an active catalyst of the form $[Ir(NHC)(S)_3(H)_2]Cl$, where S = substrate, NHC = N-heterocyclic carbene. (a) Dissociative substrate exchange. (b) Associative H_2 exchange involving the intermediate $[Ir(NHC)(S)_2(H_2)(H)_2]Cl$. The colours for the hydrogen atoms indicate from which H_2 pair they derived.

*Table 2.4 - Recalculated ^1H enhancements, polarization, and molar polarization for **py** with varying substrate excess using the enhancement magnitudes.*

Catalyst concentration (mM)	Substrate concentration (mM) [excess]	Avg. ^1H enhancement (fold)	Avg. ^1H polarization (%)	Molar polarization (mM %)
5	25 [5]	260 ± 10	0.8 ± 0.1	110 ± 5
5	50 [10]	300 ± 50	1.0 ± 0.2	240 ± 40
5	100 [20]	370 ± 20	1.2 ± 0.1	590 ± 40
5	200 [40]	190 ± 30	0.6 ± 0.1	630 ± 80
5	400 [80]	70 ± 20	0.2 ± 0.1	440 ± 140
5	600 [120]	30 ± 10	0.1 ± 0.1	330 ± 110

2.4 SABRE in neat liquids

For a polarized target using SABRE, ideally the target material consists solely of the polarizable substrate in order to maximise the dilution factor. Typically SABRE is performed with the substrate dissolved in solution at low (mM) concentrations alongside the catalyst. While the use of a solvent is essential for substrates that are solid under the reaction conditions (typically at room temperature under a few bars of pressure), it raises the question of whether a solvent is necessary for liquid substrates that can themselves solubilize the SABRE catalyst, such as pyridine.

To investigate this, SABRE experiments were performed using neat **py**, where it acts as both the substrate and the solvent, accompanied by only the SABRE catalyst in solution. A solution of neat **py** has a molar concentration of 12.4 M, 2-3 orders of magnitude higher than is typically used in a SABRE experiment. This will introduce limitations to the achievable polarization levels, as the hydrogen solubility in solution will remain similar, and thus the ratio of dissolved hydrogen to **py** will be significantly lower compared to typical SABRE conditions. To partially mitigate for this effect, a mixture of **py** and **py-*d*$_5$** would be used, as it has been shown that the polarization spin bath provided by *p*-H_2 will not be depleted if an unpolarizable nuclei such as ^{2}H is bound to the catalyst [73].

The samples contained a 0.6 mL solution of 1% by volume **py** in **py-*d*$_5$**, methanol-*d*$_4$, or a 50/50 **py-*d*$_5$**/methanol-*d*$_4$ mixture, initially compared at a 6.2 mM catalyst concentration. The catalyst concentration was then varied for the solvent **py-*d*$_5$** between 3.1 mM and 99.2 mM. Additionally, a sample was investigated with a higher **py** concentration, at 5% v/v. The samples were prepared and activated as described in Section 7.2.1 and were polarized using the 'Shake and drop' method as described in Section 7.2.2.

2.4.1 Results

It was found that ^{1}H enhancement levels were around 40 times lower for **py** in **py-*d*$_5$** compared to in methanol-*d*$_4$, with enhancements of -3.7-fold and 160-fold respectively, as shown in Table 2.5. Changing the solvent to a 50/50 mixture of **py-*d*$_5$** and methanol-*d*$_4$ resulted in similar enhancements to the **py-*d*$_5$** solvent, at -3.5-fold. Increasing the proportion of **py** to 5% v/v in **py-*d*$_5$** resulted in a slight decrease in enhancements to -3.1-fold.

As it appeared that the catalyst availability was limiting for the 6.2 mM sample of 1% v/v **py** in **py-*d*$_5$**, it was decided to investigate the dependence of the enhancement factor on the catalyst concentration. It was found that for catalyst concentrations in the range of 3.1 to 99.2 mM that the ^{1}H enhancements ranged from -1.8-fold to -16.7-fold, with increasing catalyst concentrations

providing increasing enhancements. The dependence of the ^{1}H enhancements on the catalyst concentrations was approximately logarithmic, as can be seen in Figure 2.5. A logarithmic fitting yielded the equation $\varepsilon = 4.37 \ln(0.42x)$, where ε is the signal enhancement factor and x is the catalyst concentration in mM.

2.4.2 Discussion

These results can be understood by considering substrate binding dynamics. Both **py** and **py-*d*$_5$** can ligate to the catalyst, and under 'neat' pyridine conditions with 6.2 mM of catalyst, the effective substrate excess is approximately 2000-fold. Given typical ^{1}H SABRE exchange rates of 1-10 s^{-1} (optimal around 4.5 s^{-1} [75]), most substrate molecules will not bind to the catalyst over the polarization window, and thus cannot be polarized. In contrast, a 1% v/v solution of **py** in methanol-*d*$_4$ with 6.2 mM of catalyst has a substrate excess of only 20-fold, and thus each substrate molecule will have many more interactions with the catalyst over the polarization window.

The slight decrease in the enhancement factor observed when increasing the **py** concentration from 1% to 5% v/v in **py-*d*$_5$** may be attributed to a decrease in the T_1 from a higher density of ^{1}H nuclei in solution. Additionally, a larger fraction of protonated substrate increases the rate of *p*-H_2 depletion, further limiting polarization transfer.

The lack of improvement in enhancements when using a **py-*d*$_5$**/methanol-*d*$_4$ solvent mixture compared to **py-*d*$_5$** alone is somewhat unexpected. Based on the reduced substrate excess, an increase in enhancements of up to 100% might have been anticipated, but this was not observed.

The logarithmic relationship between enhancements and catalyst concentration (Figure 2.5) suggests diminishing returns as the catalyst loading increases. Within the solubility limits of **IMes** in **py**, this trend indicates that significant polarization levels (e.g. >1%) are not possible to achieve using **py** as a neat liquid, even with the use of **py-*d*$_5$** such that the polarization spin bath will not be significantly depleted. It is postulated that the limiting factor for polarization at low catalyst concentrations is the high substrate excess, whilst at high concentrations polarization is limited by the low *p*-H_2 excess relative to pyridine resulting in too slow rates of *p*-H_2 exchange.

In summary, ^{1}H signal enhancements achieved using neat pyridine were substantially lower than those achieved with the conventional methanol-*d*$_4$ solvent. Enhancement levels showed a logarithmic dependence on catalyst concentration, but the solubility limits of the catalyst prevent significant (>1%) polarization levels being reached with this approach. It is proposed that higher *p*-H_2 pressures could increase the achieved polarization levels, however this approach is not considered promising for producing highly polarized solutions of neat material.

*Table 2.5 - Summary of experimental results for SABRE in **py-d_5**, methanol-d_4 and a **py-d_5**/methanol-d_4 mixture. The samples contained 124 or 600 mM of **py** and 3.1-99.2 mM of **IMes** in 0.6 mL of solvent.*

Solvent	Substrate conc. (mM)	Catalyst conc. (mM)	Avg ^{1}H enh. (fold)
py-d_5	124	3.1	-1.8 ± 0.1
py-d_5	124	6.2	-3.7 ± 0.1
py-d_5	124	12.4	-7.0 ± 0.1
py-d_5	124	24.8	-10.1 ± 0.5
py-d_5	124	49.6	-13.1 ± 1.1
py-d_5	124	99.2	-16.7 ± 0.7
py-d_5	620	6.2	-3.1 ± 0.2
py-d_5/methanol-d_4	124	6.2	-3.5 ± 0.3
methanol-d_4	124	6.2	160 ± 50

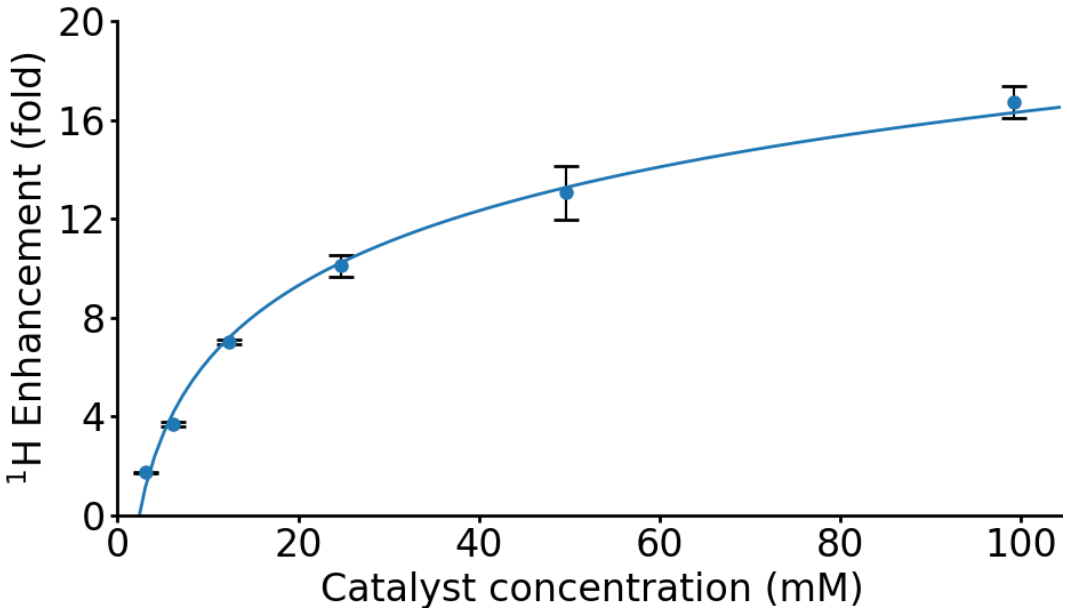

*Figure 2.5 - ^{1}H enhancements for **py** with varying catalyst concentration in solution. The samples contained 0.6 mL of 1% v/v **py** in **py-d_5**, with 3.1-99.2 mM of **IMes**.*

2.5 3,5-pyridine-d_2 - A novel selectively-deuterated substrate for SABRE

One of the key aims of this thesis is to evaluate the optimal substrate for use in a SABRE-polarized nuclear target. The initial focus was on the substrates **py** and **3,5-dcpy**. **Py** was of interest due to its high dilution factor, while **3,5-dcpy** offered the advantage of magnetically isolated protons, which are less susceptible to dipolar relaxation.

As shown in the substrate comparison study, repeated in Table 2.6, relative to the studied substrates, **py** exhibited a high average nucleon polarization, whereas **3,5-dcpy** demonstrated a long polarization T_1. It was hypothesized that selective deuteration could produce a substrate that combined both properties - a high dilution factor and an extended T_1 - by reducing dipolar relaxation through the creation of magnetically isolated proton environments.

The candidate selected for this was 3,5-pyridine-d_2 (**3,5-py-d_2**), shown in Figure 2.6. In this molecule, the deuteration of the *meta* positions isolates the *ortho* and *para* protons, which are now coupled only through weak ^{4}J couplings to each other and via ^{3}J couplings to the lower-γ nucleus ^{2}H. This substitution is expected to reduce the dipolar relaxation experienced by the *ortho* and *para* protons, which were previously strongly coupled to the high-γ *meta* protons.

Py was chosen as the candidate for selective deuteration because it is known to polarize efficiently under SABRE and possesses one of the highest dilution factors of the substrates studied - crucial, as the dilution factor inevitably decreases with deuteration.

*Table 2.6 - Comparison of characteristics of **py**, **3,5-dcpy** and **3,5-py-d_2**. Results are taken from the substrate comparison study in Section 2.2.*

Substrate	Formula	Polarization level (%)	T_1 (s)	Dilution factor, f
Pyridine	C_5H_5N	1.1 ± 0.1	39	0.063
3,5-dichloropyridine	$C_5H_3Cl_2N$	2.5 ± 0.2	84	0.020
3,5-pyridine-d_2	$C_5H_3D_2N$	TBD	TBD	0.037

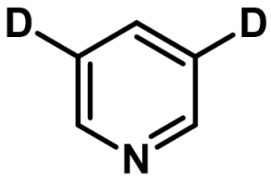

*Figure 2.6 - Structure of **3,5-py-d_2**.*

2.5.1 Synthesis

The synthesis of **3,5-py-*d*$_2$** was adapted from the methodology reported by Huber et al. [93], using 3,5-dibromopyridine (**3,5-dbpy**) as the starting material. The method proceeded as follows[ii].

A 250 mL two-neck round bottom flask was flushed with nitrogen for 20 minutes before being charged with zinc dust (18.2 g, 0.28 mol) and **3,5-dbpy** (13.3 g, 0.056 mol). A solution of sulfuric acid-d_2 (30g, 96 w%, 0.3 mol) in deuterium oxide (100 g, 5 mol) was then added and heating was commenced under mild reflux at 90 °C. The reaction progress was monitored by TLC and upon completion, typically after 24 hours, sodium hydroxide (40g, 1 mol) was added. The product was isolated by steam distillation over 8 hours, periodically replenishing the water as needed.

The resulting distillate was chilled and saturated with sodium hydroxide. After refrigeration, an organic layer had formed on the surface. This layer was separated, dried over calcium hydride, and condensed in a Young's flask under vacuum to yield the desired product, **3,5-py-*d*$_2$**, as a colourless liquid (0.5 g).

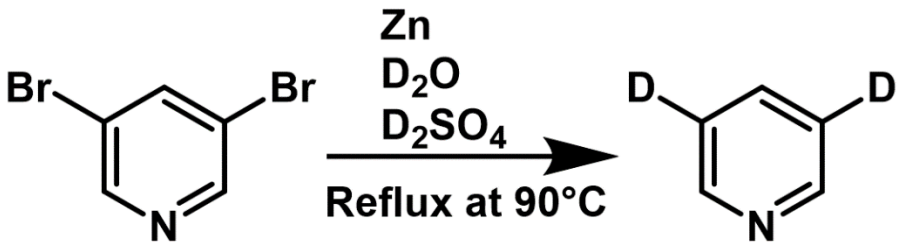

*Figure 2.7 - Diagram of the substitution reaction needed to produce **3,5-py-d$_2$**.*

Analysis of the product was undertaken by ^{1}H NMR spectroscopy. As shown in Figure 2.8, the spectrum exhibits characteristic deuterium-induced splitting, confirming that significant deuterium incorporation has occurred. This is most evident for the *para* position peak (7.72 ppm), which appears as a multiplet rather than the triplet observed for the precursor **3,5-dbpy**. The full spectral range for the aromatic region is shown for **3,5-py-*d*$_2$** in Figure 2.9. It can be seen by comparison with a ^{1}H spectrum of **py** (Figure 2.10) that the position at which the *meta* peak would typically occur (7.45 ppm) is almost entirely vacant for the spectrum of **3,5-py-*d*$_2$**. There is however a small resonance observed at this position at approximately 1% the intensity of the *ortho* position peak. This is likely due to a small proportion of **3-py-*d*$_1$** and **py** being produced, due to the less than 100% isotopic purity of the deuterated reagents.

[ii]Synthesis of 3,5-pyridine-d_2 was performed by Elliot Crocker.

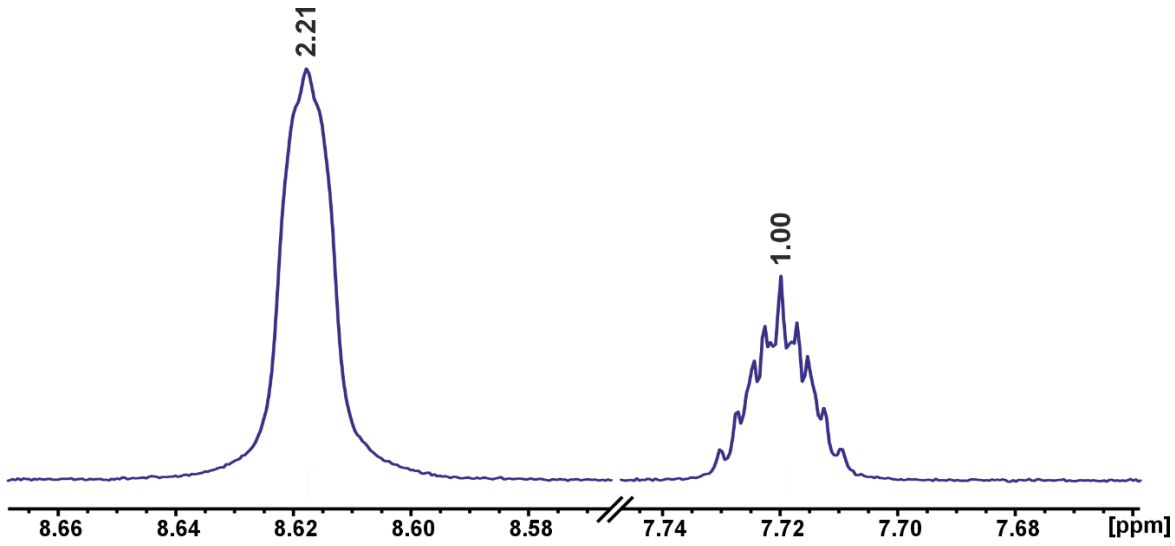

*Figure 2.8 - ^{1}H NMR spectrum of **3,5-py-d_2** over the range 7.66-8.66 ppm (400 MHz, **DCM-d_2**, 298 K).*

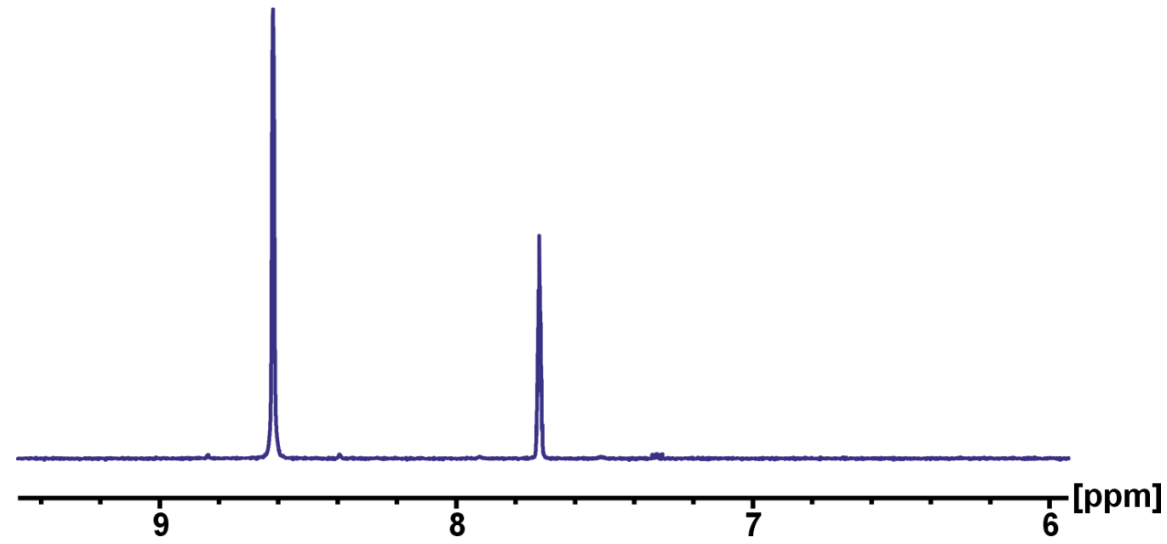

*Figure 2.9 - ^{1}H NMR spectrum of **3,5-py-**d_2 over the full aromatic region (400 MHz, **DCM-d_2**, 298 K).*

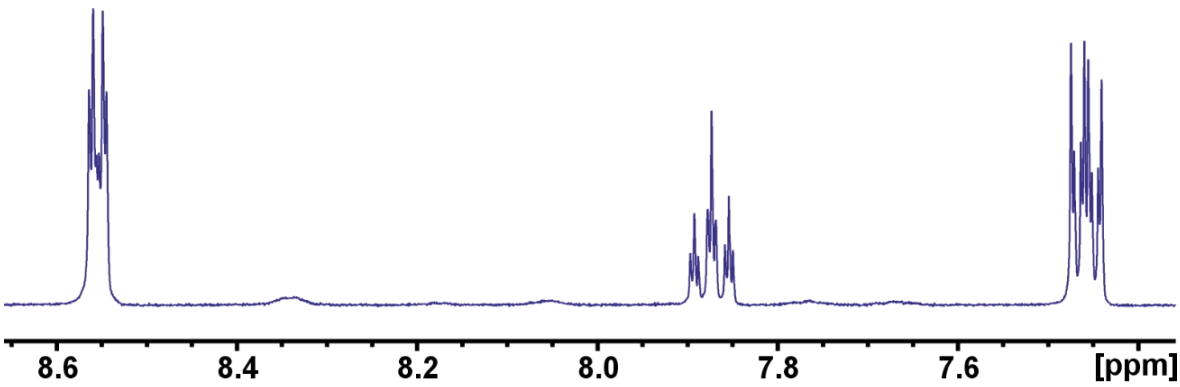

*Figure 2.10 - ^{1}H NMR spectrum of **py*** (400 MHz, **DCM-d_2**, 298 K).

2.5.2 Issues with deuteration of the *ortho* protons

For an initial investigation into the polarization of **3,5-py-d_2,** samples were chosen to contain 5 mM of **IMes** and 25 mM of **3,5-py-d_2** in 0.6 mL of methanol-d_4, conditions which had previously produced high polarization yields with **py**.

During this study, rapid deuteration of the *ortho* proton site in **3,5-py-d_2** was observed. Deuterium substitution from the solvent to the substrate when using methanol-d_4 is a known phenomenon in SABRE, occurring due to catalyst-mediated exchange between the hydroxyl deuterium atom in methanol-d_4 and the *ortho* proton in the substrate molecule.

This effect was mitigated for by changing the solvent to the partially-deuterated methanol-d_3, containing a protonated hydroxyl group. As shown in Figure 2.11, the ratio of the integrals for the *ortho* and *para* protons in **3,5-py-d_2** deviated from the expected 2:1 ratio when methanol-d_4 was used, evidence for the effect. This returned to the expected ratio with the change to the solvent methanol-d_3, as shown in Figure 2.12.

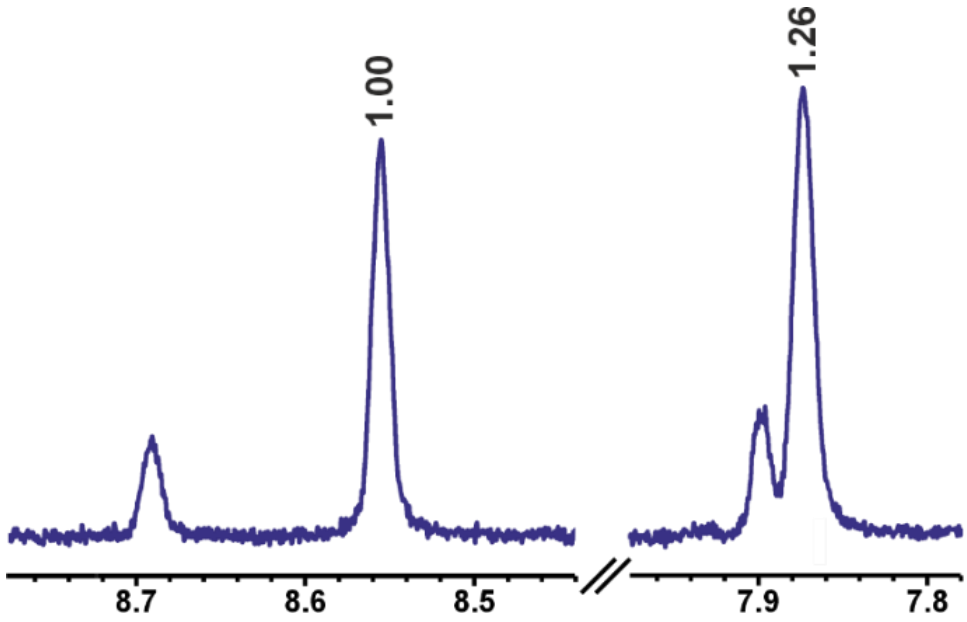

*Figure 2.11 - ^{1}H NMR spectrum for the ortho (left) and para (right) protons in **3,5-py-d_2*** (400 MHz, methanol-d_4, 298 K). *Deuteration of the ortho position is seen, and the expected 2:1 ortho:para ratio is not observed. The uncropped spectrum can be found in Figure 8.1.*

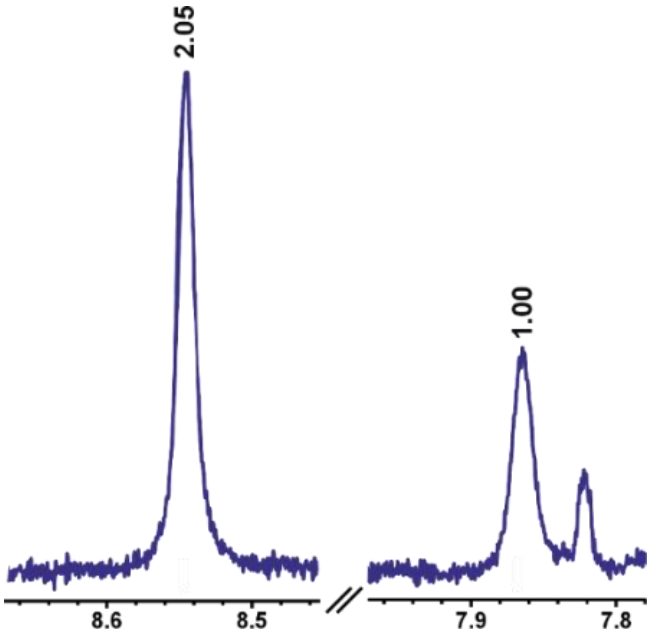

*Figure 2.12 - ^{1}H NMR spectrum for the ortho (left) and para (right) protons in **3,5-py-d_2*** (400 MHz, methanol-d_3, 298 K). *No deuteration is seen and the expected 2:1 ortho:para ratio is observed. The uncropped spectrum can be found in Figure 8.2.*

After resolving the issues with the deuteration of the *ortho* site in **3,5-py-d_2**, the polarization levels were optimized in a similar manner as for **py** in Section 2.3.1. The samples contained 5 mM of the catalysts **IMes** and **IMes-d_{22}**, with and without 4 equivalents of **DMSO-d_6**, alongside a sample containing 5 mM of the precatalyst [Ir(**SIMes**)(COD)Cl] (**SIMes**, Figure 2.13) and 4 equivalents of **DMSO-d_6**. All samples contained 25 mM of the substrate **3,5-py-d_2** and used the solvent methanol-d_3. The samples were prepared and activated as described in Section 7.2.1 and were polarized using the 'Shake and drop' method described in Section 7.2.2.

2.5.3 Results

The results from this study are presented in Figure 2.14 and Table 2.7. It was found that the average signal enhancement using **IMes** was -300-fold, which rose by 30% to -390-fold upon switching to the partially deuterated precatalyst **IMes-d_{22}**. The addition of the co-ligand **DMSO-d_6** was found to increase the enhancements with the **IMes** and **IMes-d_{22}** catalysts to -1050-fold and -1330-fold respectively, equating to gains of 250% and 240%. The precatalyst **SIMes** was evaluated with a **DMSO-d_6** co-ligand, achieving an enhancement of only 250-fold. The **SIMes** catalyst has been shown by Lloyd et al. [94] to result in faster ligand exchange than **IMes** due to the NHC ligand occupying more space around the metal centre, thus this result is indicative of the ligand exchange step becoming faster than optimal for efficient polarization transfer. Out of the 5 tested samples, polarization was found to be highest with the **IMes-d_{22}** catalyst and **DMSO-d_6**.

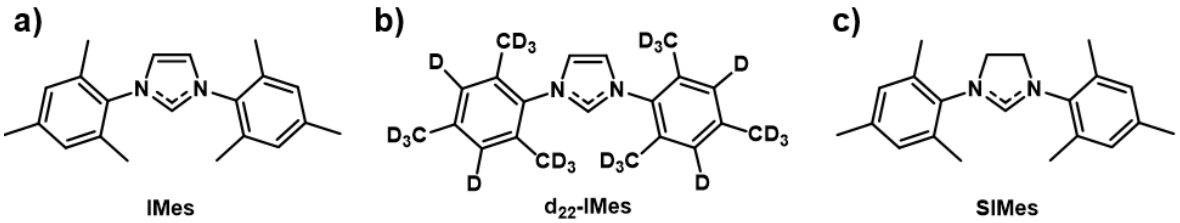

*Figure 2.13 - Structures of a) **IMes**. b) **IMes-d_{22}**. c) **SIMes** NHCs.*

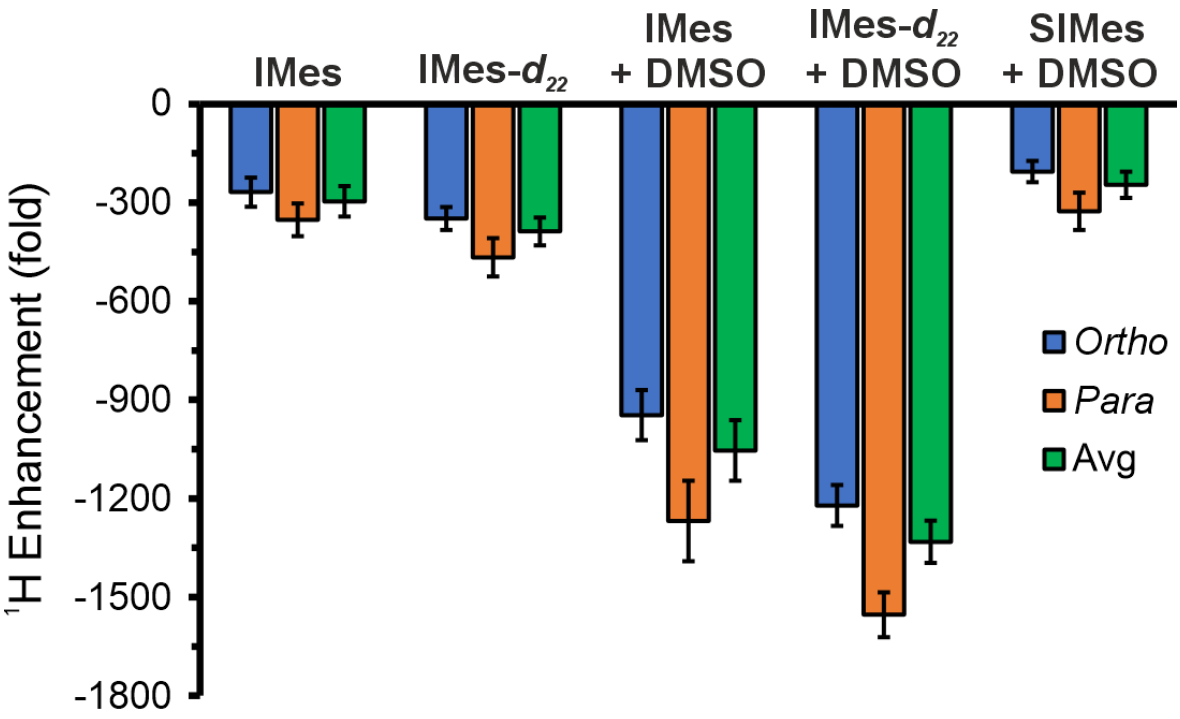

*Figure 2.14 - ^{1}H enhancements for **3,5-py-d_2** in methanol-d_3 with varying catalyst NHCs and co-ligands.*

*Table 2.7 - ^{1}H enhancements and T_1s for **3,5-py-d_2** in methanol-d_3 with varying catalyst NHCs and co-ligands.*

System	^{1}H Enhancements (fold)		
	Ortho	*Para*	Avg.
IMes	-268 ± 40	-353 ± 50	-300 ± 50
IMes-d_{22}	-350 ± 30	-470 ± 60	-390 ± 40
IMes + DMSO	-950 ± 80	-1270 ± 120	-1050 ± 90
IMes-d_{22} + DMSO	-1220 ± 60	-1550 ± 70	-1330 ± 60
SIMes + DMSO	-210 ± 30	-330 ± 60	-250 ± 40

Comparison to pyridine

The enhancements and polarization values for **3,5-py-*d*$_2$**, found in Table 2.7, used a pre-measurement delay of 10 s, contrasting the values for **py** found in Section 2.3.1 which used a pre-measurement delay of 8 s. Enhancements and polarization values for **3,5-py-*d*$_2$** were also found using a 8 s measurement delay and are presented alongside the results from **py** under the same conditions in Table 2.8.

Under the same conditions, using 5 mM of catalyst and 25 mM of substrate for their respective optimized systems, the maximum polarization achieved with **3,5-py-d$_2$** is 5.7%, 39% higher than for **py**. This represents a significant increase; however, it should be taken into consideration that the dilution factor is 70% higher for **py**. Calculating the average nucleon polarization results in a value of 0.21 for **3,5-py-*d*$_2$**, 19% lower than the value of 0.26 for **py**.

These results were achieved at a low (5-fold) substrate excess, and thus the ^{1}H substrate T_1s for both samples was very short, on the order of seconds. It is expected that at higher substrate excesses **3,5-py-d$_2$** will exhibit a longer T_1 than **py**, which can be utilized to achieve higher steady state polarization under continuous polarization. The fact that **3,5-py-*d*$_2$** does not suffer a significant drop in the average nucleon polarization upon deuteration is encouraging, and it is proposed that **3,5-py-*d*$_2$** represents a more attractive candidate for a continuously polarized SABRE target.

*Table 2.8 - Comparison of the signal enhancements and average nucleon polarizations achieved with optimized systems for **py** and **3,5-py-d$_2$** under comparable conditions.*

System	^{1}H Enhancements (fold) [%]				Average nucleon polarization (%)
	Ortho	*Para*	Meta	Avg	
Py, IMes-*d*$_{22}$	-1930 ± 110	-1530 ± 130	-500 ± 70	-1280 ± 100 [4.1 ± 0.3]	0.26 ± 0.02
3,5-py-*d*$_2$, IMes-*d*$_{22}$, DMSO-*d*$_6$	-1630 ± 70	-2050 ± 60	-	-1770 ± 70 [5.7 ± 0.2]	0.21 ± 0.01

Polarization back-propagation

To evaluate the performance of **3,5-py-*d*$_2$**, it was necessary to calculate the maximum polarization achieved prior to any pre-measurement decay during the transfer process. The was achieved by applying back-propagation calculations to the measured polarization values, using experimentally determined polarization decay rates during transfer. The transfer time to the spectrometer was fixed at 10 s, 8 s of which occurred at the residual magnetic field of the room (here referred to as 'Earth's field'), with the remaining 2 s occurring within the 400 MHz spectrometer at a magnetic field strength of 9.4 T.

The T_1 at 'Earth's field' was determined by measuring the polarization after varying wait times at this field. These polarization values showed the expected exponential decay with time, allowing for an exponential fit to be applied to find the T_1. The effective T_1 at 9.4 T was obtained using the hyperpolarized T_1 recovery procedure described in Section 7.3.2. These two relaxation values were used to back-calculate the polarization levels to the point of production, following the procedure outlined in Section 7.4.5.

The measured T_1 values at both fields are shown in Table 2.9. Notably, the high-field T_1 values are significantly lower than those presented from the T_1 inversion recovery of **3,5-py-*d*$_2$** that follows. This is expected due to the low substrate excess and the use of a partially-deuterated solvent.

Although the T_1 values for the *ortho* and *para* positions differ significantly at high field, they converge under 'Earth's field' conditions. This suggests that the spins are no longer distinct and have entered the strongly coupled regime, where the spin-spin coupling ($J_{ortho-para}$) exceeds the difference in their chemical shifts, i.e. $J_{ortho-para} > \delta_{ortho} - \delta_{para}$, with all values expressed in Hz. In this regime the spins are expected to relax as a coupled system, resulting in effectively identical relaxation times.

After applying the back-propagation calculations, the average polarization for **IMes** rose by 430% to 18%, and by 260% for **IMes-d$_{22}$** to 15%. Here it is found that the corrected polarization for **IMes** now exceeds that of **IMes-*d*$_{22}$**[iii], due to the lower T_1 at Earth's field increasing the correction factor. Thus, it may be that the higher polarization values seen using **IMes-*d*$_{22}$** compared to **IMes** can be entirely explained by slower relaxation rates after the polarization process, rather than higher polarization values being achieved initially.

[iii] It should be noted that this result does not achieve statistical significance.

*Table 2.9 - Polarization levels found from and T_1s used in the polarization back-propagation calculations for **3,5-py-d_2**, for the **IMes** and **IMes-d_{22}** catalysts.*

System	Measured polarization (%)		'Earth's field' T_1 (s)		High field T_1 (s)		Corrected polarization (%)		
	Ortho	*Para*	*Ortho*	*Para*	*Ortho*	*Para*	*Ortho*	*Para*	Avg.
IMes + DMSO-d_6	3.1 ± 0.2	4.1 ± 0.4	5.39 ± 0.06	5.42 ± 0.08	7.8 ± 0.3	22.2 ± 1.9	17.4 ± 1.4	19.6 ± 1.9	18.1 ± 1.2
IMes-d_{22} + DMSO-d_6	3.9 ± 0.2	5.0 ± 0.2	7.0 ± 0.4	7.4 ± 1.0	9.7 ± 0.5	28.7 ± 7.4	15.0 ± 1.2	15.8 ± 2.4	15.3 ± 1.1

T_1

The T_1 values for **3,5-py-d_2** were found using a thermal T_1 inversion recovery sequence (Figure 2.15), detailed in Section 7.3.3. These values were found for a 40-fold substrate excess, in accordance with the measured T_1s in the substrate comparison study in Section 2.2. The T_1s for **3,5-dcpy** under these conditions were found to be 61±1 s and 102±4 s for the *ortho* and *para* positions respectively, resulting in an average T_1 of 75±1 s. This represents an increase of 90% over the average T_1 of **py** of 39.0 ± 0.7 s, found in Section 2.2.1. It is also only 11% lower than the average T_1 of **3,5-dcpy**, also found in Section 2.2.1. It can thus be concluded that the selective deuteration process has had the desired effect of extending the polarization lifetime similarly to chloride-substituted pyridines, however with a lower decrease to the dilution factor than would occur with halogenation.

2.5.4 Conclusion

In summary, selective deuteration of **py** was able to significantly extend polarization relaxation times. Specifically, a 90% increase in the T_1 from 39 s to 75 s was found for **3,5-py-d_2** when compared to **py** at a 40-fold substrate excess. It is anticipated that further increasing the substrate excess could yield even longer relaxation times.

Measured polarization levels were also increased with **3,5-py-d_2** relative to **py.** Under comparable conditions, it was found that an average polarization of 5.7% could be achieved with **3,5-py-d_2**, 39% higher than the 4.1% achievable with **py**. While the average polarization value is higher for **3,5-py-d_2**, it should be noted that the average nucleon polarization decreases by 19% relative to **py**.

Upon correcting for polarization decay prior to measurement, it was found that the maximum polarization achieved was 18% using the **IMes** catalyst and a **DMSO-d_6** co-ligand. This represents a

significant advancement towards achieving polarization levels closer to those found in polarized targets utilizing DNP.

The strategy of selective deuteration to improve SABRE performance has previously been demonstrated by Rayner et al. with methyl-4,6-d_2-nicotinate [67,70]. However, this work presents a selectively deuterated substrate with a significantly higher dilution factor than has been reported previously, 0.037 compared to 0.014 for methyl-4,6-d_2-nicotinate.

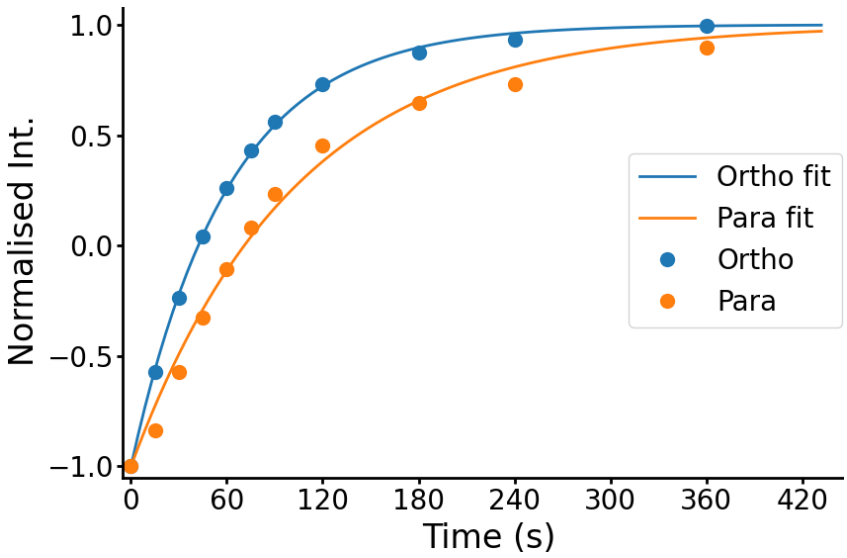

*Figure 2.15 - Thermal T_1 inversion recovery for **3,5-py-d₂**. The sample contained 1.88 mM of **IMes** and 75 mM of **3,5-py-d₂** in 0.6 mL of **DCM-d₂**. Errors were unable to be estimated for this data, as repeats were not performed and the signal noise within the scans did not account for the observed variation (SNR > 4000). Errors are expected to be introduced through the quality of the NMR shimming reducing over the course of the 12+ hour experiment. Errors in the fitted T_1 values are found from the fitting uncertainties.*

2.6 Perfluorocarbons - Novel solvents for increased *p*-H_2 solubility

As discussed in Section 1.4.3, perfluorocarbons (PFCs) are fluorinated liquids characterised by having high gas solubility, as well as being chemically inert and immiscible with water. This section aims to assess whether the high gas solubility of PFCs can be used to increase ^{1}H polarization levels in SABRE, by increasing the dissolved *p*-H_2 concentrations relative to traditional SABRE solvents. Some solvents in this section, such as methyl perfluorobutylether (**8**), will not strictly meet the definition of a PFC, which necessitates the absence of C-H bonds, however they will be referred to here as PFCs for simplicity.

2.6.1 Candidate selection

For a solvent to be optimal for SABRE, several criteria must be satisfied. These include the high solubility of both the SABRE catalyst and substrate, minimal concentrations of high-γ nuclei that contribute to substrate relaxation, and critically, high solubility of *p*-H_2. While PFC solvents contain a high concentration of ^{19}F nuclei - strong contributors to dipolar relaxation - their performance with respect to the other criteria required further investigation.

H_2 mole fraction

This investigation started by evaluating the hydrogen solubility of a range of traditional and perfluorinated solvents by calculating their inverse Henry's constants. Henry's constant, H, represents the mole fraction of H_2 in solution per unit pressure (Eq. 2.3), while the inverse Henry's constant, H_{inv}, is its reciprocal (Eq. 2.4). The values for H_{inv} for the tested solvents were determined using ^{1}H NMR spectroscopy at 298 K, and are shown in Table 2.10[iv].

$$H(MPa^{-1}) = \frac{H_2\ mole\ fraction}{H_2\ pressure(MPa)} \qquad (Eq.\ 2.3)$$

$$H_{inv}(MPa) = \frac{1}{H(MPa^{-1})} \qquad (Eq.\ 2.4)$$

It is important to note that a higher value of H_{inv} corresponds to a lower H_2 solubility, thus a solvent with an H_{inv} value twice that of another will dissolve half as much H_2 per unit pressure.

As shown in Table 2.10, the nine best-performing solvents in terms of H_2 solubility were all perfluorinated. Among the tested PFCs (**8-16**) the mole fraction of dissolved H_2 per unit pressure

[iv] Inverse Henry's constants were found by Dr Callum A. Gater and Orry J. Mayne. This work has been published and can be found in [95]. Selected results from this section are presented within the same publication.

was between 7 and 54 times greater than that of methanol-d_4 (**2**). This represented a substantial improvement and positioned PFCs as highly promising SABRE solvent candidates in terms of their H_2 mole fraction.

*Table 2.10 - Inverse Henry's constants for various solvents measured using ^{1}H NMR spectroscopy at 298 K. **1**-**7** are traditional solvents and **8**-**16** are perfluorinated solvents. Results are from [95].*

Solvent	H_{inv} (MPa)
Deuterium oxide (**1**)	5090 ± 150
Methanol-d_4 (**2**)	450 ± 20
Acetonitrile-d_3 (**3**)	395 ± 9
Ethanol-d_6 (**4**)	346 ± 7
Dichloromethane-d_2 (**5**)	368 ± 9
Tetrahydrofuran-d_8 (**6**)	227 ± 6
Toluene (**7**)	190 ± 7
Methyl perfluorobutylether (**8**)	62 ± 2
Perfluorodecalin (**9**)	54 ± 2
Perfluorononane (**10**)	45 ± 2
Perfluorohexane (**11**)	22.2 ± 1.0
Perfluoro-1-decene (**12**)	20.1 ± 0.8
Methyl perfluorocyclohexane (**13**)	19.4 ± 0.8
Perfluoroheptane (**14**)	19.0 ± 1.0
1-Bromoheptadecafluorooctane (**15**)	13.9 ± 0.5
Perfluorooctane (**16**)	8.3 ± 0.7

Catalyst solubility

Of the investigated solvents, perfluorooctane was found to have the highest H_2 mole fraction per unit pressure. It was however necessary to determine which of these solvents would exhibit strong solubility of the SABRE catalyst. Thus, the solubility of **IMes** was measured in the traditional SABRE solvents methanol-d_4 (**2**) and **DCM-*d*$_2$** (**5**), as well as the fluorinated solvents **8-16**, with the results being shown in Table 2.11.

Catalyst solubility in **8-16** was measured using ^{1}H NMR with an internal reference standard of dioxane, while catalyst solubility in **2** and **5** was measured by visual inspection. For reference, typical catalyst loadings used in the results of this thesis are 5 mM in a 0.6 mL sample, equating to 1.92 mg per sample at a concentration of 3.2 mg mL^{-1}.

Here it can be seen that for fluorinated solvents **9**-**11**, **13**, **14**, **16** the solubility of **IMes** is below 0.1 mg mL^{-1}, less than 3% of that used in a typical experiment. For this reason, these solvents were immediately discounted, leaving the fluorinated solvents methyl perfluorobutylether (**8**), perfluoro-1-decene (**12**), and 1-bromoheptadecafluorooctane (**15**).

*Table 2.11 - Solubility of **IMes** in traditional SABRE solvents (**2**,**5**) and selected perfluorocarbon solvents (**8**-**16**). Results for (**8**-**16**) are from [95].*

Solvent	Catalyst solubility (mg mL^{-1})
Methanol-*d*$_4$ (2)	High (>5)
Dichloromethane-*d*$_2$ (5)	High (>5)
Methyl perfluorobutylether (8)	0.89
Perfluoro-1-decene (12)	0.22
1-Bromoheptadecafluorooctane (15)	0.38
9, 10, 11, 13, 14, 16	<0.1

H_2 solubility per unit volume

Henry's constant, H, relates the molar fraction of H_2 in solution to the vapour pressure of H_2 above the solution. For a SABRE experiment, the more relevant quantity is the number of moles of H_2 in solution per unit volume, which will influence the *p*-H_2 exchange rates. Here, the adjusted Henry's constant (H_{adj}) will be introduced, that is scaled by the molar density of the solvent to have units of moles of H_2 per unit volume per unit pressure (mmol L^{-1} MPa^{-1}) as shown in Eq. 2.5.

$$H_{adj}\ (mmol\ L^{-1}\ MPa^{-1}) = H\ (MPa^{-1}) \times solvent\ molar\ density\ (mmol\ L^{-1}). \quad (Eq.\ 2.5)$$

Table 2.12 shows H_{adj} for the traditional SABRE solvents **2** and **5** alongside the fluorinated solvents which exhibited reasonable catalyst solubility: **8**, **12** and **15**. These values show that for a fixed volume and pressure, it would be expected that **8**, **12** and **15** would exhibit H_2 solubility that is 1.8, 3.4, and 5.1 times that of **2** respectively.

*Table 2.12 - H_{adj} for selected solvents and their H_2 solubility relative to (**2**).*

Solvent	H_{adj} (mmol L^{-1} MPa^{-1})	Performance relative to 2
Methanol-*d*$_4$ (2)	55	1
Dichloromethane-*d*$_2$ (5)	43	0.78
Methyl perfluorobutylether (8)	98	1.8
Perfluoro-1-decene (12)	190	3.4
1-Bromoheptadecafluorooctane (15)	280	5.1

2.6.2 Experiments at low catalyst loadings

To assess whether the increased H_2 solubility exhibited by these fluorinated solvents would translate into higher polarization values, polarization measurements were performed and contrasted to that of the traditional SABRE solvent, **2**.

Here, the fluorinated solvent **8** was chosen, due to demonstrating the highest solubility of **IMes** of the PFCs investigated. It could thus be used in conditions closest to the typical operating conditions for SABRE. For this study, samples were prepared containing 1 mM of **IMes** and 20 mM of **py**, in 0.6 mL of **8** or **2.** The catalyst loading of 1 mM was chosen as it was close to the highest concentration that could be completely dissolved by **8**.

The samples were prepared and activated as described in Section 7.2.1 and were polarized using the 'Shake and drop' method described in Section 7.2.2. As PFCs are known to contribute to dipolar relaxation due to their high concentration of ^{19}F nuclei, it was anticipated that the polarization of the ^{15}N nucleus in **py** may see a greater benefit than for ^{1}H polarization, as ^{15}N is less susceptible to dipolar relaxation. Thus, here ^{15}N polarization measurements were made alongside the ^{1}H measurements, following the approach described in Section 7.2.2 and using a polarization transfer field (PTF) of -3 mG. Further ^{15}N results are presented in Section 2.7.

*Table 2.13 - ^{1}H signal enhancements and ^{15}N polarization values for **py** in **8** and **2** with various co-ligands.*

System		^{1}H enhancement (fold)					^{15}N polarization (%)
		Ortho	*Para*	*Meta*	Avg.	Avg. Mag.	
No co-ligand	***8***	*-170 ± 10*	*-180 ± 10*	*-130 ± 10*	*-160 ± 10*	*160 ± 10*	*13.0 ± 1.1*
	2	810 ± 110	-1410 ± 60	-270 ± 40	-70 ± 70	710 ± 70	8.5 ± 0.6
DMSO-d_6	**8**	-380 ± 30	-390 ± 30	-270 ± 30	-340 ± 30	340 ± 30	2.6 ± 0.2
	2	490 ± 70	-1230 ± 10	-690 ± 200	-330 ± 110	720 ± 110	3.4 ± 0.6
MPSO-d_8	**8**	-90 ± 10	-100 ± 10	-60 ± 10	-80 ± 10	80 ± 10	3.9 ± 0.3
DPSO-d_{10}	**8**	-70 ± 10	-70 ± 10	-50 ± 10	-60 ± 10	60 ± 10	3.9 ± 0.7

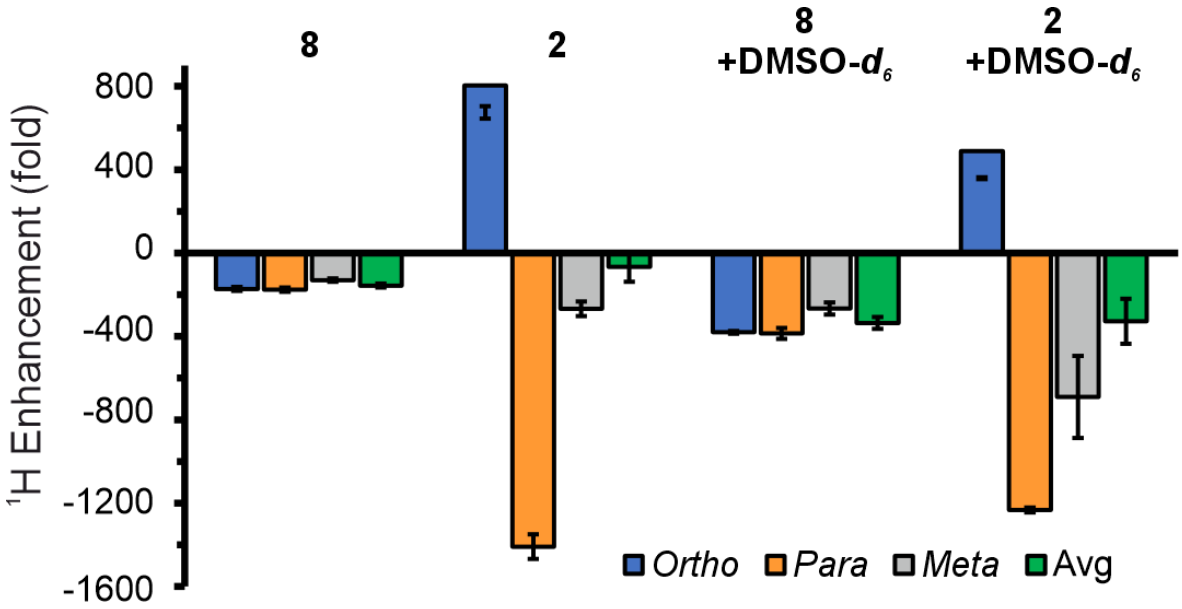

*Figure 2.16 - ^{1}H enhancements for **py** in **2** and **8** with and without **DMSO-d_6**.*

Initial polarization results

As shown in Table 2.13 and Figure 2.16, the average ^{1}H signal enhancement magnitudes for **py** without a co-ligand were found to be 160-fold in **8** compared to 710-fold in **2**, a reduction of 77% despite the increased *p*-H_2 solubility in **8**. In contrast to the poor ^{1}H enhancements seen in **8**, ^{15}N polarization levels were seen to be higher in **8** relative to **2** (Figure 2.18). ^{15}N polarization levels of **py** increased from 8.5% in **2** to 13.0% in **8**, a gain of 53%.

Notably, the signal enhancements for all ^{1}H sites of **py** in **8** are negative, while in **2** the *ortho* position is positively enhanced and the *para*/*meta* positions are negatively enhanced. If the signs of the enhancements are accounted for, the average enhancements for **py** in **8** are larger, with enhancements of -160-fold in **8** compared to -70-fold in **2**.

The active catalyst formed with **py** in **8** was found to be $[Ir(Cl)(H)_2(IMes)(\mathbf{py})_2]$ which differs from the active catalyst found with **py** in **2** which was $[Ir(H)_2(IMes)(\mathbf{py})_3]^{+}Cl$ [95]. This suggests that nonpolar perfluorocarbons favour the formation of the neutral catalyst, rather than the charged catalyst that forms in polar organic solvents such as **2** [57]. Catalytic complexes were characterized using ^{1}H NMR spectroscopy.

Co-ligands

The ^{1}H enhancements for **py** in **8** were significantly improved by the addition of the co-ligand **DMSO-*d*$_6$**, added at 5 equivalents with respect to the catalyst. Under these conditions, the average enhancement magnitudes increased by 110% from 160-fold to 340-fold. In contrast, the addition of **DMSO-*d*$_6$** to **2** showed little improvement in the enhancement magnitudes of **py**. The addition of a co-ligand brought the signal enhancement magnitudes of **py** in **8** closer to the values in **2** (Table 2.13), however they remained 53% lower. ^{15}N polarization levels fell by 80% and 60% in **8** and **2** respectively upon the addition of **DMSO-*d*$_6$**. This fall is reflective of a slowing in ligand exchange rates and confirms that the poor ^{1}H performance in **8** is reflective of too rapid ligand exchange.

Alternative sulfoxide co-ligands, methyl phenyl sulfoxide-d_8 (**MPSO-*d*$_8$**) and diphenyl sulfoxide-d_{10} (**DPSO-*d*$_{10}$**) were also investigated, added at 5 equivalents. Average ^{1}H enhancement magnitudes for **py** in **8** with **MPSO-*d*$_8$** and **DPSO-*d*$_{10}$** were considerably lower than with **DMSO-*d*$_6$**, at 80-fold and 60-fold respectively (Figure 2.17). ^{15}N polarization levels rose slightly when changing from a **DMSO-*d*$_6$** co-ligand to a **MPSO-*d*$_8$** or **DPSO-*d*$_{10}$** co-ligand, however both ^{15}N polarization levels were lower than in the absence of a co-ligand, as shown in Figure 2.18. Figure 2.17 shows the ^{1}H enhancements

for **py** in **8** for all investigated co-ligands, where it can be seen that **DMSO-*d*$_6$** gives the largest enhancements.

^{1}H T_1 values were measured using a hyperpolarized T_1 recovery sequence as described in Section 7.3.2. In **8**, the average T_1 ranged from 16.0 to 19.6 s depending on the co-ligand used, whereas in **2** the T_1s ranged from 22.0 to 24.0 s. On average, the ^{1}H T_1 in **8** was 18 s, 22% shorter than in **2** (23 s). This difference may partially account for the lower enhancement magnitudes observed in **8**, with greater polarization losses during both the build-up and the transfer steps.

^{15}N T_1 values could only be reliably measured for samples without co-ligands, due to the insufficient signal strengths for the samples containing co-ligands which achieved a lower polarization. The ^{15}N T_1 values for **py** were 53 ± 1 s in **8** and 54 s ± 3 s in **2**, the same to within error. The observation of shorter ^{1}H T_1s in **8** than in **2** is consistent with the higher gyromagnetic ratio of ^{19}F, approximately 6 times larger than that of ^{2}H [96], thus contributing more strongly to ^{1}H relaxation. In contrast, ^{15}N T_1 values are less affected by relaxation from the solvent, attributed to the lower gyromagnetic ratio of ^{15}N relative to ^{1}H.

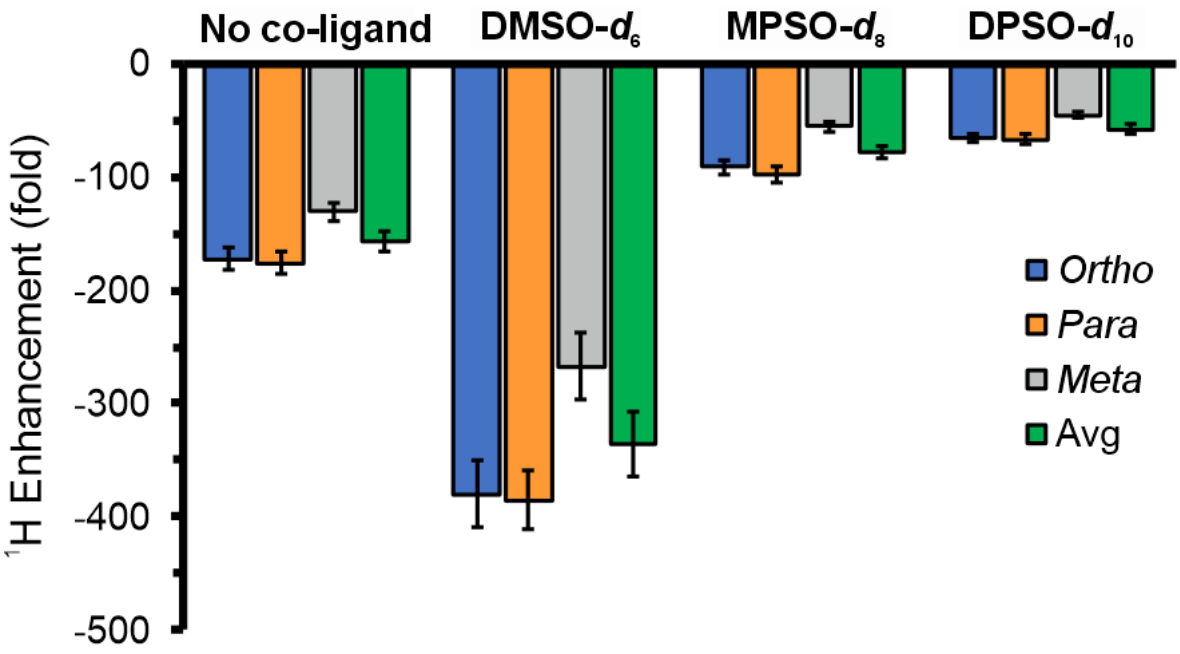

*Figure 2.17 - ^{1}H signal enhancements for **py** in **8** with various co-ligands.*

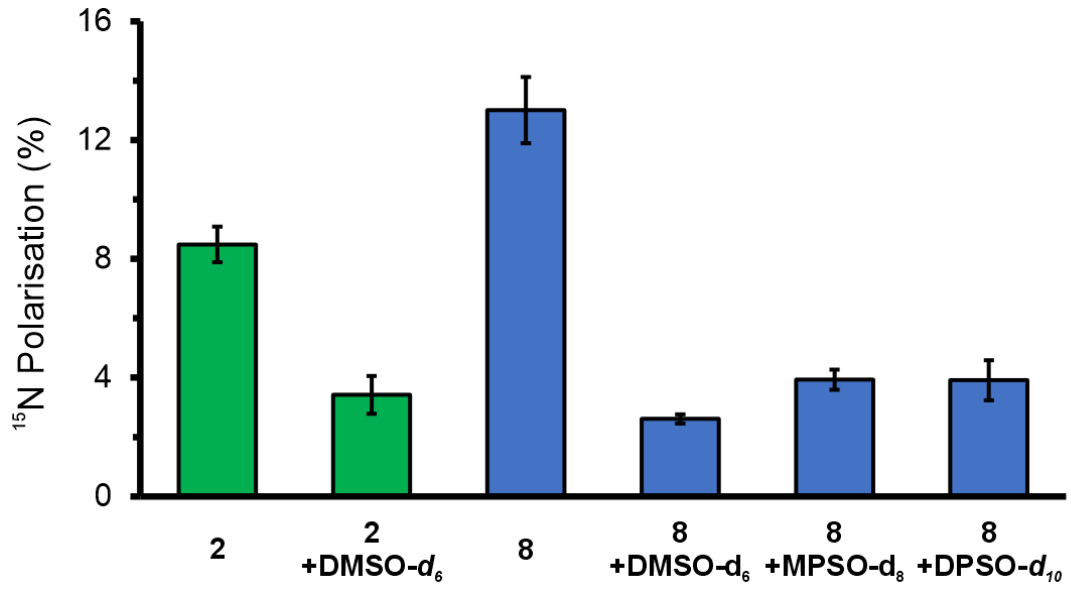

*Figure 2.18 -^{15}N polarization for **py** in **8** and **2** with various co-ligands.*

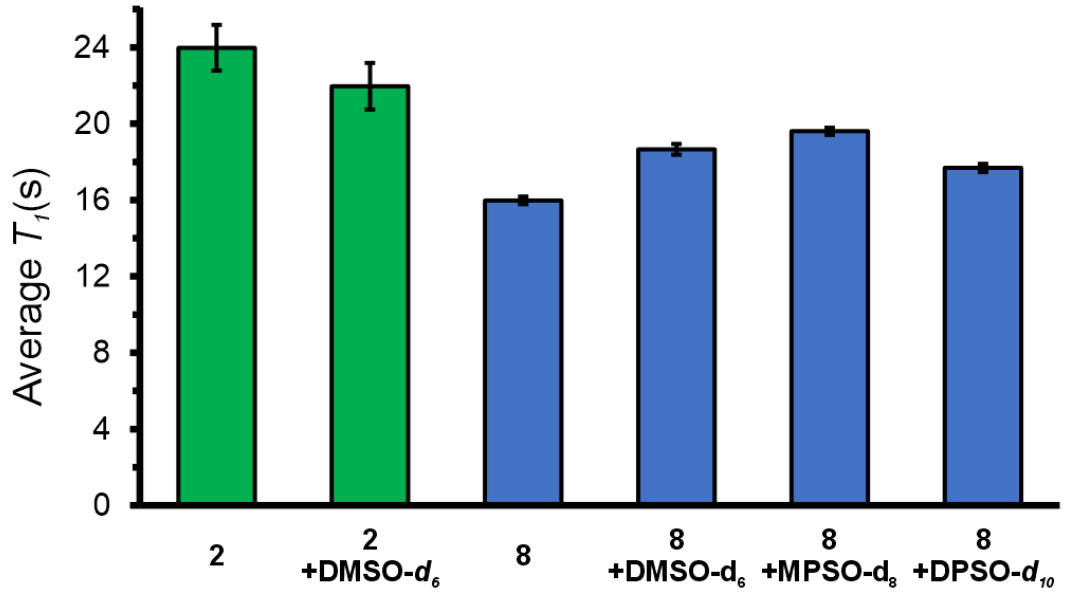

*Figure 2.19 - Average ^{1}H T_1s for **py** in **8** and **2** with various co-ligands.*

Varying catalyst NHC

The catalyst NHC was also varied in these studies in an attempt to optimize the exchange rate of **py** in **8** to improve the ^{1}H polarization relative to **2**. The system of **py** with **DMSO-*d*$_6$** was used, as this performed best for ^{1}H enhancements in **8**. The chosen NHCs swapped the mesityl groups in **IMes** for *para*-substituted xylyl groups, such as the electron-withdrawing chloride group and the electron-donating dimethyl amino group, shown in Figure 2.20.

The ^{1}H enhancements, ^{15}N polarization, and substrate exchange rates are presented in Table 2.14. Substrate exchange rates were found by exchange spectroscopy (EXSY) as described in Section 7.3.4. The exchange rates for the *para*-chloro substituted (**IXyl-*p*-Cl**) and *para*-dimethyl amino substituted (**IXyl-*p*-NMe$_2$**) catalysts were 2.3 s^{-1} and 5.5 s^{-1} respectively, 41% lower and 41% higher respectively compared to the 3.9 s^{-1} rate found using **IMes**. Both ^{1}H enhancements and ^{15}N polarization levels were found to be significantly lower for both catalysts. A possible explanation for this is that these catalysts exhibited poorer solubility in **8** than was found for **IMes**, and thus the 1 mM of these catalysts that was used did not dissolve completely.

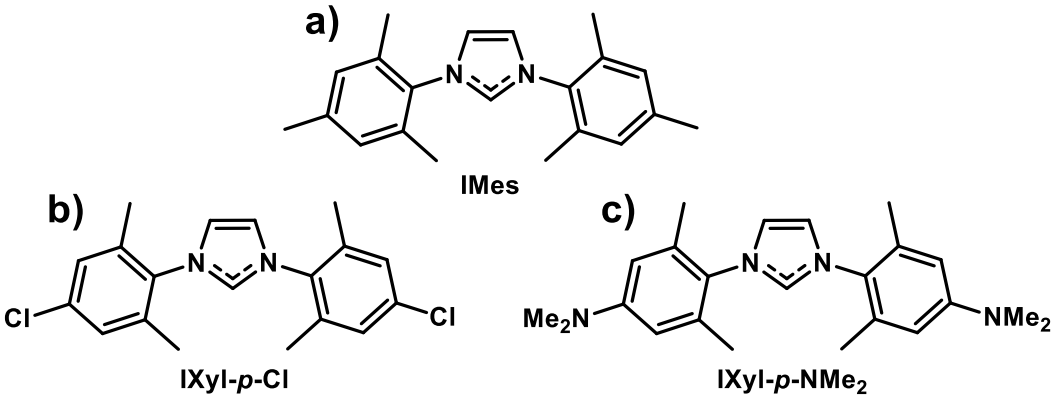

Figure 2.20 - NHC choices for the SABRE precatalyst: a) IMes, b) IXyl-p-Cl, c) IXyl-p-NMe$_2$.

*Table 2.14 - ^{1}H enhancements and ^{15}N polarization levels for **py** in **8** with varying catalyst NHCs.*

NHC	Avg ^{1}H Enhancements (fold)	^{15}N polarization (%)	Exchange rate, k (s^{-1})
IXyl-*p*-Cl	24 ± 1	0.7 ± 0.2	2.3 ± 0.1
IMes	340 ± 30	2.6 ± 0.2	3.9 ± 0.1
IXyl-*p*-NMe$_2$	70 ± 10	0.8 ± 0.1	5.5 ± 0.1

2.6.3 Experiments at high catalyst loadings

In the preceding section, experiments comparing the polarization levels of **py** in **8** and **2** were performed at low catalyst loadings due to the limited solubility of **IMes** in **8**. This prompted further investigation into whether a mixture of solvents may be able to provide the high H_2 solubility of **8** with the superior catalyst solubility of **2**, potentially enabling higher polarization levels than in **2** alone. Given that SABRE experiments are typically conducted with 5 mM catalyst concentrations, this was selected as the target catalyst loading.

The mixture of solvents chosen composed of 80% **8** and 20% **2** by volume. It was found that this mixture was able to fully solubilize 5 mM of **IMes**. Samples were prepared with 5 mM of **IMes** and 25 mM of **py** in 0.6 mL of the solvent mixture, with and without 4 equivalents of **DMSO-*d*$_6$**, and in **2**.

As shown in Table 2.15, average ^{1}H enhancement magnitudes were found to be highest in **2** at 450-fold, compared to 250-fold and 230-fold for the **8**/**2** mixture with and without **DMSO-*d*$_6$** respectively. Notably, here the ^{1}H signal enhancements for **py** in **2** were all of the same sign (Figure 2.21), unlike at low catalyst loadings. In the **8**/**2** mixtures, some ^{1}H sites (*meta* proton without **DMSO-*d*$_6$**, *ortho* proton with **DMSO-*d*$_6$**) exhibited particularly weak enhancements. This indicates inefficient polarization transfer, with the incomplete conversion of *p*-H_2-derived spin order into singlet spin states. ^{15}N polarization values were found to increase in the **8**/**2** mixture, with and without **DMSO-*d*$_6$**, relative to in **2**.

The T_1 values of these samples, presented in Table 2.16, were notably lower than those seen at the lower catalyst loading, attributed here to the lower substrate excess (5-fold compared to 20-fold). Under these conditions, the average ^{1}H T_1s in the **8**/**2** mixture were 36% and 26% lower than in **2** with and without **DMSO-*d*$_6$** respectively. The ^{15}N T_1 could only be measured for the **8**/**2** mixture with **DMSO-*d*$_6$** due to low signal strengths for the other samples. This gave a value of 26 s, around a factor of two reduction on the previously measured values at lower catalyst loadings.

*Table 2.15 - ^{1}H enhancements and ^{15}N polarization levels for **py** in **2** and an 80/20 mixture of **8** and **2**, with and without **DMSO-*d*$_6$**, all at a 5 mM catalyst loading.*

Solvent	^{1}H Enhancements (fold) [%]					^{15}N Polarization (%)
	Ortho	*Para*	*Meta*	Avg.	Avg. Mag.	
[8]/[2] mixture	-370 ± 40	-420 ± 40	0 ± 20	-230 ± 30	230 ± 30	5.7 ± 0.8
[8]/[2] mixture + DMSO	-30 ± 110	-810 ± 100	-200 ± 50	-250 ± 90	250 ± 90	6.8 ± 0.6
2	-600 ± 20	-670 ± 40	-190 ± 20	-450 ± 20	450 ± 20	3.4 ± 0.4

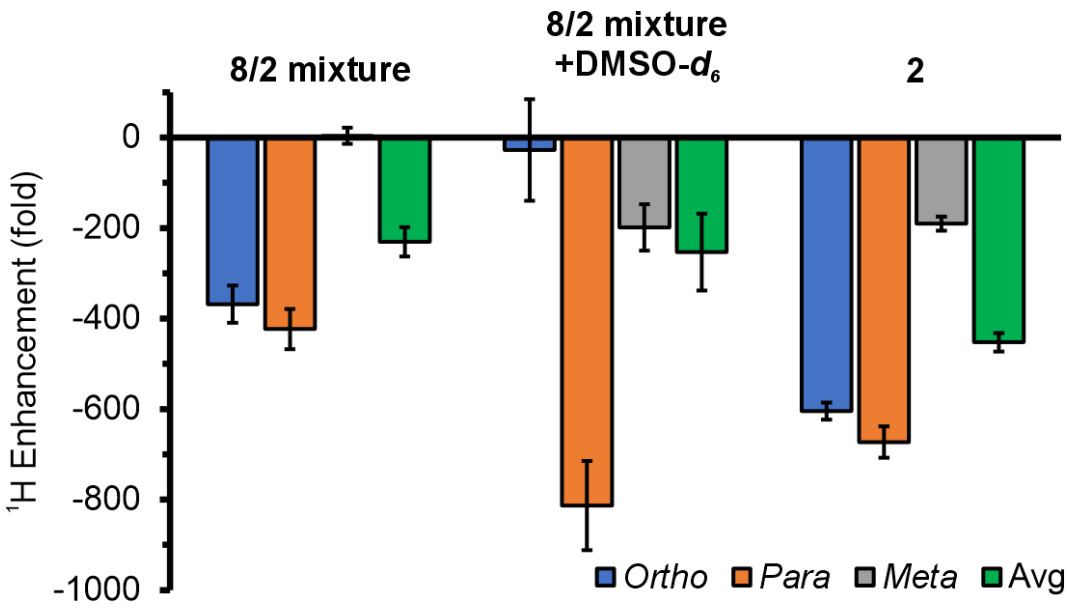

*Figure 2.21 - ^{1}H enhancements for **py** in **2** and an 80/20 mixture of **8** and **2**, with and without **DMSO-d_6**, all at a 5 mM catalyst loading.*

*Table 2.16 - ^{1}H and ^{15}N T_1s for **py** in **2** and an 80/20 mixture of **8** and **2**, with and without **DMSO-d_6**, all at a 5 mM catalyst loading.*

Solvent	Average ^{1}H T_1 (s)	^{15}N T_1 (s)
2	12.0 ± 0.5	-
[8]/[2] mixture	8.9 ± 0.2	-
[8]/[2] mixture + DMSO-d_6	7.7 ± 0.2	26 ± 2

2.6.4 Discussion and conclusion

In conclusion, perfluorocarbon solvents were found to exhibit significantly increased H_2 solubility relative to the traditional SABRE solvents **2** and **5**. Among the PFCs tested, **8** was found to be the most promising, demonstrating the ability to achieve significant ^{1}H and ^{15}N polarization levels with SABRE, attributed to it having the highest catalyst solubility of the tested PFCs. Despite this, the maximum soluble catalyst concentration was found to be only around 1 mM. It was found that an 80/20 mixture by volume of **8** and **2** is able to solubilize five times the mass of catalyst that could be dissolved in **8** alone, reaching the 5 mM concentrations typically used in SABRE experiments.

At low catalyst concentrations, the optimal ^{1}H performance in **8** was achieved with the **IMes** catalyst and **DMSO-d_6**, however the enhancement magnitudes were only half that achieved using **2**. For ^{15}N it was found that polarization levels in **8** were 53% higher than in **2**, and the addition of **DMSO-d_6** decreased ^{15}N polarization levels in **2** and **8**.

At high catalyst concentrations, it was found that the **8**/**2** mixture with and without **DMSO-*d*$_6$** resulted in ^{1}H enhancements that were 49% and 44% lower than those achievable in **2** respectively. ^{15}N polarization levels were 68% and 100% higher in the **8**/**2** mixture than in **2** with and without **DMSO-*d*$_6$** respectively.

These trends can be rationalized as follows. The addition of **DMSO** to **8** has the effect of increasing the ^{1}H polarization values and lowering the ^{15}N polarization values. This can be linked to the slower exchange of **DMSO-*d*$_6$**-containing catalytic species which improves ^{1}H and reduces ^{15}N SABRE efficiency. This effect is slightly compounded by the lengthening of the ^{1}H T_1 upon the addition of **DMSO-*d*$_6$**.

The poorer ^{1}H polarization levels seen in **8** relative to **2** can partly be attributed to the lower ^{1}H T_1s seen in **8**, but this cannot entirely explain the effect. It is thus likely that the substrate dissociation rates in **2** are better suited to efficient ^{1}H polarization transfer.

The increase in ^{15}N polarization seen with **8** relative to **2** at low catalyst concentrations, and with the **8**/**2** mixture relative to **2** at high catalyst concentrations, can be attributed to a combination of higher *p*-H_2 solubility in solution and the fact that ^{15}N polarization is less susceptible to relaxation from the ^{19}F nuclei in the solvent.

It is proposed that further work regarding the optimization of SABRE in perfluorocarbon solvents may allow for increased ^{1}H polarization relative to traditional SABRE solvents, however PFCs have been shown to be more valuable to the polarization of heteronuclei, such as ^{15}N, which are less affected by the high gyromagnetic ratio of ^{19}F. The issues with catalyst solubility faced by perfluorinated solvents may be possible to overcome with the use of perfluorinated catalyst NHCs, such as those demonstrated by Ettedgui et al. [80], discussed in Section 1.4.3.

2.7 Polarization of ^{15}N

2.7.1 Introduction

Alongside polarization of the ^{1}H nucleus, the ability to polarize heteronuclei, specifically ^{15}N, was investigated for the possible application of ^{15}N polarized targets. It has been previously been shown that SABRE is able to polarize ^{13}C, ^{15}N, ^{19}F and other heteronuclei [54,63-66], with ^{15}N typically yielding the highest polarization values [68]. Two substrates were chosen for these investigations, **py**, due to its interest for ^{1}H polarization and the possibility to have a dual $^{1}H/^{15}N$ polarized substrate, and acetonitrile-d_3 (**acn-*d*$_3$**) due to its high dilution factor.

Detecting ^{15}N by NMR presents additional challenges compared to ^{1}H, primarily due to two factors: the low gyromagnetic ratio and the low natural isotopic abundance of ^{15}N. The gyromagnetic ratio of ^{15}N (-27 MRad s^{-1} T^{-1}) is approximately ten times lower than that of ^{1}H (268 MRad s^{-1} T^{-1}), and its natural abundance is only 0.36% compared to 99.99% for ^{1}H. Taken together, these factors make ^{15}N 260,000 times harder to detect by conventional NMR methods [97].

This challenge is typically addressed by using highly concentrated or isotopically-labelled samples, often accompanied by extensive signal averaging, however SABRE offers a powerful alternative. SABRE-enhanced ^{15}N signals can experience signal enhancements in excess of 10,000-fold [68], eliminating the need for such methods, even at natural isotopic abundance.

Since ^{15}N is a spin-1/2 nucleus, resulting from one unpaired proton, it may be considered that only one nucleon is in fact 'polarizable'. As shown in Table 2.17, both investigated substrates for ^{15}N polarization exhibit a lower dilution factor than is typical for ^{1}H polarization, with the dilution factor for **acn-*d*$_3$** being roughly twice as high as for **py**.

*Table 2.17 - Chemical formulas, dilution factors and structures for **py** and **acn-*d*$_3$**.*

Substrate	Formula	Dilution factor, *f* (^{15}N)	Structure
Pyridine	$C_5H_5{}^{15}N$	0.013	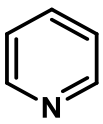
Acetonitrile-*d*$_3$	$CD_3C^{15}N$	0.022	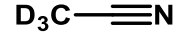

2.7.2 Pyridine

Field sweep

In ^{1}H SABRE the LAC condition (discussed further in Section 1.4.1) needed for optimal polarization transfer occurs consistently at around 6 mT, however for ^{15}N polarization there is generally more variance seen in the optimum polarization transfer field. To determine the optimum ^{15}N PTF for **py**, it was decided to perform a polarization study sweeping over all possible PTFs.

Here the sample used contained 5 mM of **IMes** and 100 mM of non-isotopically labelled **py** in 0.6 mL of **DCM-*d*$_2$**. The PTF field was varied across the range -7 mG to 7 mG (-0.7 µT to 0.7 µT) in 1 mG increments. The samples were prepared and activated as described in Section 7.2.1 and were polarized using the 'Shake and drop' method for ^{15}N described in Section 7.2.2. The results are shown in Figure 2.22.

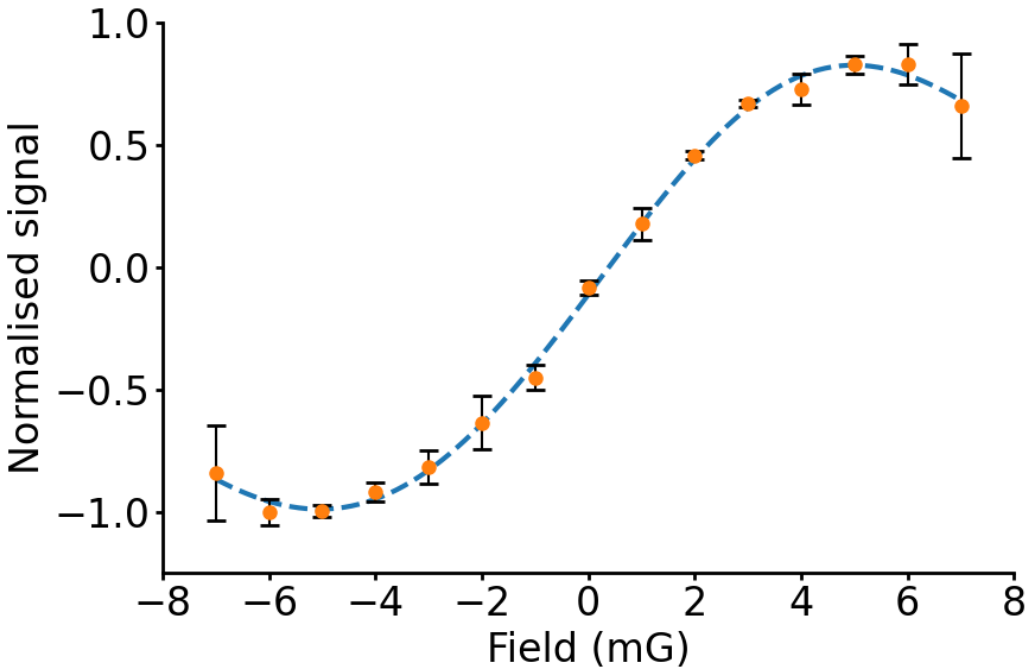

*Figure 2.22 - ^{15}N polarization level of **py** at various polarization transfer fields. The blue dashed line indicates the applied fitting.*

The positive and negative fields resulting in the highest polarization amplitudes were found by fitting the sum of two independent gaussian functions to the data to model the dependency around each LAC condition. It was noticed that this fitting did not pass through the origin, and thus it was determined the milligauss meter was incorrectly calibrated, resulting in corrections of -0.4 mG to the measured field values. Here it was found that the highest polarization amplitudes occurred at -5.1 mG and +4.1 mG, with the maximum polarization using a positive PTF being only 89% of that achievable using a negative PTF.

Effect of substrate excess

^{15}N polarization levels, molar polarization and T_1s were measured for **py** at varying substrate excesses between 5-fold and 120-fold. The samples contained 5 mM of **IMes** with 25-600 mM of ^{15}N-labelled **py** in 0.6 mL of **DCM-*d*$_2$**. The samples were prepared and activated as described in Section 7.2.1 and were polarized using the 'Shake and drop' method for ^{15}N described in Section 7.2.2, at a field of -3 mG.

As shown in Figure 2.23 and Table 2.18, there was a negative dependence of the polarization level on the substrate excess, with polarization levels dropping by a factor of four over the investigated range from 7.8% at a 5-fold excess to 1.9% at a 120-fold excess.

The molar polarization metric is the product of the concentration of ^{15}N nuclei in solution and the average ^{15}N polarization. The molar polarization rose between a 5-fold and an 80-fold substrate excess by a factor of 7.6 from 190 mM % to 1450 mM %, after which it began to fall.

As can be seen in Figure 2.24, the ^{15}N T_1 for **py** increases with increasing substrate excess. A factor of 2 gain from 28 s to 57 s is seen with an increase from a 5-fold excess to an 80-fold excess, however no further increase is seen at a 120-fold substrate excess.

These results can be rationalized similarly to those in Section 2.3.2 for the ^{1}H polarization of **py** at varying substrate excesses. Here the expected negative dependence on substrate excess is shown. This was not observed in Section 2.3.2, which is theorized to be due to higher rates of pre-measurement decay negatively biasing the measured polarization of the low-excess samples. Due to the longer T_1 of ^{15}N relative to ^{1}H this does not occur here. The molar polarization decreasing at higher substrate excesses can be explained as in Section 2.3.2, whereby the increased substrate concentration reduces the rate of *p*-H_2 exchange, thus reducing the rate of polarization transfer.

*Table 2.18 - ^{15}N polarization, molar polarization and T_1s for **py** at varying substrate excess.*

Catalyst concentration (mM)	Substrate concentration (mM) [Excess]	^{15}N Polarization (%)	^{15}N Molar polarization (mM %)	^{15}N T_1 (s)
5	25 [5]	7.8 ± 0.8	190 ± 20	28 ± 1
5	50 [10]	7.5 ± 1.5	380 ± 80	35 ± 1
5	100 [20]	6.8 ± 0.5	680 ± 50	48 ± 1
5	200 [40]	4.7 ± 0.5	930 ± 100	48 ± 1
5	400 [80]	3.6 ± 0.5	1450 ± 200	57 ± 1
5	600 [120]	1.9 ± 0.2	1120 ± 90	55 ± 1

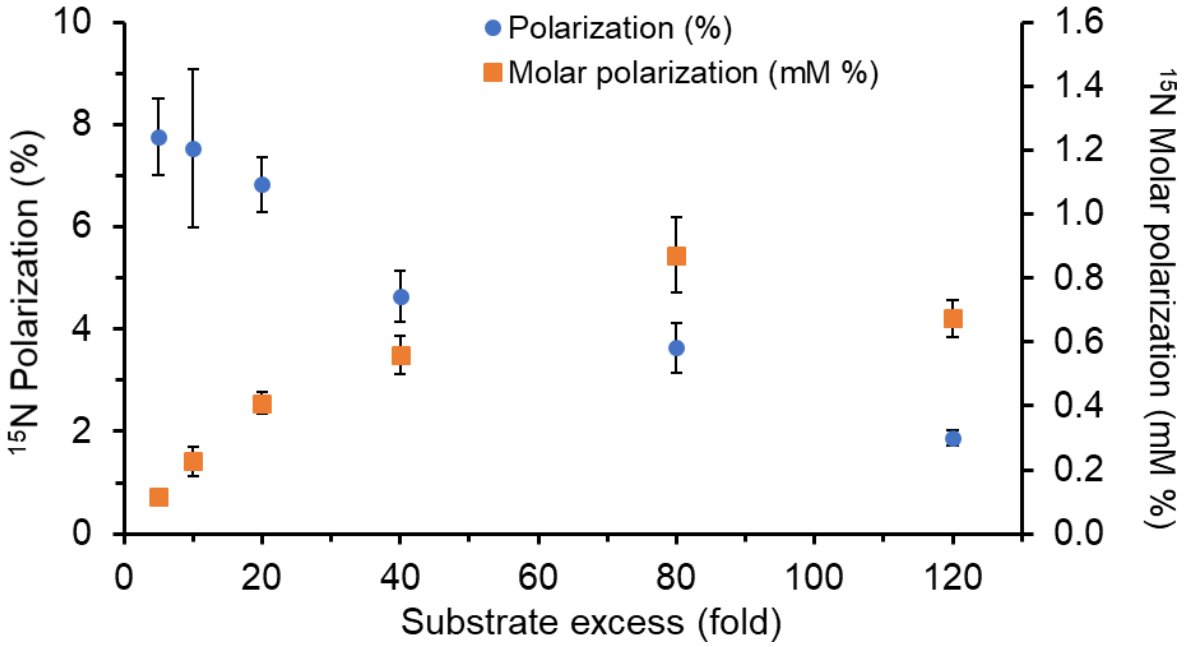

Figure 2.23 - ^{15}N polarization and molar polarization of **py** at varying substrate excesses.

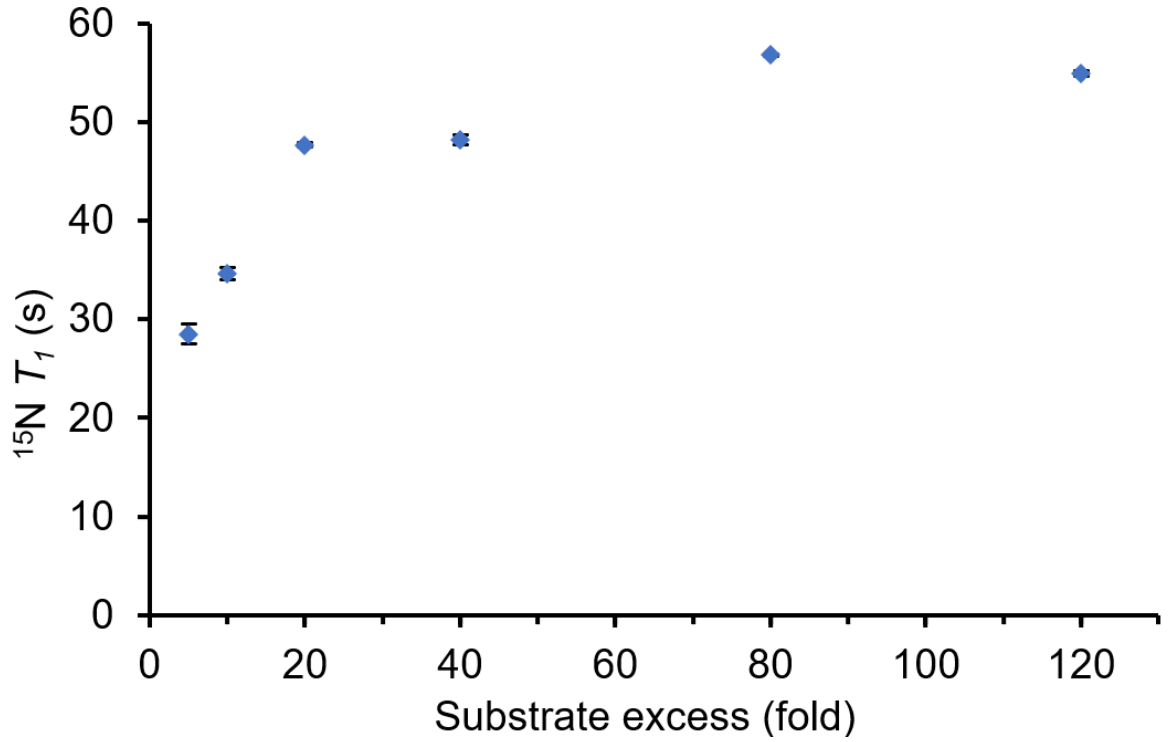

*Figure 2.24 - ^{15}N T_1 for **py** at varying substrate excesses. Error bars are present for all points but may not always be visible.*

2.7.3 Acetonitrile

Acn-d_3 was the target of a polarization optimization study due to its characteristics that make it a promising substrate for use in a ^{15}N polarized target; its high polarization yield and high dilution factor. Polarization of the ^{15}N nuclei in **acn-d_3** of up to 31% has been demonstrated previously [68], and the higher dilution factor of 0.022 compared to 0.013 for **py** results in a FoM 3.2 times higher for the same polarization yield.

This study varied the co-ligand used for the polarization of **acn-d_3**. The samples contained 5 mM of **IMes**, 200 mM of **acn-d_3** and 25 mM of co-ligand in 0.6 mL of **DCM-d_2**. The samples were prepared and activated as described in Section 7.2.1 and were polarized using the 'Shake and drop' method for ^{15}N, described in Section 7.2.2, at a field of -3 mG.

Results and discussion

The ^{15}N polarization of **acn-d_3** was found to be strongly dependent on the co-ligand identity, as shown in Figure 2.25 and Table 2.19, with the polarization ranging from undetectable levels up to 7.9%, equivalent to a signal enhancement of 24,000-fold. Here the detectability threshold is estimated to be a polarization level of around 0.05%.

It was found that the co-ligands **DMSO-d_6** and 3-amino-1,2,4-triazine (**3-atz**) both resulted in **acn-d_3** polarization lower than without a co-ligand, with no detectable polarization occurring using **DMSO-d_6**, and a polarization level of 0.35% found using **3-atz**, compared to 0.59% for the sample without a co-ligand. The samples containing the co-ligands **py** and benzylamine (**bza**) both saw improvements in polarization relative to the sample without a co-ligand, with polarization levels of 2.6% and 7.9% respectively.

Notably, the co-ligand most beneficial for ^{15}N polarization here is different to that for ^{1}H polarization found previously. **DMSO-d_6** has frequently been seen to increase polarization levels for ^{1}H, however here decreases the ^{15}N polarization by over an order of magnitude. The effect a co-ligand has on the polarization levels of the substrate is primarily due its effect on the substrate exchange rate. Due to the larger strength of the J_{HN} couplings for ^{15}N polarization compared to the J_{HH} coupling for ^{1}H polarization, the optimal substrate exchange rate for ^{15}N is found to be much higher than for ^{1}H [95]. Thus **DMSO-d_6**, known to slow down substrate exchange, resulting in decreased ^{15}N polarization levels is expected.

^{15}N T_1 values could only be measured for samples containing the **py** and **bza** co-ligands, due to low signal strengths for other samples. The T_1s measured using either co-ligand were similar, 162 s with the co-ligand **py** and 146 s with the co-ligand **bza**.

Table 2.19 - ^{15}N polarization levels and T_1s for **acn-d₃** with varying co-ligands.

Co-ligand	^{15}N polarization (%)	T_1 (s)
DMSO-*d*₆	No detectable signal	-
3-amino-1,2,4-trizaine	0.35 ± 0.09	-
No co-ligand	0.59 ± 0.04	-
Pyridine	2.6 ± 0.3	162 ± 5
Benzylamine	7.9 ± 0.8	146 ± 2

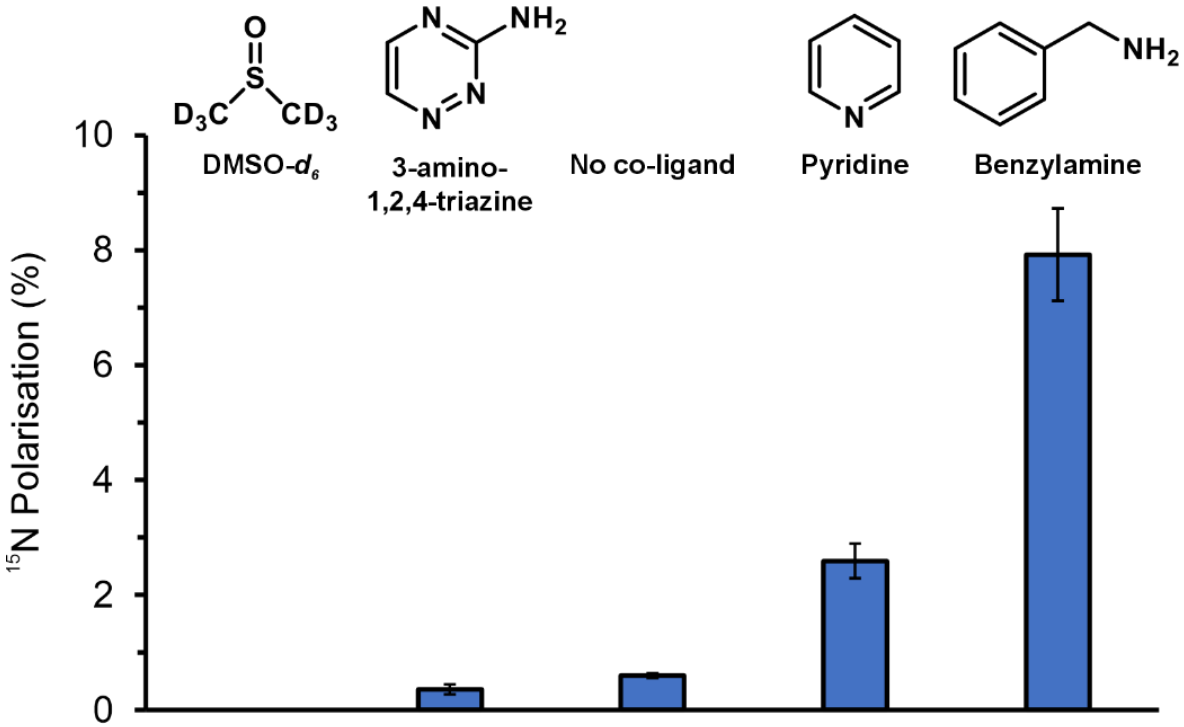

*Figure 2.25 - ^{15}N polarization levels for **acn-d₃** with varying co-ligands.*

2.7.4 Conclusion

In conclusion, it has been found that the optimal PTF for ^{15}N polarization of **py** occurs at -5.1 mG. The maximum ^{15}N polarization of **py** was found to be 7.8%, achieved at a 5-fold substrate excess, and the highest molar polarization was found to be 1450 mM %, occurring at an 80-fold substrate excess. The ^{15}N T_1 for **py** was found to increase up to a maximum and plateau at around an 80-fold excess, with a maximum measured T_1 of 57 s, 46% longer than the average ^{1}H T_1 found for **py** in the substrate comparison study in Section 2.2.1.

^{15}N polarization of **acn-*d*$_3$** was found to massively benefit from the presence of a co-ligand, with the sample containing the co-ligand **bza** achieving a polarization of 7.9%, over ten times that which could be achieved in the absence of a co-ligand. It is notable that polarization levels decreased significantly with the use of the co-ligand **DMSO-*d*$_6$**, known to work well for ^{1}H polarization. It is speculated that this is due to slower exchange rates than are optimal for ^{15}N polarization, as **DMSO-*d*$_6$** is known to slow substrate exchange.

2.8 Chapter 2 Conclusions

In this chapter, it has been found in the substrate comparison study that the highest ^{1}H average nucleon polarization (the product of the polarization and the dilution factor) could be achieved with the substrates **py** and **pz**. Additionally, the longest T_1 of the SABRE-polarizable substrates was achieved with **3,5-dcpy**. **Py** and **3,5-dcpy** were chosen to be studied further for their high polarization yield and polarization lifetimes respectively.

In the study focusing on the polarization optimization of **py**, the highest polarization levels were achieved using **py** and the **IMes-*d*$_{22}$** catalyst. Here the deuteration of the catalyst NHC reduced the rate of relaxation of the spin order during polarization transfer. In the substrate excess study for **py** it was found that the highest signal enhancements occurred at a 20-fold substrate excess, while the highest molar polarization was found to be similar for the 20-fold and 40-fold excess samples. The molar polarization decreased above a 40-fold substrate excess, here attributed to slower rates of *p*-H_2 exchange with increasing substrate concentrations.

When investigating SABRE in neat liquids, without an additional solvent, it was found that polarization levels of **py** in a 1% v/v solution with **py-*d*$_5$** were around 40-fold lower than in a 1% v/v solution with methanol-*d*$_4$. The polarization levels in 'neat' **py** could be increased by raising the catalyst concentration, however the dependence was approximately logarithmic, and it was not possible to reach the levels achieved in methanol-*d*$_4$ within the solubility limits of the catalyst. It is proposed that SABRE in neat liquids is limited by the low catalyst and dissolved *p*-H_2 concentrations relative to the substrate, and is not a feasible solution to producing highly concentrated solutions of polarized material.

In this chapter the successful synthesis of a novel selectively-deuterated substrate **3,5-py-*d*$_2$** is demonstrated. When comparing the polarization achievable on this substrate to **py**, it was found that a measured average polarization of 5.7% could be achieved using the **IMes-*d*$_{22}$** catalyst and the co-ligand **DMSO-*d*$_6$**. This represented a 39% increase over the 4.1% achievable with **py** under optimized conditions, despite the average nucleon polarization suffering a slight decrease. After correcting for pre-measurement decay, the maximum average ^{1}H polarization achieved with **3,5-py-*d*$_2$** was 18%, a significant achievement. Here the **IMes** catalyst and the co-ligand **DMSO-*d*$_6$**. were used.

An increase in the T_1 of 90% for **3,5-py-*d*$_2$** compared to **py** was observed at a 40-fold substrate excess, from 39 s to 75 s. This demonstrates the successful achievement of synthesizing a selectively-deuterated substrate that combines the high polarization values seen in **py** with the long

relaxation times seen in **3,5-dcpy**. This substrate also represents a significant increase in the dilution factor compared to previous instances of selectively-deuterated substrates [67,70].

In an investigation into novel, high gas-solubility solvents, it was found that perfluorocarbons had significantly higher levels of H_2 solubility than the traditional SABRE solvents methanol-d_4 and **DCM-d_2**. PFCs did however exhibit limited catalyst solubility, with only three of the nine tested PFCs having a catalyst solubility of over 0.1 mg L^{-1} - just 3% of that needed for a typical SABRE experiment. As catalyst solubility was deemed to be the limiting factor for polarization, methyl perfluorobutylether (**8**), which had the highest, was chosen to be investigated further.

At low catalyst concentrations, the ^{1}H polarization level of **py** in **8** was found to benefit from the co-ligand **DMSO-d_6**, however the average signal enhancement magnitudes were only half of that achievable in methanol-d_4. In the absence of a co-ligand the substrate exchange rates were too rapid for efficient ^{1}H polarization transfer and too slow for ^{15}N polarization transfer, confirmed by the addition of **DMSO-d_6** which improved and worsened the ^{1}H and ^{15}N polarization levels respectively. It is proposed that with further studies to better optimize the exchange rates of **py** in **8**, continued gains in the achievable polarization level relative to traditional SABRE solvents will be made. Additionally, the issues with catalyst solubility faced by perfluorinated solvents may be possible to overcome with the use of perfluorinated catalyst NHCs.

Higher soluble catalyst concentrations could be achieved using a mixture of **8** and methanol-d_4, which was able to solubilize 5 mM of **IMes**, the level used in a typical SABRE experiment. It was found here however that the ^{1}H polarization levels using this solvent mixture were again only around half that achievable using methanol-d_4.

PFCs did however outperform traditional SABRE solvents for ^{15}N polarization. At low catalyst concentrations, the ^{15}N polarization of **py** in **8** was 53% higher than in methanol-d_4, at 13.0% compared to 8.5%. The mixture of **8** and methanol-d_4 used for high catalyst concentrations performed even better relative to methanol-d_4, achieving double the ^{15}N polarization - 6.8% compared to 3.4%. Strong ^{15}N polarization using **8** was attributed to the lack of sensitivity of the ^{15}N nucleus to dipolar relaxation from the ^{19}F nuclei in the solvent

In a study on the polarization of the ^{15}N nucleus, it was found that the maximum polarization of **py** was achieved at a 5-fold substrate excess, with the highest molar polarization occurring at an 80-fold excess. For the ^{15}N polarization of **acn-d_3**, the polarization in the absence of a co-ligand was very poor, however polarization levels of 7.9% could be achieved with the use of the co-ligand **bza,** an order of magnitude higher than in the absence of a co-ligand. This result is attributed primarily

to changes in the ligand exchange rates, which are an ongoing area of investigation within the group.

The results of this chapter regarding the high polarization levels of **3,5-py-d_2** will be used in Chapter 5 in order to achieve polarization levels in excess of 20% using a continuously polarized prototype SABRE target. The substrate **3,5-dcpy**, notable for its long polarization relaxation times found in the substrate comparison study, will be investigated further in Chapter 3.

Chapter 3 - Studies in Relaxation

3.1 Introduction

This chapter investigates the factors that influence relaxation, the process by which non-equilibrium magnetization returns to equilibrium. It will focus on longitudinal relaxation, which governs the time taken for the Z-component of magnetization to return to equilibrium, and is characterized by the time constant T_1. T_1 influences the repetition times used in thermally polarized NMR experiments and, importantly, characterizes the lifetime of hyperpolarized states.

A long polarization T_1 is desirable for the application of SABRE to polarized targets for a few reasons. A lower rate of relaxation means that a lower rate of polarization is necessary to continuously maintain a fixed polarization level. This is important as polarization rates in SABRE are often constrained by limiting factors such as the available concentration of *p*-H_2 in solution and the catalytic activity. Another benefit to a long T_1 is that it allows for more time for processing a solution of hyperpolarized material after polarizing subsides, for example to reduce the quantities of catalyst and solvent and thus increase the dilution factor of the material - a key feature in the Figure of Merit for polarized target experiments.

The factors influencing T_1 that are investigated in this chapter are: sample temperature, external magnetic field strength, substrate concentration, and catalyst concentration. These factors have previously been studied to a limited extent, however they are critical for the application of SABRE to polarized targets. Additionally, there will be a discussion of the RASER effect observed during these studies, a phenomenon which involves the stimulated emission of RF-photons in hyperpolarized samples.

The main substrate of interest in this chapter will be 3,5-dichloropyridine (**3,5-dcpy,** Figure 3.1), chosen for its exceptionally low rate of intrinsic ^{1}H T_1 relaxation, due to the magnetic isolation of the ^{1}H nuclei. This allows for a more precise investigation into factors affecting the T_1 than would otherwise be possible. Additionally, the achievable polarization and the dilution factor are higher for **3,5-dcpy** than for other substrates with a similarly long T_1.

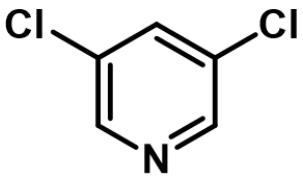

*Figure 3.1 - The structure of **3,5-dcpy**.*

3.2 T_1 dependence on temperature

The temperatures needed to operate a DNP polarized target are one of the key engineering challenges associated with DNP. For high intensity beams, the continuously polarized targets used operate at around 1 K using a ^{3}He or ^{4}He evaporation refrigerator [21]. For experiments restricted by low luminosities, the frozen-spin targets used operate at even lower temperatures of just tens of mK using a ^{3}He/^{4}He dilution refrigerator [2]. The low temperatures needed for DNP targets bring significant drawbacks, such as a restriction in the allowable heat deposition within the target, limiting the allowable beam current. In addition to this there is the associated costs with the cryogens and energy usage, alongside the necessity for expert technical support [98,99].

One of the key advantages of SABRE is that it has been demonstrated to operate well at room temperature. The efficiency of polarization transfer in SABRE is highly sensitive to the chemical kinetics of the system used, however if care is taken in the choice of co-ligand for the SABRE catalyst it is frequently possible for the optimum substrate exchange rate to occur at close to room temperature [100,101]. Knowing this, it is also important to understand the temperature dependence of the relaxation rate of the polarization.

To investigate the dependence of T_1 on temperature, it was decided to use thermal T_1 inversion recovery experiments, eliminating the need for the SABRE catalyst and consequently any effects of catalyst-induced relaxation. The chosen sample composition was 200 mM of the substrate **3,5-dcpy** in 0.6 mL of methanol-d_4, chosen due to its higher boiling point compared to **DCM-d_2**. The temperature range investigated was 243 K to 323 K (-30.2 °C to 49.9 °C), chosen due to practical limitations. The sample temperature was altered using the variable temperature functionality of the NMR spectrometer, and the samples were prepared and activated as described in Section 7.2.1.

3.2.1 Results

The results of this 9.4 T study, seen in Figure 3.2 and Table 3.1, show a significant dependence of T_1 on the sample temperature, also showing that a maximal T_1 lies within the investigated temperature range for both ^{1}H positions. The average T_1 for **3,5-dcpy** ranges from 47.5 ± 0.3 s at 243 K, increasing to 113 ± 1 s at 303 K, before falling to 62 ± 2 s at 323 K, with a percentage increase of 140% from the minimal to the maximal value. The minimal and maximal T_1s for the *ortho* and *para* positions are found at the same temperatures, 243 K and 303 K respectively, with a larger percentage change observed for the *para* position. Also shown in Figure 3.2 is the absolute value of the rate of change of the average T_1 between data points, $\left|\Delta T_{1,avg}/\Delta \mathrm{T}\right|$. $\left|\Delta T_{1,avg}/\Delta \mathrm{T}\right|$ is found to be highest between 305.5 K and 308 K (32.4-34.9 °C), reaching a maximum of 6.2 ± 0.9 s K^{-1}, equating to a maximum percentage rate of change of around 7% K^{-1}for the average T_1. $\left|\Delta T_{1,avg}/\Delta \mathrm{T}\right|$

is generally lowest far from the optimal temperature for the T_1, falling to 1.03 ± 0.03 s K^{-1} and 0.9 ± 0.3 s K^{-1} at low and high temperature extremes respectively.

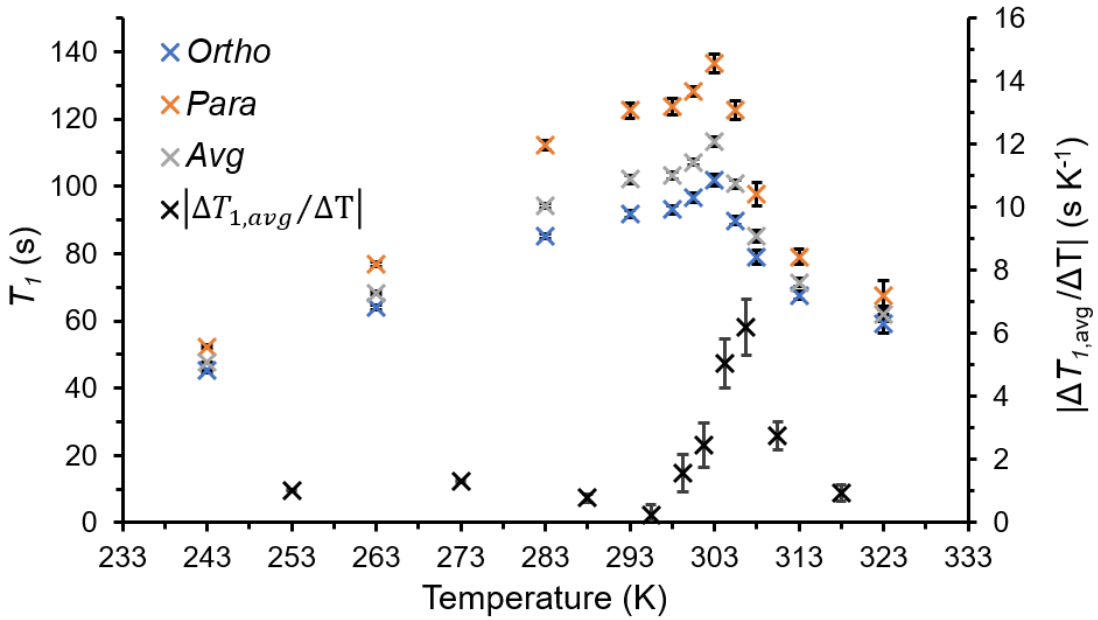

*Figure 3.2 - ^1H T_1s and the absolute value of the rate of change of the average T_1 ($|\Delta T_{1,avg}/\Delta T|$) for **3,5-dcpy** at varying sample temperatures over the range 243-323 K. All measurements were acquired at 9.4 T (400 MHz).*

*Table 3.1 - ^1H T_1s and the absolute value of the rate of change of the average T_1 ($|\Delta T_{1,avg}/\Delta T|$) for **3,5-dcpy** at varying sample temperatures over the range 243-323 K. All measurements were acquired at 9.4 T (400 MHz).*

Temperature (K) [°C]	**^1H T_1 (s)**			$\left\|\frac{\Delta T_{1,avg}}{\Delta T}\right\|$ **(s K^{-1})**
	Ortho	*Para*	Avg	
243 [-30.2]	45.1 ± 0.4	52.4 ± 0.4	47.5 ± 0.3	1.03 ± 0.03
263 [-10.2]	63.9 ± 0.7	76.8 ± 0.8	68.2 ± 0.5	1.30 ± 0.04
283 [9.9]	85.2 ± 0.6	112 ± 1	94.2 ± 0.6	0.8 ± 0.1
293 [19.9]	92 ± 1	122 ± 2	102 ± 1	0.3 ±0.3
298 [24.9]	93 ± 1	124 ± 4	103.3 ± 1	1.6 ± 0.6
300.5 [27.4]	97 ± 1	128 ± 1	107 ± 1	2.5 ± 0.7
303 [30.9]	102 ± 2	137 ± 3	113 ± 1	5.0 ± 0.8
305.5 [32.4]	90 ± 1	123 ± 3	101 ± 1	6.2 ± 0.9
308 [34.9]	79 ± 2	98 ± 3	85 ± 2	2.8 ± 0.4
313 [39.9]	68 ± 1	79 ± 2	71 ± 1	0.9 ± 0.3
323 [49.9]	59 ± 3	68 ± 4	62 ± 2	

3.2.2 Discussion

As described in Section 1.2.2, one of the causes of intermolecular relaxation is the interaction between the thermal motion of molecules and the precession of their magnetic moment. The rate of rotation of molecules in solution is given by their correlation time, τ_c, where:

$$\tau_c \propto \frac{\eta}{T}. \qquad (Eq. 3.1)$$

Here T is the temperature and η is the viscosity of the solution, which also exhibits temperature dependence. The distribution of the rates of rotation of molecules in solution is given by the correlation function, $G(\tau_c)$. The Fourier pair of the correlation function, the spectral density function, $J(\omega)$, gives the distribution of the rotational frequencies of these molecules. The magnitude of $J(\omega)$ at the Larmor frequency for the relaxed nucleus (ω_0) determines the strength of relaxation experienced [37]. The temperature dependence of the intermolecular relaxation experienced is brought in through the temperature dependence of τ_c and thus $J(\omega_0)$ [102].

Considering this, it might be expected that T_1 would be lowest at the temperature which maximized $J(\omega_0)$ and would rise either side of this temperature. V-shaped distributions such as this for the temperature dependence of the T_1 are predicted by Bakhmutov and Hore [102,103], citing the dependence of the T_1 on τ_c.

Here, however, the opposite trend is seen, where a local maxima in the T_1 is observed which decreases at either side. It should be noted that τ_c is not the only contributing factor to T_1. Another such temperature-dependent contribution is the increasing rate of molecular collisions at higher temperatures. This enhanced collision rate, or other mechanisms, could account for the deviation from the dependence predicted by Bakhmutov and Hore.

The maximum T_1 occurring at 30.9 °C in this study is encouraging for polarized target applications of SABRE, as this temperature is easily achievable and indicates that the optimum temperature for polarization transfer efficiency and for relaxation may be similar. This optimum temperature for relaxation strongly contrasts to DNP systems which strive for sub-Kelvin temperatures to minimize relaxation [2]. In addition, the maximum temperature sensitivity of the T_1 is only 7% K^{-1}, orders of magnitude lower than for DNP below 1 K, thus suggesting that heat deposition won't be an issue for a SABRE-polarized target.

3.3 T_1 dependence on holding field

Alongside the temperatures needed for DNP, the other significant engineering constraint comes from the strong magnetic fields needed. Both continuously polarized and frozen-spin targets require superconducting magnets which, similarly to the refrigeration systems, need liquid helium to operate. The superconducting magnets necessary for continuously polarized targets are a particular issue, due to the large amount of material within the detector restricting its angular acceptance.

The field dependence of the polarization transfer efficiency in SABRE is well studied - the dependence of the T_1 on the external field however is less well understood. It is known that for ^{1}H nuclei the optimum polarization transfer field lies at around 6 mT [52], however for a SABRE-polarized target there is a need for the preservation of polarization after polarization transfer has concluded, especially if the target is of a non-continuous design, such as a frozen pellet target (discussed in Section 5.6).

For polarized target applications of SABRE there is a need to perform processing of the polarized material to isolate the polarized substrate and thus increase the dilution factor. During the processing of the material it is important to minimize the decay of polarization, therefore this process should take place in a field where the T_1 is at its maximum, if feasible. It is thus desirable to understand the dependence of the T_1 on the holding field of the target material.

In this study, the T_1 of **3,5-dcpy** was measured using the hyperpolarized T_1 recovery sequence described in Section 7.3.2. The external field, ranging from 1.0-11.7 T, was supplied by the various spectrometers used, the Magritek Spinsolve Carbon benchtop NMR and three Bruker high-field NMRs, details of which are given in Section 7.1.

Four identical samples were made up containing of 2.5 mM of **IMes** precatalyst and 50 mM of **3,5-dcpy** in 0.6 mL of **DCM-*d*$_2$.** The samples were prepared and activated as described in Section 7.2.1 and were polarized using the 'Shake and drop' approach described in Section 7.2.2.

3.3.1 Results[v]

As can be seen in Figure 3.3 and Table 3.2, both the *ortho* and *para* positions in **3,5-dcpy** show very little variance in T_1 with the change in holding field. The average T_1 varies from a minimum of 76.7 s at 7.0 T to a maximum of 82 s at 1.0 T, a percentage increase of only 7%. In fact, it happens that three out of the four values of the average T_1 (1.0 T, 7.0 T, 11.7 T) are the same to within one standard deviation of each other.

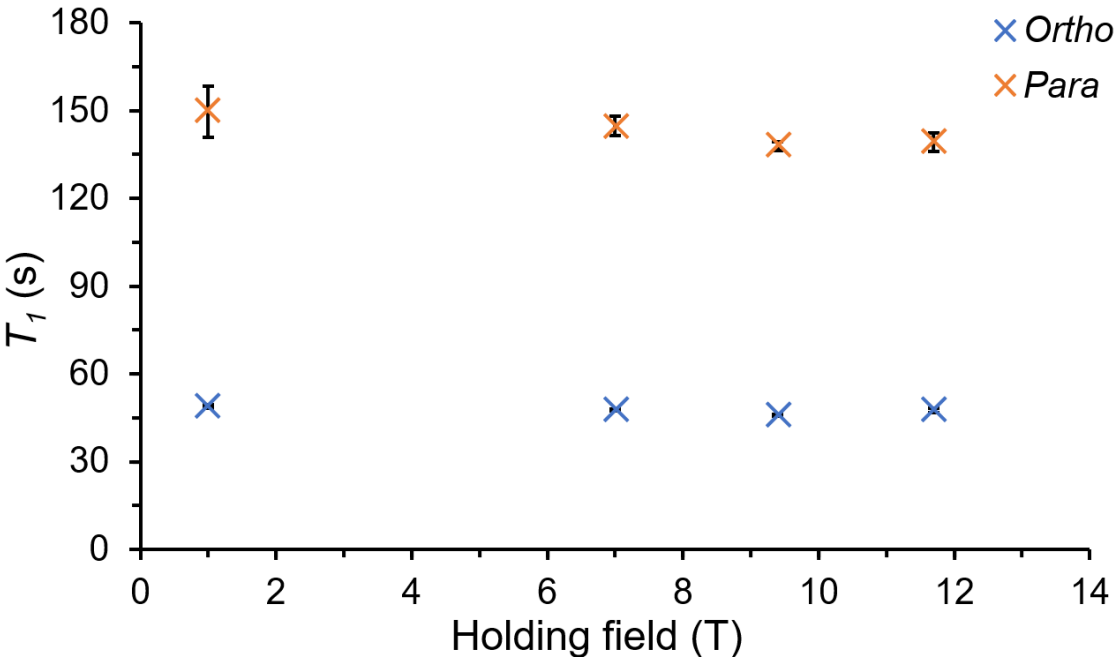

Figure 3.3 - ^{1}H T_1s for **3,5-dcpy** at varying field strengths. Error bars are present for all points but may not always be visible.

*Table 3.2 - ^{1}H T_1s for **3,5-dcpy** at varying holding field strengths.*

Field (T)	**^{1}H T_1 (s)**		
	Ortho	Para	Avg
1.0	48.8 ± 0.6	150 ± 9	82 ± 3
7.0	47.6 ± 0.3	145 ± 3	80 ± 1
9.4	46.0 ± 0.3	138 ± 2	76.7 ± 0.5
11.7	47.5 ± 0.7	139 ± 3	78 ± 1

[v] Selected results from this study have been published and can be found in [56].

3.3.2 Discussion

According to Bakhmutov [102], in the extreme narrowing limit, characterized by $\omega_0\tau_c \ll 1$, the T_1 loses its dependence on the external field strength while retaining its dependence on temperature. The conditions to meet for the extreme narrowing limit are:

- Small molecule sizes.
- High temperatures.
- Low viscosity solvents.

It is thus suggested that the samples in this study (and the previous study) fall into this regime due to satisfying each of these criteria. This would suggest that the lack of dependence of the T_1 on the holding field strength is to be expected. The lack of field dependence of the T_1 is also evidence that chemical shift anisotropy (CSA) is not a large contributor to the ^{1}H relaxation of **3,5-dcpy**, as it is known that the CSA contribution to T_1 relaxation scales with B_0^2 [102].

The consequences of this result are that a holding field of a strength similar to that used in continuously polarized DNP targets will not be necessary for a SABRE-polarized target. An upper limit on the holding field necessary to maintain the polarization of SABRE-polarized material can be set at 1 T, achievable with either permanent magnets or conventional electromagnets and ruling out the need for cryogen-cooled superconducting magnets. This will allow SABRE-polarized targets to be capable of 4π angular acceptance, which is crucial for maximizing counting rates. As will be seen in Chapter 4, long T_1 times of a few minutes for **3,5-dcpy** are able to be achieved on a benchtop MRI with an internal field strength of 0.33 T, effectively setting a new upper limit on the maximum strength needed for a storage field.

As the transfer of spin order in SABRE is a reversible process, once the supply of *p*-H_2 is stopped and the polarization step has concluded it is necessary to remove the sample from the polarization transfer field. This is because SABRE is a reversible equilibration and allowing the backwards equilibration to occur would result in fast relaxation of the generated polarization. For ^{1}H SABRE, coherent evolution of the spin states at the LAC is maximal at around 6 mT, however frequently this is not a sharp resonance [104], and thus field strengths similar to this should be avoided. It is also the case that at zero field the energy levels of the spin states become degenerate and thus polarization is quickly lost.

In dissolution-DNP, applied fields are necessary for the transfer of polarized material between the polarizing magnet and spectrometer. Here fields of 75 mT are typical in order to ensure that Zeeman splitting dominates over other spin interactions, such as dipole-dipole interactions, J-coupling, or chemical shift anisotropy. The applied field also acts to supress the thermal mixing

between ^{1}H and heteronuclei (such as ^{13}C) spins in the sample. It is thus suggested that a suitable lower limit for the field strength needed to maintain ^{1}H SABRE-derived polarization lies between 75 mT and 1.0 T.

3.4 T_1 dependence on substrate concentration

Typically SABRE experiments are conducted in dilute fashion with substrate concentrations of tens to hundreds of millimolar. Dilute samples are used in SABRE partly due to economic considerations, but also because more concentrated samples will likely have lower polarization levels as *p*-H_2 availability is frequently a limiting factor. Looking back to the Figure of Merit:

$$FoM = Lf^2P^2 \qquad (Eq. 3.2)$$

where L is the beam luminosity, f is the dilution factor and P is the target polarization, it is clear that the dilution factor of potential target material must be optimized due to the quadratic dependence of the FoM on f. This would involve increasing the substrate concentration as high as possible, whether this occurs before the polarization step or in a processing step after polarization has concluded.

In contrast to the concentrations commonly used in SABRE samples, neat **py** has a concentration of 12 M and a saturated solution of **3,5-dcpy** in **DCM** has a concentration of around 5 M. It is expected that T_1s will shorten as sample concentrations increase due to the increased intermolecular interactions between substrate molecules, and thus it is important to understand to what extent this occurs.

This study investigates the T_1 of **3,5-dcpy** at varying substrate concentrations. Here it was chosen to directly vary the mass fraction, where:

$$Substrate\ mass\ fraction\ (\%) = \frac{Mass\ of\ substrate}{Mass\ of\ solution} \times 100. \qquad (Eq. 3.3)$$

This is because the mass fraction values could be known in advance, however the substrate concentration would depend on the final volume after the substrate was dissolved in the solvent.

DCM-*d₂* was chosen for the solvent in this study due to its ability to solubilize high concentrations of **3,5-dcpy**, and 10 mM of **DMSO-*h₆*** was added to the **DCM-*d₂*** in order to act as an internal reference standard. The integrals of the **DMSO** peak for each sample were used to calculate the increase in volume that had occurred for the solution after the substrate had been added. These new volumes were used in order to find the corrected substrate concentrations. In this study the substrate mass fraction was varied from 1% mass, expected to give close to the maximum T_1 of **3,5-dcpy**, up to 40% by mass, which lies near the solubility limit of **3,5-dcpy** in **DCM-*d₂*.**

3.4.1 Results

As can be seen in Figure 3.4 and Table 3.3, the expected relationship of a decreasing T_1 with increasing substrate concentration is observed. It is found that the average T_1 decreases from 135 s at the lowest mass fraction of 1% to 44 s at the highest mass fraction of 40%, a drop of 67%. Interestingly, it is found that there is a significant drop-off in the T_1 for both the *ortho* and *para* positions between the 5% and 10% substrate mass fractions. Here it is found that there is a 40% reduction in the average T_1 with just an approximate doubling of the substrate concentration.

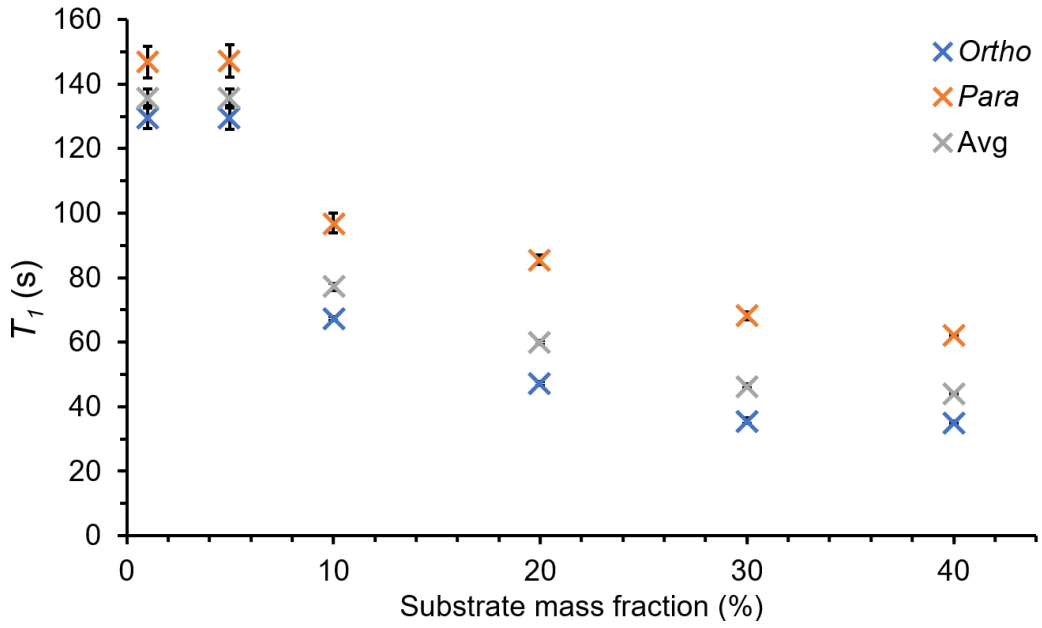

*Figure 3.4 - ^1H T_1s for **3,5-dcpy** with varying substrate mass fractions in solution. The samples contained 1-40% by mass (8-545 mg) **3,5-dcpy**. Error bars are present for all points but may not always be visible.*

*Table 3.3 - ^1H T_1s for **3,5-dcpy** with varying substrate mass fractions in solution. The samples contained 1-40% by mass (8-545 mg) **3,5-dcpy**.*

Mass fraction (%)	Corrected concentration (mM)	^1H T_1 (s)		
		Ortho	*Para*	Avg
1	90	130 ± 4	147 ± 5	135 ± 3
5	470	130 ± 4	147 ± 5	136 ± 3
10	970	67.3 ± 0.6	97 ± 3	77 ± 1
20	1930	47 ± 1	86 ± 2	60 ± 1
30	3070	36 ± 1	68 ± 1	46 ± 1
40	3900	35.1 ± 0.4	62.1 ± 0.4	44 ± 0.3

3.4.2 Discussion

It is proposed that the results seen in Figure 3.4 and Table 3.3 are caused by a change in the dominant source of relaxation between the low and high mass fraction samples. For the 1% and 5% mass samples the measured T_1 values are identical to within error, despite an approximate 5-fold increase in the substrate concentration. This suggests that the dominant source of relaxation is the intramolecular dipolar relaxation between ^{1}H nuclei, which is inherently low for **3,5-dcpy** due to the magnetic isolation of the ^{1}H nuclei. A 40% reduction in the average T_1 with a further doubling of the substrate concentration suggests that here intermolecular dipolar relaxation between molecules now contributes strongly to relaxation. Changes in the T_1 may also arise from the changing viscosity of the solution. **DCM-*d*$_2$** is a low viscosity solvent [105], and thus the viscosity of the solution is expected to increase considerably as the substrate mass fraction becomes significant.

The results seen here show that the maximum substrate mass fraction that is usable without being detrimental to the T_1 is 5%, equivalent to 470 mM. It is undetermined as to what this value would be for higher dilution factor substrates, such as **py** or **3,5-py-*d*$_2$**, which are more promising for polarized target applications, however for these substrates a concentration of 470 mM equates to a percentage by volume of approximately 4%.

The 67% drop in the T_1 seen in this study between the lowest and highest substrate mass fraction would result in a significant decrease in the maximum achievable polarization for a continuously polarized target utilizing SABRE. It is thus proposed that it is necessary to stay below the limit at which intermolecular interactions contribute significantly to relaxation, shown here to be 5% mass (470 mM) for **3,5-dcpy**.

Alongside the concentration of substrate in solution, another important factor influencing the substrate T_1 is the molar excess of the substrate relative to the SABRE catalyst. This is investigated in the following section.

3.5 T_1 dependence on catalyst concentration

In the substrate comparison study in Section 2.2, conducted at a 40-fold substrate excess relative to the catalyst, **3,5-dcpy** was found to have the one of the highest $T_1 s$. Interactions of the substrate with the SABRE catalyst are known to be a large contributor to T_1 relaxation [52]. Therefore, the dependence of the T_1 of **3,5-dcpy** on its molar excess over the catalyst was investigated to determine the extension to the T_1 that could be achieved at a large substrate excess.

This dependency was investigated for both the **IMes** and **IMes-*d*$_{22}$** catalysts, to determine the effect of the replacement of high-γ ^{1}H nuclei with low-γ ^{2}H nuclei in the catalyst NHC. It was hypothesized that the T_1 at large substrate excess (low catalyst limit) would be the same for both catalysts, but that the **IMes-*d*$_{22}$** samples would reach the maximal T_1 at a lower substrate excess.

These studies were conducted at a fixed substrate concentration of 40 mM to avoid any effect on the T_1 from intermolecular interactions at high substrate concentrations. The precatalysts **IMes** and **IMes-*d*$_{22}$** were used in concentrations ranging from 8 mM to 0.2 mM resulting in substrate excesses of 5-fold to 200-fold, and the solvent used was **DCM-*d*$_2$**. The T_1s were measured using the hyperpolarized T_1 recovery sequence detailed in Section 7.3.2, utilizing 30 scans with an inter-scan delay of 10 s. The samples were prepared and activated as described in Section 7.2.1 and were polarized using the 'Shake and drop' approach as described in Section 7.2.2.

3.5.1 Results[vii]

The results of this study for both catalysts can be seen in Figure 3.5-Figure 3.6 and Table 3.4-Table 3.5. It can be seen that there is a very strong dependence of the T_1 on the substrate excess for both the *ortho* and *para* position protons in **3,5-dcpy** for both catalysts. For the **IMes** catalyst, a 6-fold increase is seen in the average T_1 from a 5-fold to a 200-fold excess, increasing from 32 s to 192 s. For the **IMes-*d*$_{22}$** catalyst, a 5.1-fold increase is found, from 35 s to 178 s.

Looking at Figure 3.5 and Figure 3.6, it can be seen that the T_1 approaches its maximum value at a faster rate for the **IMes-*d*$_{22}$** catalyst, confirming expectations. This is evidenced at an 80-fold excess, where, for the **IMes** catalyst, the *ortho* and *para* positions are at 69% and 76% of their maximum values (200-fold excess) respectively. In contrast, for the **IMes-*d*$_{22}$** catalyst, by an 80-fold excess the *ortho* and *para* positions have reached 78% and 90% of their maximum values.

[vii] Selected results from this study have been published and can be found in [56].

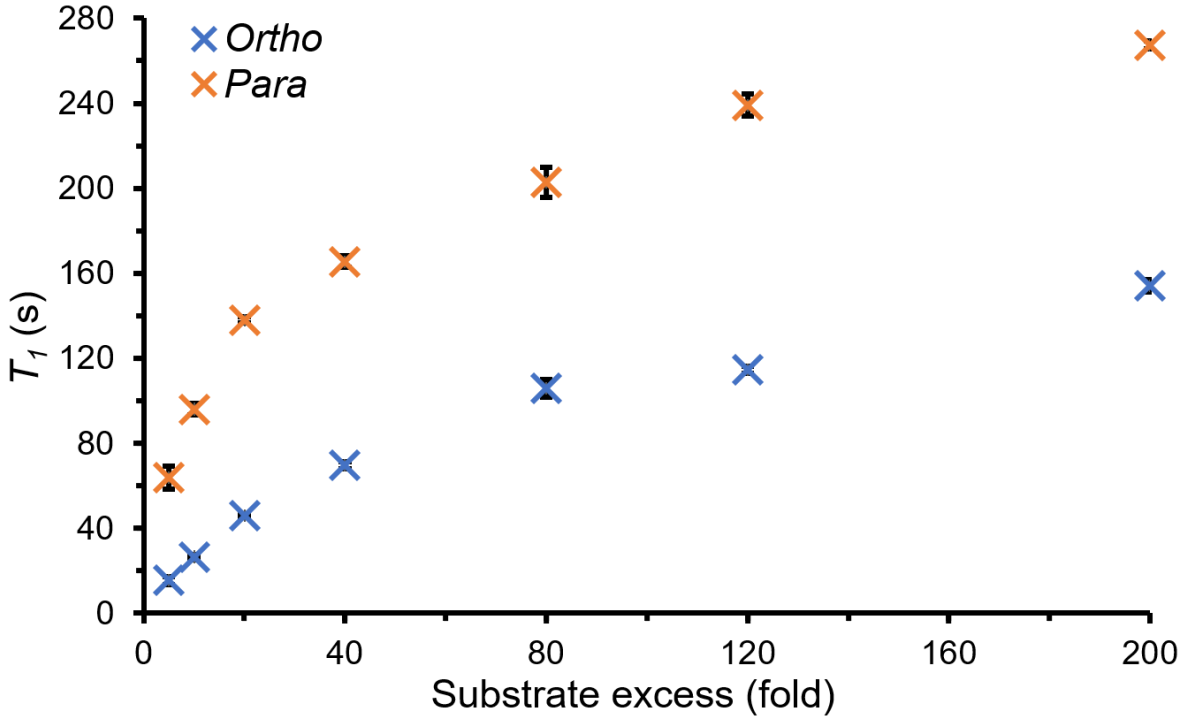

*Figure 3.5 - T_1 of **3,5-dcpy** at varying substrate excesses relative to the **IMes** catalyst. Error bars are present for all points but may not always be visible.*

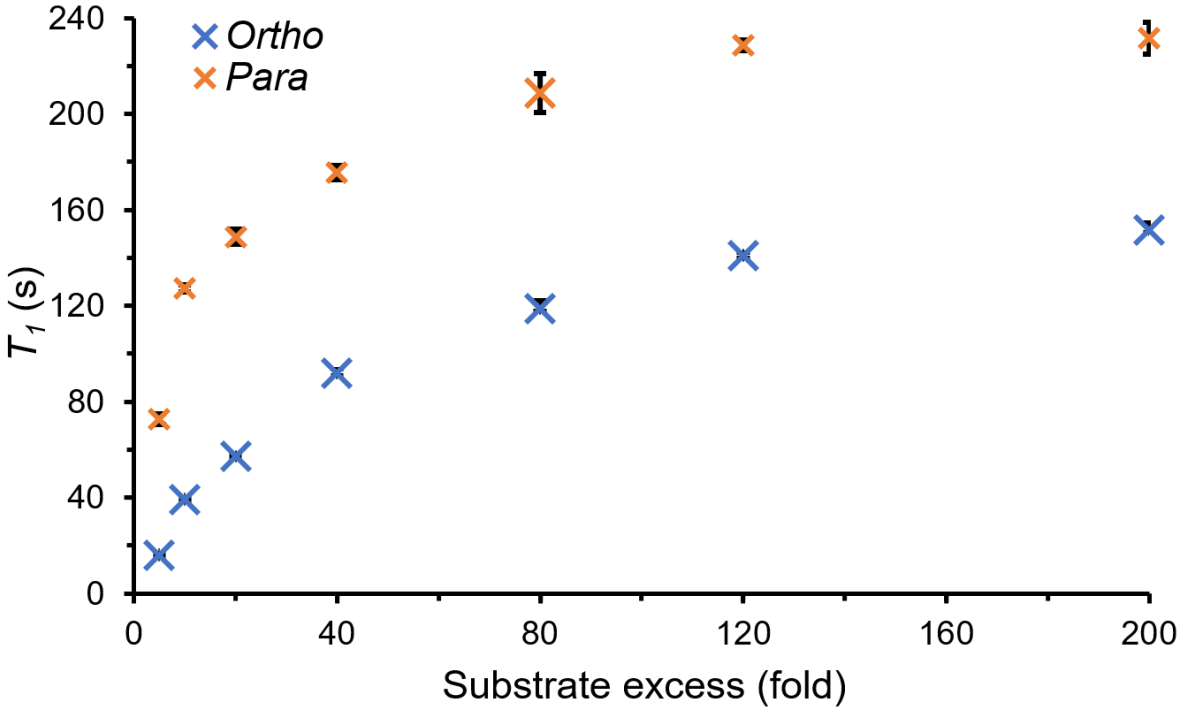

*Figure 3.6 - T_1 of **3,5-dcpy** at varying substrate excesses relative to the **IMes-d_{22}** catalyst. Error bars are present for all points but may not always be visible.*

*Table 3.4 - T_1 of **3,5-dcpy** with varying substrate excesses relative to the **IMes** catalyst.*

Catalyst concentration (mM)	**Substrate concentration (mM) [Excess]**	**^{1}H T_1 (s)**		
		Ortho	*Para*	Avg
8	40 [5]	16 ± 2	64 ± 5	32 ± 3
4	40 [10]	27 ± 1	96 ± 3	50 ± 2
2	40 [20]	46.0 ± 0.3	138 ± 2	76.7 ± 0.7
1	40 [40]	70 ± 2	165 ± 3	102 ± 2
0.5	40 [80]	106 ± 4	203 ± 7	138 ± 4
0.33	40 [120]	115 ± 2	239 ± 5	156 ± 2
0.20	40 [200]	154 ± 3	267 ± 2	192 ± 3

*Table 3.5 - T_1 of **3,5-dcpy** with varying substrate excesses relative to the **IMes-d_{22}*** catalyst.

Catalyst concentration (mM)	**Substrate concentration (mM) [Excess]**	**^{1}H T_1 (s)**		
		Ortho	*Para*	Avg
8	40 [5]	16.1 ± 0.9	73 ± 2	35 ± 1
4	40 [10]	39.3 ± 0.3	127 ± 2	68.6 ± 0.5
2	40 [20]	57.3 ± 0.7	149 ± 3	88 ± 1
1	40 [40]	92 ± 2	176 ± 3	120 ± 2
0.5	40 [80]	119 ± 4	209 ± 8	149 ± 4
0.33	40 [120]	141 ± 1	229 ± 2	170 ± 1
0.20	40 [200]	152 ± 3	231 ± 7	178 ± 3

3.5.2 Discussion

An unexpected result from this study is that the T_1 for the *para* position in **3,5-dcpy** was found to be 16% higher for the 200-fold excess sample with **IMes** compared to **IMes-*d*$_{22}$**. It is proposed that there is no physical mechanism for this observed difference, and that this difference is due to fitting errors.

Due to the measurement period of 290 s, for the 200-fold excess samples the *para* position will only experience around 1 T_1 through the measurement period, falling to around $\frac{1}{3}$ of its initial value. Because of this, there can be large differences in the fitting parameter T_1 which will have little effect on the quality of the fitting. It is thus proposed that the error stated for these values, calculated from the standard deviation of the fitted T_1s for repeat measurements, underestimates the true error. It is also noted that small discrepancies from the stated sample compositions may result in noticeable differences in the measured T_1. It is thus likely that the true T_1 for the *para* position of **3,5-dcpy** for the 200-fold excess samples with **IMes** and **IMes-*d*$_{22}$** is similar, likely lying in the range 240-260 s.

Despite this, to the author's knowledge, the measured T_1s of >240 s for the *para* position in the 200-fold excess samples of **3,5-dcpy** are likely the highest reported ^{1}H T_1s measured in room temperature solution state NMR - an exciting result. A study that has found similarly long ^{1}H T_1s was performed by Rayner et al. [70], in which a T_1 of 177 s was measured for the 3-position in 2,4-pyridazine-d_2, shown in Figure 3.7. Unsurprisingly, properties that both of these ^{1}H nuclei share is the isolation from other high-γ nuclei, the sample being devoid of any paramagnetic O_2, and low/no catalyst being present.

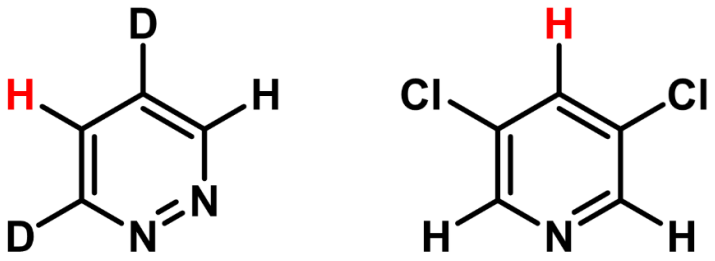

*Figure 3.7 - 2,4-pyridazine-d_2 from [70] in which a T_1 of 177 s was measured (left), **3,5-dcpy** from this study in which a T_1 of >240s was measured (right). The site for which the T_1 was achieved is coloured in red.*

This study demonstrates the massive extensions that can be made to substrate T_1s by reducing the catalyst concentration - the concentration in the 200-fold excess sample here is 25 times lower than a typical 5 mM loading used for SABRE experiments. Knowing that T_1s of the length observed here are possible to achieve with SABRE substrates has significant implications for the applications of SABRE. As mentioned previously, long T_1s are important to the maximal polarization that can be achieved with a continuously polarized target, however the results shown here also enabled the experiment described in the following chapter, testing the resilience of SABRE polarization to an incident photon beam at an accelerator facility. This was an experiment that due to practical limitations was only possible to achieve for SABRE samples that had a detectable signal that lasted in excess of 10 minutes.

These studies into the effects of catalyst concentration on the substrate T_1 hint at what the optimal substrate to catalyst ratio may be for use in a polarized target. These results cannot answer that question fully as the maximal steady-state polarization that can be achieved will also depend on the rate of polarization. We can see however that for the **IMes-*d*$_{22}$** catalyst that only a 5% increase in the average T_1 of **3,5-dcpy** is observed between the 120-fold and 200-fold excess samples whilst the catalyst concentration decreases by 40%. If SABRE is occurring in a regime that isn't *p*-H_2 limited, then it seems likely that the decrease in catalyst concentration, and thus catalytic output, will outweigh the marginal increase in T_1. Thus, for **3,5-dcpy** the optimal substrate excess for maximizing steady state polarization will be unlikely to exceed 120-fold.

It is anticipated that the dependence of T_1 on catalyst concentration will have a similar profile for other substrates, with changes to the horizontal asymptote and the rate at which the asymptote is approached. A study investigating the optimal substrate excess for a similar substrate will be presented in Section 5.4.2.

3.6 RASER effect

3.6.1 Introduction

When the study in Section 3.2 was initially attempted, it was observed that there were large distortions to the baselines of the acquired NMR spectra that obfuscated the results. After further examination of the FID signals, it appeared that these samples were exhibiting evidence of the RASER effect, with spontaneous emission of radiofrequency (RF) waves.

The RASER (Radio Amplification by Stimulated Emission of Radiation) effect is analogous to lasers [106,107] and masers [108,109] which emit coherent radiation in the optical and microwave regimes. It has been seen previously in PHIP and SABRE experiments [110-114], however the observation of the effect is recent.

The theory of stimulated emission of radiation was first conceived by Einstein in 1917 [115]. For stimulated emission to occur, the system must have discrete energy levels, and there must be a population inversion in which the excited state has a higher population than the lower energy state. The energy difference when a transition from the excited state (E_1) to a lower energy state (E_0) occurs is released as a photon of this energy ($E_1 - E_0$), shown in Figure 3.8. This photon then has the necessary energy to trigger the emission of a photon when it encounters another spin in an excited state. If the right conditions are met then a chain reaction can be triggered. The necessary conditions include a high proportion of spins in an excited state, and that the excited state is stable over the necessary timescales.

For the RASER effect observed in SABRE samples, the population inversion is produced by the hyperpolarization process producing an overpopulation of the excited nuclear spin state. Due to the energy gap between the spin states, the emitted photons are in the RF range, similar to the RF waves that are used in the pulse for an NMR experiment. If the right conditions are met in a SABRE-polarized sample then a chain reaction of RF-photon production can occur, with the transitions between spin states being measurable in an FID acquisition.

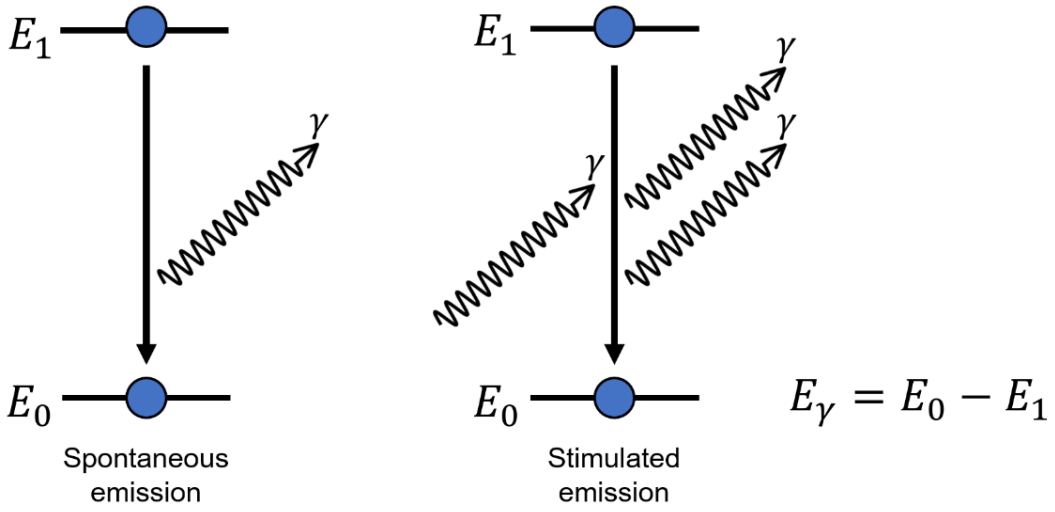

Figure 3.8 - Diagram of spontaneous emission (left) and stimulated emission (right) of radiation.

3.6.2 Evidence of the RASER effect[viii]

Evidence of the RASER effect can be seen in Figure 3.9. Figure 3.9a shows a 90° pulse FID from a sample which exhibited signs of the RASER effect. Here it is difficult to notice anything unusual in the FID until it is enlarged, shown inside the green box.

Figure 3.9b and Figure 3.9c show the FIDs acquired after a 1° pulse and with no RF pulse respectively, with a longer acquisition time. Here the RASER effect is much more prominent as all signal acquired after around 2 s for Figure 3.9b and all signal for Figure 3.9c would not be expected to be seen in the absence of the RASER effect. An FID of a sample not exhibiting the RASER effect is shown in Figure 3.10.

The effect is further confirmed by Figure 3.9d which shows the spectrum produced from an FID acquired on a hyperpolarized sample exhibiting the RASER effect with no RF pulse applied. Here it can be seen that only peaks visible in the spectrum are from the *ortho* and *para* positions of the hyperpolarized substrate, **3,5-dcpy.** These peaks have been excited due to the RASER phenomenon and there are no other peaks visible, such as from the catalyst or solvent, due to the lack of an RF pulse to excite them.

The sample used for these results contained 5.2 mM of **IMes**, 26 mM of **DMSO-*d*$_6$** and 104 mM of **3,5-dcpy** in **DCM-*d*$_2$**. The RASER effect was also observed in other samples, with the effect being confined to samples that formed the neutral SABRE catalyst in the presence of **DMSO**.

[viii] Selected results from this study have been published and can be found in [56].

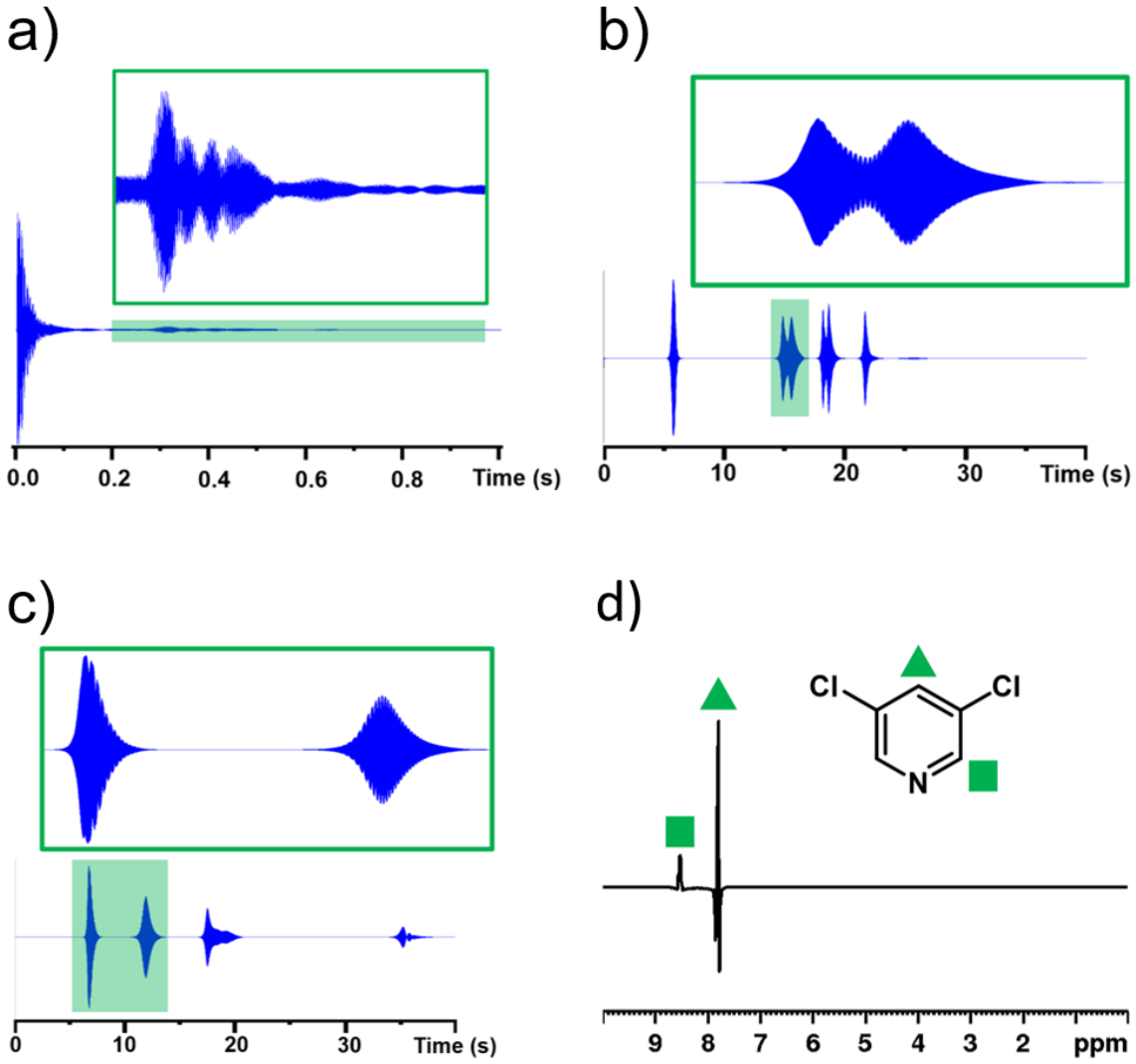

Figure 3.9 - a) ^{1}H FID after 90° pulse. b) ^{1}H FID after 1° pulse with longer acquisition. c) ^{1}H FID recorded after no RF excitation. d) ^{1}H NMR spectra recorded without RF excitation (1 s acquisition). All spectra are recorded at 9.4 T (400 MHz) and do not share the same vertical scale. Parts of the FID, coloured in green, are shown expanded in the green inserts.

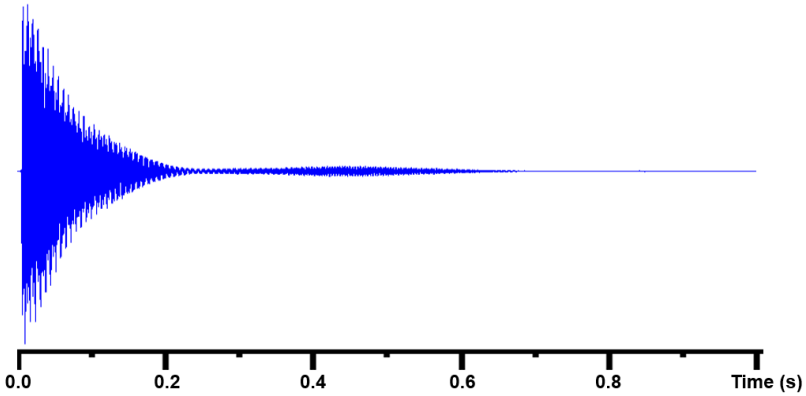

Figure 3.10 - ^{1}H FID that does not exhibit the RASER effect. Recorded at 9.4 T (400 MHz).

3.7 Chapter 3 Conclusions

In this chapter, a number of key results on the factors influencing the T_1 of hyperpolarized material have been presented. These results have been acquired for the SABRE substrate **3,5-dcpy** which was chosen for its exceptionally low rate of intrinsic ^{1}H T_1 relaxation. This allowed for a more precise investigation into factors affecting the T_1 than would otherwise be possible.

In the investigation of the temperature dependence of T_1 relaxation for **3,5-dcpy**, it was found that there was strong variation in the T_1 over the measured temperature range of 243-323 K. The average T_1 across all ^{1}H sites exhibited a 130% increase from its minimum to maximum value, reaching a peak of 112 s at 303 K (30.9 °C). The average T_1 continuously decreased for temperatures further from the optimum. It was found that the percentage rate of change of the T_1 with temperature peaked at 7% K^{-1} between 305.5 and 308 K, a sensitivity that is orders of magnitude lower than is observed below 1 K for polarized target material utilizing DNP. This demonstrates that a SABRE-polarized target will be able to withstand significantly higher heat deposits than are possible with DNP targets.

In the investigation of the magnetic field dependence of T_1, very little field dependence was observed over the investigated range of 1.0-11.7 T. It was found that the minimal and maximal values for the average T_1 over this range were 78 s and 82 s respectively, only differing by 7%, with three out of the four investigated field strengths giving the same average T_1 to within error. This lack of field dependency of the T_1 is predicted for the relaxation of molecules in the extreme narrowing limit, characterized by small molecule sizes, high temperatures, and low viscosity solvents - conditions satisfied here.

These two studies have given important insight into the physical conditions under which SABRE will perform optimally as a polarized target material. T_1 relaxation for **3,5-dcpy** at 9.4 T has been demonstrated to be lowest at just above room temperature, coinciding with the temperatures which are frequently optimal for polarization transfer. It has also been shown that the maximal holding field necessary to maintain SABRE polarization, specifically for **3,5-dcpy**, is 1.0 T, with no measurable increase in T_1 at stronger fields than this. This knowledge is of importance for the processing of polarized material or for non-continuous polarized target designs, such as a frozen pellet target.

In the study of the T_1 of **3,5-dcpy** with varying substrate concentrations, it was found that the average T_1 decreases from 135 s at the lowest mass fraction of 1% to 44 s at the highest mass fraction of 40%, a drop of 67%. It is found that there is a significant drop-off in the T_1 for both ^{1}H

positions between the 5% and 10% substrate mass fractions, with a 40% reduction in the average T_1 coming from a doubling of the substrate concentration.

It is proposed that this effect is caused by a change in the dominant source of relaxation between the low and high mass fraction samples, with the dominant source of relaxation changing from intramolecular dipolar relaxation to intermolecular dipolar relaxation. Changes in the T_1 may also arise from the increasing viscosity of the solution with increasing substrate concentration.

It is found that the maximum substrate mass fraction that is usable without being detrimental to the T_1 is around 5%, equivalent to 470 mM. For **py** or **3,5-py-*d*$_2$** a similar concentration would be equivalent to a percentage by volume of approximately 4%. The drop in the T_1 seen in this study at substrate mass fractions >5% would result in a significant decrease in the maximum achievable polarization for a continuously polarized target, thus it is proposed that it is necessary to stay below this limit.

In the investigation of the dependence of T_1 on the catalyst concentration it was found that the corresponding increase in the substrate excess at low catalyst concentrations resulted in significant increases to the substrate T_1. It was found for the **IMes** and **IMes-*d*$_{22}$** catalysts that the average T_1 increased by 6-fold and 5.1-fold from 32 s to 192 s and 35 s to 178 s respectively, between the 5-fold and 200-fold excess samples. It was also seen that the T_1 approaches its maximum value at a faster rate for the **IMes-*d*$_{22}$** catalyst, confirming prior expectations.

Unexpectedly, the T_1 for the *para* position in **3,5-dcpy** was found to be higher for the 200-fold excess sample with **IMes** than with **IMes-*d*$_{22}$**, when it was anticipated that they would reach the same value in the low catalyst limit. It is proposed that there is no physical mechanism for this observed difference, and that this difference is due to fitting errors. The measured T_1s of >240 s for the *para* position in the 200-fold excess samples of **3,5-dcpy** are likely the highest reported ^{1}H T_1s measured in room temperature solution state NMR.

This chapter also presents evidence for the RASER effect, a recently observed phenomenon analogous to lasers [106,107] and masers [108,109] that involves the stimulated emission of RF photons in hyperpolarized samples. Further understanding of the conditions that give rise to this effect is important, as the effect could result in the unwanted rapid depolarization of polarized material.

Chapter 4 - Radiation resilience of polarized material

4.1 Introduction

This chapter will detail the first ever test of the resilience of SABRE-polarized material to an incident particle beam, a test conducted at the Mainz Microtron (MAMI) accelerator facility [Section 4.2] in the A2 experimental hall. The A2 facility [Section 4.2.1] impinges the intense MAMI electron beam on a thin metallic foil radiator to produce a beam of energy-tagged Bremsstrahlung photons. This photon beam was used for in-beam measurements of the polarization levels of SABRE-polarized material, to test for any depolarization effects. The MAMI electron beam was also used to expose a sample of SABRE material to a high radiation dose in order to test for the effects of radiation damage in the sample.

Section 4.3 discusses the aims of the experiment and details the methodology used to monitor the in-beam decay of polarization. Section 4.4 presents the results of any influence on the polarization decay for SABRE-polarized material in-beam, for three different substrates. Section 4.5 presents the results for a sample exposed to a higher dose (near the electron beam dump) during the run period. Section 4.6 discusses the implications of the new measurements for establishing the capabilities for SABRE-polarized material to be used in particle beams. Further experiments necessary to increase the understanding of the effect of incident radiation on SABRE-polarized material are also discussed in Section 4.7.

4.1.1 Motivation of the experiment

Polarized nuclear targets utilizing DNP are known to suffer beam-induced depolarization effects, particularly with high intensity electron beams. One such depolarizing effect is beam heating, where the energy deposited by the beam warms the sample, increasing the rate of T_1 relaxation. This effect can be mitigated for by using techniques such as beam rastering [33], sweeping the beam spot over the target surface to irradiate the target evenly, however it cannot be completely eliminated. The other commonly observed depolarizing effect is the production of radicals in the sample, which act as a source of paramagnetic relaxation.

Ammonia (NH_3), first used at Brookhaven AGS in 1982 [116], is the current target material of choice for polarized proton targets needed to withstand high beam intensities. This is due its lower tendency to produce radicals, resulting in it somewhat replacing the alcohol targets used

previously. The depolarizing dose for polarized NH_3 targets has been found to be over an order of magnitude higher that of butanol or HD targets [116,117], as shown in Figure 4.1.

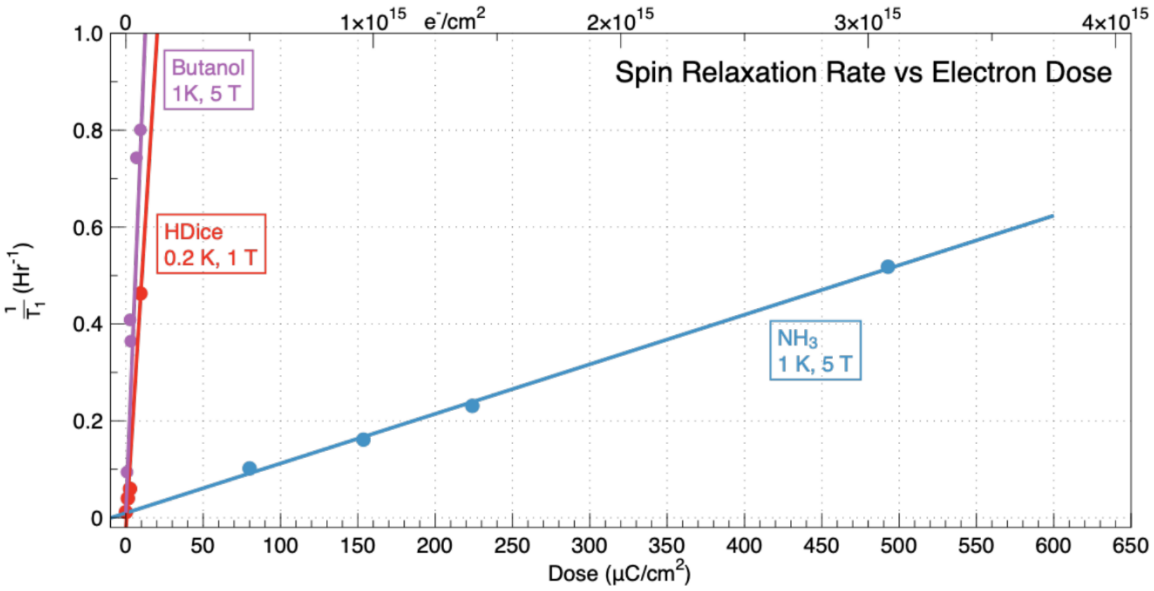

Figure 4.1 - The relaxation rate ($^1/_{T_1}$) for protons in ammonia, butanol and HD targets at Jefferson Lab as a function of total accumulated dose from an electron beam. From [118].

Beam-induced depolarization effects are particularly restrictive for experiments utilizing frozen-spin targets with a charged particle beam. Frozen-spin targets are currently the only option for achieving close to 4π angular acceptance using fixed polarized targets. A frozen-spin NH_3 target was chosen for Drell-Yan measurements by the COMPASS collaboration with a π^- beam [15], however, in this experiment the beam current was limited to just 16 pA - 500 times lower than for recent e-p measurements at Jefferson Lab using a continuously polarized target [35]. This was due to the high sensitivity of the T_1 to beam-induced heat deposition at the target temperature of 60 mK, required for frozen-spin operation. The average polarization of the target decreased from its maximum of 86% to between 68% and 76% during operation, a consequence of the roughly 40% drop in the T_1 observed even at these low beam currents.

When commissioning a transversely polarized target to complement the new longitudinally polarized target used with CLAS12 at Jefferson Lab Hall B, both the brute force frozen-spin target HDice and a DNP frozen-spin NH_3 target were considered. The requirement was that polarization must be maintained for at least 21 days under an electron beam current of 1 nA in order to minimize wasted running time [118]. Under similar conditions, HDice exhibited a T_1 of only 4-6 hours due to the effects of beam heating and radical production [31]. For a frozen-spin NH_3 target, calculations showed that achieving the required T_1 would require a holding field of at least 2.5 T, accounting for

the expected rate of heat deposition. A field of this strength would also be suitable for a continuously polarized target, maintaining polarization for significantly longer due to the replenishment of polarization, and thus this is the current candidate for a transversely polarized target.

For the continuously polarized longitudinal target at Hall B, beam currents of 4-8 nA are used [35], yet this still only reaches 2.5-5% of the maximum beam current that can be delivered in Hall B of 160 nA [119]. Even at the restricted beam current used, targets have to be replaced after 2-3 days of running because of unacceptably low polarization levels due to radiation damage of the NH_3 target material [35].

As discussed in Chapter 1, there is a clear need in the international community of nuclear and particle physics for polarized target methodologies that can operate at the frontiers of intensity. The measurements that will be presented in this chapter are a step towards that goal, giving the first constraint on the resilience of SABRE-polarized material to an incident particle beam and high radiation doses. It is the hope that SABRE can address the issues facing the use of DNP targets with intense charged particle beams.

4.2 The Mainz Microtron facility

The Mainz Microtron (MAMI) is a particle accelerator facility located at the Institut für Kernphysik at Johannes Gutenberg University (JGU) in Mainz, Germany. MAMI is a fixed-target electron accelerator capable of beam energies of up to 1.6 GeV [120] and continuous-wave (CW) operation. This electron beam can be fed into one of the three experimental halls: A1, A2 or A4, seen in Figure 4.3.

MAMI differs from other electron accelerator facilities due to its unique design using three Race Track Microtrons (RTMs) and one Harmonic Double Sided Microtron (HDSM). These microtrons allow for CW operation, where the accelerator delivers a steady uninterrupted beam of particles, rather than delivering particles in bunches.

The A1 collaboration uses high precision electron scattering experiments to research the structure of atomic nuclei [121], whereas the A4 collaboration focuses on measuring parity violating scattering asymmetries in order to probe nucleon structure [122]. The experiment described in this chapter was performed at the A2 collaboration which, unlike at the A1 and A4 collaborations, performs experiments using energy-tagged Bremsstrahlung photons.

4.2.1 The A2 collaboration

The A2 collaboration at MAMI investigates a range of topics in hadron physics using a combination of unpolarized, linearly, or circularly polarized tagged photons with unpolarized or polarized targets [123]. The beam derives from the production of Bremsstrahlung photons during the passage of the MAMI electron beam through a thin radiator [120], with the energy of these photons being provided through measurement of the scattered electrons by the Glasgow-Mainz tagging system [124]. For unpolarized targets, liquid hydrogen or deuterium is typically used, whereas for polarized target experiments a frozen-spin DNP target [27] is implemented using a variety of target materials.

4.2.2 The A2 photon beam

As previously mentioned, the photon beam at A2 at MAMI is produced through the Bremsstrahlung process. As the electron beam passes through the radiator, the electrons lose energy through interactions with the electromagnetic field of a nucleus in the radiator material. This energy loss is emitted as a photon in a process called Bremsstrahlung (breaking) radiation [125], shown in Figure 4.2. Radiators for Bremsstrahlung production are typically either amorphous (high-Z materials e.g. W, Pb, Cu) or crystalline, (e.g. diamond). Crystalline radiators are necessary for the production of linearly-polarized photon beams through coherent Bremsstrahlung radiation. A2 at

MAMI has a selection of three radiators, copper, diamond, and a Møller radiator. The Møller radiator was used in this experiment, and is made from the alloy VACOFLUX 50 (49% Co, 49% Fe, 2% V), with a thickness of 10 µm.

The energy spectrum of amorphous Bremsstrahlung photon production follows the distribution:

$$N(E_\gamma) \propto {}^{1}/_{E_\gamma} \qquad (Eq.\,4.1)$$

where $N(E_\gamma)$ is the relative probability of a photon containing an energy E_γ.

In this chapter, the intensity of the photon beam at A2 will be referred to with units of nA, despite being a neutral particle beam. Here the beam current refers to the current of the electron beam which produces the Bremsstrahlung photons. The beam current, I, is calculated as:

$$I(Cs^{-1}) = q(C) \cdot N(s^{-1}) \qquad (Eq.\,4.2)$$

where q is the charge of the electron and N is the number flux of electrons. Thus, a beam current of 10 nA equates to an electron flux of $6.2 \times 10^{10}\ s^{-1}$.

The electron beam energy used in this experiment was 855 MeV, produced using the first three RTMs at MAMI. The maximum photon energy of the photon beam was thus 855 MeV, and the relative intensities of photon energies will follow the 1/E distribution seen in Eq. 4.1.

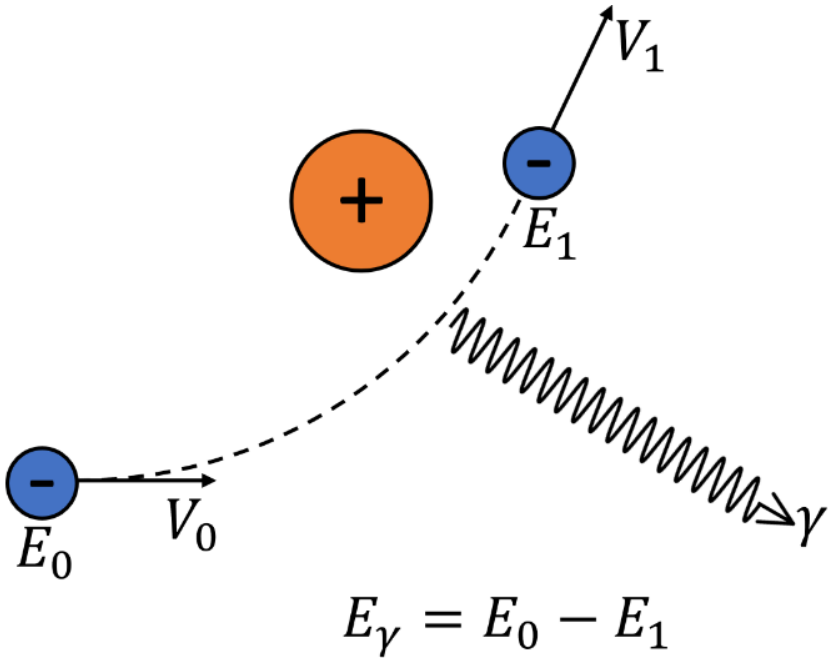

Figure 4.2 - Diagram of the Bremsstrahlung process.

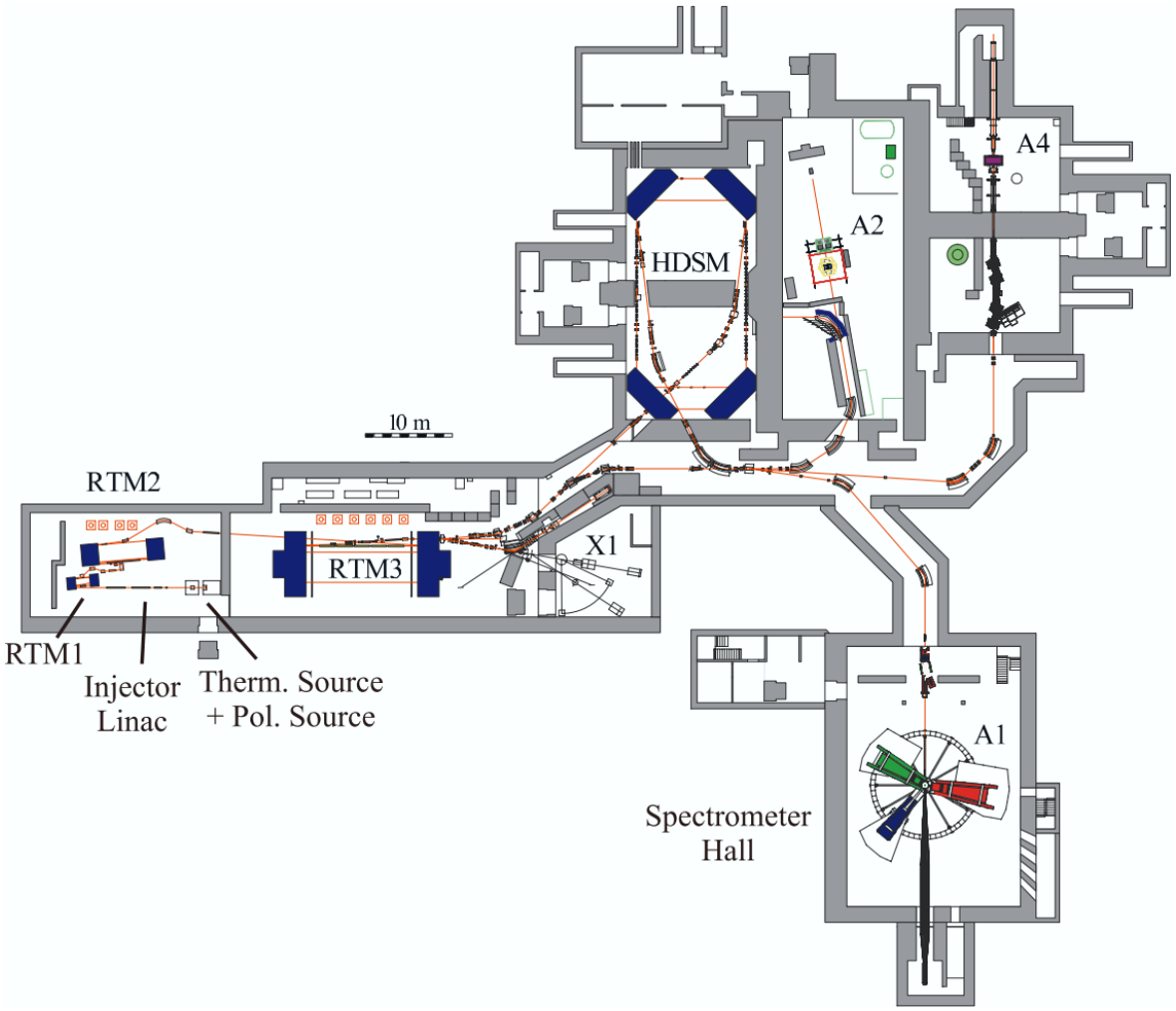

Figure 4.3 - Floorplan of the MAMI accelerator facility. From [126].

4.3 Experiment aims and methodology

4.3.1 Aims

The first of the two aims of this experiment was to measure the changes to the polarization decay rate of SABRE-polarized material in the presence of the A2 photon beam. This was done for three SABRE-compatible substrates: 3,5-dichloropyridine (**3,5-dcpy**), 3,5-dibromopyridine (**3,5-dbpy**), and 2,6-dichloropyrazine (**2,6-dcpz**), which were chosen because of the long lifetimes of their hyperpolarized states, a necessity for this experiment. Three different substrates were investigated such that it could be determined whether any beam-induced depolarization effects were substrate dependent.

These measurements were important for understanding the capability of SABRE material to offer a low-cost alternative to DNP targets for use in photoproduction experiments. Additionally, they demonstrated a novel methodology for in-beam polarization decay measurements that could be adapted for use with a charged particle beam.

The second aim of the experiment was to measure the effects of a high radiation dose on the achievable polarization levels and relaxation rate of SABRE material. This was necessary in order to understand whether SABRE material would be subject to high rates of radical production, thus shortening the T_1. It also provided information on whether the SABRE catalyst was stable under such high doses. Both of these combined would inform an estimate as to what the usable beam currents might be for a SABRE-polarized target operating with an incident electron beam.

4.3.2 Methodology

In-beam polarization decay measurements

The procedure for the in-beam polarization decay measurements was as follows. SABRE samples were prepared in a custom-made polarization cell, consisting of glass tubing separated into two regions using a semi-circular insert, as is shown in Figure 4.4.

Before each run, spent gas in the polarization cell from the previous run was removed and was replenished with 5 bar of *p*-H_2. The sample was polarized through the 'Shake and drop' method, described in Section 7.2.1, whereby the sample was placed within a 6 mT handheld Halbach array and shaken for 45 s in order to allow for the build-up of polarization.

After polarizing, the polarization cell was inserted horizontally into a benchtop MRI, oriented with the bore along the axis of the beam, and the decay of polarization was measured using a series of low tip-angle FIDs as is described in Section 7.3.2. For each substrate, the same sequence of tip

angles would be used for all runs such that any differences in the decay rates could not be attributed to the measurement sequence.

Immediately after the sample was inserted into the MRI, the experimental hall was quickly vacated and the photon beam was then turned on, whilst the hyperpolarized T_1 recovery sequence was running. Typical wait times between the end of the polarization step and the beam being operational were a few minutes. This necessitated the use of substrates with long polarization lifetimes, such that sufficient signal remained once the beam was operational. The polarization decay profiles of samples in the beam were compared to those of control runs in which the beam was not turned on, to quantify the change in decay rates. A diagram of the experimental procedure can be seen in Figure 4.5.

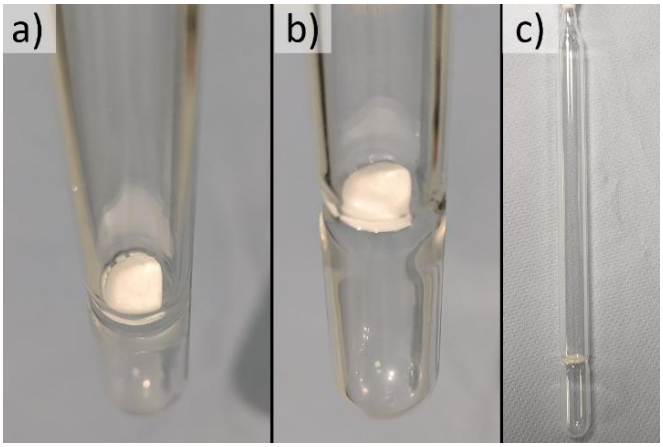

Figure 4.4 - a-b) The fritted glass insert in the polarization cell. c) The full polarization cell.

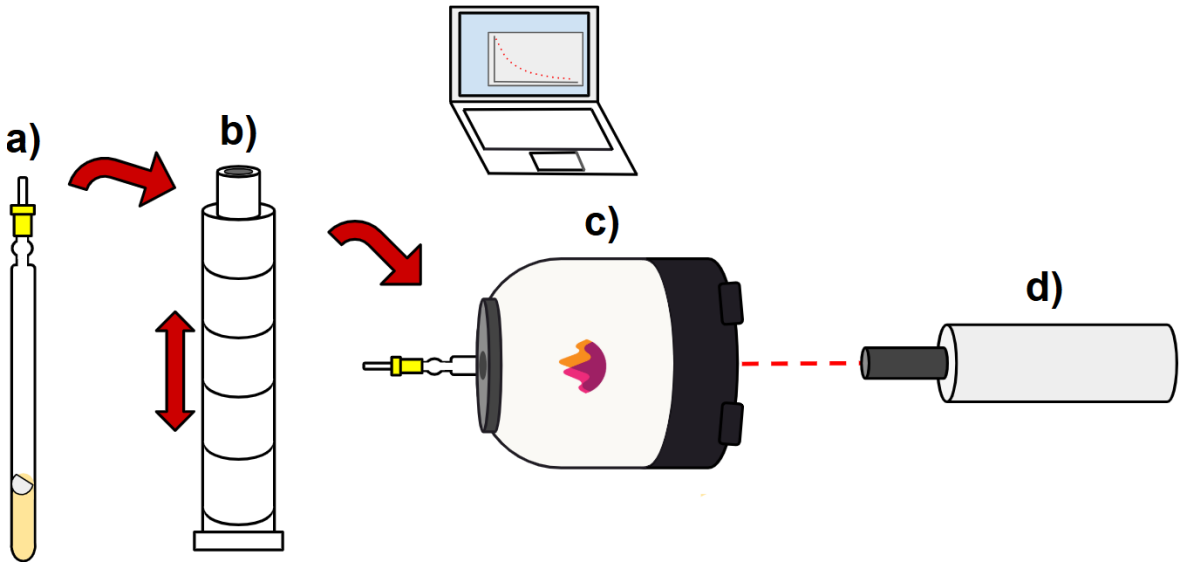

Figure 4.5 - Diagram of the experimental procedure. a) Prepare sample and fill with p-H_2. b) Transfer to Halbach array and shake for 45 s. c) Transfer to MRI and start acquisition. d) Vacate hall and turn on photon beam.

High dose sample irradiation

Throughout the four-day beamtime, a cell containing a SABRE sample was placed near the electron beam dump in the A2 hall. The relative polarization values and $T_1 s$ were compared on the sample before and after the irradiation dose. The electron beam dump was chosen as it was the area of the experimental hall in which the sample would come under the highest radiation bombardment. The location at which the sample was placed can be seen in Figure 4.6.

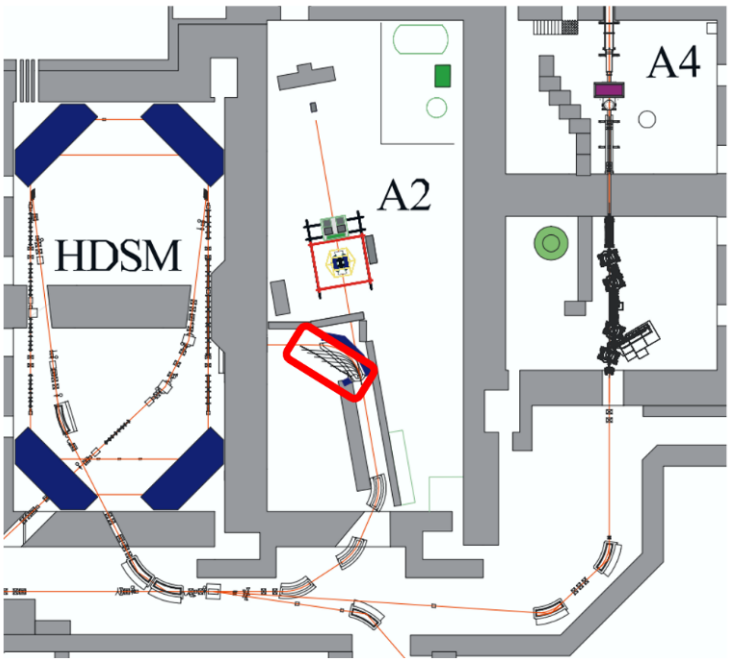

Figure 4.6 - Location of the irradiated sample within the A2 experimental hall, circled in red. Floorplan adapted from [126].

Sample preparation

All investigated samples contained 0.63 mM of **IMes-d_{22}** precatalyst, 75 mM of substrate and 3.1 mM of **DMSO-d_6** co-ligand in 5 mL of **DCM-d_2**, representing a 120-fold substrate excess and 5-fold co-ligand excess over the catalyst. The samples were degassed using a custom-built apparatus comprising of a vacuum pump, cold trap and nitrogen line, shown in Figure 4.7. This was connected to the polarization cell as shown in Figure 4.9. The samples were degassed three times using the freeze-pump-thaw technique, described in Section 7.2.1, with nitrogen purges being performed between each degassing run. The samples were then pressurized with *p*-H_2 (5 bar) and left to activate fully over 3 hours to form their respective active SABRE catalysts. The *p*-H_2 was supplied by the ZULF NMR group at JGU Mainz and had an enrichment percentage of >98%. The *p*-H_2 filling setup is shown in Figure 4.8 and Figure 4.10.

Figure 4.7 - Picture of the degassing apparatus for the polarization cell.

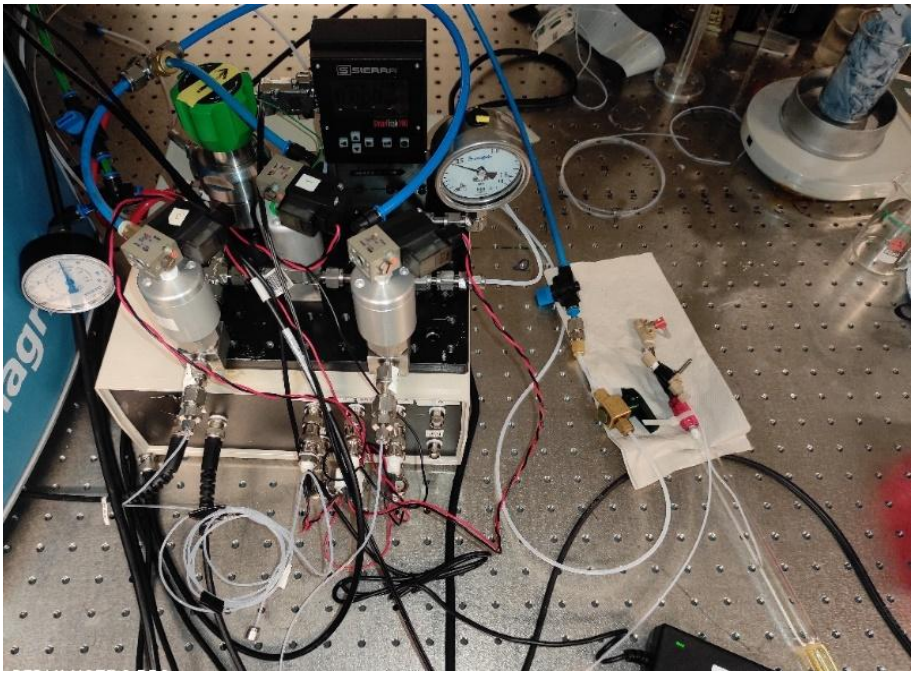

Figure 4.8 - Picture of the p-H_2 filling setup for the polarization cell.

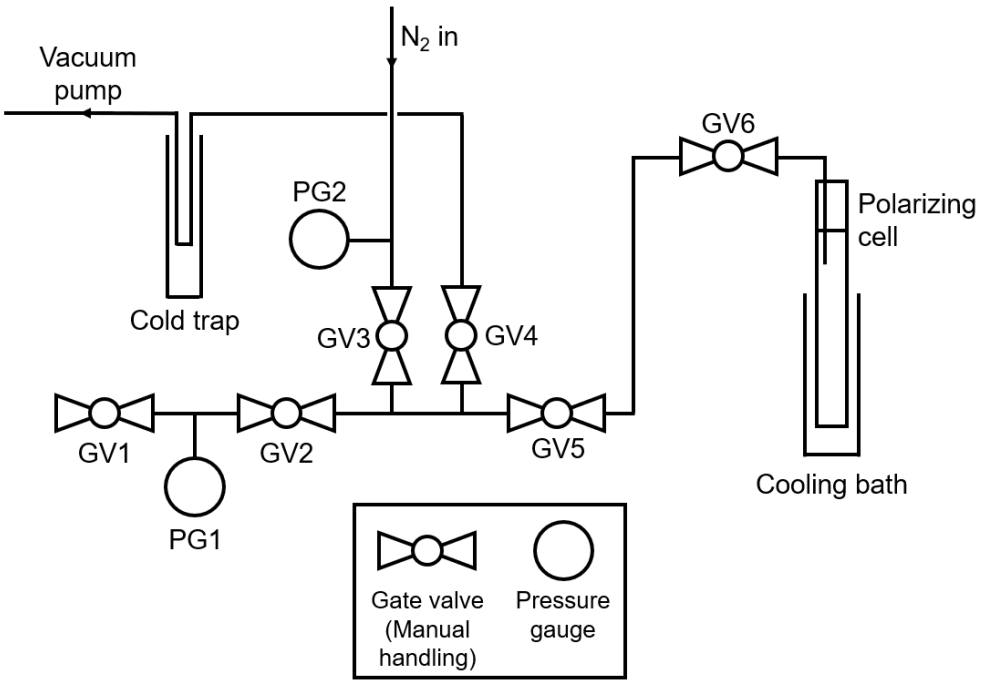

Figure 4.9 - P&ID for the polarization cell degassing apparatus.

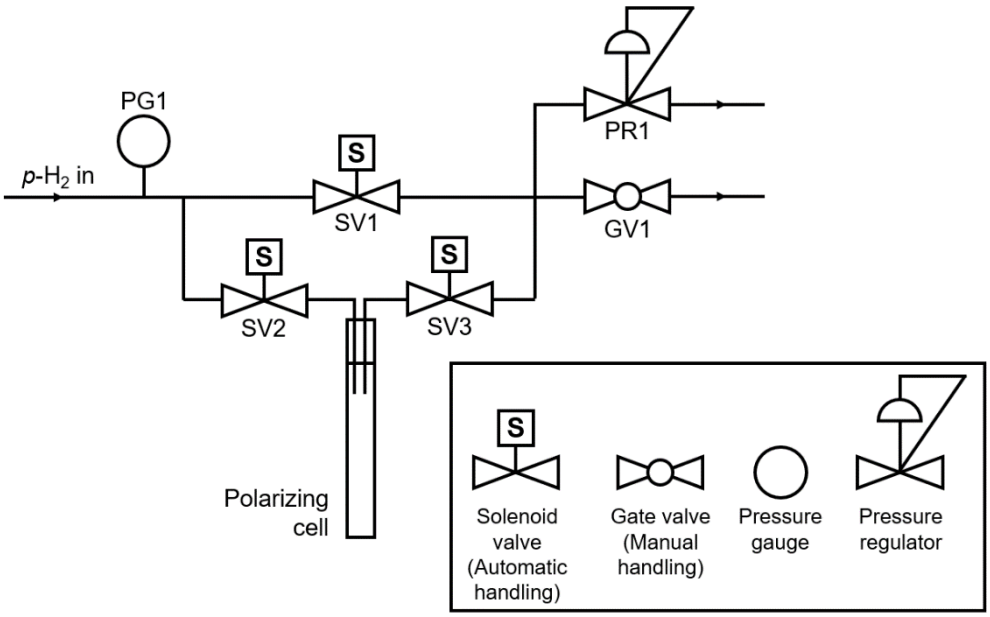

Figure 4.10 - P&ID for the p-H_2 filling setup for the polarization cell.

Measurement setup

The experimental setup used for the in-beam measurement of the polarization decay can be seen in Figure 4.11 and Figure 4.12. As is shown, the MRI was positioned on its side with the axis of the bore parallel to the beamline, such that the internal 15 mm bore was precisely aligned with the centre of the photon beam. A lead collimator (not shown) with 3 mm internal diameter and 200 mm length, located upstream of the MRI, was used in order to control the cross-sectional size of the beam. The hollow bore of the MRI allowed the photon beam to impact directly onto the bottom face of the polarization cell.

The polarization cell itself can be seen in Figure 4.4. The cell was custom-made and consisted of 15 mm heavy-walled borosilicate glass tubing, separated into two regions by a semicircular insert made from fritted glass. The cell was sealed at the top using two Idex™ shut-off valves which allowed for connection to the degassing and *p*-H_2 filling apparatuses. The fritted glass insert (not liquid permeable) seen in this cell allows for the mixing of the two regions of the cell (containing the sample volume and *p*-H_2 headspace) upon vigorous shaking, which is necessary for the 'Shake and drop' polarization approach that was used. At the end of the polarization step the cell could be tilted vertically to allow the sample volume to flow into the lower region of the cell. At this point the cell could be tilted horizontally with the sample volume remaining in the lower region of the cell, held there by the surface tension of the fluid. This design was necessary in order to ensure homogeneity within the sensitive region of the MRI probe.

Figure 4.11 - Close-up of the SABRE sample in the benchtop MRI.

Figure 4.12 - MRI positioning next to the beamline.

4.4In-beam polarization test

This section will start with calculations of the dose received by the samples from the A2 photon beam. This will be followed by the results of the measurements quantifying the in-beam polarization decay rate of SABRE-polarized material for three SABRE substrates: 3,5-dichloropyridine (**3,5-dcpy**), 3,5-dibromopyridine (**3,5-dbpy**), and 2,6-dichloropyrazine (**2,6-dcpz**). The section will conclude with a discussion of these results.

4.4.1 Sample dose

In this experiment, the collimator effectively filters out lower-energy Bremsstrahlung photons which exhibit a larger scattering angle. Consequently, the photon beam exiting the collimator predominantly consists of photons with energies exceeding 10 MeV. At these energies, electron-positron pair production is the dominant energy loss mechanism [125]. These electrons and positrons are then free to dissipate energy further through Bremsstrahlung radiation, in a repeating process called an electromagnetic cascade.

The total photon flux for ≥10 MeV photons at a beam current of 10 nA was found to be 4.2 x 10^8 Hz. This was found by extrapolating data from the Glasgow-Mainz tagger (over the range 40-855 MeV) using the 1/E dependence of Bremsstrahlung photons[ix]. These photon flux measurements were then combined with the average energy deposition per photon, found for varying photon energies using a Geant4 simulation of the target material[x]. This gave a total rate of energy deposition of 6.4 x 10^{-4} J s^{-1}.

Depolarization was expected to occur primarily through radiolysis, the generation of free radicals by ionizing radiation. Radiolysis of the substrate molecule directly would be expected to destroy the polarization, whereas more generally the presence of radicals in solution has the effect of decreasing the T_1 due to the high magnetic moment of the electron [37].

Assuming a uniform energy deposition across the sample, the calculated rate of beam heating was only 5 mK min^{-1}. Some areas of the sample will have experienced a higher local rate of heating, however it is expected that due to convection within the sample and losses to the surrounding environment that no significant temperature gradients would form. Thus, the temperature changes due to beam heating were significantly less than those required to produce a measurable effect on the T_1, as shown by the temperature dependence study in Section 3.2, and can therefore be safely ignored as an influencing factor.

[ix] Photon flux measurements were conducted by Mamad Eslami during this experiment.
[x] Geant4 simulation results were performed by Dr Mikhail Bashkanov.

Table 4.1 - Photon flux, energy deposition, and beam heating for samples within the A2 photon beam.

Sample dose	
Photon flux	4.2×10^{8} Hz
Energy deposition rate	6.4×10^{-4} J s^{-1}
Beam heating	5×10^{-3} mK min^{-1}

4.4.2 Polarization decay profiles

The normalized polarization decay profiles and fitted T_1s for all runs for all substrates in the A2 photon beam are shown in Figure 4.13 and Table 4.3-Table 4.5. As can be seen in Figure 4.13, there is no visible deviation between the beam-on runs and the control runs after the beam is applied, showing that there is no pronounced change to the relaxation rate in the presence of the beam. A quantitative analysis of the polarization decay rates will be presented next.

It can be seen in the logarithmic plots of the polarization decay profiles in Figure 8.3 that small discontinuities in the decay profile are sometimes observed with a change in tip angle in the measurement sequence. An explanation for this will be proposed in Section 4.4.5.

The data for the decay profiles has been cut short for each substrate to the point at which it was deemed that the signal to noise ratio (SNR) had dropped below an acceptable threshold. The sequence of tip angles used and the measurement times used for the decay profiles of each substrate can be seen in Table 4.2.

Table 4.2 - Tip angle sequence, inter-scan delay, and measurement times for each substrate.

Substrate	Tip angle sequence[xi]	Inter-scan delay (s)	Total measurement time	Cut measurement time
3,5-dcpy	15x 1°, 10x 5°, 25x 10°	25	20 min 25 s (50 scans)	12 min 55 s (32 scans)
3,5-dbpy	20x 2°, 30x 5°	15	12 min 15 s (50 scans)	6 min 30 s (27 scans)
2,6-dcpz	20x 2°, 50x 5°	15	17 min 15 s (70 scans)	9 min 45 s (40 scans)

For **3,5-dcpy** the average T_1s of the beam-on runs for the full decay, before the beam, and after the beam were 166.7 s, 165 s and 152 s, 2% lower, 3% lower and 3% lower than for the control run respectively. It should be noted here that run 1 had a lower than intended beam current of 5 nA,

[xi]Here the requested tip angles are shown, but the actual delivered tip angles may differ due to errors in the RF pulse length calibration. For each sample, this calibration error is expected to act as a constant multiplicative factor across all pulses. This deviation should not exceed ~10% of the requested angle.

as a 10 nA current was unable to be delivered for this run. For **3,5-dbpy** the average T_1s of the beam-on runs for the full decay, before the beam, and after the beam were 105.3 s, 107s and 100 s, 1% lower, 1% lower, and no change from the control run. For **2,6-dcpz** the average T_1s of the beam-on runs for the full decay, before the beam, and after the beam were 174 s, 162 s and 148 s, 2% lower, no change, and 1% lower than for the control run. Thus, for all three substrates, the average T_1s for the beam-on runs lie close to or within one standard deviation (SD) from the control run, showing no evidence for an increased decay rate.

*Table 4.3 - ^1H T_1s for **3,5-dcpy**, for the full decay, the decay before the beam is turned on, and the decay after the beam is turned on.*

Run	Time of beam (s)	^{1}H T_1 (s)		
		Full	Before	After
Control	280[xii]	169.9 ± 0.8	170 ± 2	156 ± 4
Run 1 (5 nA)	280	165.3 ± 0.7	161 ± 2	153 ± 2
Run 2 (10 nA)	280	168.1 ± 0.9	168 ± 3	150 ± 8
Beam-on Avg	280	166.7 ± 0.6	165 ± 2	152 ± 4

*Table 4.4 - ^1H T_1s for **3,5-dbpy**, for the full decay, the decay before the beam is turned on, and the decay after the beam is turned on.*

Run	Time of beam(s)	^{1}H T_1 (s)		
		Full	Before	After
Control	220[xii]	105.3 ± 0.8	107 ± 2	100 ± 20
Run 1 (10 nA)	290	106.2 ± 0.5	106.5 ± 0.8	90 ± 30
Run 2 (10 nA)	280	105.6 ± 0.7	106 ± 1	-
Run 3 (10 nA)	220	102 ± 1	104 ± 3	100 ± 10
Beam-on Avg	260	104.6 ± 0.4	106 ± 1	100 ± 20[xiii]

*Table 4.5 - ^1H T_1s for **2,6-dcpz**, for the full decay, the decay before the beam is turned on, and the decay after the beam is turned on.*

Run	Time of beam (s)	^{1}H T_1 (s)		
		Full	Before	After
Control	220[xii]	174 ±1	162 ± 2	148 ± 1
Run 1 (10 nA)	225	166.4 ± 0.9	161 ± 1	143.2 ± 0.9
Run 2 (10 nA)	215	176 ± 1	163 ± 2	150 ± 2
Beam-on Avg	220	171.2 ± 0.7	162 ± 1	147 ± 1

[xii] Control runs had no beam applied. 'Before' and 'after' values correspond to the time of beam for beam-on runs. The time of beam used for the control runs is noted.
[xiii] Average found from runs 1 and 3. The T_1 after the beam could not be found for run 2 due to a low SNR.

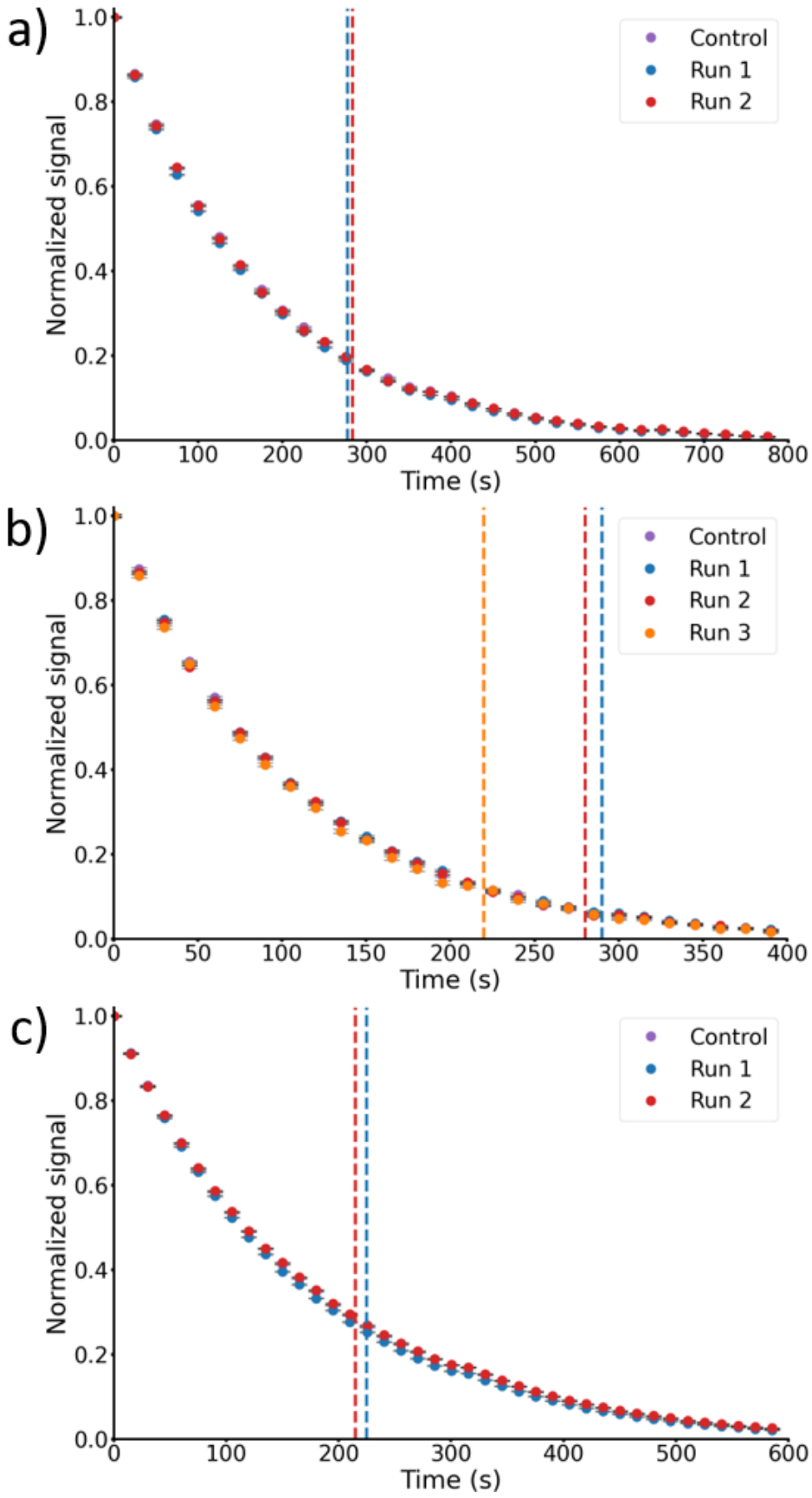

Figure 4.13 - Normalized polarization decay profiles for a) 3,5-dcpy. b) 3,5-dbpy. c) 2,6-dcpz. The dotted lines indicate the time of beam. Error bars are present for all points but may not always be visible.

4.4.3 Ratio of runs

To better display the deviation of the beam-on runs from the control runs, the ratio of the normalized decay profiles for the beam-on to the control runs was calculated. The results are presented in Table 4.6 and Figure 4.14.

At the time the beam was turned on, the average beam-on to control ratios for the normalized decay profiles were 0.98 ± 0.03 for **3,5-dcpy**, 1.04 ± 0.04 for **3,5-dbpy**, and 0.98 ± 0.05 for **2,6-dcpz**, all of which are statistically indistinguishable from unity.

At the end of the runs, the average ratios were 1.00 ± 0.19 for **3,5-dcpy**, 0.92 ± 0.17 for **3,5-dbpy**, and 0.99 ± 0.13 for **2,6-dcpz**, again showing no significant deviation from unity. These results indicate changes of +2%, -12%, and +1% from the time of beam to the end of runs for the three substrates respectively, demonstrating no systematic variation.

Given the absence of a systematic effect in the decay profile ratios, it was decided to undertake a statistical analysis of the instantaneous decay rates of the in-beam samples, presented in Section 4.4.4.

Table 4.6 - Ratio of the beam-on runs to the control runs for all investigated substrates.

Substrate	**Ratio of beam-on runs to control run**							
	Beam turned on				**End of run**			
	Run 1	Run 2	Run 3	Avg	Run 1	Run 2	Run 3	Avg
3,5-dcpy	0.96	1.00	-	0.98 ± 0.03	0.86	1.13	-	1.00 ± 0.19
3,5-dbpy	1.09	1.04	0.99	1.04 ± 0.04	1.10	0.88	0.77	0.92 ± 0.17
2,6-dcpz	0.94	1.01	-	0.98 ± 0.05	0.89	1.08	-	0.99 ± 0.13

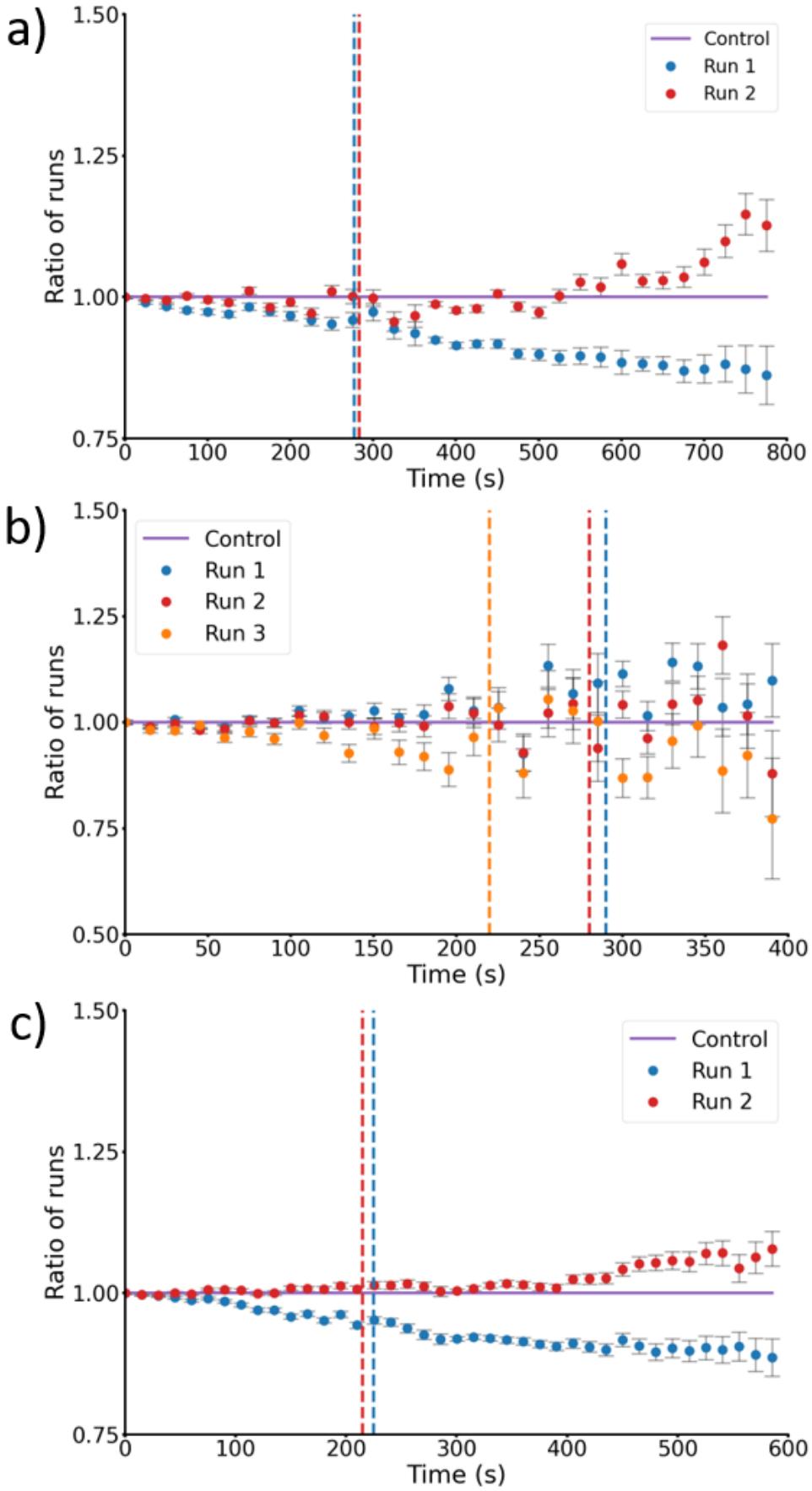

Figure 4.14 - Ratio of the normalized polarization decay profiles for the beam-on runs to the control runs for a) ***3,5-dcpy.*** *b)* ***3,5-dbpy****. c)* ***2,6-dcpz****. The dotted lines indicate the time of beam.*

4.4.4 Ratio of log differentials

To statistically assess whether the rate of decay of each sample changed in the presence of the beam, the instantaneous decay rates were compared between the beam-on and control runs.

For this, a logarithmic transform was applied to the normalized decay profiles, $y_2(t) = \ln(y_1(t))$, where $y_1(t)$ is the normalized decay profile, which linearizes the exponential decay. The gradient of $y_2(t)$ is directly proportional to the decay rate of the polarization.

The discrete gradients between consecutive data points were calculated as:

$$\left(\frac{\Delta y_2(t)}{\Delta t}\right)_n = \frac{y_2(t_{n+1}) - y_2(t_n)}{t_{n+1} - t_n} \qquad (Eq. 4.3)$$

where t is the time elapsed since the start of the decay measurement, and n is the scan number. For the beam-on and control runs, these gradients were defined as:

$$G_{n,beam-on} = \left(\frac{\Delta y_2(t)}{\Delta t}\right)_{n,beam-on} \qquad (Eq. 4.4)$$

$$G_{n,control} = \left(\frac{\Delta y_2(t)}{\Delta t}\right)_{n,control}. \qquad (Eq. 4.5)$$

The relative change in the decay rate in the beam was quantified by the ratio:

$$R_n = \frac{G_{n,beam-on}}{G_{n,control}}. \qquad (Eq. 46)$$

A value of $R_n = 2$ indicates that the polarization of the beam-on sample has decayed twice as fast over that time interval, whilst $R_n = 0.5$ would indicate a decay rate half as fast.

The quantities G_n and R_n will be referred to as the log differentials, and the ratio of log differentials respectively. The ratios R_n were calculated for each beam-on run across all substrates and are shown in Figure 4.15. The average of the ratios R_n, $\overline{\mathbf{R}}_\mathbf{n}$, for before and after the beam for each substrate are presented in Table 4.7-Table 4.9.

Results

For **3,5-dcpy**, the average value of $\overline{\mathbf{R}}_\mathbf{n}$ for the beam-on runs was 1.01 ± 0.07 before the beam and 1.01 ± 0.10 after the beam, representing no change in value with both lying within error of unity. This can be interpreted as the rate of decay of the polarization of **3,5-dcpy** in the photon beam being ≤11% higher than that of the control run to a confidence level of 1σ, and ≤21% higher to a confidence level of 2σ.

For **3,5-dbpy**, the average value of $\overline{\mathbf{R}}_{\mathbf{n}}$ for the beam-on runs was 1.0 ± 0.1 before the beam and 1.3 ± 0.7 after the beam, representing a 30% increase and a significant widening of the standard deviation. Here it is deemed that the error is too large to pose sensible limits on the rate of relaxation, for which the reason will be discussed later.

For **2,6-dcpz**, the average value of $\overline{\mathbf{R}}_{\mathbf{n}}$ for the beam-on runs was 1.02 ± 0.04 before the beam and 1.00 ± 0.07 after the beam, representing a 2% decrease with both values lying within error of unity. Thus, it is found that the rate of decay of the polarization of **2,6-dcpz** in the photon beam is ≤7% higher than that of the control run to a confidence level of 1σ, and ≤14% higher to a confidence level of 2σ - the strictest confidence level out of the tested substrates.

*Table 4.7 - Average ratio of log differentials, $\overline{R}_n$, for **3,5-dcpy** for before and after the beam was turned on.*

Run	$\overline{R}_{n,before}$	$\overline{R}_{n,after}$
Run 1 (5 nA)	1.02 ± 0.05	1.04 ± 0.07
Run 2 (10 nA)	1.00 ± 0.12	1.01 ± 0.10
Beam-on Avg	1.01 ± 0.07	1.01 ± 0.10

*Table 4.8 - Average ratio of log differentials, $\overline{R}_n$, for **3,5-dbpy** for before and after the beam was turned on.*

Run	$\overline{R}_{n,before}$	$\overline{R}_{n,after}$
Run 1 (10 nA)	1.0 ± 0.1	1.3 ± 0.9
Run 2 (10 nA)	1.01 ± 0.08	1.4 ± 1.1
Run 3 (10 nA)	1.1 ± 0.2	1.2 ± 0.9
Beam-on Avg	1.0 ± 0.1	1.3 ± 0.7

*Table 4.9 - Average ratio of log differentials, $\overline{R}_n$, for **2,6-dcpz** for before and after the beam was turned on.*

Run	$\overline{R}_{n,before}$	$\overline{R}_{n,after}$
Run 1 (10 nA)	1.04 ± 0.06	1.03 ± 0.09
Run 2 (10 nA)	0.99 ± 0.05	0.98 ± 0.09
Beam-on Avg	1.02 ± 0.04	1.00 ± 0.07

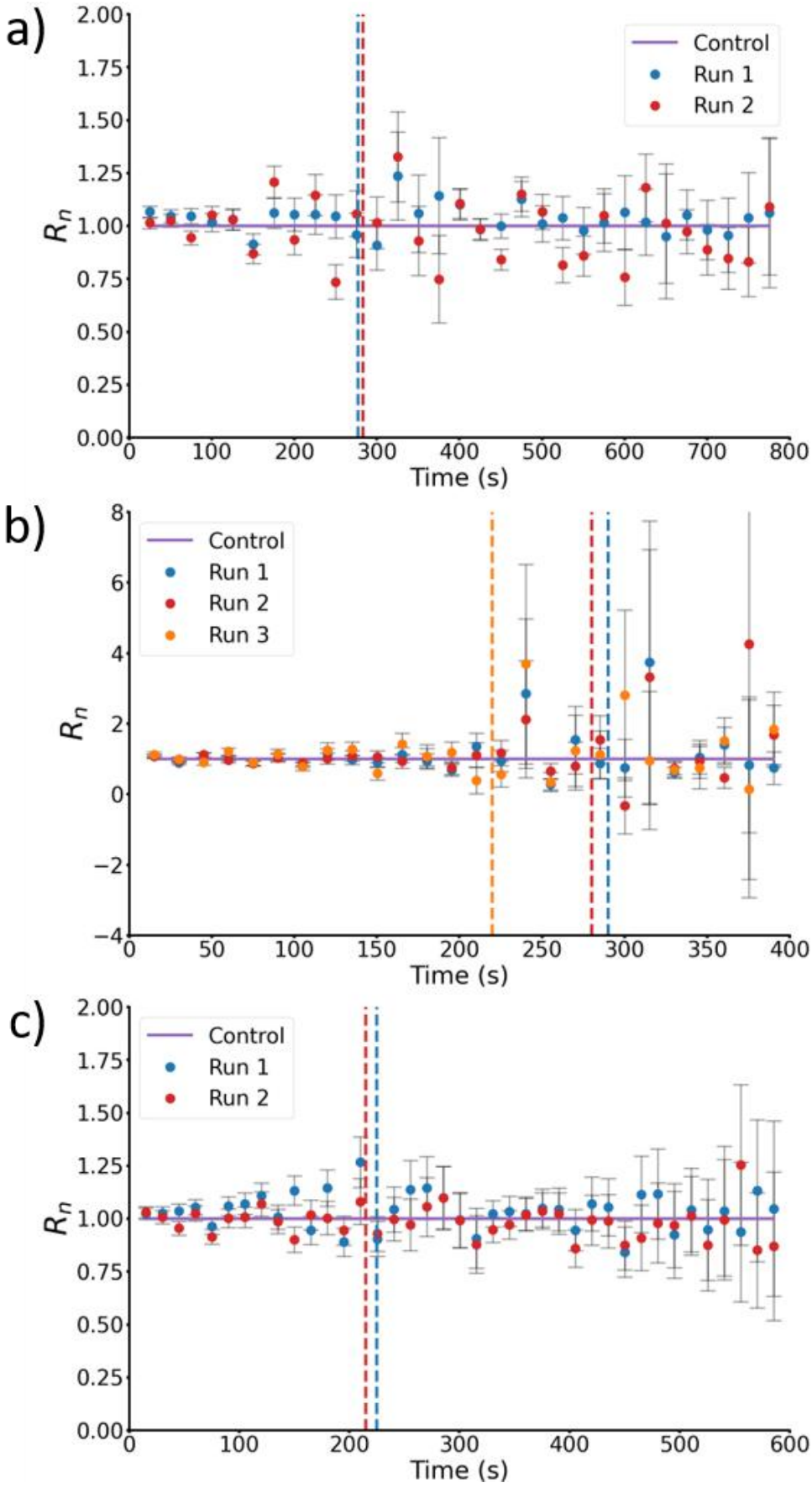

Figure 4.15 - Ratios of log differentials, R_n, for a) ***3,5-dcpy****. b)* ***3,5-dbpy****. c)* ***2,6-dcpz****. The dotted lines indicate the time of beam.*

4.4.5 Discussion

It has been found in this experiment that there is no evidence for an increased rate of depolarization for samples subject to the A2 photon beam. This was found for all three methods of analysis, the decay rate fittings, the ratio of beam-on to control runs, and the analysis of point-to-point decay rates using the ratios of log differentials. The strictest limits on the changes to the rate of decay were found for the substrates **3,5-dcpy** and **2,6-dcpz**, finding that the decay rates in the A2 photon beam increased by ≤11% and ≤7% respectively, to a confidence level of 1σ.

As illustrated by Figure 4.15, the behaviour of R_n for **3,5-dbpy** becomes erratic in the latter region of the decay, after around 220 s, where R_n fluctuates between 0 and 5. In contrast, R_n remains more stable for the substrates **3,5-dcpy** and **2,6-dcpz**, varying within the ranges 0.7-1.4 and 0.8-1.3 respectively. This behaviour is illustrative of the low SNR for the **3,5-dbpy** sample in the latter stages of the decay, seen for this substrate because of the reduced polarization levels and shorter T_1 relative to **3,5-dcpy** and **2,6-dcpz**. Due to the low statistical precision of measurements after the beam for **3,5-dbpy**, strict limits on the in-beam changes to the decay rate cannot be set, however once again there is no evidence for beam-induced depolarization.

Decay profile discontinuities

It can be observed in Figure 4.13 and Figure 8.3, that for all substrates the polarization decay profile is not a smooth exponential decrease as expected, and contains small discontinuities. These occur with a change in the tip angle in the measurement sequence, and are observed for both the beam-on runs and the control runs, thus can be ruled out as being a beam induced effect.

The proposed explanation for this effect is a calibration error in the length of the RF pulse necessary to produce a specified tip angle in the sample. During the degassing procedure there was some loss of sample volume which led to the sample volume dropping below that needed to completely fill the lower portion of the cell. If the sample volume within the detector coil of the MRI is less than what was calibrated for, the tip angle produced by the RF pulse would be larger than specified. This would explain why the calculated T_1s for both the beam-on and control runs were slightly lower for the latter stages, as more of the Z-magnetization was being used up than had been calibrated for.

4.5 High dose sample irradiation

This section will present measurements on the effects of a high radiation dose to a SABRE sample, achieved through proximity to the intense electron beam at MAMI. These measurements will help to inform whether a SABRE-polarized target is able to operate at the frontiers of intensity for electron scattering experiments, potentially becoming the only technology allowing for 4π acceptance to be able to operate with electron beam currents of ≥1 nA - where DNP frozen-spin targets fail. This section will present measurements on the polarization level and T_1 before and after the high dose, assessing the results for information on the radiation damage to the sample.

4.5.1 Sample dose

The sample chosen to be irradiated in this study was a replicate of the **3,5-dcpy** SABRE sample used for the in-beam tests. As is shown in Figure 4.6, the sample was positioned against the electron beam dump in the A2 hall. The sample was positioned vertically, with the liquid volume occupying a height of 5 cm and a diameter of approximately 1.1 cm, with a volume of 5 mL. The calculated electron flux through this position was 20 MHz, and the dose estimates will be made for an estimated running time of 80% over 4 days, equal to 2.8 x 10^5 s of beam-on time. Calculating the total electron flux:

$$(2 \times 10^7\ Hz) \times (2.8 \times 10^5\ s) = Total\ electron\ flux\ of\ 5.5 \times 10^{12}.$$

$$= 15\ minutes\ at\ 1\ nA\ beam\ current. \qquad (Eq.\ 4.7)$$

It is found that the total electron flux received is equivalent to that received from 15 minutes of irradiation at an electron beam current of 1 nA.

Calculating the total dose received by the sample using an average energy deposition of 23.6 MeV, found by Geant4 simulation[xiv]:

$$(5.5 \times 10^{12}\ particles) \times (23.6\ MeV\ particle^{-1}) = Total\ dose\ of\ 20.9\ J.$$

$$20.9\ J\ /6.8 \times 10^{-3}\ kg = 3.1 \times 10^3\ Gy. \qquad (Eq.\ 4.8)$$

The value for the energy deposition found from the Geant4 simulation of $23.6\ MeV\ particle^{-1}$ lies between the collisional losses of $4.1\ MeV\ particle^{-1}$ and the total collisional and radiative losses of $38.8\ MeV\ particle^{-1}$ (both calculated by hand), and is thus verified as a sensible estimate.

It is found that over the 4 days of irradiation the total dose was 3.1 kGy. Here it is assumed that the sample is irradiated uniformly, since over the long irradiation period molecular diffusion and convective mixing are expected to distribute the dose evenly.

[xiv] Geant4 simulation results were performed by Dr Mikhail Bashkanov.

4.5.2 Results

Figure 4.16-Figure 4.17 and Table 4.10-Table 4.11 present the results of this experiment. Figure 4.16 indicates a slightly decreased decay rate in the normalized decay profile following irradiation, visible for the first 400 s, after which point the SNR becomes poor in both runs. This observation is borne out by the fitted T_1values: 125 ± 3 s before and 139 ± 7 s after irradiation respectively - 11 ± 6% higher after irradiation, on the verge of statistical significance. Consistently Figure 4.17 shows the ratio of the post- to pre-irradiation decay profiles reaching a maximum value of 1.24 at 375 s, however the SNR became poor after this point. This is due to the polarization decaying to a point where the intensity of the measured signals did not significantly exceed the signal noise, illustrated by the increasing size of the error bars in Figure 4.17.

The relative polarization after irradiation was found to be 17% lower than before. Absolute polarization levels could not be measured due to insufficient MRI sensitivity and resolution to acquire a thermal spectrum. Repeats to find the statistical significance of this measurement were also not possible due to time constraints.

A control measurement, run upon return to York, is shown in Table 4.11. Here a sample of identical composition was prepared, and its polarization and T_1 were measured before and after a 4-day period, replicating the duration of the MAMI experiment. This control was designed to exclude the effects of sample aging from the results found at MAMI.

In this experiment it was found that the T_1 was 153 ± 2 before and 153 ± 4 after the 4-day duration, representing no change. Additionally, the relative polarization after four days was 0.99 ± 0.06. Here the T_1 values were found to be longer than that at MAMI, attributed to a more thorough degassing procedure being possible in York. These results found no evidence for effects on the polarization level or T_1 after 4 days, however, cannot rule out small changes.

A possible reason for the observed changes in the T_1 and polarization for the irradiated sample at MAMI is the deactivation of the catalyst through radiolysis. A lower concentration of active catalyst in solution would be expected to produce lower polarization levels in the sample, alongside increasing the substrate T_1. Both effects would occur due to the resulting increase in substrate excess, causing lower catalytic productivity for polarization transfer, as well as a reduced rate of relaxation experienced by the substrate molecules through catalyst interactions. As the results from MAMI do not exhibit statistical significance, no definitive conclusions on catalyst deactivation can be made.

In order to accurately quantify the effects of radiation damage on a SABRE sample, further experiments will be needed in future. This experiment, however, provides a first test of the

radiation resistance of a SABRE sample, showing that significant repolarization of the sample is possible, with no decrease to the T_1, after a high radiation dose has been received.

*Table 4.10 - T_1s and relative polarization values for the irradiated sample of **3,5-dcpy**.*

Sample	^{1}H T_1 (s)	Relative polarization
Before irradiation	125 ± 3	1
After irradiation	139 ± 7	0.83

*Table 4.11 - T_1s and relative polarization values for a control sample of **3,5-dcpy** left to age for four days, conducted back at York.*

Sample	^{1}H T_1 (s)	Relative polarization
Before	153 ± 2	1
After	153 ± 4	0.99 ± 0.06

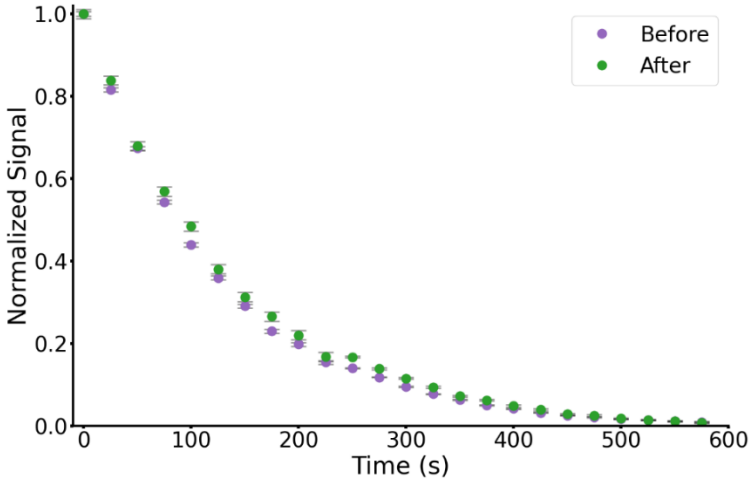

Figure 4.16 - Normalized signal decay for the sample before and after irradiation.

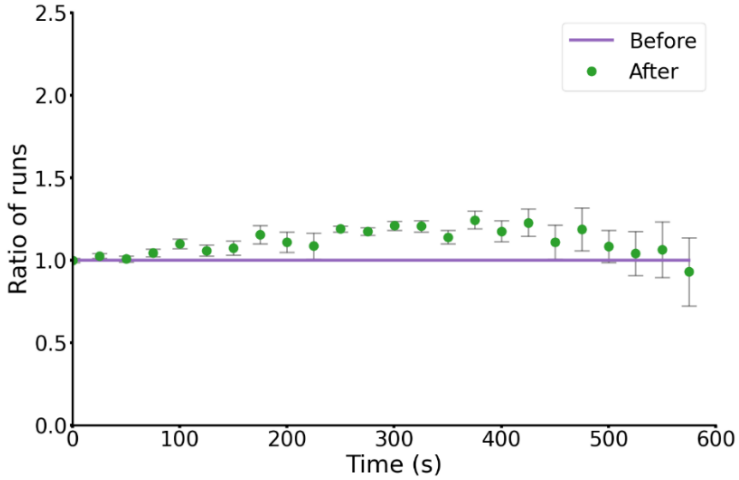

Figure 4.17 - Ratio of normalized decay profiles for the sample before and after irradiation.

4.6 Experiment implications

4.6.1 Polarized targets for photon beams

The results from the in-beam tests show that the T_1 of SABRE-polarized material will not be significantly affected by a photon beam of a similar intensity, and thus SABRE-polarized material would be well suited in this manner for use as a polarized target with photon beams. The in-beam T_1s of **3,5-dcpy** and **2,6-dcpz** have been measured to be >150 s, however as no evidence for beam-induced depolarization was observed it is thought that this could be improved upon with an alternative sample composition. A T_1 of this length would be long enough for the build-up of significant levels of polarization in the sample, and is twice as long as that of a continuously polarized SABRE sample achieving >20% polarization that will be presented in Chapter 5.

A current experiment that operates using an intense photon beam is the GlueX experiment at Jefferson Lab Hall D [127]. Here typical running conditions are a 9 GeV electron beam (optimal for linear polarization [128]), with a beam current of 150 nA, incident on a 60 μm ($5 \times 10^{-4}\ X_0$) diamond radiator [129]. The Møller radiator used at A2 has a thickness of 10 μm, equal to $6 \times 10^{-4}\ X_0$, and thus it is expected that the photon flux at GlueX under typical conditions would be around ten times higher than was found for this experiment at MAMI. Further experiments are needed in order to show that SABRE can operate in photon beams of this intensity, however the results here show promise.

There is currently demand for a polarized target at Hall D in order to measure the high-energy contribution to the GDH sum rule [130,131], however the cost has proved prohibitive. SABRE-polarized targets may prove an attractive low-cost alternative to traditional DNP polarized targets for such situations.

4.6.2 Polarized targets for electron beams

In this experiment it has been shown that SABRE material retains a high level of polarizability and no reduction to the T_1 after a dose equivalent to 15 minutes at 1 nA for an electron beam.

As SABRE polarization is built up over timescales of tens of seconds to minutes in the solution state, it is possible for the complete replacement of SABRE material in a potential target within a few minutes, without significant detriment to the polarization levels. This gives SABRE a large advantage in terms of the rate of radiation damage it can withstand relative to DNP, for which targets need to last days at a minimum in order to reduce running time losses due to target replacements.

As SABRE material can be quickly replaced within a polarized target, the results obtained at MAMI suggest a conservative lower estimate for the operable beam currents in an electron scattering experiment without significant polarization losses of around 5 nA. This is comparable to the 8 nA beam currents achievable with the most radiation resistant class of current-generation DNP targets, continuously polarized NH_3 targets [34,35].

Here it is assumed that only the total absorbed dose is relevant. Although the MAMI sample received its dose over a much longer timescale than would occur with a continuous direct electron beam, this distinction is unimportant for a SABRE target. Unlike DNP targets, which are operated at cryogenic temperatures and can accumulate long-lived radiation-induced radicals, SABRE targets operate at room temperature where radicals are short-lived and do not build up.

SABRE further benefits from low temperature sensitivity, so beam heating effects are expected to be minimal. As shown in Section 3.2, near the optimum temperature the T_1 of **3,5-dcpy** is reduced by at most 7% per °C of warming. Thus, with respect to radiation damage, the main concern is the destruction of the SABRE catalyst and substrate through radiolysis, both of which are determined by the total dose rather than the irradiation timescale.

Beam-induced radiation damage is an issue for traditional polarized targets (DNP or brute force) due to the loss in running time from the replacement and repolarization of the target material. Brute force targets such as HDice take months to build up polarization [20], whereas DNP NH_3 targets take hours to polarize, not including the hours/days taken for the pre-irradiation of the sample, and annealing the sample once radiation damage has occurred [34].

In contrast, SABRE samples can be prepared simply and can be activated in 1-3 hours, prior to polarization. The polarization can be built up within minutes, and the samples can be continually replenished to avoid radiation damage, without need for experiment downtime. Additionally, the polarizing field needed for SABRE is around 6 mT for ^{1}H polarization, for which the full T_1 can be maintained in fields <1 T, as shown in Section 3.3. The lack of superconducting magnets needed shows that 4π angular acceptance is achievable. These advantages of SABRE relative to traditional polarized target technologies show why this technique is very promising for polarized target applications.

4.7 Future work

This experiment has shown that it is readily achievable to measure the in-beam decay of SABRE-polarized material and has placed an upper bound on the rate of beam-induced depolarization of this material in the A2 photon beam at MAMI. In addition to this, the polarization levels and T_1 of SABRE material have been found to be minimally affected by an electron beam radiation dose equivalent to 15 minutes at 1 nA.

It is proposed that future experiments could be performed to improve upon the results utilizing the A2 photon beam by increasing the statistical precision of the measurements and by making measurements at a facility capable of a higher photon beam intensity. The statistical precision of these results was limited by the equipment sensitivity, which could be improved upon with the use of a dedicated benchtop NMR spectrometer for polarization measurements of the sample.

Additionally, a future experiment that should be performed is an investigation of the effects of a higher dose from an electron beam than was possible in this experiment. Ideally, a SABRE-polarized target would be able to operate for hours within a ≥1 nA electron beam before significant radiation damage of the target material occurred. This would involve a total dose over 10 times higher than was possible to deliver in this experiment.

These tests should be performed with a continuously polarizing cell, such as that presented in Chapter 5. This would allow for investigation into the effects of a photon or electron beam on the achievable steady-state polarization of the SABRE target material. This will pose some challenges in the experimental design, as the facilities where these experiments would be possible use evacuated beamlines, unlike at A2.

4.8 Chapter 4 Conclusions

In this chapter, the results of an experiment representing the first in-beam measurements of depolarization effects on SABRE-polarized material have been presented. These measurements were made for the SABRE substrates **3,5-dcpy**, **3,5-dbpy**, and **2,6-dcpz** and were achieved at the A2 facility at MAMI with the use of a portable benchtop MRI positioned in line with the photon beam. Additionally, measurements were made of the effects of a high radiation dose, attained in proximity to the MAMI electron beam, on the polarization levels and relaxation rate of a SABRE sample.

These results place an upper limit on the influence on the decay rate of SABRE-polarized material due to exposure to a gamma particle beam with the aforementioned properties. The strongest constraints can be obtained from the data of the substrates **3,5-dcpy** and **2,6-dcpz** - in which the SNR for the period after the beam was operational remained strong. Weaker limits are imposed for the substrate **3,5-dbpy** for which the SNR at later times was poorer. The general trend found, using a method based on the ratios of the log differentials, R_n, is that there is no evidence to support an increased rate of polarization decay with the photon beam incident on the sample for any of the substrates. Consequently, there is also no evidence to show any substrate dependence of the effects of beam-induced depolarization.

The results from this experiment show that the T_1 of SABRE-polarized material will not be significantly affected by a photon beam of a similar intensity. The in-beam T_1 was found to be >150s for the substrates **3,5-dcpy** and **2,6-dcpz**, well in excess of that needed to achieve high levels of polarization using SABRE, where polarization levels of >20% have been achieved with a T_1 of 70 s using a continuously polarizing cell (see Chapter 5). Current experiments with photon beams use intensities up to an order of magnitude higher than possible at MAMI [127], and thus further experiments are needed in order to show that SABRE can operate in photon beams of such intensity. The results here, however, show promise.

For the sample subject to a high radiation dose, positioned near the electron beam dump, a high level of polarizability (>80%) was retained, with no detriment to the T_1 being measured. This was after a dose equivalent to 15 minutes at 1 nA from the electron beam. Further experiments are needed to show whether the slightly decreased polarization is due to radiation damage of the sample, as repeat measurements were not possible and the polarization technique has inherent variability.

As SABRE material can potentially be replaced within minutes if necessary, combined with the lack of radiation damage seen with the high dose sample at MAMI a lower estimate for the operable

beam currents for a SABRE target in an electron scattering experiment is found to be 5 nA. This is similar to the highest beam currents usable with DNP polarized targets [34,35].

Although this work provides a first measurement of a SABRE cell in a particle beam - it is important for future work to extend the limits of heat and radiation deposition from particle beams. High intensity electron beams are a clear next step. There are challenges in achieving this as such beams, due to their strong ionization, are transported in evacuated beam pipes. Future work in York will explore the challenges in introducing polarised SABRE materials into vacuum.

Chapter 5 - Prototype SABRE-polarized target

5.1 Introduction

This chapter presents the development, operation, and performance of a prototype SABRE-polarized target, designed for continuous polarization with precise digital timing and flow rate control. It begins with a description of the target's design, followed by an overview of its operation. Initial results are then presented, examining the effects of the flow rate, substrate excess and increased pressure in the polarization cell. Finally, the performance of this prototype target is compared to the current generation of DNP targets, followed by the proposal of necessary improvements to adapt the prototype for use in particle physics experiments.

5.2 Design

The prototype target (Figure 5.1) achieves *p*-H_2 delivery in a different way to how has been described previously with the 'Shake and drop' method. Here, rather than a sealed cell which is filled with *p*-H_2 and then shaken to disperse *p*-H_2 in solution, this cell operates by bubbling *p*-H_2 continuously through the cell by means of a pressure differential. Similar 'bubbling cell' approaches to SABRE have been taken previously, such as by Sheberstov, Kircher, and Blanchard [132-134].

Figure 5.1 - Image of the prototype SABRE-polarized target, alongside benchtop MRI (used for polarization measurements), and Halbach array (used to provide the polarization transfer field).

5.2.1 *Para*hydrogen supply

The *para*hydrogen supply for the prototype target is produced using a custom-built *p*-H_2 generator (Figure 5.2), using a generation method that has been described previously [135]. It operates by passing H_2 gas from a cylinder over a paramagnetic iron (III) oxide catalyst at 28 K which facilitates the spin transfer process. The generator produces a constant supply of *p*-H_2 with a purity of >99% [45]. The outlet pressure of the *p*-H_2 generator can be altered by regulating the pressure of the inlet gas.

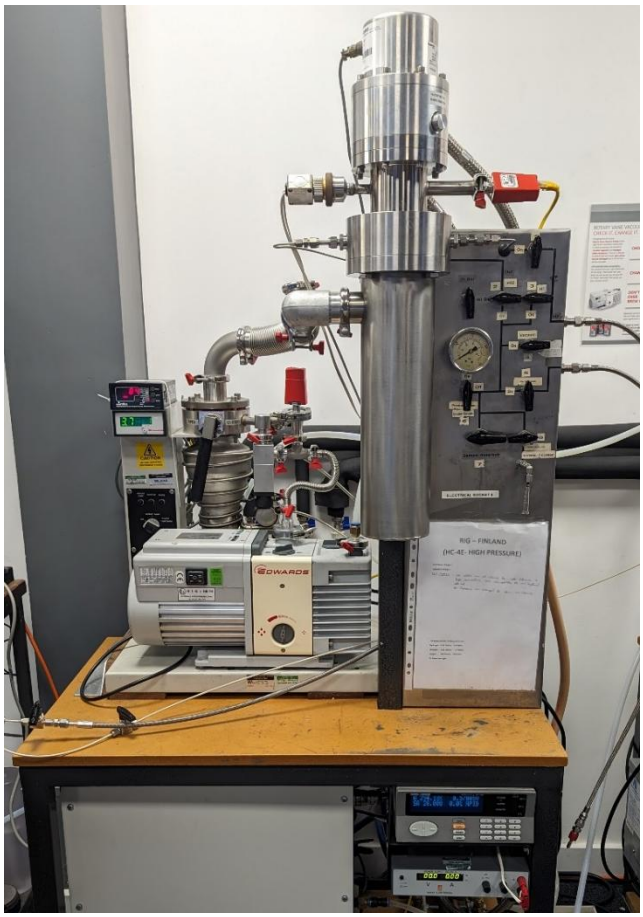

Figure 5.2 - Photo of custom-built parahydrogen generator, capable of producing >99% pure p-H_2 at temperatures of 28 K.

5.2.2 Prototype polarized target

The *p*-H_2 supply is fed into a mass flow controller, which enables precise regulation of the flow rate and is adjustable via computer control. Solenoid valves manage the timing of the *p*-H_2 flow. When the solenoid valves are open, a pressure differential is established across the polarization cell due to the difference between the inlet and back pressures, allowing *p*-H_2 to flow through the solution. Once the solenoid valves close, the pressure on either side of the polarization cell equalizes within <1 s, stopping the flow of *p*-H_2. A digital timer controls the solenoid valve operation, ensuring precise bubbling times.

The pressure differential across the polarization cell is controlled by adjusting the inlet *p*-H_2 pressure, monitored using a digital manometer, and the back pressure, monitored using an analogue pressure gauge. As can be seen in Figure 5.3, a bypass loop allows for gas flow through the system without passing through the polarization cell. This bypass is used for flushing residual oxygen from the lines before operation. During operation, the polarization cell is placed within a 6 mT Halbach array which provides the necessary polarization transfer field for ^{1}H polarization. The apparatus components are connected using a combination of 1/16" and 1/8" OD PEEK tubing, selected for its chemical resistance, with connections made via IDEX™ and Swagelok™ fittings. Further detail can be found in the P&ID schematic of the prototype target in Figure 5.4 and the equipment specifications in Section 7.1.3.

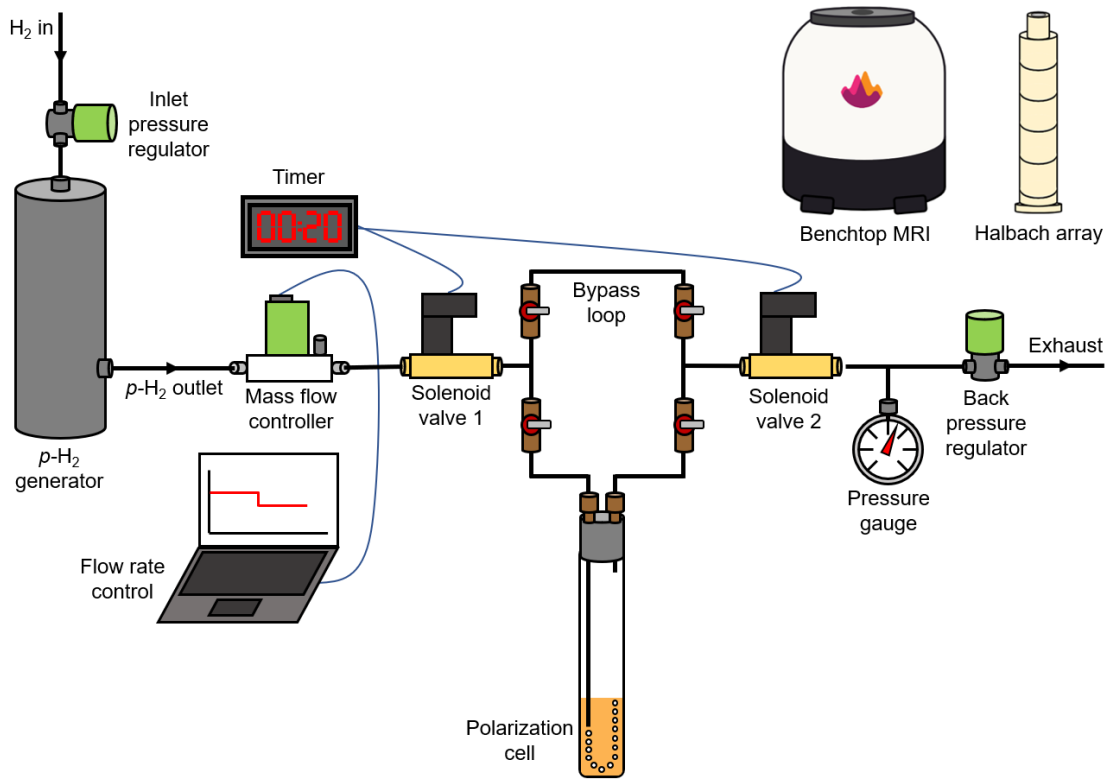

Figure 5.3 - Diagram of prototype target apparatus.

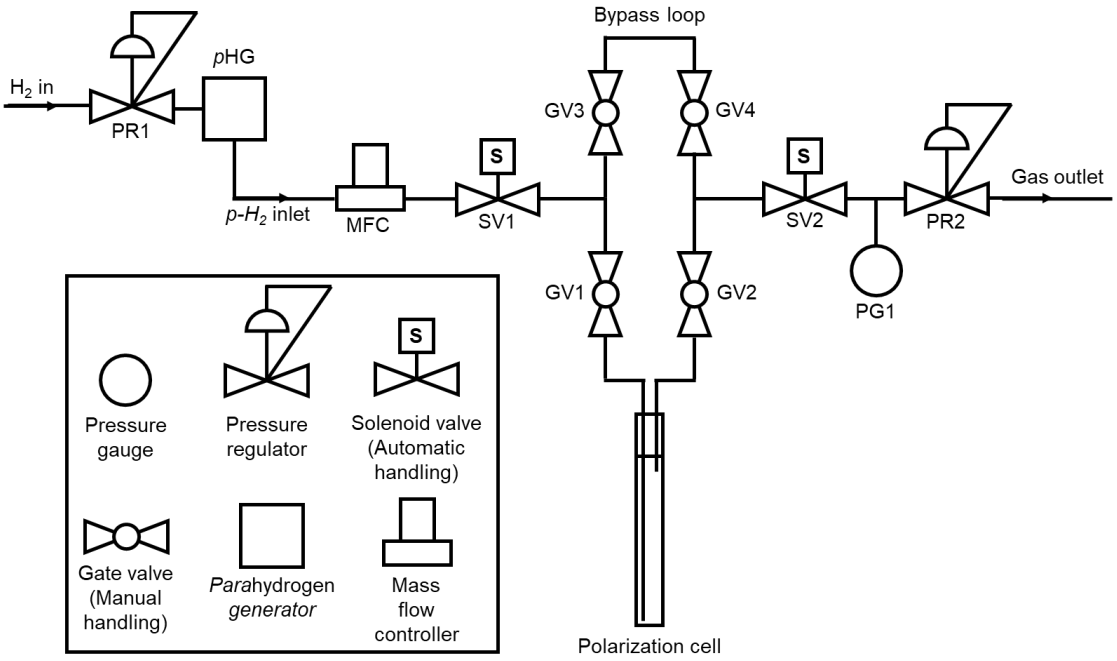

Figure 5.4 - P&ID of prototype target apparatus.

5.2.3 Polarization cell

The polarization cell, shown in Figure 5.5, is constructed from 10 mm OD heavy wall borosilicate glass tubing and is connected to the gas inlet and outlets via a custom-made fitting. *p*-H_2 is delivered into the solution through 1/16” OD PEEK tubing which extends close to the bottom of the cell. The cell can be isolated using IDEX™ shutoff valves positioned upstream and downstream of the cell.

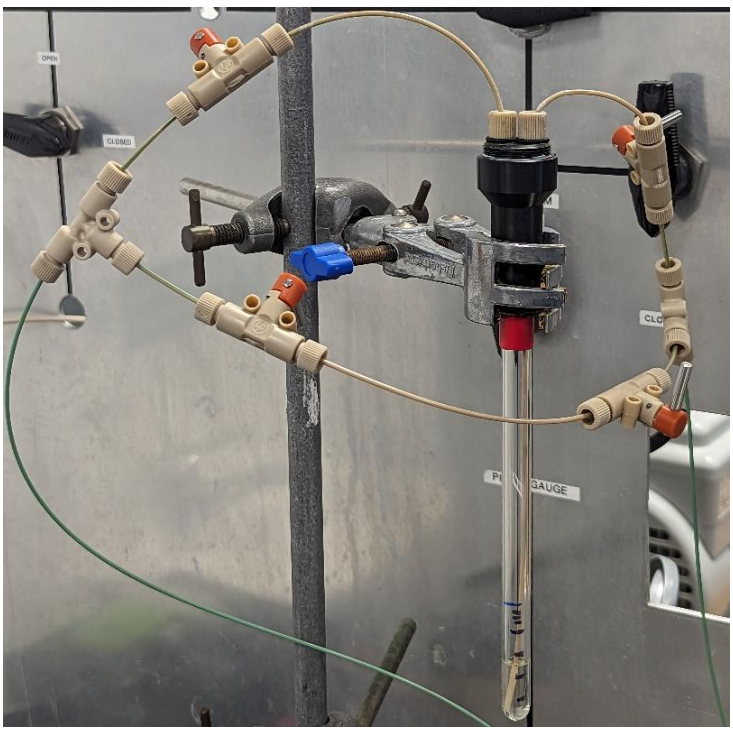

Figure 5.5 - Close-up of polarization cell.

5.3 Operation

5.3.1 Operation of the prototype polarized target

For experiments with the prototype polarized target the typical operating procedure was as follows.

1) Flush line with H_2 to remove traces of O_2.
2) Activate sample under low flow rate of *p*-H_2 for 1-3 hours.
3) Collect reference data for sample at thermal equilibrium polarization.
4) Perform hyperpolarized T_1 measurements.
5) Measure polarization at varying bubbling times or flow rates.

To minimize oxygen contamination, samples were prepared in a glovebox using degassed solvents and the apparatus was flushed with H_2 before use. Sample activation was conducted under a low flow rate of *p*-H_2 to reduce the rate of solvent evaporation. Activation commenced for 1-3 hours, depending on the solvent, until a colour change from yellow-orange to clear was observed. Additionally, this *p*-H_2 flow helped purge any residual oxygen from the samples. Polarization measurements were obtained by manually transferring the polarization cell from the Halbach array to a benchtop MRI.

5.3.2 Choice of solvent

When selecting a solvent for experiments with the prototype SABRE target, the desirable criteria were:

1) Efficient polarization transfer.
2) Low contribution to dipolar relaxation.
3) Low tendency to evaporate.

These factors all significantly impact the achievable polarization levels of the target material. The first two criteria determine the rate of spin order transfer and relaxation, which directly influence the maximum steady-state polarization achievable at a fixed *p*-H_2 flow rate. The third criterion governs the *p*-H_2 flow rates that can be used whilst maintaining acceptable levels of solvent evaporation.

Initially, methanol-d_3 (CD_3OH) was selected as the solvent for experiments, due to issues with the traditional SABRE solvents methanol-d_4 and dichloromethane-d_2, shown in Table 5.1. However, samples utilizing methanol-d_3 exhibited an increased rate of dipolar relaxation due to its higher concentration of ^1H nuclei compared to fully deuterated solvents. As a result, a new solvent was sought to meet all three criteria. This led to the selection of 1,2-dichloroethane-d_4, which addressed

the issues of substrate deuteration, rapid solvent evaporation and shortened polarization relaxation times seen with the other solvents. The primary drawback of dichloroethane-d_4 was its high cost per unit volume relative to the other solvents.

Table 5.1 - Boiling points, approximate purchase prices, and issues for tested solvents with the prototype target. Prices for 1,2-dichloroethane-d_4 and methanol-d_3 are from the most recent purchase for quantities of 20 g, whilst prices for methanol-d_4 and dichloromethane-d_2 are found online from Sigma Aldrich for quantities of 25 g.

Solvent	Boiling point (°C)	Cost (£/mL)	Issues
Methanol-d_4 (CD_3OD)	65	10	Caused deuteration of the *ortho* site in **3,5-py-d_2**.
Dichloromethane-d_2 (CD_2Cl_2)	40	22	High rate of solvent evaporation.
Methanol-d_3 (CD_3OH)	65	5	Increased contribution to dipolar relaxation relative to CD_3OD.
1,2-Dichloroethane-d_4 ($C_2D_4Cl_2$)	83	57	High cost.

5.3.3 Quantification of substrate polarization levels

The substrate polarization levels in the prototype target sample were calculated using slightly different methods depending on the solvent. In both cases, it was necessary to calculate the integral of the substrate signal on the MRI at thermal equilibrium polarization levels (P_{TE}) to determine the substrate signal enhancement, and thus polarization levels.

For samples using methanol-d_3 (CD_3OH), the hydroxyl proton provided a detectable signal at P_{TE} on the MRI, allowing for a thermally polarized spectrum to be acquired. In contrast, samples using 1,2-dichloroethane-d_4 had no detectable signal at P_{TE} on the MRI, therefore a separate sample of CD_3OH was run on the MRI to use as a reference signal, I_{ref}. Because the imaging response from the MRI lacked chemical shift information, it was not possible to identify the contributions from the substrate or solvent signals to any acquired spectra. For this reason, high-field NMR measurements were required when using either solvent.

For the methanol-d_3 samples, thermally polarized integrals for the substrate peaks and for the full spectrum were measured using the NMR spectrometer. The ratio of these integrals was then used, combined with the integral from the thermal spectrum from the MRI, in order to calculate the thermally polarized substrate signal on the MRI, I_{TE}.

For the 1,2-dichloroethane-d_4 samples, the integral of the substrate peaks was compared to that for a reference methanol-d_3 sample, both on the NMR spectrometer. The ratio of these integrals, along with I_{ref}, were then used to calculate I_{TE}.

Similarly, to how is described for the 'Shake and drop' method in Section 7.4.1, the signal enhancement factor, ε, was calculated for the substrate as:

$$\varepsilon = \frac{I_{hyp}}{I_{TE}} \qquad (Eq. 5.1)$$

where I_{hyp} is the integral for the hyperpolarized substrate signal, and I_{TE} is the calculated integral for the substrate signal at P_{TE}. The signal enhancement factor can then be combined with the known thermal equilibrium polarization for ^1H at the field and temperature of the benchtop MRI, P_{TE}, in order to calculate the substrate polarization levels:

$$P = \varepsilon \times P_{TE}. \qquad (Eq. 5.2)$$

5.4 Results

5.4.1 Varying the *p*-H_2 flow rate

The rate of flow of *p*-H_2 through the polarization cell was expected to strongly influence the rate of polarization. This is because during SABRE polarization transfer the *p*-H_2 polarization feedstock is converted into unusable *o*-H_2. If the concentration of *o*-H_2 becomes a significant fraction of the total dissolved H_2, wasted catalytic cycles occur in which polarization transfer does not take place for an unpolarized substrate molecule. If a polarized substrate molecule is bound to a catalyst molecule containing *o*-H_2 it will undergo the backward equilibration, losing its polarization. Evidently, high *o*-H_2 concentrations will reduce the polarization rate.

To investigate the effect of the *p*-H_2 flow rate on achievable polarization levels in the prototype target, experiments were conducted using a sample containing 2 mM of **IMes** and 10 mM of **py** in 2 mL of methanol-d_3. The inlet and exit pressures were set to 4 bar and 3.5 bar respectively, and the flow rate was varied from 10-1000 scc min^{-1}, where 1 scc min^{-1} corresponds to 1 cm^3 of H_2 per minute at standard temperature and pressure (0°C, 1 bar).

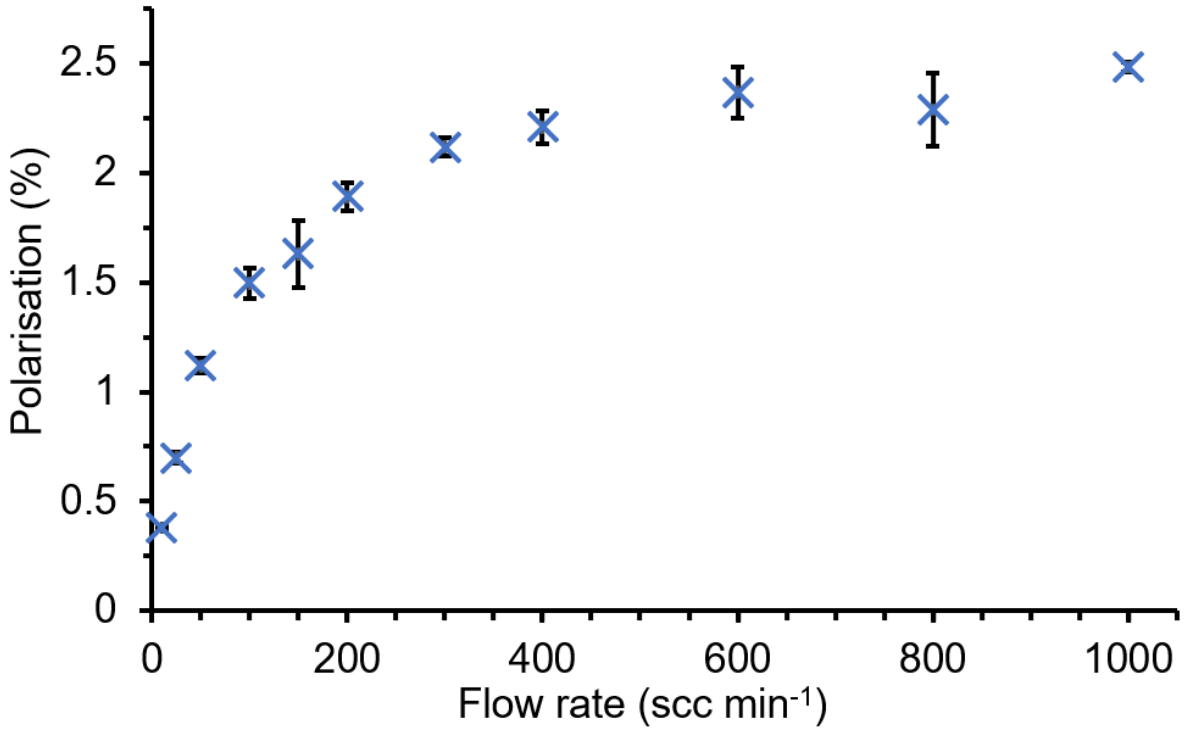

*Figure 5.6 - Polarization of **py** with varying flow rates of p-H_2. Error bars are present for all points but may not always be visible.*

Results

As shown in Figure 5.6 and Table 5.2, the results of this study demonstrate a strong trend of increasing substrate polarization levels with rising *p*-H_2 flow rate, up to 600 scc min^{-1}. However, beyond this point further gains are diminished, evidenced by the polarization values for 600, 800 and 1000 scc min^{-1} all falling within error of each other. As the substrate T_1 will be constant throughout this study, the polarization levels reached will reflect the changing rate of polarization transfer.

This behaviour aligns with expectations: at low *p*-H_2 flow rates, polarization transfer is primarily constrained by *p*-H_2 influx, leading to a quasi-linear relationship between flow rate and polarization, as observed for flow rates between 10 and 50 scc min^{-1}. At higher flow rates, the *para* fraction of dissolved H_2 approaches unity, meaning that further increasing the flow rate yields only marginal improvements in polarization.

Additionally, higher flow rates may enhance polarization not only by replenishing 'spent' *p*-H_2 more rapidly but also by improving gas dispersion through more vigorous bubbling. Further investigation is needed to determine the extent to which improved dispersion may contribute to the observed increase in polarization at higher flow rates.

*Table 5.2 - Polarization of **py** with varying p-H_2 flow rates.*

Flow rate (scc min^{-1})	Polarization (%)
10	0.38 ± 0.01
25	0.70 ± 0.02
50	1.12 ± 0.03
100	1.50 ± 0.07
150	1.6 ± 0.2
200	1.89 ± 0.06
300	2.12 ± 0.04
400	2.21 ± 0.07
600	2.4 ± 0.1
800	2.3 ± 0.2
1000	2.48 ± 0.02

5.4.2 Substrate excess study for 3,5-pyridine-d_2

As demonstrated in Section 2.3.2 and Section 3.5, the substrate-to-catalyst ratio strongly influences key polarization metrics, including the maximal polarization (P_{Max}) and the decay constant (T_1). This study investigates how these metrics vary with substrate excess for the substrate **3,5-py-*d*$_2$** in the prototype SABRE-polarized target.

To assess the effect of altering the substrate excess, the substrate concentration was held constant whilst the catalyst concentration was varied. The samples contained 40 mM of **3,5-py-*d*$_2$**, with **IMes** precatalyst concentrations ranging from 0.5-8 mM and **DMSO-*d*$_6$** co-ligand concentrations ranging from 2-32 mM, maintaining a 4:1 co-ligand-to-catalyst ratio. The solvent used was 1.6 mL of methanol-d_3, with the apparatus operating at inlet and exit pressures of 4 bar and 3.5 bar respectively. To minimize solvent evaporation, the *p*-H_2 flow rate was set to 50 scc min^{-1}. T_1s were measured using a hyperpolarized T_1 recovery sequence as described in Section 7.3.2, performed on the MRI at conditions of 0.33 T and 30°C.

Polarization build-up data was collected by measuring the polarization level at varying bubbling durations, allowing the polarization to fully decay between each measurement. To characterize polarization dynamics, a new metric, the polarization build-up constant (T_B) is introduced. T_B is the time constant by which a steady-state polarization in the cell is approached, where the rate of polarization is balanced by the rate of relaxation. P_{Max} and T_B were determined by fitting the polarization build-up data to the equation:

$$P(t) = P_{Max}\left(1 - e^{-t/T_B}\right) \qquad (Eq.\,5.3)$$

where P_{Max} is the maximal polarization reached and T_B is the polarization build-up constant with units of s. An example graph showing how P_{Max} and T_B are found by fitting Eq. 5.3 to polarization build-up data is found in Figure 5.8.

Results

The results of this study, seen in Figure 5.7 and Table 5.3, show a strong dependence of the maximal polarization (P_{Max}), the decay constant (T_1), and the polarization build-up constant (T_B), on substrate excess. The highest polarization levels were achieved at a substrate excess of 60-fold, reaching a value of P_{Max} of 4.26%, with the lowest value for P_{Max} of 1.07% being achieved at a 5-fold substrate excess.

The value of T_1 increased with substrate excess, eventually reaching a plateau above a 40-fold excess. T_1s for the 40-fold to 80-fold excess samples lie almost within 1 SD of each other at approximately 26 s.

In contrast to T_1, T_B continued to rise over the investigated range without showing signs of saturation, reaching a maximum of 22.6 s for the 80-fold excess sample. Notably, the build-up constant remained lower than the decay constant under all tested conditions.

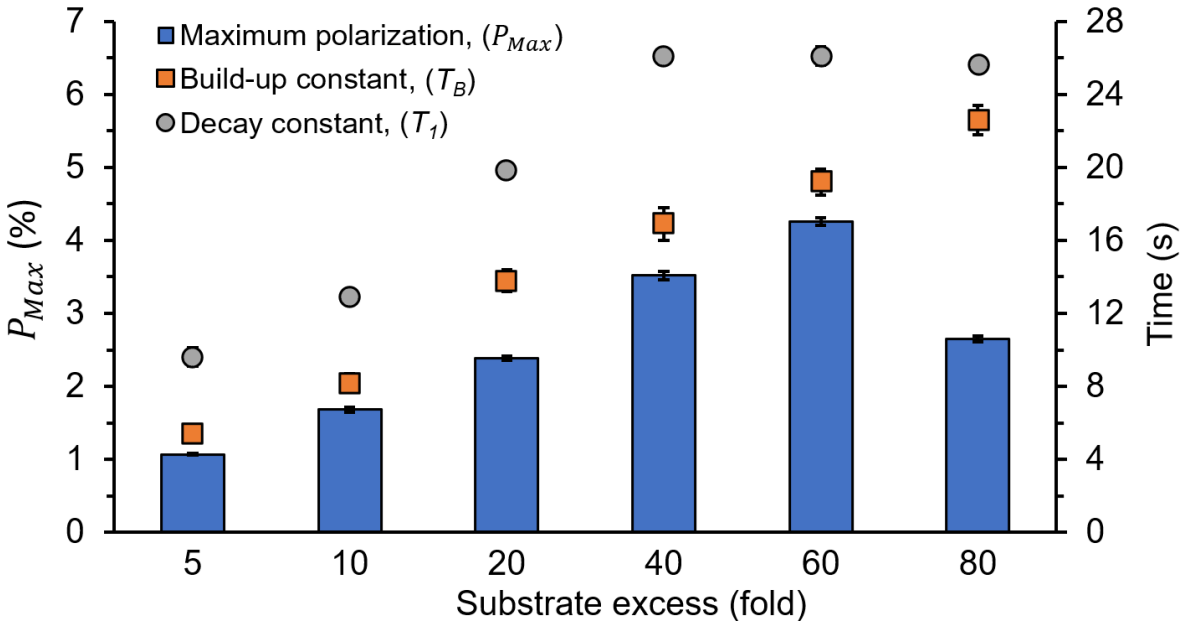

*Figure 5.7 - Key polarization metrics for **3,5-py-d_2** at varying substrate excesses. Note here that the x-axis is not a linear scale. Error bars are present for all points but may not always be visible.*

Table 5.3 - *Key polarization metrics for **3,5-py-d_2** at varying substrate excesses.*

Substrate excess (fold)	Maximum polarization, P_{Max} (%)	Build-up constant, T_B (s)	Decay constant, T_1 (s)
5	1.07 ± 0.01	5.4 ± 0.2	9.6 ± 0.5
10	1.68 ± 0.03	8.2 ± 0.5	12.9 ± 0.4
20	2.39 ± 0.03	13.8 ± 0.6	19.8 ± 0.2
40	3.52 ± 0.06	16.9 ± 0.9	26.1 ± 0.1
60	4.26 ± 0.05	19.2 ± 0.7	26.1 ± 0.5
80	2.65 ± 0.04	22.6 ± 0.8	25.6 ± 0.3

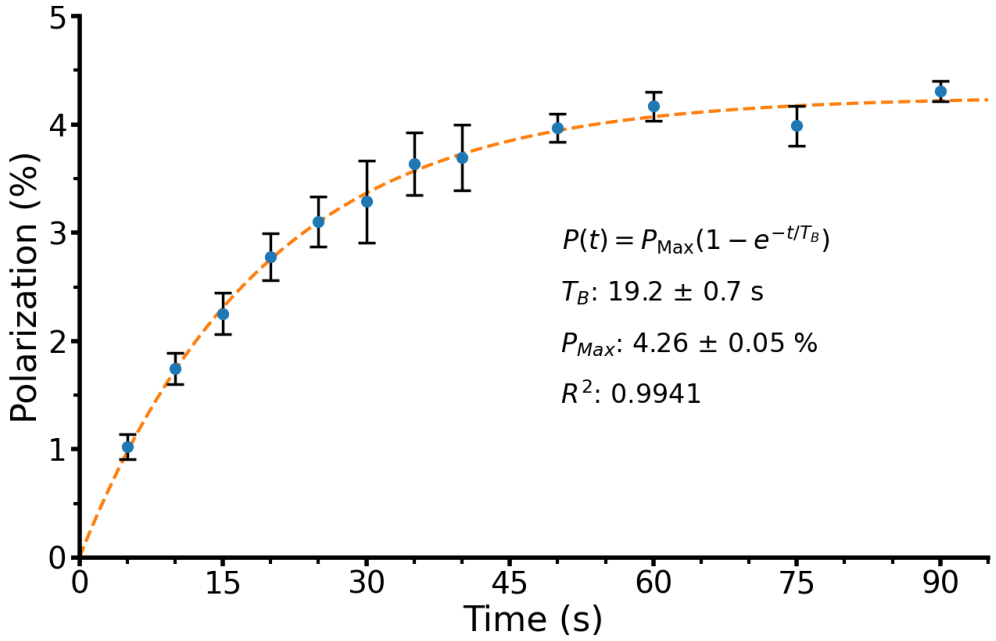

Figure 5.8 - Polarization levels at varying bubbling durations for the 60-fold excess sample of ***3,5-py-d₂****. P_{Max} and T_B are found by fitting the polarization build-up data to Eq. 5.3.*

Discussion

It was expected that P_{Max} would reach a maximum within the investigated range of substrate excesses, due to the competing effects of decreasing rates of polarization transfer and increasing T_1 with lower catalyst concentrations. Figure 5.7 and Table 5.3 show that the T_1 of the substrate reached its maximum by a 40-fold substrate excess. Based on this, it was anticipated that the maximal polarization level would decrease for higher substrate excesses due to a further reduction in catalyst concentration and no additional increase in T_1.

Contrary to expectations, the maximal polarization level for the 60-fold excess sample was 21% higher than for the 40-fold excess sample. A proposed explanation for this is that here ligand exchange at the catalyst is primarily dissociative but exhibits associative qualities. This means that whilst ligand dissociation is the rate-determining step, the incoming ligand can influence the exchange process. A purely dissociative process would suggest that ligand exchange is independent of substrate concentration, whereas if associative qualities are present the incoming ligand can weakly interact with the complex before full dissociation of the outgoing ligand.

Higher relative ligand concentrations increase the probability of such interactions, stabilizing the intermediate complex, and thereby accelerating the exchange process. It is thus proposed that faster ligand exchange occurs with a 60-fold substrate excess, bringing exchange closer to the optimal rate and thus increasing the efficiency of spin order transfer.

An additional explanation is that the lower co-ligand concentration found in the 60-fold excess sample would result in reduced competitive binding for catalyst sites. This would decrease the formation of complexes with two equatorially bound co-ligands (trans to the hydrides) which, due to the lack of an equatorially bound substrate molecule, do not contribute to spin order transfer in that catalytic cycle.

In this study, the T_1 was expected to be lower for these samples than was seen previously in Section 2.5.3 due to the use of the partially-deuterated solvent methanol-d_3, and thus a maximum T_1 of 26 s was not unexpected. Section 5.4.3 will present the results of an experiment that uses an alternative solvent, 1,2-dichloroethane-d_4, which allows for the inherently long T_1 of **3,5-py-d_2** to be utilized.

T_B was found to rise continuously with increasing substrate excess, however was found to always be less than T_1. The following section will give a mathematical proof for why T_B must be strictly less than T_1 under the same conditions. It should be noted that in this study T_B was found from the build-up of polarization that was generated at 6 mT, whilst the T_1 data was acquired at the 0.33 T field of the MRI, and thus the relation $T_B < T_1$ does not strictly apply.

Polarization build-up model

Whilst operating under consistent conditions (flow rate, pressure, temperature, field strength), the rate of change of the polarization within the polarization cell can be approximated as:

$$\frac{dP(t)}{dt} = G(1-P) - \frac{P}{T_1} \qquad (Eq.\,5.4)$$

where P is the fractional polarization level of the cell, t is the time since polarization transfer started with units of s, G is the maximal rate of polarization through SABRE (equal to $\left.\frac{dP}{dt}\right|_{P=0}$) with units of s^{-1}, and T_1 is the time constant for the polarization decay with units of s. The rate of polarization transfer is modulated by the term $(1-P)$, as only unpolarized material can undergo polarization through SABRE and thus the rate of polarization transfer decreases as polarization levels increase. Eq. 5.4 can be integrated to give:

$$P(t) = \frac{G}{\frac{1}{T_1}+G} + \left(P_0 - \frac{G}{\frac{1}{T_1}+G}\right) e^{-\left(\frac{1}{T_1}+G\right)t} \qquad (Eq.\,5.5)$$

which describes the polarization level in the cell at time t. This simplifies to Eq. 5.6 when the polarization level is 0 at $t = 0$ (a good approximation for $P_{TE} \ll P_{Max}$):

$$P(t) = \frac{G}{\frac{1}{T_1} + G}\left(1 - e^{-\left(\frac{1}{T_1}+G\right)t}\right), \qquad P(0) = 0. \qquad (Eq. 5.6)$$

By taking the limit $t \to \infty$ for Eq. 5.6 we find that the exponential term tends towards zero and thus the steady-state polarization of the polarized material is given by:

$$P_{Max} = \frac{G}{\frac{1}{T_1} + G} = \frac{GT_1}{1 + GT_1}. \qquad (Eq. 5.7)$$

Substituting P_{Max} into Eq. 5.6 gives:

$$P(t) = P_{Max}\left(1 - e^{-\left(\frac{1}{T_1}+G\right)t}\right). \qquad (Eq. 5.8)$$

Looking at Eq. 5.8 it can be seen that the time dependence of the polarization is characterized by the term:

$$e^{-\left(\frac{1}{T_1}+G\right)t} \qquad (Eq. 5.9)$$

which determines the rate at which the steady-state polarization is approached. Comparing Eq. 5.8 to our fitting for the polarization build-up constant (T_B) in Eq. 5.3, it can be seen that the bracketed term in Eq. 5.9 is equal to T_B^{-1}, and thus:

$$T_B = \frac{T_1}{1 + GT_1} \qquad (Eq. 5.10)$$

where T_1 is the polarization decay constant and G is the maximal rate of polarization transfer through SABRE. Looking at Eq. 5.10 it can be seen that $T_B < T_1$, as G has been defined to be a positive quantity. It can also be seen that T_B approaches two different limits for the cases $GT_1 \ll 1$ and $GT_1 \gg 1$:

$$T_B \approx \begin{cases} T_1, & GT_1 \ll 1 \\ \frac{1}{G}, & GT_1 \gg 1 \end{cases}. \qquad (Eq. 5.11)$$

Finally, looking back to Eq. 5.7 it can be seen that the steady-state polarization of the cell, P_{Max}, is only dependent on the term GT_1. This dependence is shown in Figure 5.9.

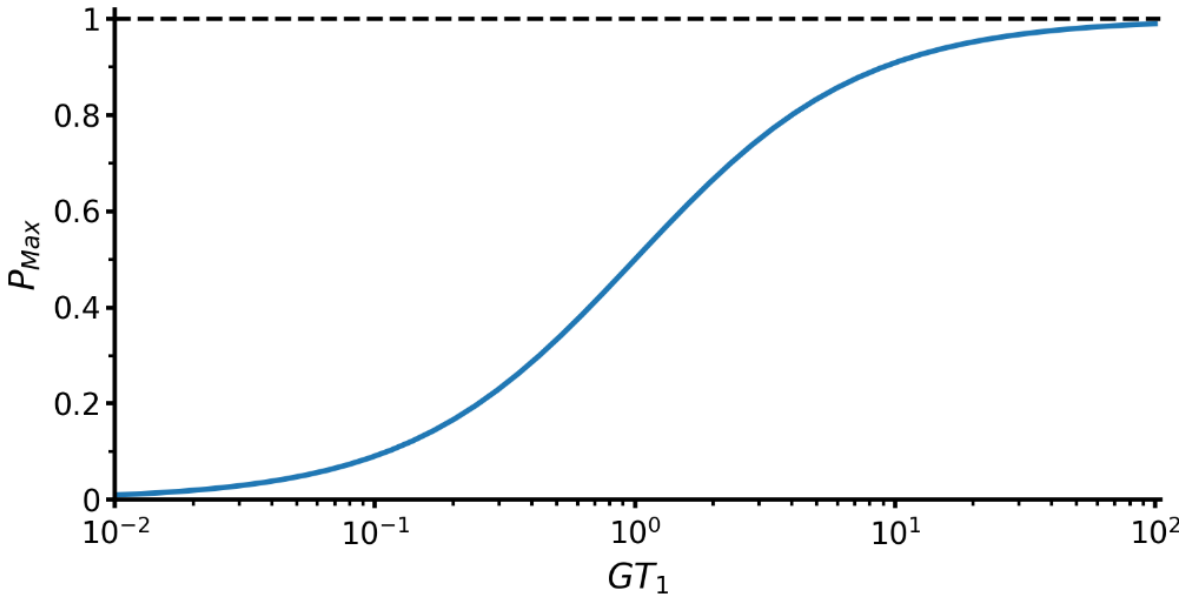

Figure 5.9 - The dependence of P_{Max} on GT_1.

5.4.3 Pressure study for 3,5-pyridine-d_2

It is well known that the rate of polarization transfer in SABRE is often constrained by the availability of *p*-H_2 - the polarization feedstock. This comes in two forms, where either the total concentration of H_2 in solution is limiting, resulting in slower than optimal rates of H_2 exchange with the catalyst, or the *p*-H_2 fraction of the dissolved H_2 is significantly less than 1, resulting in wasted catalytic cycles (or even the relaxation of polarization through the backwards equilibration).

Due to safety limitations when working with pressurized gasses in sealed glassware, SABRE experiments are typically performed at pressures <10 bar. A SABRE-polarized target used for scattering experiments would likely make use of alternate materials that would allow operation at higher pressures, such as metal alloys (e.g. titanium alloys), carbon fibre composites or high strength polymers, such as PEEK. All of these materials satisfy the criteria of being non-magnetic, having a high tensile strength, and being suitably chemically resistant.

Since a SABRE-polarized target would be able to operate at higher pressures than the prototype described in this thesis, it was decided to investigate whether increasing the operating pressure could enhance polarization levels. To assess this, polarization measurements of **3,5-py-d_2**, were conducted at various pressures achievable with the polarized target, such that the results could be extrapolated to higher pressures. This experiment was performed using an optimized system for achieving the highest polarization levels with SABRE. A similar experiment performed by Duchowny et al. [76] is discussed in Section 1.4.3.

For this experiment the samples contained 40 mM of **3,5-py-d_2**, 0.67 mM of **IMes-d_{22}** and 2.67 mM of **DMSO-d_6** in 1.6 mL of 1,2-dichloroethane-d_4. This is similar to the composition of the 60-fold excess sample in Section 5.4.2, however here the **IMes-d_{22}** catalyst replaces the **IMes** catalyst and the solvent 1,2-dichloroethane-d_4 replaces methanol-d_3. **IMes-d_{22}** was chosen as it has been shown to result in higher polarization levels than **IMes** for **3,5-py-d_2** in Section 2.5.3, and 1,2-dichloroethane-d_4 was chosen due to its higher boiling point and lower concentration of ^{1}H nuclei than methanol-d_3.

Pressures were varied across the range 2.5-5.5 bar and *p*-H_2 flow rates were varied across the range 40-200 scc min^{-1}, with an additional run at 300 scc min^{-1} performed for the sample at 5.5 bar. Lower pressures were not attempted as it was expected that solvent evaporation rates would be too high at the desired flow rates. The pressure was varied by adjusting the back pressure, which will be approximately equal to the pressure in the polarization cell, via the regulator. The inlet pressure was adjusted to always be 0.5 bar higher than the back pressure, keeping a constant pressure differential. Replicate samples of the same composition were used for each studied pressure due

to solvent losses through evaporation. Full polarization build-up data was acquired for each sample, however only for the flow rate 40 scc min^{-1}. Thus, polarization values are compared at their values after a bubbling time of 2 minutes for each pressure and flow rate, rather than the fitted parameter P_{Max} as is seen in Section 5.4.2.

Results

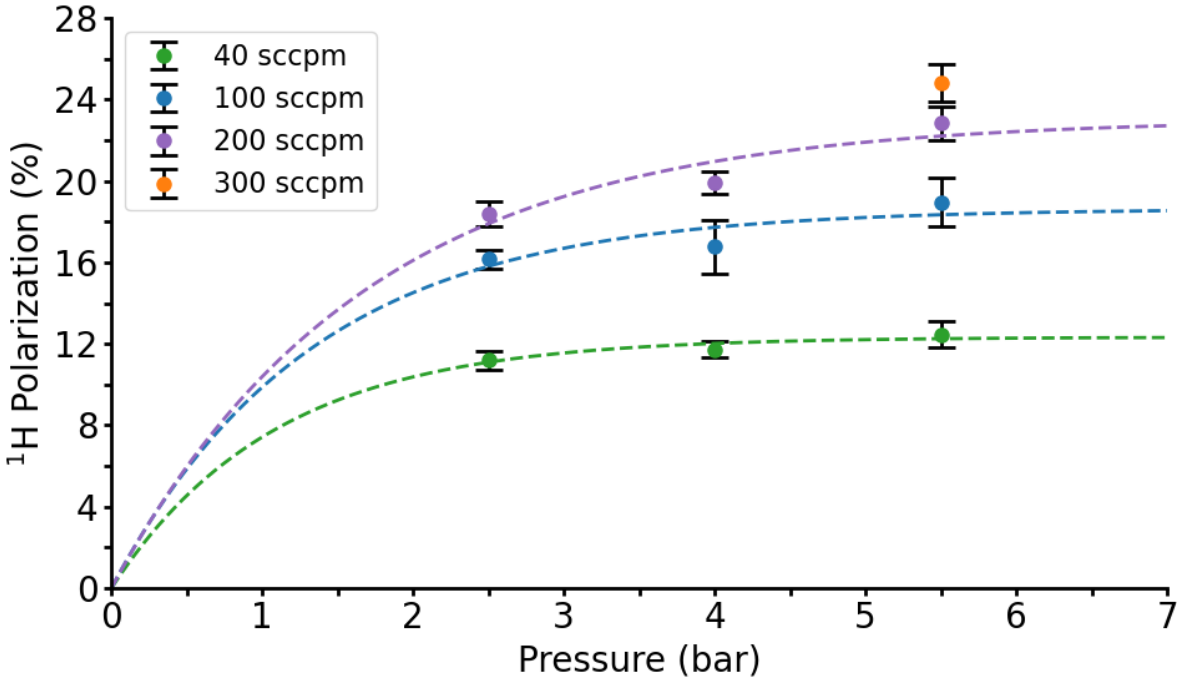

*Figure 5.10 - Polarization levels of **3,5-py-d₂** with varying back pressure and p-H_2 flow rates. Polarization values were taken for a fixed bubbling time of 2 minutes. The fittings here are used as a guide for the eye.*

*Table 5.4 - Polarization levels of **3,5-py-d₂** with varying back pressure and p-H_2 flow rates. Polarization values were found for a fixed bubbling time of 2 minutes.*

Pressure (bar)	**^{1}H Polarization (%)**			
	40 scc min^{-1}	100 scc min^{-1}	200 scc min^{-1}	300 scc min^{-1}
2.5	11.2 ± 0.4	16.2 ± 0.5	18.4 ± 0.6	-
4	11.7 ± 0.4	16.8 ± 1.3	19.9 ± 0.6	-
5.5	12.5 ± 0.6	19.0 ± 1.2	22.8 ± 0.8	24.8 ± 0.9

It was found that the polarization levels exhibited limited dependence on the pressure within the polarization cell, however they were are strongly influenced by the *p*-H_2 flow rate, as shown in Figure 5.10 and Table 5.4. At a flow rate of 40 scc min^{-1}, increasing the pressure from 2.5 to 5.5 bar (a 120% increase) results in only an 11% rise in polarization. A larger increase in polarization with pressure is found at a flow rate of 200 scc min^{-1}, rising by 24% between 2.5 and 5.5 bar, however this is still far from the linear increase that would be expected if the sample was strongly *p*-H_2 deficient.

In contrast, the polarization increases significantly with higher *p*-H_2 flow rates. At 5.5 bar, increasing the flow rate from 40 to 100 scc min^{-1} (a 150% increase) leads to a 52% polarization gain, with a further 20% increase observed when increasing the flow rate from 100 to 200 scc min^{-1}. Due to the higher boiling point of the solvent at 5.5 bar, the rate of solvent evaporation was low enough that a run at a flow rate of 300 scc min^{-1} could be performed. Here it was found that a maximum polarization level of 24.8% could be reached after 2 minutes of bubbling. The average T_1 over the three replicate samples was 70 ± 2 s, measured on the MRI at conditions of 0.33 T, 303.2 K.

Back-propagation calculations were used to account for polarization decay during transfer to the MRI. The T_1 at Earth's magnetic field was measured to be 31 ± 2 s for this sample, and the transfer time was 4 ± 0.5 s, yielding a correction factor of 1.14 ± 0.03.

Discussion

The weak dependence of polarization on pressure here indicates that the system is not in the strongly *p*-H_2 deficient regime, where polarization would scale linearly with pressure due to the changes in hydrogen solubility, an effect demonstrated by Duchowny et al. [76]. This suggests that the rate of H_2 exchange is not the rate limiting step in the catalytic cycle, and that further increases in the pressure may not be expected to result in significant increases in the polarization level.

The strong dependence of polarization on the *p*-H_2 flow rate suggests a substantial rate of *p*-H_2 to *o*-H_2 conversion in solution, and implies that even higher polarization levels could be achieved with increased flow rates. The maximum polarization level at varying flow rates is shown for the 5.5 bar sample in Figure 5.11, where the data appears to be well suited to a logarithmic fitting over the studied range. Extrapolating this trend predicts polarization levels of around 34% with a flow rate of 1200 scc min^{-1}. Solvent evaporation rates limit the maximum usable flow rate in this experiment to 300 scc min^{-1}, however addressing this challenge through either the use of higher pressures, a solvent recovery system, or a less volatile solvent could allow these potential polarization gains to be realized.

Such high polarization levels being reached is primarily attributed to the use of a fully deuterated solvent, with an average T_1 of 70 s being measured in this experiment, almost three times longer than the 26 s T_1 seen for a similar sample in Section 5.4.2. This long T_1 allows for the build-up of polarization over a longer time period, as seen in Figure 5.12 where the build-up constant of the polarization is 58 s, also around three times longer than was seen in Section 5.4.2. The use of the deuterated catalyst **IMes-*d*$_{22}$** is also attributed to the high polarization levels seen here.

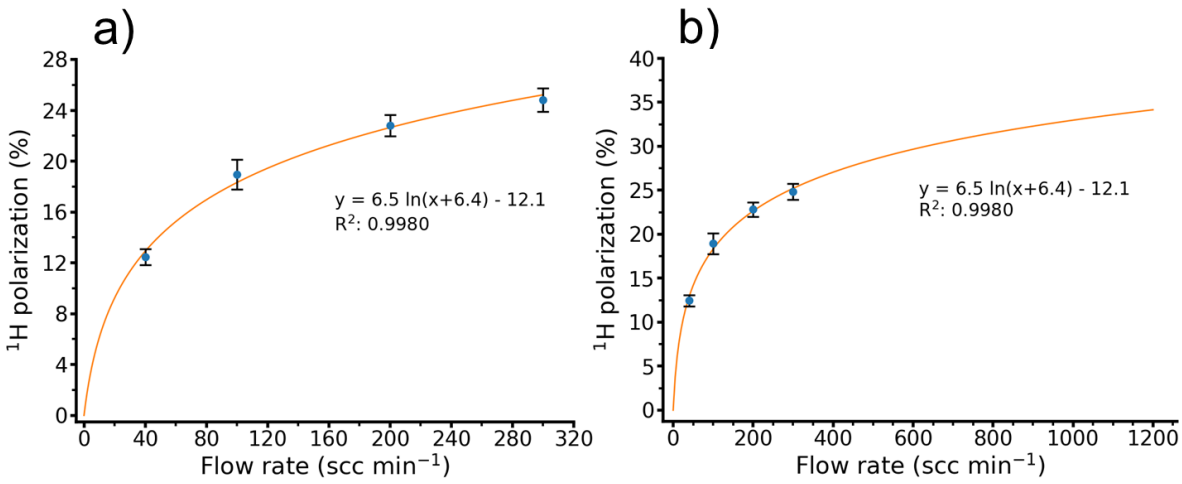

Figure 5.11 - Polarization levels with varying flow rates for the sample at 5.5 bar with a logarithmic fitting. a) shows the range 0-300 scc min^{-1}. b) shows the range 0-1200 scc min^{-1}.

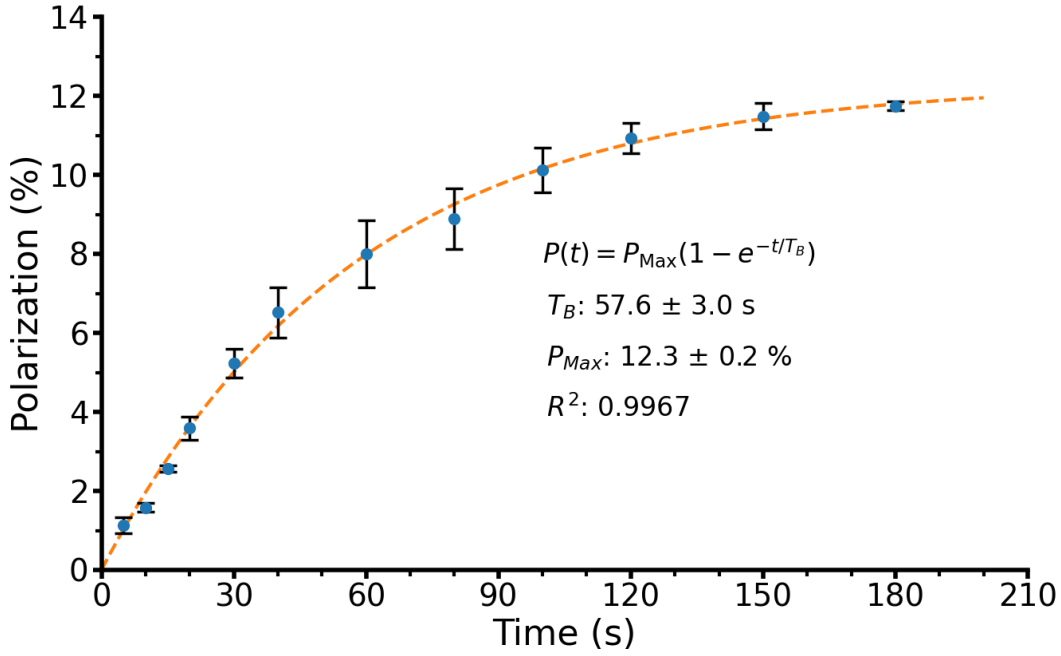

Figure 5.12 - Polarization build-up for the sample at 5.5 bar with a flow rate of 40 scc min^{-1}. Here the corrections for the pre-measurement decay have not yet been applied.

5.5 Performance in relation to current targets

In this section, the performance of the prototype SABRE-polarized target will be compared to that of existing DNP targets. As discussed in Chapter 1 and Chapter 4, frozen-spin targets, such as FROST at Jefferson Lab, have been limited to photoproduction experiments due to their susceptibility to heat deposition. Attempts to use frozen-spin targets with a charged particle beam, such as at COMPASS, found that significant polarization losses are observed using beam currents as low as 16 pA [15].

Conversely, continuously polarized targets, such as the longitudinally polarized target at Jefferson Lab Hall B, can operate at much higher electron beam currents if regular target annealing is performed, with recent data acquisition at Hall B occurring at 8 nA [35]. However, the strong polarizing magnets needed places significant amounts of additional material in the detector. The proposed design for a transverse target for Hall B expects acceptance angles of just ±25° in the vertical plane and ±60° in the horizontal [118]. This would greatly reduce the acceptance of many measurements in the CLAS12 programme, particularly those with a high multiplicity of particles produced in the final state. Additionally, these targets will not satisfy the needs for a polarized target that can operate with the upcoming high luminosity upgrade for CLAS12 - from 10^{35} cm^{-2} s^{-1} to 10^{37} cm^{-2} s^{-1} [136]. SABRE-polarized targets aim to address the beam intensity limitations of frozen-spin targets for e-p scattering experiments whilst also being able to provide 4π angular acceptance.

5.5.1 SABRE target specifications

For a SABRE-polarized target, it is estimated that a realistic yield of isolated polarized material lies in the range 1-5 g. Based on this, target dimensions of approximately 1 cm in diameter and 4 cm in length are proposed, corresponding to about 3.2 g of material for the candidate substrates **py** and **3,5-py-*d*$_2$**. Unlike for FROST and the Hall B continuously polarized target, which are limited by the photon beam width and the energy deposition per unit area respectively, a SABRE target may operate with a smaller diameter due to reduced constraints from the rates of heat deposition and radiation damage.

As shown in Section 3.2, the T_1 of **3,5-dcpy** decreases by only 7% per °C of warming near its optimal temperature. Furthermore, Section 4.5 demonstrates that a SABRE sample exposed to a radiation dose equivalent to 15 minutes at 1 nA of electron beam current retained a high amount of polarizability with no detriment to the T_1. Given the potential for continuous material

replenishment, a lower limit for the operable electron beam intensity for a SABRE target is expected to lie at around 5 nA.

5.5.2 Comparison metric

As has previously been stated, the productivity of a scattering experiment utilizing a polarized target is determined by the Figure of Merit (FoM):

$$FoM = Lf^2P^2 = NIf^2P^2 \qquad (Eq. 5.12)$$

where L is the luminosity (cm^{-2} s^{-1}), N is the areal density of the material (nucleons cm^{-2}), I is the beam intensity (particles s^{-1}), f is the dilution factor, and P is the polarization. In order to arrive at a metric that is independent of the beam intensity, I, a new quantity will be introduced, the adjusted Figure of Merit (FoM'), where:

$$FoM' = Nf^2P^2 = \frac{FoM}{I} \qquad (Eq. 5.13)$$

which can be used for a comparison of the effectiveness of different targets. The areal density, N, of the target material can be calculated as:

$$N = \frac{\rho l N_A n}{M}(\times \kappa) \qquad (Eq. 5.14)$$

where ρ is the mass density (g cm^{-3}), l is the target length (cm), M is the molar mass of the material, N_A is the Avogadro constant, n is the number of nucleons per molecule, and κ (where applicable) is the filling factor.

5.5.3 Frozen-spin

The specifications for the frozen-spin target at Jefferson Lab (FROST) are as follows. For the target material, the mass density of frozen C_4H_9OH is around 0.9 g cm^{-3} [137] and the dilution factor is 10/74 = 0.135. The diameter and length of the target used were 1.5 cm and 5 cm respectively [2]. For the spherical pellets of butanol used, the filling factor has been found in other experiments to be about 0.55 [15]. The volume fraction of water and the nitroxyl radical TEMPO in the target will be taken to be negligible. The average polarization of the target during operation was found to be approximately 80% [2]. Putting these values into FoM':

$$N = \frac{0.9\ g\ cm^{-3} \times 5\ cm}{74.1\ g\ mol^{-1}} \times 6.02 \times 10^{23} \times 74 \times 0.55 = 1.5 \times 10^{24}\ nucleons\ cm^{-2}$$

$$P = 0.8, f = 0.135$$

$$\therefore FoM'_{FROST} = 1.7 \times 10^{22}\ nucleons\ cm^{-2}. \qquad (Eq. 5.15)$$

5.5.4 Continuously polarized

For the new continuously polarized target at Jefferson Lab Hall B, the mass density of the frozen NH_3 target material is 0.817 g cm^{-3} [15] and the dilution factor is 3/17 = 0.176. The diameter and length of the target used were 2 cm and 5 cm respectively [35], and the filling factor will also be taken to be 0.55 [15]. The average polarization of the target during operation was found to be around 70% [35]. Putting these values into FoM':

$$N = \frac{0.853\ g\ cm^{-3} \times 5\ cm}{17.0\ g\ mol^{-1}} \times 6.02 \times 10^{23} \times 17 \times 0.55 = 1.4 \times 10^{24}\ nucleons\ cm^{-2}$$

$$P = 0.7, f = 0.176$$

$$\therefore FoM'_{Hall\_B} = 2.1 \times 10^{22}\ nucleons\ cm^{-2}. \qquad (Eq. 5.16)$$

Here it is found that FoM' is similar to that of the butanol target used in FROST.

5.5.5 SABRE

To compare the performance of these targets with the performance of the prototype SABRE-polarized target, it will be assumed that the polarized material of **3,5-py-*d*₂** can be isolated from solution without significant polarization losses. For pure **3,5-py-*d*₂**, the mass density at 20°C is approximately 1.01 g cm^{-3}, and the dilution factor is 3/81= 0.037. As **3,5-py-*d*₂** is a liquid under the room temperature operating conditions of SABRE, the filling factor can be taken as 100%. Using the maximum achieved polarization value of 25% with the prototype target, we can calculate FoM' for a target of length 4 cm as:

$$N = \frac{1.01\ g\ cm^{-3} \times 4\ cm}{81.1\ g\ mol^{-1}} \times 6.02 \times 10^{23} \times 81 = 2.4 \times 10^{24}\ nucleons\ cm^{-2}$$

$$P = 0.25, f = 0.037$$

$$\therefore FoM'_{SABRE} = 2.1 \times 10^{20}\ nucleons\ cm^{-2}. \qquad (Eq. 5.17)$$

Comparing this value to those for FROST and the Hall B continuously polarized target we find that the adjusted Figure of Merit is around two orders of magnitude lower for the SABRE prototype target. This is due to the values of P and f for the SABRE target, which are approximately 3-fold and 4-fold lower than for the DNP targets respectively. The areal density, N, however, is higher than that of the DNP targets.

As was discussed in Section 5.4.3, if solvent evaporation was not a concern, higher flow rates would be able to be used in the prototype target. Extrapolating the dependence of polarization on flow

rate for the results at 5.5 bar (Section 5.4.3) finds that measured polarization levels at a flow rate of 1200 scc min^{-1} could reach 34%. Using this polarization value for FoM' gives:

$$FoM'_{SABRE} = 3.8 \times 10^{20}\ nucleons\ cm^{-2} \qquad (Eq.\ 5.18)$$

which is approximately 45-fold and 55-fold lower than for the targets at Jefferson Lab.

5.5.6 Comparison

Although FoM' is significantly lower for the prototype SABRE target, it is thought that for charged particle beams a SABRE-polarized target may be able to operate at higher beam intensities than DNP targets, especially frozen-spin targets.

Comparing the performance to frozen-spin targets, currently the only fixed-target technology capable of close to 4π acceptance, we find that for the full FoM, taking the 16 pA beam current used at COMPASS and the 5 nA lower estimate of the operating limit of a SABRE target:

$$FoM_{FROST} = 1.7 \times 10^{30}\ cm^{-2}s^{-1} \qquad (Eq.\ 5.19)$$

$$FoM_{SABRE} = 1.2 \times 10^{31}\ cm^{-2}\ s^{-1}. \qquad (Eq.\ 5.20)$$

Thus, even at the lower estimate of operable beam intensity SABRE targets are expected to outperform frozen-spin DNP targets by a factor of 7 for use with charged particle beams[xv].

For the new Hall B continuously polarized target operating with an electron beam current of 8 nA, the full FoM is:

$$FoM_{Hall_B} = 1.1 \times 10^{33}\ cm^{-2}s^{-1}. \qquad (Eq.\ 5.21)$$

This is significantly higher than for a SABRE target operating with a 5 nA beam. In order for a SABRE target to surpass the FoM of a continuously polarized DNP target such as that at Hall B, the operable beam current would have to be >100 nA, even with expected improvements in the polarization level coming from further optimizations of SABRE. This figure however does not consider the increased angular acceptance expected of a SABRE target. Further investigation is needed to determine whether SABRE targets can be operated under such conditions.

[xv] This comparison relies on two assumptions. First, that the polarized material produced via SABRE can be isolated from solution with negligible loss of polarization. Second, that the flow rate dependence of the polarization observed with the prototype target in the range 0-300 scc min^{-1} will persist up to flow rates of 1200 scc min^{-1}.

5.6 Future improvements to prototype design.

There are two ways in which a SABRE-polarized target may be used for particle physics experiments, in fixed target experiments and in internal target experiments. For fixed target experiments a continuous or pulsed beam is fired at a stationary target, whereas for internal targets, used at storage ring facilities such as the upcoming Electron-Ion Collider, a circulating beam continuously interacts with the target. The experiments discussed thus far in this thesis have all used fixed targets.

The requirements for a SABRE-polarized target for fixed target and internal target experiments are similar with notable key differences. For both applications it is necessary to optimize the dilution factor and polarization of the target material, and thus the issues of solvent evaporation and the isolation of polarized material need to be addressed. For fixed target experiments, it is also necessary to produce large quantities of polarized material in order to maximize the areal density, thus increasing the FoM and decreasing the required running times. For internal targets, lower quantities of polarized material are needed, however, as will be explained, it will be necessary that the polarization is preserved through a phase change from liquid to solid. Potential ways to resolve these challenges will be addressed in this section.

5.6.1 Fixed target experiments

Solvent evaporation

As was shown in Section 5.4.3, the achievable polarization levels for the prototype target were restricted by the usable *p*-H_2 flow rates due to solvent evaporation. There are multiple ways of addressing the issue of solvent evaporation. One such way is by utilizing a solvent with a higher boiling point or by increasing the pressure in the polarization cell. Another such way, proposed by Blanchard et al., is to presaturate the incoming *p*-H_2 gas with solvent vapour. This was found to reduce the rate of evaporation of the methanol solvent in an experiment by over an order of magnitude [134]. Lastly, a solvent condenser apparatus could be used in order to recover lost solvent and reintroduce it into the polarization cell.

Isolation of polarized material

Removal of the catalyst from the polarized solution is necessary in order to increase the dilution factor and reduce background contributions to the experimental signal from unwanted nuclei. As was described in Section 2.3.2, the desire to produce catalyst-free solutions of SABRE-polarized material has given rise to the field of CASH-SABRE. CASH-SABRE typically produces catalyst-free

solutions by utilizing a phase separation, leaving the catalyst dissolved in the organic layer whilst the polarized substrate remains dissolved in an aqueous layer. This technique may not be suitable for a SABRE-polarized target, as whilst this technique will effectively reduce the catalyst concentration in the aqueous solution, it will be difficult to extract the polarized substrate out of solution for the candidate substrates **py** and **3,5-py-*d*$_2$**, due to their high miscibility with water and similar boiling points. An alternative technique for catalyst removal, proposed by Barskiy et al., is the use of metal-scavenging agents. It was found that the use of commercially available mercaptopropyl silica gel resulted in almost the complete removal of the SABRE catalyst from solution in a matter of seconds [89].

Alongside catalyst removal, solvent removal is also necessary in order to increase the dilution factor of a SABRE-polarized target. The proposed method for this is the rapid evaporation of the solvent after polarization has taken place. This has been attempted by Duchowny et al. who achieved signal enhancements using liquified pressurized CO_2 as a solvent for SABRE [76]. Chloromethane-d_3 may prove a more suitable candidate for a quickly removable solvent, with a boiling point of 77.3 °C at 20 bar allowing for solution state polarization transfer at achievable pressures, and a boiling point of -24.0 °C at 1 bar allowing for rapid removal upon depressurization. This solvent also has similarities to the chlorinated solvents dichloromethane and 1,2-dichloroethane which have been shown to work well with SABRE.

Quantity of polarized material

The sample that achieved the highest polarization within the prototype SABRE-polarized target had a substrate concentration of just 40 mM in a 1.6 mL solution, with a total substrate mass of just 5.2 mg. Scaling up SABRE by increasing the total volume of the solution or by increasing the substrate concentration is trivial for moderate increases, however for larger increases in volume there is demand for higher rates of *p*-H_2 supply, whilst for more concentrated solutions there are constraints from intermolecular relaxation and the availability of *p*-H_2 in solution.

Section 3.4 showed that above a 5% mass fraction (470 mM) of **3,5-dcpy** in **DCM-*d*$_2$**, intermolecular relaxation starts to dominate and significant losses in the substrate T_1 occur. It is thus proposed that substrate concentrations stay below this level during the polarization build-up process, in order to not see a drop in the achievable steady-state polarization. For the substrates **py** and **3,5-py-*d*$_2$** this concentration is equivalent to a solution containing around 4% by volume of the substrate.

As seen in Section 5.4.3, there was limited increase in the polarization when increasing the pressure above 2.5 bar for a 40 mM concentration of **3,5-py-*d*$_2$**. It is thus proposed that for a 4% by volume (470 mM) solution of **3,5-py-*d*$_2$**, the pressure would have to be around 30 bar in order for *p*-H_2

concentrations in solution to not be limiting. This should not pose significant engineering challenges. The rate of *p*-H_2 generation should also not be an issue as it has been shown that *p*-H_2 is stable for months when stored correctly. Hövener et al. found that the relaxation constant for *p*-H_2 to o-H_2 conversion in an aluminium storage cylinder was around 120 days [138].

5.6.2 Internal targets

DNP targets, commonly used in fixed-target experiments, are unsuitable for storage ring facilities due to their high material thickness and their demanding engineering requirements (strong magnetic fields, cryogenic cooling, microwave irradiation) to achieve polarization. Storage rings require extremely thin targets to minimize beam interactions that could lead to beam degradation or unwanted scattering effects. Instead, gas targets and frozen pellet targets are used. Gas targets, such as the atomic H gas target at COSY [139], are produced using a polarized atomic beam source. They cause minimal beam degradation, however suffer from low areal density leading to a reduced luminosity.

An alternative is frozen pellet targets, such as that used at CELSIUS/WASA [140]. These targets use µm-sized frozen droplets of gases injected into the beamline, offering higher areal densities than gas targets whilst maintaining a minimal impact on the beam. They are also compatible with ultra-high vacuum (UHV) environments, making them an attractive candidate for internal targets at the upcoming Electron-Ion Collider. However, for a frozen pellet target to deliver SABRE-polarized material, the polarization must survive the liquid-to-solid phase transition caused by vacuum freezing in UHV conditions. This is a phenomenon in which the outer layer of the droplet vaporizes in the low-pressure environment, freezing the inner layer of the droplet.

Phase change

As was discussed in Section 1.4.3, preservation of polarization through a phase change has been demonstrated for SABRE-polarized material by Schmidt et al. in a process coined Re-Dissolution SABRE (Re-D SABRE) [84]. Re-D SABRE involves the precipitation and redissolution of the SABRE substrate within an applied field, in order to produce a catalyst-free aqueous solution of the polarized substrate. Re-D SABRE has to this date only been shown for ^{13}C polarization, and it is yet to be shown whether this technique can be applied to a high-γ nucleus such as ^{1}H.

Successful preservation of ^{1}H polarization through a phase change has been achieved with dissolution-DNP [82], which rapidly injects hot water over a DNP-polarized sample within an applied field to thaw it. It is thus thought likely that a frozen-pellet target utilizing SABRE could be developed, where the polarization of the material would persist through the phase change.

5.7Chapter 5 Conclusions

This chapter has presented a prototype SABRE-polarized target capable of continuous polarization with precise digital timing and flow rate control. The operating principles of this target are that a pressure differential is used to drive *p*-H_2 flow through the apparatus, which is delivered into the solution within the polarization cell through a thin capillary, where polarization transfer then occurs. The operating pressure of this prototype can be adjusted by altering the inlet and back pressures of the apparatus, the *p*-H_2 flow rates can be adjusted digitally using a mass flow controller, and the flow durations can be adjusted via a digital timer.

It has been shown in Sections 5.4.1 and 5.4.3 that there is a strong dependence of the polarization levels that can be achieved on the *p*-H_2 flow rate. For low flow rates there is a quasi-linear dependence, whilst diminishing gains are seen at flow rates in excess of 600 scc min^{-1}. The flow rates that could be used during operation were restricted due to the high levels of solvent evaporation seen at higher rates.

It was shown in Section 5.4.2 that the key polarization metrics, the maximal polarization (P_{Max}), the polarization build-up constant (T_B) and decay constant (T_1) all had a strong dependence on the substrate excess relative to the catalyst. The highest P_{Max} of 4.3% was found for the 60-fold excess sample, whilst the T_1 was found to peak at around 26 s for samples with a 40-fold or higher excess. T_B was found to increase continuously over the studied range, reaching a maximum of 23 s. Here the T_1s were limited by the use of the partially-deuterated solvent methanol-d_3.

In Section 5.4.3 it was found for an optimized sample that there was only a weak dependence of the polarization on the pressure over the range 2.5-5.5 bar. This showed that the rate of H_2 exchange in solution was not the rate-limiting step, and that significant polarization increases would not result from higher pressures. Higher pressures could however be used for polarizing a more concentrated solution whilst maintaining the *p*-H_2 to catalyst excess in solution. With this optimized sample it was found that at pressures of 5.5 bar a polarization level of 25% could be reached after 2 minutes of bubbling. Extrapolating the flow rate dependence in this study predicts that at higher flow rates it may be possible to achieve 34% polarization for this sample.

The high polarization levels seen in this study were attributed the long T_1 of 70 s, allowing for significant polarization build-up before a steady state was reached. This was possible due to the switch from the partially-deuterated solvent methanol-d_3 to the fully-deuterated solvent 1,2-dichloroethane-d_4.

In Section 5.5, the performance of the prototype SABRE-polarized target was compared to current generation DNP targets: the frozen-spin target FROST and the Hall B continuously polarized target, both at Jefferson Lab. It was found that for the adjusted Figure of Merit (FoM'), a comparison metric independent of the beam intensity, that due to the lower polarization levels and dilution factor of the prototype SABRE target, FoM' was around 50 times lower than for the DNP targets.

It is predicted that a SABRE-polarized target will be able to operate at higher beam intensities than DNP targets, due its much lower sensitivity to heat deposition and ability to continually replenish radiation damaged material. A lower estimate for the operable electron beam currents for a SABRE target is set at 5 nA, based on preliminary radiation resilience testing at MAMI. It was found that at this lower estimate of usable beam current that the SABRE target would outperform the Jefferson Lab frozen spin target (FROST) by a factor of 7, based on the beam currents used at COMPASS [15]. In order to outperform the Hall B continuously polarized target, a SABRE target would have to operate with beam currents in excess of 100 nA, unless significant gains were made in the achievable polarization or the areal density of the target. Further investigation is needed to determine whether operating under these conditions is possible.

Lastly, in Section 5.6, the future improvements to the prototype target necessary for its use at an accelerator facility are discussed, including fixed-target and internal-target applications. Improvements that are necessary for both applications include reduced solvent evaporation rates and a method for isolating the polarized material from solution. For the former it is proposed that a condenser loop could be added to reintroduce lost solvent back into the polarization cell, in combination with a solvent vapour presaturator in order to reduce evaporative losses. For the latter it has been proposed that catalyst scavengers could be implemented in order to reduce the catalyst content, whilst a quickly removable solvent, for example a pressurized gas such as chloromethane-d_3, could be used in order to rapidly separate the substrate from solution.

For fixed target applications, it is necessary that large quantities of polarized material are produced in order to maximise the areal density of the target. Realistic estimates of target dimensions are a 1 cm diameter and a 4 cm length, equating to 3.2 g of target material for the prospective substrates **py** and **3,5-py-d_2**, three orders of magnitude higher than the substrate mass of 5.2 mg used in the prototype target in Section 5.4.3.

Scaling up the quantity of polarized material is anticipated to increase demand for rates of *p*-H_2 supply, alongside potentially causing issues with increased rates of relaxation and low availability of *p*-H_2 in solution. It is proposed that these issues can be resolved by generating and storing *p*-H_2 in advance (shown to be stable for months), limiting substrate concentrations to ≤4% by volume

during polarization build-up, and increasing pressures within the polarization vessel up to around 30 bar.

For internal target applications, SABRE is best suited for use in frozen pellet targets. This would involve the rapid vacuum freezing of μm-sized droplets of SABRE-polarized material. The successful preservation of ^{1}H SABRE-derived polarization through a liquid-to-solid phase transition is yet to be demonstrated. However, this transition has been successfully demonstrated for ^{13}C polarization in Re-D SABRE, and the reverse (solid-to-liquid) transition has been demonstrated for ^{1}H polarization with d-DNP. It is thus considered highly likely that the preservation of polarization through this phase transition is achievable.

Chapter 6 - Conclusions

The central aim of this thesis was to evaluate whether the shortfalls in the current methodologies for producing polarized nuclear targets for nuclear and particle physics experiments could be addressed with the recently developed nuclear polarization method Signal Amplification By Reversible Exchange (SABRE). Currently, polarized targets for fixed-target experiments are produced by dynamic nuclear polarization (DNP), a technology that utilizes the high gyromagnetic ratio of the electron to produce high levels of nuclear polarization under strong magnetic fields and sub-kelvin temperatures. DNP targets have proved very successful for polarized target experiments, allowing for a far greater understanding of the spin distribution within the nucleon in the physics community, alongside allowing for the measurement of many other spin-dependent observables. DNP targets do however face a number of limitations, restricting their usefulness within polarized target experiments.

The low temperatures needed for DNP greatly restrict the heat deposition that can occur within the target before polarization losses occur, limiting the beam intensities the targets can be used with. In addition to this, the large superconducting magnets needed for continuously polarized DNP targets place large amounts of material within the detector, greatly reducing the angular acceptance for scattered particles within experiments. 'Frozen-spin' targets, were developed to address this, where the polarization is maintained by lower holding fields after generation, allowing for greater angular acceptance. Frozen-spin targets however face their own limitations. The temperatures needed for frozen-spin operation are even lower than for continuous DNP polarization, on the order of tens of millikelvin, further restricting the allowable heat deposition from the beam and primarily restricting their use to photoproduction experiments. Additionally, both continuously polarized and frozen-spin DNP targets suffer from beam-induced radiation damage, reducing the productive running time of experiments due to time losses for target replacements. With a new generation of particle accelerator facilities, such as the 12 GeV upgrade at Jefferson Lab and the upcoming Electron-Ion Collider at Brookhaven National Laboratory, there is a demand for polarized target technologies that can operate at the frontiers of beam intensity.

SABRE is a recently developed hyperpolarization technique that is a subset of the *para*hydrogen-induced polarization methods, making use of the high spin order of the singlet nuclear spin isomer of molecular hydrogen, *para*hydrogen (p-H_2). SABRE is a technique which catalytically transfers spin order from p-H_2 to a target molecule in solution, operating at room temperature in weak (millitesla) magnetic fields. These target molecules are typically nitrogen-containing heterocycles, such as pyridine, which are able to coordinate to the (typically) iridium catalyst used for SABRE. In order for

SABRE to be suitable for producing material for polarized targets, it must be capable of producing material with a high dilution factor (fraction of polarizable nucleons) and a high polarization level, such that it favourably compares to DNP targets in the Figure of Merit - a metric determining the productivity of polarized scattering experiments. Additionally, it needed to be determined whether SABRE-polarized material is able to withstand the high radiation doses received by polarized targets.

In Chapter 2, a study into SABRE polarization efficiency, it was found that the highest average nucleon polarization among a range of tested substrates was achieved with pyridine (**py**), whilst the longest polarization relaxation time was achieved with 3,5-dichloropyridine (**3,5-dcpy**). Both of these qualities were desirable for polarized target applications, as long polarization relaxation times (T_1s) can allow for the sustained build-up of polarization, allowing for a high steady-state polarization to be reached within a continuously polarized target.

These findings inspired the synthesis of a novel selectively-deuterated substrate, 3,5-pyridine-d_2 (**3,5-py-*d*$_2$**). This allowed for the creation of magnetically isolated *ortho* and *para* proton sites, which would experience lower rates of dipolar relaxation than were seen in **py**, whilst maintaining its high polarization transfer efficiency. It was found that the polarization levels achieved with **3,5-py-*d*$_2$** were 39% higher than could be achieved with **py** under comparable conditions, however this represented a decrease in the average nucleon polarization of 19% due to the lower dilution factor of **3,5-py-*d*$_2$**. After correcting for the pre-measurement polarization decay, it was found that the average ^{1}H polarization level of **3,5-py-*d*$_2$** reached 18% using the [Ir(**IMes**)(COD)Cl] (**IMes**) catalyst and the co-ligand dimethyl sulfoxide-d_6 (**DMSO-*d*$_6$**) - a significant step towards achieving the high polarization levels possible with DNP. The average ^{1}H T_1 of **3,5-py-*d*$_2$** was found to be 75 s at a 40-fold substrate excess, representing a 90% increase over **py** and only an 11% decrease compared to **3,5-dcpy** under comparable conditions. It was thus determined that the selective deuteration of **py** to form **3,5-py-*d*$_2$** was successful in combining the high polarization levels of **py** with the long T_1s of **3,5-dcpy**, in order to create a substrate that was promising for polarized target applications.

Chapter 2 also investigated the possibility of performing SABRE within a 'neat' liquid, where a separate solvent is not used and the SABRE catalyst is dissolved within a neat solution of the substrate. Here a 1% by volume solution of **py** in **py-*d*$_5$** was used, with the deuterated form of the substrate **py** being used to minimize the depletion of the *p*-H_2 spin bath. It was found that polarization levels with this sample were significantly lower than could be achieved in the traditional SABRE solvent methanol-d_4, theorized to be due to the low catalyst and *p*-H_2 concentrations relative to the substrate. This led to a lower catalytic activity and slower rates of

p-H_2 exchange than were needed for efficient polarization transfer, and thus it is proposed that this is not a promising approach to producing highly polarized concentrated solutions of SABRE material.

Also in this chapter, perfluorocarbons (PFCs) were investigated as a potential SABRE solvent, with the aim to use their high gas solubility to increase the low dissolved *p*-H_2 concentrations commonly found in SABRE samples, frequently limiting for polarization transfer. Generally, the solubility of the SABRE catalyst in PFCs was found to be poor, however moderate solubility was found using the PFC methyl perfluorobutyl ether (**8**). At low catalyst loadings, the polarization of **py** in **8** was found to benefit from the addition of **DMSO-*d*$_6$**, however polarization levels were significantly lower than could be achieved in the traditional SABRE solvent methanol-d_4. Higher dissolved catalyst concentrations could be achieved using a mixture of **8** and methanol-d_4, however this still performed poorer than the traditional SABRE solvent. PFCs are considered mildly promising for ^{1}H polarization, however are more promising for heteronuclei polarization, such as for ^{15}N, as the ^{15}N nucleus is less susceptible to dipolar relaxation from the high-γ ^{19}F nucleus. ^{15}N polarization levels were found to be 53% higher with **8**, and 100% higher in the mixture of **8** and methanol-d_4, than could be achieved with methanol-d_4 alone.

Polarization of the ^{15}N nucleus was also investigated in Chapter 2, with **py** considered as a candidate for a dual ^{15}N/^{1}H polarized target, while acetonitrile-d_3 (**acn-*d*$_3$**) was studied due to its high dilution factor. ^{15}N polarization of 8% was achieved for **py** at a 5-fold substrate excess, while the molar polarization of the solution was found to peak at an 80-fold substrate excess. For **acn-*d*$_3$**, it was found that the presence of the co-ligand benzylamine was found to significantly increase the polarization levels, rising to 8%, an order of magnitude higher than those achieved without a co-ligand.

In Chapter 3, a study into the factors that influence relaxation, the substrate **3,5-dcpy** was of primary interest due to its long T_1 allowing for a more precise investigation into the influencing factors. A key result here was the temperature dependence of the T_1, where it was found that the T_1 for **3,5-dcpy** peaked at 31°C, and demonstrated a maximum temperature sensitivity of only 7% °C^{-1}. This showed that the T_1 of the substrate was highest at similar temperatures to those optimal for polarization transfer, alongside showing that the sensitivity of the T_1 to heat deposition was not a significant concern, unlike for DNP targets. It was also found that the T_1 of **3,5-dcpy** showed little sensitivity to the applied magnetic field strength over the range 1.0-11.4 T, demonstrating that the polarization can be preserved without the need for strong superconducting magnets, which would reduce the acceptance angles in scattering experiments. The preservation

of polarization is thought necessary for the processing of SABRE-polarized material, in order to remove it from solution and thereby increase the dilution factor.

The dependence of the T_1 on the substrate excess relative to the catalyst was also investigated for **3,5-dcpy**. It was found that for both the **IMes** and **IMes-*d*$_{22}$** catalysts that the T_1 was strongly dependent on the substrate excess, with the T_1 starting to plateau at around a 200-fold excess. It was found that the T_1 of **3,5-dcpy** approached its maximum value at a lower excess with **IMes-*d*$_{22}$** compared to with **IMes**, with it also being found that the maximum T_1 for the *para* position approached a value of around 240 s at a 200-fold excess, likely the longest ^{1}H T_1 measured in room temperature solution-state NMR - an exciting result. This long T_1 was necessary to facilitate an experiment measuring the influence of an incident particle beam on the T_1 of SABRE-polarized material, presented in Chapter 4.

Alongside the dependence of the T_1 on the relative catalyst concentration, the dependence of the T_1on the substrate concentration in solution was also measured. Here it was found that there was no change seen between a substrate mass fraction of 1% and 5% in solution, however substrate mass fractions of 10% and higher in solution saw a significant decrease in the T_1. This thus informed that it was necessary to stay below this substrate concentration in solution in order to maximize the T_1, and thus the achievable steady-state polarization of SABRE material. This 5% mass fraction was equivalent to a substrate concentration of 470 mM, equating to a concentration of 4% by volume for the candidate SABRE substrates for polarized target applications, **py** and **3,5-py-*d*$_2$**.

Chapter 4 detailed the first ever test of the resilience of the polarization of SABRE material to an incident particle beam, alongside subjecting a SABRE sample to a high radiation dose to test for the effects of radiation damage. These tests were performed in the A2 hall at the Mainz Microtron (MAMI) facility using a portable benchtop MRI spectrometer as a novel method for measuring the polarization level of samples in-beam.

The polarization levels over time of three halogenated substrates, **3,5-dcpy**, 3,5-dibromopyridine (**3,5-dbpy**) and 2,6-dichloropyrazine (**2,6-dcpz**), chosen for their long T_1s, were measured within the A2 photon beam at MAMI. These samples were subject to a Bremsstrahlung photon flux of 4×10^8 Hz, produced from a 10 nA beam current of the 855 MeV MAMI electron beam incident on a thin Möller radiator, with a calculated energy deposition rate of 0.6 mJ s^{-1}. It was found through multiple methods of analysis that there was no evidence for any beam-induced polarization decay effects, with the tightest limits being set for the substrates **3,5-dcpy** and **2,6-dcpz**, for which it was found that the decay rates increased by ≤11% and ≤7% respectively, to a confidence level of 1σ.

Weaker limits were set for the substrate **3,5-dbpy**, for which the SNR after the beam turned on was poor, however this sample also exhibited no evidence for an increased decay rate in-beam.

The MAMI electron beam was also used to subject a SABRE sample to a high radiation dose, by positioning it in close proximity to the electron beam dump. The sample was left to accumulate a dose over four days of running, with the total accumulated dose being equivalent to that from a 1 nA electron beam for 15 minutes. It was found that the sample retained significant potential for repolarization after the received dose, achieving in excess of 80% of its original polarization, with no loss to the T_1. As a polarized target making use of SABRE is theorized to be capable of continuous replacement of the target material on a timescale of minutes, a lower estimate of the operable electron beam currents for a SABRE-polarized target is set at 5 nA. The rapid replacement of target material with SABRE owes to its room-temperature, solution-state nature, in combination with fast polarization build-up times.

Future work proposed after the experiment at MAMI includes in-beam polarization decay measurements at a facility capable of producing a higher photon flux, in addition to achieving increased measurement precision using a measurement device with higher sensitivity, such as a benchtop NMR spectrometer. It is also proposed that future work should extend the limits of heat and radiation deposition from particle beams, with high intensity electron beams being the logical next step. These experiments should make use of a continuously polarizing prototype SABRE target, such as that presented in Chapter 5, alongside exploring the challenges of introducing polarized material into vacuum.

Chapter 5 presented the development, operation and performance of a prototype SABRE polarized target. This prototype target operates under continuous polarization, in contrast to the 'Shake and drop' approach where the quantity of *p*-H_2 available for polarization transfer was constrained by the volume of the cell. The prototype target makes use of a pressure differential across the apparatus, delivering *p*-H_2 into the polarization cell through a thin capillary. The *p*-H_2 flow rates are adjustable via a mass flow controller, the flow timings can be adjusted through a digital timer connected to solenoid valves upstream and downstream of the polarization cell, and the operating pressures can be adjusted by controlling the back pressure and the input pressure from the *p*-H_2 generator.

It was found that the polarization levels achievable with the prototype target exhibited a strong dependence on the flow rate of *p*-H_2 through the polarization cell. For the substrate **py**, a quasi-linear dependence of the polarization on the *p*-H_2 flow rate was seen at low rates (<50 scc min^{-1}), while diminishing returns were seen for rates in excess of 400 scc min^{-1}.

The key polarization metrics, the maximal polarization (P_{Max}), the polarization build-up constant (T_B) and the decay constant (T_1) were all found to have a strong dependence on the substrate excess relative to the catalyst for the substrate **3,5-py-*d*$_2$**. Using the solvent methanol-d_3, the polarization was found to peak at 4% at a substrate excess of 60-fold, whilst the T_1 peaked at 26 s for a 40-fold excess. T_B was found to continually rise across the investigated range of substrate excesses, reaching 23 s at an 80-fold excess.

It was found that the polarization of **3,5-py-*d*$_2$** was only weakly dependent on the pressure within the polarization cell over the range 2.5 bar to 5.5 bar, however a much stronger dependence was found on the flow rate of *p*-H_2. At a flow rate of 300 scc min^{-1} and a pressure of 5.5 bar it was found that the polarization of **3,5-py-*d*$_2$** reached 25% after 2 minutes of bubbling, found upon correcting for the pre-measurement decay when using the solvent 1,2-dichloroethane-d_4. Extrapolating the dependence of polarization on the flow rate found that polarization levels of 34% would be achievable at a flow rate of 1200 scc min^{-1}, however issues with solvent evaporation prevented the use of flow rates this high. These high polarization levels were attributed to the long T_1s achievable using a fully-deuterated solvent, with an average T_1 of 70 s being measured in this investigation, alongside the benefits from the deuterated catalyst **IMes-*d*$_{22}$**.

When comparing the performance of the prototype SABRE target to the frozen-spin target FROST and the upgraded Hall B continuously polarized target, both at Jefferson Lab, it was found that although the areal density of the prototype target exceeded these DNP targets, the adjusted Figure of Merit (FoM') was around 50 times lower than these targets, owing to the lower polarization levels and dilution factor of the material within the SABRE target. For the full Figure of Merit, inclusive of the beam current, it was found that for experiments using electron beams that the prototype target performed favourably compared to FROST, outperforming it by a factor of 7 using the 5 nA lower estimate for operable beam intensities of the SABRE target and the beam currents used at COMPASS [15]. In order to outperform the Hall B continuously polarized target, beam currents in excess of 100 nA would have to be utilized, unless significant gains to FoM' were made for the SABRE target.

Future improvements to the prototype that are necessary for implementing SABRE-polarized targets include reducing the rate of solvent evaporation and isolating the polarized material from solution. In addition to this, for fixed-target applications it is necessary that the quantity of material polarized by SABRE is increased, whereas for internal target applications it is necessary that SABRE-derived polarization can be demonstrated to survive the liquid to solid phase transition necessary for frozen pellet targets. Suggestions of how to achieve these improvements have been proposed.

In conclusion, SABRE has been shown to be a promising candidate for addressing the issues faced by DNP polarized targets at the intensity frontier. This comes from the ability of SABRE to operate at room temperature, with a corresponding high tolerance for heat deposition, alongside the ability for SABRE-derived polarization to be generated and maintained without the need for superconducting magnets, allowing for 4π angular acceptance in particle scattering experiments.

Chapter 7 - Experimental

7.1 Equipment and materials

7.1.1 NMR spectrometers

Magnetic field (T)	^{1}H Resonance Frequency (MHz)	Spectrometer Information
1.0	43	Magritek Spinsolve Carbon
7.0	300	300 MHz Fourier Magnet, Bruker Avance III console, BBO probe with Z-gradient.
9.4	400	400 MHz Ultrashield™ Magnet, Bruker Avance III console, BBI probe with Z-gradient.
11.7	500	500 MHz Ascend™ Magnet, Bruker Avance III HD console, BBI probe with Z-gradient.

7.1.2 Benchtop MRI

Magnetic field (T)	^{1}H Resonance Frequency (MHz)	Spectrometer Information
0.33	14	Resonint Ilumr

7.1.3 Prototype target equipment specifications

Component	Model	Notes
Mass flow controller	Sensirion SFM5500-2SLM	Flow rate range of 0.002-2 scc min^{-1} (1 scc min^{-1} = 1 L min^{-1} at 0°C, 1 bar).
Solenoid valves	Festo VZWD-L	
Tubing	PEEK, 1/8” and 1/16”	
Benchtop MRI	Resonint Ilumr	0.33 T Halbach array
PTF magnet	Custom-built	6 mT Halbach array

7.1.4 *Para*hydrogen generation

The parahydrogen (p-H_2) used for 'shake and drop' studies was produced by passing hydrogen gas from a cylinder over a paramagnetic iron (III) oxide catalyst at 28K. This facilitates the spin transfer process to produce a constant supply of p-H_2 with a purity of >99%. Pressures for these experiments were read as absolute pressure.

7.1.5 Solvents and substrates

Substrates and solvents were purchased from Alfa-Aesar, Fluorochem, Apollo Scientific or Sigma Aldrich and were used without any further processing or purification.

All ^{15}N labelled substrates were purchased from Cambridge Isotope Laboratories or Sigma-Aldrich and used without further processing or purification.

All the iridium pre-catalysts utilised in this work were synthesised by Dr Victoria Annis, Dr Peter J. Rayner or Dr Kieren J. Evans according to literature procedures.

7.2 General experimental procedures

7.2.1 Sample preparation and activation

Degassing

Samples prepared inside NMR tubes sealed with a J Young's valve were removed of paramagnetic oxygen through degassing. The procedure varies according to the solvent, however the general procedure is as follows. A degassing cycle involves cooling the sample followed by exposing the sample to a strong vacuum. The sample is exposed to vacuum until the pressure in the system is below 0.1 µbar if achievable, however pressures below 1 µbar are tolerated. The sample is then gently thawed/warmed back to room temperature before the next cycle. Samples are typically subject to 3 cycles of this procedure. Additional information is given in Table 7.1.

Solvent	Information
Methanol-d_3/d_4	Samples are cooled using a bath of dry ice/acetone and thawed by hand.
Dichloromethane-d_2 **1,2-Dichloroethane-d_4**	Samples are frozen using a bath of liquid nitrogen. Samples are thawed by running room temperature acetone against the NMR tube.
Methyl perfluorobutylether	Samples are frozen using a bath of liquid nitrogen. Samples are thawed by running room temperature acetone against the NMR tube. Samples are subject to 5 cycles due to increased gas solubility.

Table 7.1 - Additional information for the degassing procedures of various solvents.

Glovebox

Samples not compatible with the above procedure are prepared within a glovebox to ensure they are free of oxygen. The solvents used for the preparation of these samples are themselves degassed according to the above procedure inside a Schlenk tube before being transferred to the glovebox.

Sample activation

Subsequent to the removal of paramagnetic impurities, samples are pressurized with 4 bar of H_2 and left to activate. Typical activation times vary from 1-3 hours. Activation of the catalyst is confirmed via ^{1}H NMR spectroscopy.

7.2.2 'Shake and drop' polarization method

After activation, H_2 is removed from the headspace of the sample and replaced with 4 bar of *p*-H_2. The headspace of the sample is replenished with 'fresh' *p*-H_2 for each polarization run. Polarization transfer occurs at room temperature (293 K).

^{1}H

Samples are placed within a 6 mT handheld Hallbach array and shaken vigorously for a specified time (normally 10-30 s), before rapid transfer to an NMR spectrometer or MRI for measurement.

^{15}N

Samples are polarized using a polarization field generated by a tuneable copper coil connected to a 12V power supply. The achieved magnetic field can vary between -10 and 10 mG (-1 µT to 1 µT). The coil is housed within a handheld mu-metal shaker, providing shielding from the Earth's magnetic field. Samples are shaken vigorously inside the applied field for a specified time (10-30 s) before rapid transfer to an NMR spectrometer for measurement.

Transfer for measurement

Samples are transferred for measurement subsequent to the polarization step by ceasing shaking the sample, removing it from the applied field, and transferring to the measurement device (NMR/MRI) by hand. Typically transfer times were fixed at 10 s for reproducibility and alternative transfer times will be stated.

7.3 Measurements

7.3.1 Signal enhancements and polarization

Signal enhancements and polarization measurements of hyperpolarized samples were found using a single 90° tip angle FID when using NMR spectroscopy. For measurements made using the benchtop MRI, there was no functionality for a variable receiver gain and thus an appropriate tip angle FID was chosen in order for the signal amplitude to remain within acceptable limits.

7.3.2 Hyperpolarized $\boldsymbol{T_1}$ recovery

A series of small tip-angle FID scans with a fixed time interval was used to sample the polarization decay. Typically, 10-30 scans with a fixed tip angle were used. The tip angle was chosen to maximise the transverse magnetization in the final scan in order to maximise the longevity of the sequence. Eq. 7.1 and Eq. 7.2 describe how the longitudinal and transverse components of the magnetization within the sample evolve with each scan:

$$M_{Z,n} = M_{Z,n-1} \cdot \cos(\theta_n) \qquad (Eq.\,7.1)$$

$$M_{XY,n} = M_{Z,n-1} \sin(\theta_n) \qquad (Eq.\,7.2)$$

where $M_{Z,n}$ is the longitudinal magnetization after the nth scan, $M_{XY,n}$ is the transverse magnetization after the nth scan, and θ_n is the tip angle used in the nth scan.

7.3.3 $\boldsymbol{T_1}$ inversion recovery

T_1 inversion recovery measurements were performed using the standard pulse sequence available on TopSpin™. This sequence applies a 180° tip angle pulse which rotates the magnetization vector from the +Z to the -Z axis. This is followed by a delay time, τ, which allows the magnetization to partially relax back towards the +Z axis, followed by a 90° tip angle pulse which rotates the recovered component of the magnetization vector into the XY-plane for acquisition.

Experiments were performed using a series of τ values which range from $\tau \ll T_1$ (allowing for little relaxation after the inversion pulse), to $\tau \gg T_1$ (allowing for full recovery after the inversion pulse). It is necessary that a delay period of at least five times T_1 is allowed before the inversion pulse to ensure that the magnetization has returned to thermal equilibrium. A diagram of the pulse sequence used can be seen in Figure 7.1.

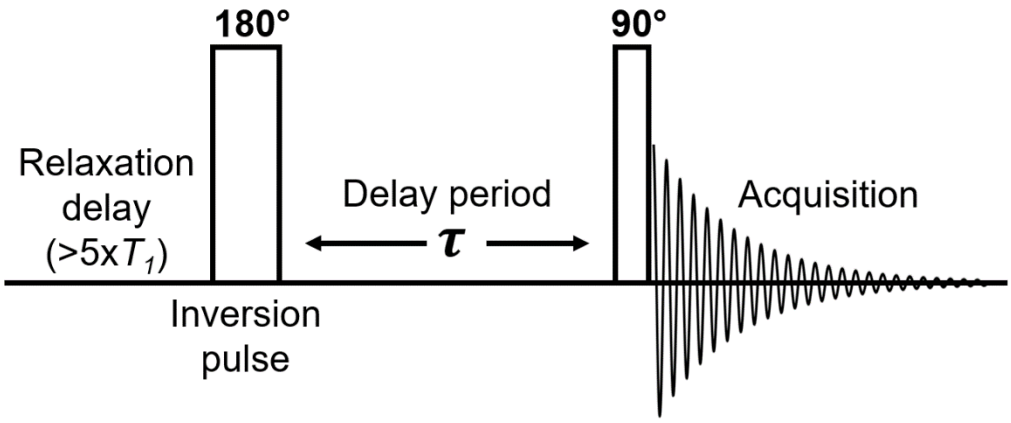

Figure 7.1 - Pulse sequence used in T_1 inversion recovery experiment.

7.3.4 Exchange spectroscopy

Measuring the exchange rates of substrates in solution was done using exchange spectroscopy (EXSY). The measurements used a standard selective 1D NOESY experiment which selectively excites the ^{1}H resonance of interest before leaving a time delay, known as the mixing time, where chemical exchange is allowed to occur. The magnetization is aligned with the -Z axis by the initial 90°-180°-90° pulses and is refocused by another 180° pulse before a 90° pulse is used for acquisition. This pulse sequence is shown in Figure 7.2. The mixing time is varied over the length of time that exchange is expected to occur, typically between 0.01 s and 5 s. Integrals of the bound and free peaks at varying mixing times are used to quantify the substrate dissociation rate.

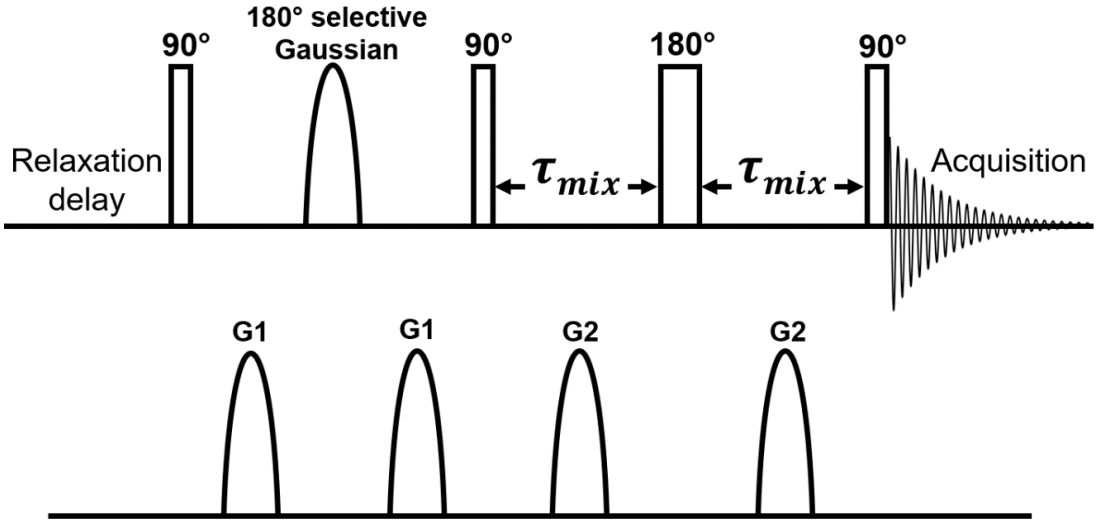

Figure 7.2 - Pulse sequence for 1D NOESY experiment, showing the RF pulses (top) and the gradient pulses (bottom).

7.4Calculations

7.4.1 Signal enhancements and polarization

The signal enhancement factor for ^{1}H and ^{15}N polarization was calculated using Eq. 7.3, where ε is the signal enhancement factor and I_{hyp} and $I_{thermal}$ are the integrals of the hyperpolarized and thermally polarized substrate signals:

$$\varepsilon = \frac{I_{hyp}}{I_{TE}}. \qquad (Eq. 7.3)$$

Both spectra were recorded using the same acquisition parameters. For calculating ^{15}N enhancements when using a non-labelled sample, thermally polarized signals were unable to be acquired and thus a ^{15}N-labelled external reference sample was used. The external reference used was a 5 M solution of $^{15}NH_4Cl$ in D_2O.

The thermal polarization of nuclei is given by:

$$P_{TE} = \tanh\left(\frac{\gamma \hbar B_0}{2k_B T}\right) \qquad (Eq. 7.4)$$

where γ is the gyromagnetic ratio of the nucleus, $\hbar$ is the reduced Planck constant, B_0 is the magnitude of the applied field, k_B is the Boltzmann constant and T is the temperature in Kelvin.

The polarization of a hyperpolarized sample is thus given by

$$P_{hyp}(\%) = \varepsilon \times P_{TE}(\%). \qquad (Eq. 7.5)$$

7.4.2 Hyperpolarized T_1 recovery

After the hyperpolarized T_1 recovery sequence, the signal integrals ($I_{hyp,n}(t)$) are performed and collated. Throughout the sequence, the longitudinal and transverse components of the magnetization evolve as:

$$M_{Z,n}(t,\theta) = M_{Z,0} \cdot \left(\prod_{i=1}^{n} \cos(\theta_i)\right) \cdot e^{-\frac{t}{T_1}} \qquad (Eq. 7.6)$$

$$M_{XY,n}(t,\theta) = M_{Z,0} \cdot \left(\prod_{i=1}^{n-1} \cos(\theta_i)\right) \cdot \sin(\theta_n) \cdot e^{-\frac{t}{T_1}} \qquad (Eq. 7.7)$$

where $M_{Z,0}$ is the longitudinal magnetization before the first scan at time $t = 0$, and t is the time in seconds since the start of the sequence. As the measured signal integrals are proportional to the transverse magnetization, it is necessary to remove the dependence on the pulse angle sequence

in order to find the time dependence of the magnetization decay. This is done by applying a correction factor, A_n:

$$I_{corr,n}(t) = A_n(\theta) \times I_n(t,\theta) \quad (Eq.7.8)$$

$$A_n = \left[M_{Z,0} \cdot \left(\prod_{i=1}^{n-1} \cos(\theta_i) \right) \cdot \sin(\theta_n) \right]^{-1} \quad (Eq.7.9)$$

Here $I_n(t,\theta)$ is the uncorrected integral from the nth scan and $I_{corr,n}(t)$ is the integral after the correction factor has been applied. Once the integrals $I_{corr,n}$ have been found, they are normalized such that:

$$I_{corr,norm,0} = 1 \quad (Eq.7.10)$$

where $I_{corr,norm,n}$ are the normalized corrected integrals. The value of T_1 was found by fitting an exponential decay to the normalized corrected integrals using the graphing software Origin.

7.4.3 T_1 inversion recovery

After the T_1 inversion recovery sequence, the signal integrals are performed and collated. The integrals of the peaks of interest from this sequence are fitted to the equation:

$$I_{invrec} = I_0 \left(1 - 2e^{-\tau/T_1}\right) \quad (Eq.7.11)$$

where I_{invrec} is the value of the integral, I_0 is the integral at thermal equilibrium, τ is the delay between the pulses and T_1 is the time constant for longitudinal relaxation. This is performed using the graphing software Origin.

7.4.4 Exchange spectroscopy

After the EXSY sequence, measurement data is imported into python and fit parameters are found. The fitting equation used is

$$B = (100 - c)e^{-kt} + c \quad (Eq.7.12)$$

where B is the percentage of the total signal integral represented by the bound substrate, c is the asymptote for B at long mixing times, k is the substrate dissociation rate (s^{-1}) and t is the mixing time (s). Errors were calculated using jackknife resampling, whereby one data point at a time from the dataset was systematically excluded and the fit parameters were recalculated. The standard deviation from these jackknife fit parameters was taken to be the measurement error.

7.4.5 Polarization back-propagation

The back-propagated polarization values are calculated as follows:

$$P_{adj} = P_{measured} \times Correction\ factor \qquad (Eq.\ 7.13)$$

$$Correction\ factor = e^{-t_{EF}/T_{1,EF}} \cdot e^{-t_{HF}/T_{1,HF}} \qquad (Eq.\ 7.14)$$

$$\therefore P_{adj} = P_{measured} \times e^{-\left(\frac{t_{EF}}{T_{1,EF}} + \frac{t_{HF}}{T_{1,HF}}\right)}. \qquad (Eq.\ 7.15)$$

Here P_{adj} is the back corrected polarization, $P_{measured}$ is the measured polarization, t_{EF} and t_{HF} are the respective transfer times within 'Earth's field' and high field respectively, and $T_{1,EF}$ and $T_{1,HF}$ are the effective $T_1 s$ at 'Earth's field' and high field respectively.

The errors are found through standard error propagation calculations to be:

$$\frac{\sigma_{P_{adj}}}{P_{adj}} = \sqrt{\left(\frac{\sigma_{P_{measured}}}{P_{measured}}\right)^2 + \left(-t_{EF}\sigma_{(T_{1,EF})^{-1}}\right)^2 + \left(-t_{HF}\sigma_{(T_{1,HF})^{-1}}\right)^2}$$

where $\sigma_{(T_{1,EF})^{-1}}$ and $\sigma_{(T_{1,HF})^{-1}}$ are the absolute errors of the reciprocal of the measured T_1 values at 'Earth's field' and high field respectively. The error in the transfer times is taken to be negligible in comparison to the other errors.

Chapter 8 - Appendix

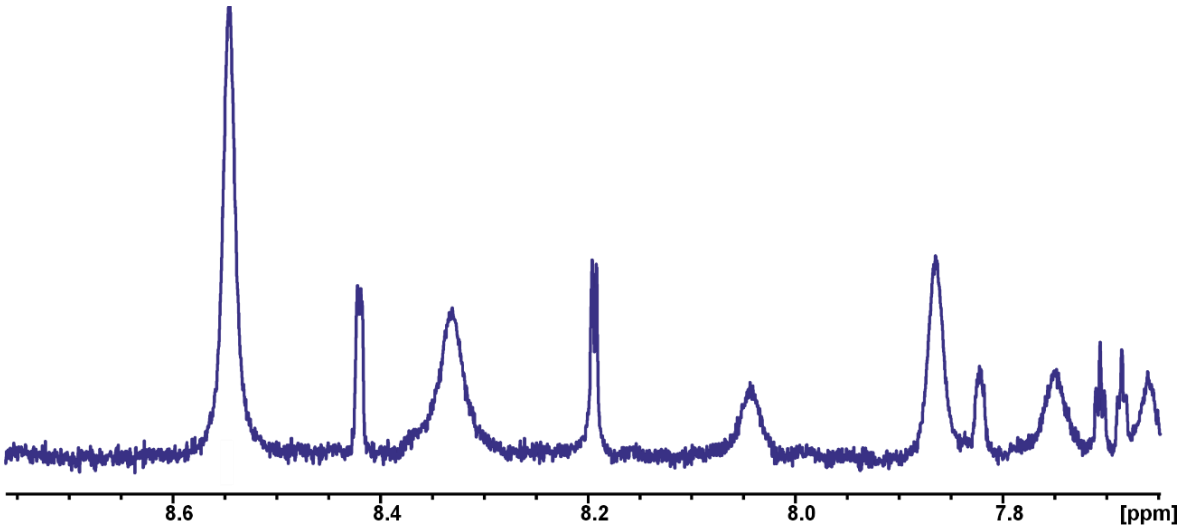

Figure 8.1 -^{1}H NMR spectrum for the free ortho (left) and free para (right) protons in ***3,5-py-d$_2$*** (400 MHz, methanol-d_3, 298 K). *The sample contains 5 mM* ***IMes,*** *25 mM* ***3,5-py-d$_2$*** *in methanol-d_3.*

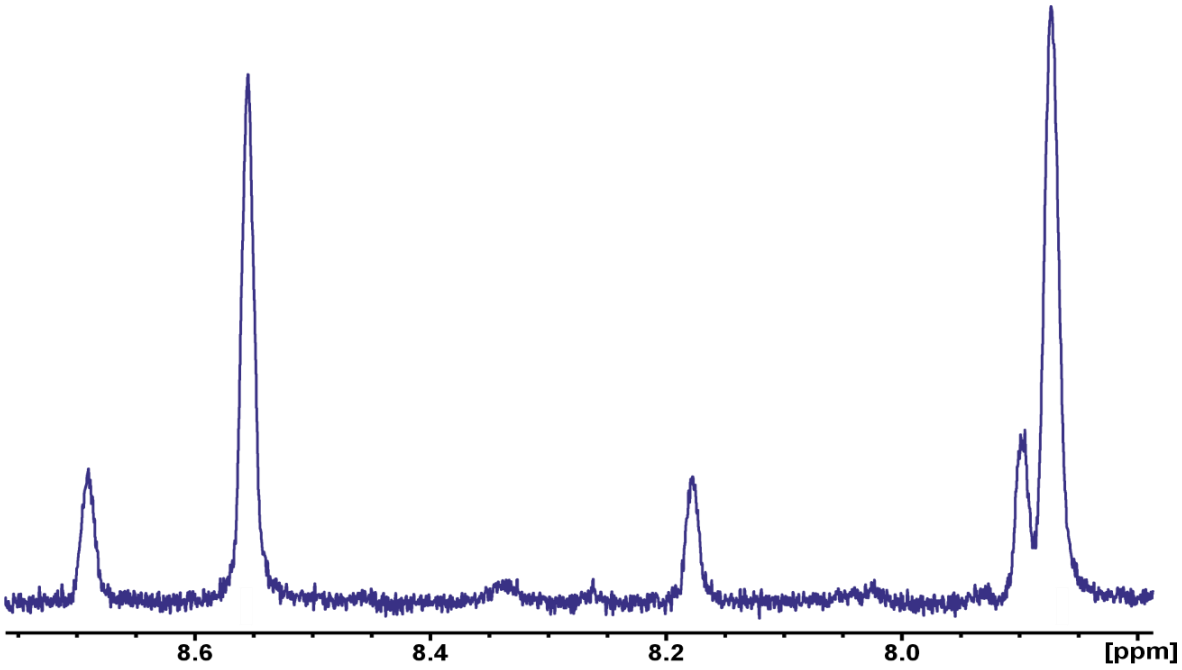

Figure 8.2 -^{1}H NMR spectrum for the free ortho (left) and free para (right) protons in ***3,5-py-d$_2$*** (400 MHz, methanol-d_4, 298 K). *The sample contains 5 mM* ***IMes,*** *20 mM* ***DMSO-d$_6$,*** *25 mM* ***3,5-py-d$_2$*** *in 0.6 mL of methanol-d_4.*

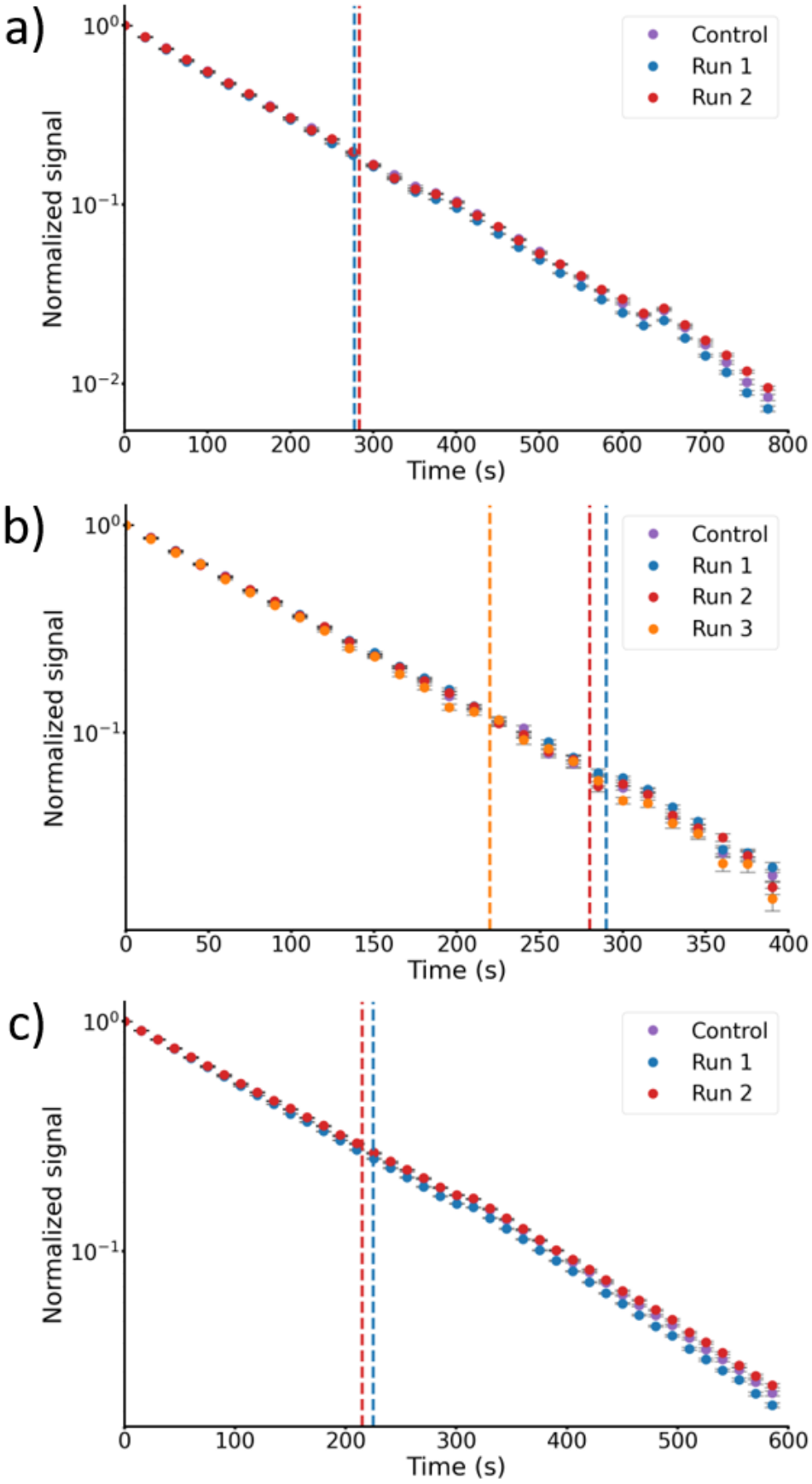

Figure 8.3 - Normalized polarization decay profiles with a logarithmic y-axis for a) ***3,5-dcpy****, b)* ***3,5-dbpy****, and c)* ***2,6-dcpz****. The dotted lines indicate the time of beam.*

List of Acronyms

CASH-SABRE - Catalyst-Separated Hyperpolarization through SABRE

CERN - Conseil Européen pour la Recherche Nucléaire

CLAS12 - CEBAF Large Acceptance Spectrometer for operation at 12 GeV beam energy

COMPASS - COmmon Muon Proton Apparatus for Structure and Spectroscopy

CPMG - Carr-Purcell-Meiboom-Gill sequence

CSA - Chemical Shift Anisotropy

CW - Continuous-wave

d-DNP - dissolution DNP

DNP - Dynamic Nuclear Polarization

EMC - European Muon Collaboration

FFT - Fast Fourier Transform

FID - Free Induction Decay

Geant4 - Particle physics simulation toolkit

HDSM - Harmonic Double-Sided Microtron

IR - Infra-red

JGU - Johannes Gutenberg University

LAC - Level anti-crossing

LASER - Light Amplification by Stimulated Emission of Radiation

MAMI - MAinz MIcrotron

MASER - Microwave Amplification by Stimulated Emission of Radiation

MR - Magnetic Resonance

MRI - Magnetic Resonance Imaging

NHC - *N*-heterocyclic carbene

NMR - Nuclear Magnetic Resonance

OD - Outer diameter

P&ID - Piping and Instrumentation Diagram

PFC - Perfluorocarbon

PHIP - *Para*hydrogen-induced Polarization

PPM - Parts Per Million

PTF - Polarization Transfer Field

RASER - Radio Amplification by Stimulated Emission of Radiation

Re-D SABRE - Re-Dissolution SABRE

RTM - Race Track Microtron

SABRE - Signal Amplification By Reversible Exchange

SABRE-SHEATH - SABRE in SHield Enables Alignment Transfer to Heteronuclei

SLAC - Stanford Linear Accelerator Centre

SNR - Signal to Noise Ratio

T_1 - Longitudinal relaxation time constant

TLC - Thin-layer chromatography

UV-vis - UV-visible light

ZULF NMR - Zero- to ultralow-field NMR

List of chemical abbreviations

2,6-dcpz - 2,6-dichloropyrazine

3,5-dbpy - 3,5-dibromopyridine

3,5-dcpy - 3,5-dichloropyridine

3,5-py-*d*$_2$ - 3,5-pyridine-*d*$_2$

3-atz - 3-amino-1,2,4-triazine

3-py-*d*$_1$ - 3-pyridine-*d*$_1$

Acn - Acetonitrile

Bpy - 2,2'-bipyridine

Bza -Benzylamine

DCM - Dichloromethane

DMSO - Dimethyl sulfoxide

IMes - 1,3-Bis(2,4,6-trimethylphenyl)-1,3-dihydro-2H-imidazol-2-ylidene

p-H_2 - *para*hydrogen

Phen - 1,10-phenanthroline

Py - pyridine

SIMes - 1,3-Bis(2,4,6-trimethylphenyl)-4,5-dihydroimidazol-2-ylidene

TMS - Tetramethylsilane

PFC study:

1 - Deuterium oxide

2 - Methanol-*d*$_4$

3 - Acetonitrile-*d*$_3$

4 - Ethanol-*d*$_6$

5 - Dichloromethane-*d*$_2$

6 - Tetrahydrofuran-*d*$_8$

7 - Toluene

8 - Methyl perfluorobutylether

9 - Perfluorodecalin

10 - Perfluorononane

11 - Perfluorohexane

12 - Perfluoro-1-decene

13 - Methyl perfluorocyclohexane

14 - Perfluoroheptane

15 - 1-Bromoheptadecafluorooctane

16 - Perfluorooctane

References

[1] C. D. Keith *et al.*, Nuclear Instruments and Methods in Physics Research Section A: Accelerators, Spectrometers, Detectors and Associated Equipment **501**, 327 (2003).

[2] C. Keith *et al.*, Nuclear Instruments and Methods in Physics Research Section A: Accelerators, Spectrometers, Detectors and Associated Equipment **684**, 27 (2012).

[3] K. Abe *et al.*, Physics Letters B **364**, 61 (1995).

[4] K. Abe *et al.*, Physical Review Letters **75**, 25 (1995).

[5] J. Ashman *et al.*, Physics Letters B **206**, 364 (1988).

[6] A. Ivanilov, in *XIV Advanced Research Workshop on High Energy Spin Physics (DSPIN-11)*, p. 246.

[7] J. Ahrens *et al.*, Physical Review Letters **87**, 022003 (2001).

[8] S. Simula, B. Saghai, N. C. Mukhopadhyay, and V. D. Burkert, *N* Physics and Nonperturbative Quantum Chromodynamics: Proceedings of the Joint ECT*/JLAB Workshop, Trento, Italy, May 18–29, 1998* (Springer Science & Business Media, 1999), Vol. 11.

[9] A. W. Overhauser, Physical Review **92**, 411 (1953).

[10] T. R. Carver and C. P. Slichter, Physical Review **92**, 212 (1953).

[11] A. Abragam, Physical Review **98**, 1729 (1955).

[12] A. A, B. M, C. P, C. J, R. P, and T. J, Physics Letters **2**, 310 (1962).

[13] O. Chamberlain, C. D. Jeffries, C. H. Schultz, G. Shapiro, and L. Van Rossum, (1963).

[14] O. Leifson and C. Jeffries, Physical Review **122**, 1781 (1961).

[15] V. Andrieux *et al.*, Nuclear Instruments and Methods in Physics Research Section A: Accelerators, Spectrometers, Detectors and Associated Equipment **1025**, 166069 (2022).

[16] W. Meyer, J. Heckmann, C. Hess, E. Radtke, G. Reicherz, L. Triebwasser, and L. Wang, Nuclear Instruments and Methods in Physics Research Section A: Accelerators, Spectrometers, Detectors and Associated Equipment **631**, 1 (2011).

[17] D. Hill, T. Kasprzyk, J. Jarmer, S. Penttilä, M. Krumpolc, G. Hoffmann, and M. Purcell, Nuclear Instruments and Methods in Physics Research Section A: Accelerators, Spectrometers, Detectors and Associated Equipment **277**, 319 (1989).

[18] V. K. Michaelis, E. Markhasin, E. Daviso, J. Herzfeld, and R. G. Griffin, The journal of physical chemistry letters **3**, 2030 (2012).

[19] D. Crabb and W. Meyer, Annual Review of Nuclear and Particle Science **47**, 67 (1997).

[20] C. Keith, in *XVIth International Workshop in Polarized Sources, Targets, and Polarimetry (PSTP2015)*2015), p. 13.

[21] C. Keith, A Dynamically Polarized Solid Target for CLAS12, 2018.

[22] G. Baum *et al.*, Physical Review Letters **51**, 1135 (1983).

[23] J. Antille *et al.*, Nuclear Physics B **185**, 1 (1981).

[24] P. R. Cameron *et al.*, Physical Review D **32**, 3070 (1985).

[25] P. Roubeau, J. Ezratty, H. Glättli, J. Vermeulen, and M. Borghini, Nuclear Instruments and Methods **82**, 323 (1970).

[26] T. Niinikoski and F. Udo, Nuclear Instruments and Methods **134**, 219 (1976).

[27] A. Thomas *et al.*, Physics of Particles and Nuclei **44**, 964 (2013).

[28] H. Dutz *et al.*, Nuclear Instruments and Methods in Physics Research Section A: Accelerators, Spectrometers, Detectors and Associated Equipment **340**, 272 (1994).

[29] P. Kapitza, Physical Review **60**, 354 (1941).

[30] A. Honig, Physical Review Letters **19**, 1009 (1967).

[31] M. Lowry *et al.*, in *Proceedings of the XVth International Workshop on Polarized Sources*2013), p. 15.

[32] E. Hughes and R. Voss, Annual Review of Nuclear and Particle Science **49**, 303 (1999).

[33] T. Liu, T. Averett, D. Crabb, D. Day, J. McCarthy, and O. Rondon, Nuclear Instruments and Methods in Physics Research Section A: Accelerators, Spectrometers, Detectors and Associated Equipment **405**, 1 (1998).
[34] C. Keith, J. Brock, C. Carlin, T. Kageya, V. Lagerquist, J. Maxwell, and P. Pandey, (2023).
[35] P. Pandey, J. Brock, T. Kageya, C. Keith, S. Kuhn, V. Lagerquist, J. Maxwell?, and X. Wei?, (2023).
[36] P. Rossi, in *International Workshop on Hadron Structure and Spectroscopy 2023" (IWHSS-2023)*Prague, Czechia, 2023).
[37] J. Keeler, *Understanding NMR spectroscopy* (John Wiley & Sons, 2010).
[38] J. Eills *et al.*, Chemical reviews **123**, 1417 (2023).
[39] M. Albert, G. Cates, B. Driehuys, W. Happer, B. Saam, C. Springer Jr, and A. Wishnia, Nature **370**, 199 (1994).
[40] H. Günther, *NMR spectroscopy: basic principles, concepts and applications in chemistry* (John Wiley & Sons, 2013).
[41] S. Meiboom, Rev Sci Instrum **29**, 688 (1959).
[42] T. R. Carver and C. P. Slichter, Physical Review **92**, 212 (1953).
[43] T. R. Carver and C. P. Slichter, Physical Review **102**, 975 (1956).
[44] C. R. Bowers and D. P. Weitekamp, Physical Review Letters **57**, 2645 (1986).
[45] E. Tzimas, C. Filiou, S. D. Peteves, and J.-B. Veyret, EU Commission, JRC Petten, EUR 20995EN, 1511 (2003).
[46] C. R. Bowers and D. P. Weitekamp, Journal of the American Chemical Society **109**, 5541 (1987).
[47] J. Natterer and J. Bargon, Progress in Nuclear Magnetic Resonance Spectroscopy **31**, 293 (1997).
[48] M. H. Levitt, *Spin dynamics: basics of nuclear magnetic resonance* (John Wiley & Sons, 2008).
[49] R. W. Adams *et al.*, Science **323**, 1708 (2009).
[50] A. N. Pravdivtsev, A. V. Yurkovskaya, H. M. Vieth, K. L. Ivanov, and R. Kaptein, ChemPhysChem **14**, 3327 (2013).
[51] A. N. Pravdivtsev, K. L. Ivanov, A. V. Yurkovskaya, P. A. Petrov, H.-H. Limbach, R. Kaptein, and H.-M. Vieth, Journal of Magnetic Resonance **261**, 73 (2015).
[52] D. A. Barskiy, S. Knecht, A. V. Yurkovskaya, and K. L. Ivanov, Progress in Nuclear Magnetic Resonance Spectroscopy **114-115**, 33 (2019).
[53] R. V. Shchepin, D. A. Barskiy, A. M. Coffey, T. Theis, F. Shi, W. S. Warren, B. M. Goodson, and E. Y. Chekmenev, ACS Sensors **1**, 640 (2016).
[54] M. L. Truong, T. Theis, A. M. Coffey, R. V. Shchepin, K. W. Waddell, F. Shi, B. M. Goodson, W. S. Warren, and E. Y. Chekmenev, The Journal of Physical Chemistry C **119**, 8786 (2015).
[55] A. S. Kiryutin, A. V. Yurkovskaya, H. Zimmermann, H.-M. Vieth, and K. L. Ivanov, Magnetic Resonance in Chemistry **56**, 651 (2018).
[56] B. J. Tickner, M. Dennington, B. G. Collins, C. A. Gater, T. F. Tanner, A. C. Whitwood, P. J. Rayner, D. P. Watts, and S. B. Duckett, ACS catalysis **14**, 994 (2024).
[57] M. J. Cowley *et al.*, Journal of the American Chemical Society **133**, 6134 (2011).
[58] W. Iali, P. J. Rayner, A. Alshehri, A. J. Holmes, A. J. Ruddlesden, and S. B. Duckett, Chemical science **9**, 3677 (2018).
[59] R. E. Mewis, R. A. Green, M. C. Cockett, M. J. Cowley, S. B. Duckett, G. G. Green, R. O. John, P. J. Rayner, and D. C. Williamson, The Journal of Physical Chemistry B **119**, 1416 (2015).
[60] E. B. Dücker, L. T. Kuhn, K. Münnemann, and C. Griesinger, Journal of Magnetic Resonance **214**, 159 (2012).
[61] S. S. Roy, K. M. Appleby, E. J. Fear, and S. B. Duckett, The Journal of Physical Chemistry Letters **9**, 1112 (2018).

[62] P. J. Rayner, B. J. Tickner, W. Iali, M. Fekete, A. D. Robinson, and S. B. Duckett, Chemical Science **10**, 7709 (2019).
[63] P. M. Richardson, A. J. Parrott, O. Semenova, A. Nordon, S. B. Duckett, and M. E. Halse, Analyst **143**, 3442 (2018).
[64] A. M. Olaru, T. B. Robertson, J. S. Lewis, A. Antony, W. Iali, R. E. Mewis, and S. B. Duckett, ChemistryOpen **7**, 97 (2018).
[65] A. M. Olaru, A. Burt, P. J. Rayner, S. J. Hart, A. C. Whitwood, G. G. Green, and S. B. Duckett, Chemical Communications **52**, 14482 (2016).
[66] M. J. Burns, P. J. Rayner, G. G. Green, L. A. Highton, R. E. Mewis, and S. B. Duckett, The Journal of Physical Chemistry B **119**, 5020 (2015).
[67] P. J. Rayner, P. Norcott, K. M. Appleby, W. Iali, R. O. John, S. J. Hart, A. C. Whitwood, and S. B. Duckett, Nature Communications **9**, 4251 (2018).
[68] M. Fekete, F. Ahwal, and S. B. Duckett, The Journal of Physical Chemistry B **124**, 4573 (2020).
[69] P. Norcott, M. J. Burns, P. J. Rayner, R. E. Mewis, and S. B. Duckett, Magnetic Resonance in Chemistry **56**, 663 (2018).
[70] P. J. Rayner, M. J. Burns, A. M. Olaru, P. Norcott, M. Fekete, G. G. Green, L. A. Highton, R. E. Mewis, and S. B. Duckett, Proceedings of the National Academy of Sciences **114**, E3188 (2017).
[71] W. Iali, S. S. Roy, B. J. Tickner, F. Ahwal, A. J. Kennerley, and S. B. Duckett, Angewandte Chemie **131**, 10377 (2019).
[72] P. J. Rayner, J. P. Gillions, V. D. Hannibal, R. O. John, and S. B. Duckett, Chemical Science **12**, 5910 (2021).
[73] R. V. Shchepin, M. L. Truong, T. Theis, A. M. Coffey, F. Shi, K. W. Waddell, W. S. Warren, B. M. Goodson, and E. Y. Chekmenev, The Journal of Physical Chemistry Letters **6**, 1961 (2015).
[74] C. M. Wong, M. Fekete, R. Nelson-Forde, M. R. Gatus, P. J. Rayner, A. C. Whitwood, S. B. Duckett, and B. A. Messerle, Catalysis science & technology **8**, 4925 (2018).
[75] D. A. Barskiy, A. N. Pravdivtsev, K. L. Ivanov, K. V. Kovtunov, and I. V. Koptyug, Physical Chemistry Chemical Physics **18**, 89 (2016).
[76] A. Duchowny, J. Denninger, L. Lohmann, T. Theis, S. Lehmkuhl, and A. Adams, International Journal of Molecular Sciences **24**, 2465 (2023).
[77] G. Gary, Chemical Communications **51**, 9857 (2015).
[78] A. Dias, C. Gonçalves, J. Legido, J. Coutinho, and I. Marrucho, Fluid phase equilibria **238**, 7 (2005).
[79] J. G. Riess, Artificial cells, blood substitutes, and biotechnology **33**, 47 (2005).
[80] J. Ettedgui *et al.*, Angewandte Chemie International Edition **63**, e202407349 (2024).
[81] M. Büscher, A. Boukharov, A. Semenov, A. Gerasimov, V. Chernetsky, and P. Fedorets, International Journal of Modern Physics E **18**, 505 (2009).
[82] J. H. Ardenkjær-Larsen, B. Fridlund, A. Gram, G. Hansson, L. Hansson, M. H. Lerche, R. Servin, M. Thaning, and K. Golman, Proceedings of the National Academy of Sciences **100**, 10158 (2003).
[83] S. Knecht *et al.*, Proceedings of the National Academy of Sciences **118**, e2025383118 (2021).
[84] A. B. Schmidt, H. de Maissin, I. Adelabu, S. Nantogma, J. Ettedgui, P. TomHon, B. M. Goodson, T. Theis, and E. Y. Chekmenev, ACS sensors **7**, 3430 (2022).
[85] M. Gierse *et al.*, Journal of the American Chemical Society **145**, 5960 (2023).
[86] W. Meyer, K. Althoff, W. Havenith, H. Riechert, E. Schilling, and G. Sternal, Nuclear Instruments and Methods in Physics Research **215**, 65 (1983).
[87] R. E. Mewis *et al.*, Magnetic Resonance in Chemistry **52**, 358 (2014).
[88] W. Iali, A. M. Olaru, G. G. Green, and S. B. Duckett, Chemistry–A European Journal **23**, 10491 (2017).
[89] D. A. Barskiy, L. A. Ke, X. Li, V. Stevenson, N. Widarman, H. Zhang, A. Truxal, and A. Pines, The Journal of Physical Chemistry Letters **9**, 2721 (2018).
[90] T. B. Robertson, L. J. Clarke, and R. E. Mewis, Molecules **27**, 332 (2022).

[91] K. M. Appleby, R. E. Mewis, A. M. Olaru, G. G. Green, I. J. Fairlamb, and S. B. Duckett, Chemical Science **6**, 3981 (2015).
[92] R. W. Adams, S. B. Duckett, R. A. Green, D. C. Williamson, and G. G. Green, The Journal of chemical physics **131** (2009).
[93] S. Huber, G. Grassi, and A. Bauder*, Molecular Physics **103**, 1395 (2005).
[94] L. S. Lloyd *et al.*, Catalysis science & technology **4**, 3544 (2014).
[95] C. A. Gater, O. J. Mayne, B. G. Collins, K. J. Evans, E. M. Storr, A. C. Whitwood, D. P. Watts, B. J. Tickner, and S. B. Duckett, The Journal of Physical Chemistry Letters **16**, 510 (2024).
[96] J. R. Zimmerman and D. Williams, Physical Review **76**, 350 (1949).
[97] P. J. Rayner, M. Fekete, C. A. Gater, F. Ahwal, N. Turner, A. J. Kennerley, and S. B. Duckett, Journal of the American Chemical Society **144**, 8756 (2022).
[98] L. A. Colnago, F. D. Andrade, A. A. Souza, R. B. Azeredo, A. A. Lima, L. M. Cerioni, T. M. Osán, and D. J. Pusiol, Chemical Engineering & Technology **37**, 191 (2014).
[99] F. Dalitz, M. Cudaj, M. Maiwald, and G. Guthausen, Progress in nuclear magnetic resonance spectroscopy **60**, 52 (2012).
[100] E. V. Stanbury, P. M. Richardson, and S. B. Duckett, Catalysis science & technology **9**, 3914 (2019).
[101] H. Zeng *et al.*, Journal of magnetic resonance **237**, 73 (2013).
[102] V. I. Bakhmutov, *Practical nuclear magnetic resonance relaxation for chemists* (John Wiley & Sons, 2005).
[103] P. J. Hore, *Nuclear magnetic resonance* (Oxford University Press, USA, 2015).
[104] E. J. Fear, A. J. Kennerley, P. J. Rayner, P. Norcott, S. S. Roy, and S. B. Duckett, Magnetic Resonance in Medicine **88**, 11 (2022).
[105] J. Wang, Y. Tian, Y. Zhao, and K. Zhuo, Green Chemistry **5**, 618 (2003).
[106] T. H. Maiman, nature **187**, 493 (1960).
[107] H. Haken, Physics Bulletin **28**, 412 (1977).
[108] N. F. Ramsey, Metrologia **1**, 7 (1965).
[109] T. Chupp, R. Hoare, R. Walsworth, and B. Wu, Physical review letters **72**, 2363 (1994).
[110] M. Suefke, S. Lehmkuhl, A. Liebisch, B. Blümich, and S. Appelt, Nature Physics **13**, 568 (2017).
[111] S. Appelt, A. Kentner, S. Lehmkuhl, and B. Blümich, Progress in nuclear magnetic resonance spectroscopy **114**, 1 (2019).
[112] B. Joalland, N. M. Ariyasingha, S. Lehmkuhl, T. Theis, S. Appelt, and E. Y. Chekmenev, Angewandte Chemie **132**, 8732 (2020).
[113] A. N. Pravdivtsev, F. D. Sönnichsen, and J. B. Hövener, ChemPhysChem **21**, 667 (2020).
[114] S. Appelt, S. Lehmkuhl, S. Fleischer, B. Joalland, N. M. Ariyasingha, E. Y. Chekmenev, and T. Theis, Journal of Magnetic Resonance **322**, 106815 (2021).
[115] A. Einstein, Phys Zeit **18**, 121 (1917).
[116] W. Meyer, Nuclear Instruments and Methods in Physics Research Section A: Accelerators, Spectrometers, Detectors and Associated Equipment **526**, 12 (2004).
[117] W. Meyer, K. Althoff, W. Havenith, O. Kaul, H. Riechert, E. Schilling, G. Sternal, and W. Thiel, Nuclear Instruments and Methods in Physics Research Section A: Accelerators, Spectrometers, Detectors and Associated Equipment **227**, 35 (1984).
[118] C. Keith, in *25th International Symposium on Spin Physics*2024), p. 214.
[119] P. Adderley *et al.*, Physical Review Accelerators and Beams **27**, 084802 (2024).
[120] A. Thomas, in *EPJ Web of Conferences* (EDP Sciences, 2016), p. 01008.
[121] K.-H. Kaiser *et al.*, Nuclear Instruments and Methods in Physics Research Section A: Accelerators, Spectrometers, Detectors and Associated Equipment **593**, 159 (2008).
[122] T. Hammel *et al.*, Nuclear Instruments and Methods in Physics Research Section A: Accelerators, Spectrometers, Detectors and Associated Equipment **564**, 1 (2006).
[123] V. Sokhoyan, in *EPJ Web of Conferences* (EDP Sciences, 2020), p. 01017.

[124] J. McGeorge *et al.*, The European Physical Journal A **37**, 129 (2008).
[125] G. F. Knoll, *Radiation detection and measurement* (John Wiley & Sons, 2010).
[126] A. Jankowiak, The European Physical Journal A-Hadrons and Nuclei **28**, 149 (2006).
[127] M. Shepherd and G. Collaboration, in *AIP Conference Proceedings* (American Institute of Physics, 2009), pp. 816.
[128] H. Al Ghoul *et al.*, in *AIP Conference Proceedings* (AIP Publishing, 2016).
[129] G. contributors, Run Coordinator report: Fall 2017, 2018.
[130] F. Afzal, M. Dalton, A. Deur, P. Hurck, C. Keith, V. Mathieu, S. Sirca, and Z. Yu, arXiv preprint arXiv:2407.06429 (2024).
[131] M. Dalton, A. Deur, C. Keith, S. Širca, and J. Stevens, arXiv preprint arXiv:2008.11059 (2020).
[132] K. Sheberstov, E. Van Dyke, J. Xu, R. Kircher, L. Chuchkova, Y. Hu, S. Alvi, D. Budker, and D. A. Barskiy, Journal of Magnetic Resonance Open **23**, 100194 (2025).
[133] R. Kircher, J. Xu, and D. A. Barskiy, Journal of the American Chemical Society **146**, 514 (2023).
[134] J. W. Blanchard, B. Ripka, B. A. Suslick, D. Gelevski, T. Wu, K. Münnemann, D. A. Barskiy, and D. Budker, Magnetic Resonance in Chemistry **59**, 1208 (2021).
[135] S. B. Duckett and C. J. Sleigh, Progress in Nuclear Magnetic Resonance Spectroscopy **34**, 71 (1999).
[136] S. Stepanyan, V. Burkert, L. Elouadrhiri, M. Mestayer, M. Ungaro, and V. Ziegler, CLAS12 Upgrade for High Luminosity Operations - Task Force Report, 2020.
[137] S. Mango, Ö. Runólfsson, and M. Borghini, Nuclear Instruments and Methods **72**, 45 (1969).
[138] J. B. Hövener, S. Bär, J. Leupold, K. Jenne, D. Leibfritz, J. Hennig, S. B. Duckett, and D. von Elverfeldt, NMR in Biomedicine **26**, 124 (2013).
[139] M. Mikirtychyants *et al.*, in *Journal of Physics: Conference Series* (IOP Publishing, 2011), p. 012148.
[140] C. Ekström and C. W. Collaboration, Physica Scripta **2002**, 169 (2002).